Characterization of industrial high speed steel roll material and effect of annealing prior to heat treatment on the structure and properties

By

Jacobus Jonck

Supervisor: **Prof. W.E. Stumpf**

Co-supervisor: **Dr. C.W. Siyasiya**

Submitted in partial fulfillment of the requirement for the degree

Master of Engineering (Metallurgy)

In the

Department of Materials Science and Metallurgical Engineering

Faculty of Engineering, Built Environment & Information Technology

University of Pretoria

South Africa

March 2017

Preface

This dissertation is submitted for the degree of MEng at the University of Pretoria. The research described herein was conducted under the supervision of Prof W.E. Stumpf and Dr C.W. Siyasiya in the department of Materials Science and Metallurgical Engineering, University of Pretoria.

Except where acknowledgements and references are made to the previous work, this work is to the best of my knowledge original. This dissertation is the result of my own work except where specifically indicated in the text. Neither this nor any substantially similar dissertation under my name has been or is being submitted elsewhere for any other degree, diploma or other qualification.

Jacobus Jonck

Date: 3 March 2017

Acknowledgements

I would like to express my sincere gratitude to the following people and institutes:

- My Lord Jesus Christ for giving me this great opportunity and the ability to undertake this study.

- My wife, for all her love and support, especially when things become overwhelming.

- Prof. Waldo Stumpf and Dr. Charles Siyasiya for your friendship, guidance and insight to help me extend my technical proficiency and grow as a professional.

- Mintek for the financial support and exceptional facilities.

- NFTN for your financial support.

- Sarco for supplying the raw material utilised and technical expertise.

- Eskom research and innovation centre for the impact testing facilities.

- Melanie Smit for all the helpful discussions, encouragement and countless proof reads.

- Richard Couperthwaite for your enthusiasm and prompt assistance with both the SEM and XRD analysis which never ceases to amaze me.

- "Oom" Peet van Tonder for friendship, technical/personal guidance and igniting a passion for the wonder that is roll metallurgy.

- Jacques Calitz for assistance with the impact testing and interpretation of the instrumented data.

- Linda Malatji from the CSIR for assistance with some of the STA analysis.

- Edson Mahuma and Eddie Innes for your assistance with some of the sample preparation.

Characterization of industrial high speed steel roll material and effect of annealing prior to heat treatment on the structure and properties

Author: **Jacobus Jonck**

Supervisor: **Prof Waldo E. Stumpf and Dr Charles W. Siyasiya**

Department of Materials Science and Metallurgical Engineering

University of Pretoria

Master of Engineering (Materials Science and Metallurgical Engineering)

Synopsis

Hot strip mills (HSM) are used to roll cast slabs down from their initial size to plate or sheet, which is then used to manufacture a wide variety of goods for many industrial markets. The working rolls that contact and deform the strip are arguably the primary element of the hot strip mills. The work rolls must have sufficient strength to apply the mechanical force to the strip, while still resisting the wear and thermal stresses inherent to the process. The history of the development of these work rolls spans more than a hundred years. The more recent advancement in work roll technology was the development of High Speed Steel (HSS) work rolls during the 1990's. The HSS rolls utilise a variety of carbide forming elements to improve the wear resistance.

The South African Roll Company (SARCO) is an established roll producer and the only one in South Africa with a well-established international client base. SARCO is currently developing a range of high quality HSS rolls and has developed an initial HSS grade, which has shown competitive performance and durability in service compared to established HSS alloys from other roll manufacturers. Although the initial trials show great promise, significant potential for development and associated improvements are available.

It has been documented that an additional annealing treatment prior to the regular heat treatment will refine the microstructure of HSS rolls, which should improve mechanical properties and performance. However, although pre-annealing has been documented, the degree of mechanical property improvement associated with the pre-annealing has not been studied and the annealing step does not appear to be commonly applied by roll producers.

The first aim of this research project was to investigate the properties of the HSS material currently produced by SARCO to elucidate the source of the combination of high wear resistance and durability. The roll material identified for characterisation consisted of four sets of samples. These were subjected to intensive characterisation, which included chemical analysis, ferrite scope measurements, metallography, hardness testing, Scanning Electron Microscopy (SEM) analysis, X-Ray Diffraction (XRD) analysis and Simultaneous Thermal Analysis (STA). The good combination of performance and durability appears to be the product of the Ni additions, W:Mo ratio, high carbon content, high austenitising temperatures and balanced carbide-former additions.

The second objective was to investigate the effect of annealing prior to the typical solution, "soft" quench and tempering heat treatment, on the structure and mechanical properties of the HSS material used for the outer shell of mill rolls. As-cast material was used for the analysis, which was subjected to similar intensive characterisation. High Chromium (HC) used in roll material appears to be more sensitive to both temperature and time variations in heat treatment than HSS. No grain refinement of the HSS material was achieved by the pre-annealing. Higher peak hardness and more gradual reduction in hardness beyond the peak was not found under simulated conditions, indicating that a desired increase in hardness will not be achieved in practice. It was evident that the industrial heat treatment condition cannot be sufficiently simulated by shorter time laboratory tests. The effects of pre-annealing should be researched on lower alloy bainitic HSS material if feasible and the improved wear resistance and toughness benefits of pre-annealing could be quantified by performing industrial trials and fracture toughness testing respectively.

Keywords: High speed steel, roll, annealing.

Publications and Conference Presentations

1. J. Jonck, J.S. Moema, W.E. Stumpf, P. van Tonder and I. Kilongozi: Characterisation of commercial HSS rolls produced at SARCO – Presented at the Microscope Society of Southern Africa annual conference, Pretoria, South Africa, 1-3 December 2015 – Published conference proceedings

2. J. Jonck, J.S. Moema, C.W. Siyasiya and W.E. Stumpf: Review of high speed steel rolls applied in hot strip mills – Submitted to Materials Characterisation 30 January 2017.

3. J. Jonck, J.S. Moema, C.W. Siyasiya and W.E. Stumpf: Relationship between laboratory scale and industrial simulated heat treatment of work rolls – In preparation.

4. J. Jonck, J.S. Moema, C.W. Siyasiya and W.E. Stumpf: Effect of annealing prior to heat treatment on a high speed steel roll – In preparation.

TABLE OF CONTENTS

LIST OF FIGURES

iii

iv

v

ix

xiii

LIST OF TABLES

LIST OF ABBREVIATIONS

HSM	Hot strip mill
CC	Centrifugal casting
SG	Spheroidal graphite
HSS	High speed steel
MCWCI	Multi-Component white cast iron
HC	High chromium
SARCO	South African Roll Company
IC	Indefinite chill
SCE	Stoichiometric Carbon Equivalent
REE	Rare earth element
HT	Hot tearing
GB	Grain boundary
HBHSS	High-boron high speed steels
DTA	Differential thermal analysis
CCT	Continuous cooling transformation
TTT	Time temperature transformation
LMP	Larson Miller Parameter
EMF	Electromagnetic field
NDT	Non-destructive testing
XRD	X-ray diffraction
SEM	Scanning electron microscopy
STA	Simultaneous thermal analysis
EDM	Electrical discharge machining
HRSEM	High-resolution scanning electron microscopy

LIST OF SYMBOLS

W_{eq} = Tungsten equivalent

γ = austenite

L = liquid

M_s = Martensite transformation start temperature

M_f = Martensite transformation finish temperature

μ_f = Friction coefficient

T = Torque

P = Load

R = Outer radius

d = density

r = Inner radius

β = Correction factor

S = Standard deviation

X = Mean value

X_i = Individual measurement

N = Total number of measurements

CV = Coefficient of variance

CL = Confidence limit

RA = Relative accuracy

t = Constant which varies with N

1. CHAPTER 1: INTRODUCTION

Hot strip mills (HSM) are used to roll cast slabs down from their initial size to plate or sheet, which are then used to manufacture a wide variety of goods for many industrial markets. The working rolls that contact and deform the strip are arguably the primary element of the hot strip mills, see Figure 1-1. These rolls are also responsible for 5-15% of the overall production cost [1]. The work rolls must have sufficient strength/hardness to apply the mechanical force to the strip, while still resisting the wear and thermal stresses inherent to the process. Roll materials are typically very hard and brittle and as a result the entire roll cannot be produced from a single material as "hard material" will result in good wear resistance but poor durability and "soft material" will result in good ductility but poor wear resistance. Hence the work rolls are typically composite rolls, consisting of a high hardness, wear resistant shell material with a lower hardness and more ductile core. Spheroidal graphite (SG) cast iron is typically used for the core.

Figure 1-1: Roll change at the 7 stand HSM at China Steel Corporation Taiwan.

Composite rolls are commonly produced via centrifugal casting (CC) or spin casting, see Figure 1-2. The CC process utilises a ceramic coated steel cylinder (chill), which is spun at high revolutions before casting the shell material into the cylinder. The centrifugal forces distribute the molten metal along the circumference of the chill enabling the solidification of the shell in the required shape. The centrifugal forces also ensure compactness of the shell material and reduce porosity and other defects. The chill is then covered by a SG buffer zone of about 15 mm thickness through spin

1

casting where after the SG core is cast in a stationary and vertical standing shell/buffer zone combination, see Figure 1-3.

Figure 1-2: Photograph of a rotating chill (>1000rpm) containing shell material.

(a)

1-Casting ladle, 2-Mold, 3- Electric motor, 4- Idler stand, 5- Idler roller, 6- Liquid metal
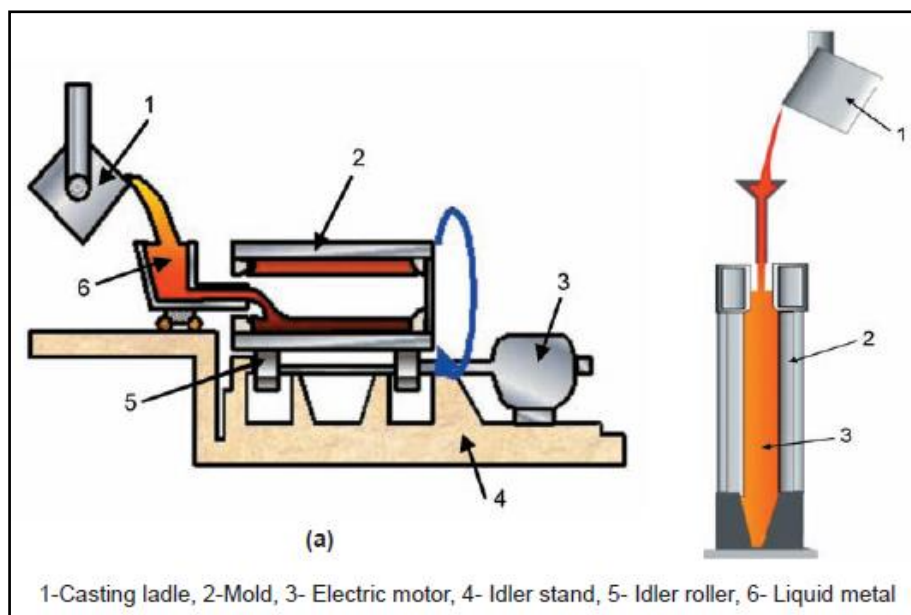
Figure 1-3: Schematic diagram of the horizontal spin casting of the shell, and vertical casting of the core [1].

There are several types of alloys being used in roll manufacture for the flat products steel production industry. The specific alloy depends on the intended purpose. The use of High Speed Steel (HSS) or Multi-Component White Cast Iron (MCWCI) rolls are relatively new developments, with advantages far outweighing preceding materials. HSS rolls were first introduced towards the end of the 1980's, see Figure 1-4. The innovation originated from the observation that HSM's require rolls to retain high strength at high temperatures similar to high speed tool steels. HSS rolls have

2

significant economic benefits over other rolls due to superior performance attributed to its low wear rates and excellent surface finish [2]. This has resulted in widespread replacement of traditional High Chromium (HC) rolls with HSS rolls.
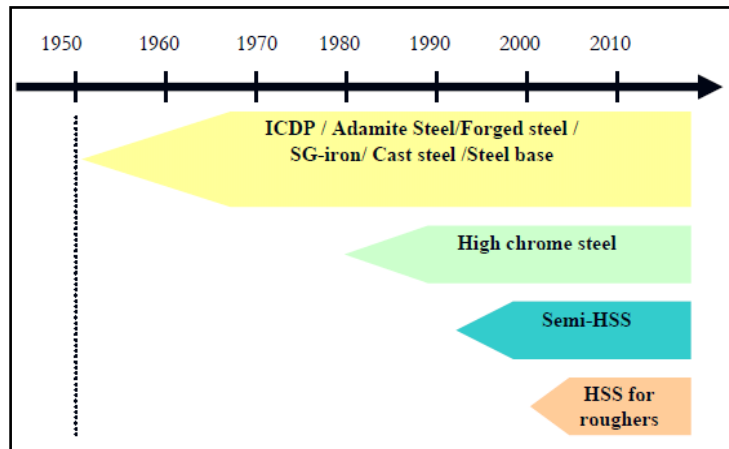
Figure 1-4: History of roughing mill work roll introduction [3].

The HSS rolls utilise a variety of carbide forming elements to improve the wear resistance up to three times, compared to HC rolls. The carbon content and carbides have also been optimised for improved toughness making the HSS rolls more durable. This has led to the rapid replacement of the HC rolls with HSS rolls in mills around the world, and it is expected that the HC rolls will eventually become obsolete.

The South African Roll Company (SARCO) is an established roll producer, one of only a few world-wide and the only roll producer in South Africa. SARCO supplies rolls to mills across the world, including South Africa, China, Taiwan, Germany, Brazil, India, America etc. A wide variety of rolls including profile rolls, back-up rolls and more importantly work rolls for flat product HSM's are produced. Traditionally only indefinite chill (IC) and HC work rolls were produced but recently a HSS roll grade was developed. In order to remain competitive within the challenging roll market and ensure its sustainability, SARCO needs to develop and produce high quality HSS rolls.

© University of Pretoria

1.1. Problem Statement

Initial feedback on service performance has shown that the trial HSS roll produced by SARCO compares well with the established HSS rolls while maintaining a high level of durability.

Modification of the typical heat treatment has also been proposed as a method to strengthen the matrix without deteriorating the toughness. The modification entails a pre-annealing heat treatment prior to austenitising. However, there is no literature available on the extent of improvement and the effect on the mechanical properties.

1.2. Objectives

The aim of this study was to investigate the structure and properties of the HSS rolls currently produced by SARCO to identify the roll characteristics. The HSS material will also be used to investigate the effect of the modification in heat treatment on the mechanical properties.

The expected outcomes of this research project were defined as follows:

I.   Confirm the attributes responsible for the performance and durability of the HSS roll material produced by SARCO.

II. Quantify the effects of the modification in heat treatment on the HSS roll material to asses if it would be amenable to industrial production.

4

2. CHAPTER 2: HSS ROLL METALLURGY

2.1. Chemical Composition

The definition of HSS rolls is encompassed in its chemical composition: Material considered to be HSS, mostly is defined when the sum of the carbon and carbide forming elements exceed 15% [2]. The mechanical properties and physical behaviour of the HSS rolls are strongly dependant on the chemical composition. Since the rolls are applied in a variety of different mills and at various stages in the mills, the HSS rolls are being produced over a wide range of compositions to meet the specific required mechanical properties, see Table 2-1. Table 2-1 also shows the optimal chemical composition in terms of wear resistance and toughness as determined by a variety of authors. The optimal compositional range agrees well with the specifications of many industrial roll manufacturers around the world [4]. The chemistry of HSS rolls has to be tailored for a specific stand in order to achieve good roll performance [2].

Table 2-1: Chemical compositions for HSS roll production [2, 5-12].

Weight %	C	W	Mo	Cr	V	Nb	Ti
HSS Range	1.4-3.0	0.0-8.0	0.5-6.0	3.0-8.0	2.8-10.0	0.0-4.0	<0.50
Optimal	1.9-2.0	3.0-4.0	3.0-4.0	5.0-7.0	4.0-6.0	1.0-2.0	-
Weight %	**Si**	**Mn**	**Ni**	**Co**	**S**	**P**	**RE**
HSS Range	0.2-1.2	0.3-1.2	0.3-1.4	0.0-5.0	<0.030	<0.030	<0.20
Optimal	-	-	0.7-0.9	1.0-2.5	<0.025	<0.025	0.04-0.08

RE: Rare Earth elements

One of the reasons why the balance of the chemical composition has a significant influence on the final microstructure is due to the high quantities of carbide formers (W, V, Mo, Cr, Nb and Ti) which determine the type and distribution of carbides formed during solidification [2]. Figure 2-1 shows a summary of the of the most common carbide types found in tool steels and the carbide forming elements associated with them. The different carbide types also span different hardness levels as shown in Figure 2-2 [13]. It should be noted that vanadium is principally associated with the MC carbide type, which is the highest hardness carbide found in HSS and is also critical to the performance of HSS rolls.

Type of carbide	Lattice type	Remarks
M_3C	Orthorhombic	This is a carbide of the cementite (Fe_3C) type, M, maybe Fe, Mn, Cr with a little W, Mo, V.
M_7C_3	Hexagonal	Mostly found in Cr alloy steels. Resistant to dissolution at higher temperatures. Hard and abrasion resistant. Found as a product of tempering high-speed steels.
$M_{23}C_6$	Face-centred cubic	Present in high-Cr steels and all high-speed steels. The Cr can be replaced with Fe to yield carbides with W, and Mo.
M_6C	Face-centred cubic	Is a W or Mo rich carbide. May contain moderate amounts of Cr, V, Co. Present in all high-speed steels. Extremely abrasion resistant.
M_2C	Hexagonal	W- or Mo-rich carbide of the W_2C type. Appears after temper. Can dissolve a considerable amount of Cr.
MC	Face-centred cubic	V-rich carbide. Resists dissolution. Small amount which does dissolve reprecipitates on secondary hardening.

Figure 2-1: General classification and properties of carbides found in tool steels [13].
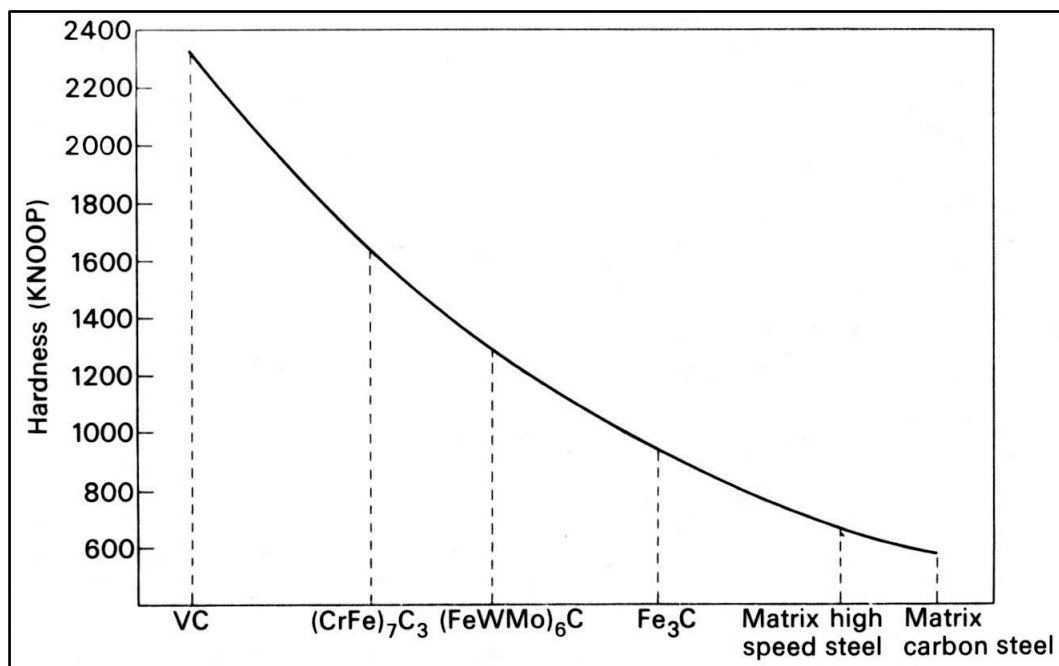
Figure 2-2: Comparison of nominal hardness values of carbides found in tool steels compared to the matrix [13].

6

2.1.1. Carbon

The carbon content has a significant influence on both the carbides and matrix components of the microstructure. The carbon present within the matrix is determined by the type and amounts of carbides formed, which results in a complex relationship between the carbon and the carbides present within the HSS rolls. The influence of carbon on the prevailing carbides is shown in Figure 2-3 [2].
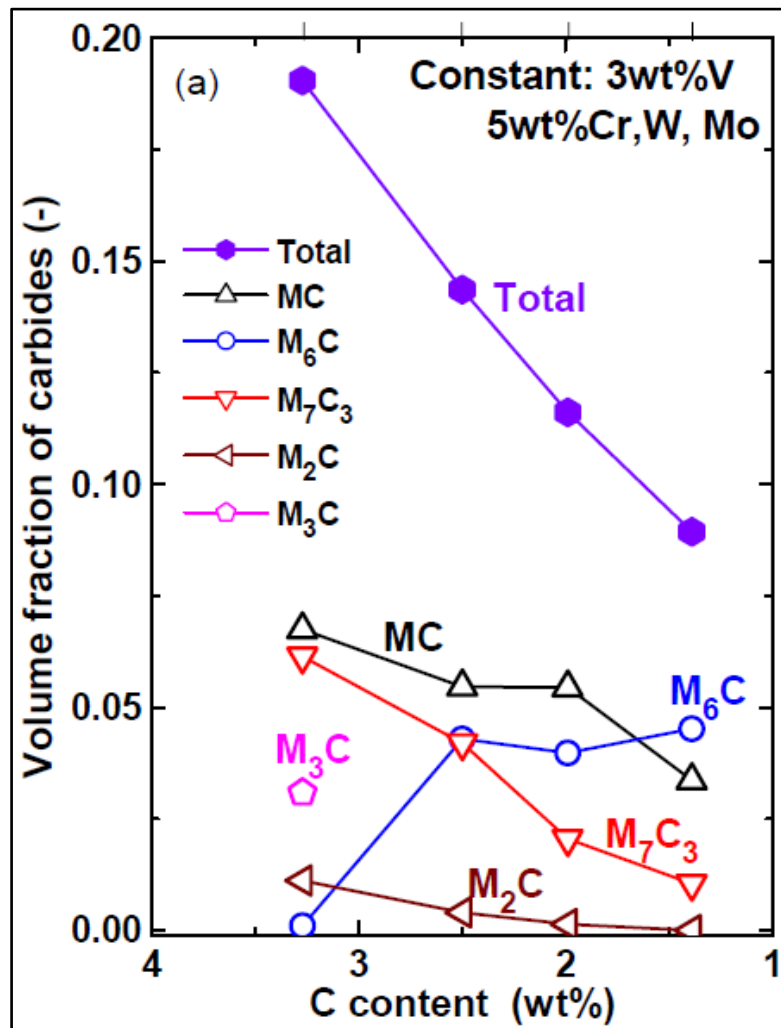
Figure 2-3: Influence of carbon on the prevailing carbides in the microstructure [16].

Typically most of the carbon in solution is consumed by the carbides. About 0.3-0.6%C remains within the grains. The carbon content also determines the type of matrix structure formed. The carbon content is specified to satisfy the following stoichiometry carbon equivalent (SCE) based on the amount of carbide formers in order to maintain the correct amount of carbon in the matrix [8, 14].

SCE = 0.06%Cr + 0.063%Mo + 0.033%W + 0.253%V...(2.1)

7

Carbon generally has a beneficial effect on the wear resistance due to the carbide volume fraction which increases with increasing carbon content. The increase is primarily associated with an increase in the MC carbide volume fraction and to a lesser extent the M_2C carbide volume fraction [2, 14, 15].

2.1.2. Vanadium

Vanadium (V) promotes the formation of MC carbides, while also influencing it's morphology and occurrence [2, 5, 17]. The beneficial effect on the MC carbides comes at the expense of a decrease in the Cr-rich M_7C_3 carbides, due to the effect of V on the eutectic transformation [5, 11], see Figure 2-4.
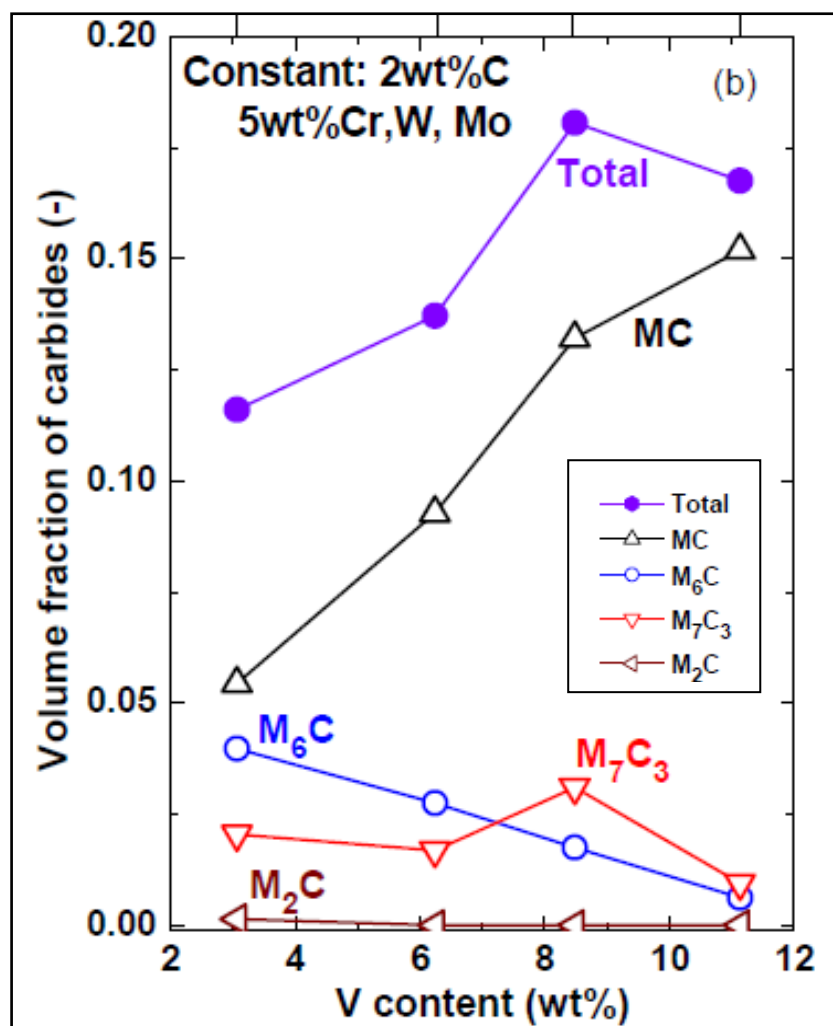
Figure 2-4: Effect of increasing V content on the carbide volume fractions [16].

Unfortunately the increase in MC carbide formation reduces the carbon content of the matrix, which also decreases the matrix's hardness. Lower matrix hardnesses could lead to preferential wear of the matrix and an increase in the friction coefficient [11].

8

At V contents in excess of 8%, it can influence the solidification sequence, enabling MC carbides to form first on solidification prior to the austenite [8].

V has also been found to show a refining effect on the microstructure at higher concentrations [5]. It was also reported that V increases the oxidation potential and can cause catastrophic oxidation if present in excessive amounts [17].

2.1.3. Molybdenum and Tungsten

Molybdenum (Mo) and Tungsten (W) generally show similar behaviour within HSS. They promote the formation of M_2C and M_6C carbides and reduce the formation of the Cr-rich M_7C_3 and $M_{23}C_6$ carbides [2, 18, 19, 20], see Figure 2-5.
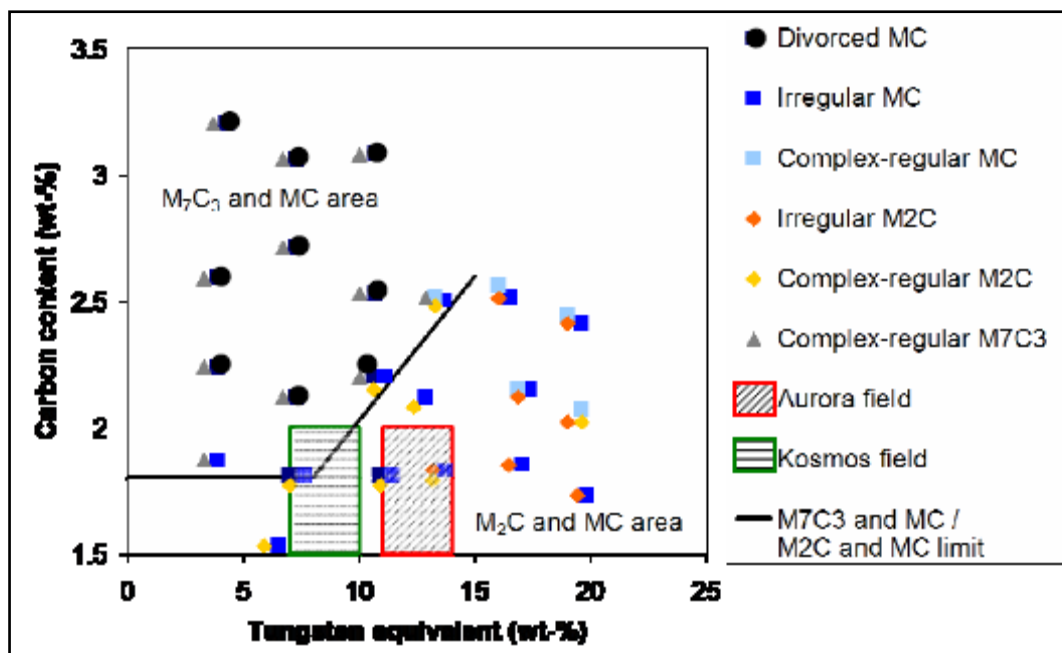
Figure 2-5: Influence of the tungsten-equivalent (W_{eq}) on the prevailing carbides [4].

These elements also improve the distribution of carbides, especially MC [8, 21]. They have a solid solution hardening effect on the matrix and improve the red hot hardness and wear resistance [4, 11]. Generally it was found that in order for Mo to have the same effect as W, it is required to be present in twice the concentration. This effect is expressed as the W-equivalent (W_{eq}) as follows with the W and Mo in weight percentages [11].

$$W_{eq} = W + 2Mo \dots\dots\dots\dots\dots\dots\dots\dots\dots\dots\dots\dots\dots\dots\dots\dots\dots\dots\dots\dots\dots\dots\dots\dots\dots\dots\dots\dots\dots\dots(2.2)$$

A decrease in Cr and an increase in W_{eq} results in a more wear resistant matrix and harder carbides by minimizing the M_7C_3 carbides present and maximizing MC and

9

M_2C carbides [4]. It should be noted that the ratio of W:Mo should also be kept low, in order to form more lath martensite and improve the toughness [8].

W has been found to decrease the austenite starting temperature as well as the total austenite content on solidification [20]. However, contrasting indications have also been found showing that W also appears to increase the as-cast cell size of the microstructure by influencing the formation and transformation temperatures [8]. Mo increases the oxidation potential [17].

2.1.4. Chromium

Chromium (Cr) generally improves the depth of hardening and is the primary contributor to the formation of $M_{23}C_6$ and M_7C_3 carbides [2, 18, 19]. Excessive amounts of Cr can embrittle the HSS due to high quantities of M_7C_3 formed at the cell boundaries. Insufficient amounts of Cr can reduce the M_7C_3 content and promote MC carbide formation, which increases the wear resistance [14]. M_7C_3 carbides can be eliminated entirely by reducing the Cr content to below approximately 5% [22]. However, a low Cr content can lead to the formation of a rough surface during rolling due to the large quantity of hard MC carbides formed. In order to achieve a smooth working surface it is recommended to keep the Cr content in the range of 8-9% [14]. Cr also has a solid solution hardening effect on the matrix [11].

Cr has the strongest influence on the oxidation potential of the HSS rolls of all the alloying elements. The oxidation potential can be significantly decreased with increasing Cr additions [23, 24].

2.1.5. Rare Earth Elements

The primary purpose of Rare Earth Element (REE) additions is to refine the microstructure, by reducing the as-cast cell size. The refining effect with REE additions is due to the increase in primary solidification temperature and decrease in eutectic transformation temperature, which widens the temperature interval of primary solidification. In addition to the change in formation temperatures REE also segregate to the solidification front, which increases the supercooling and increases the solidification rate [12, 19, 25, 26]. The refining effect also improves the hot tearing (HT) resistance during casting and reduces the scrap rate, see Table 2-2 [6].

Table 2-2: Influence of REE additions on hot tearing resistance [6].

Property	Pouring Temperature	HT Force	HT Temperature	Linear Contraction
Unmodified	1480°C	119N	1166°C	1.87%
REE modified	1480°C	158N	1147°C	1.83%

REE also affect carbide morphology by breaking down, homogenising and spheroidizing the carbide networks, which improve the mechanical properties including strength, thermal fatigue and toughness [6, 12, 19, 25, 26], see Figure 2-6.
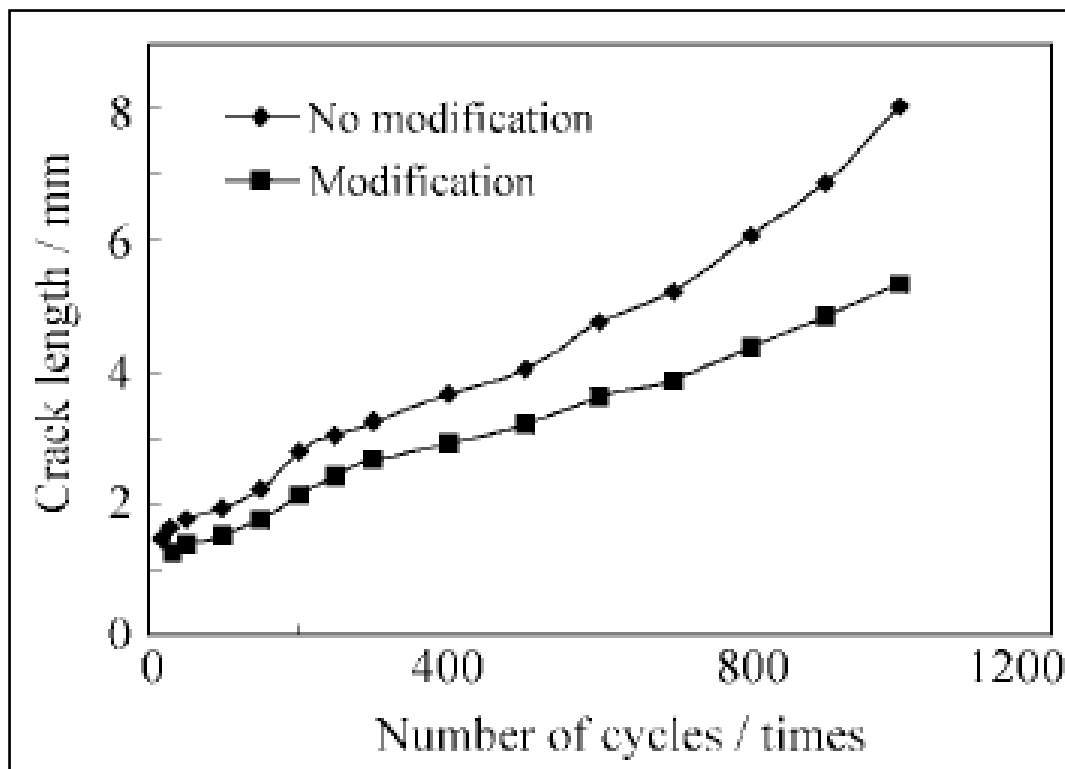
Figure 2-6: Influence of REE modification on thermal fatigue behaviour [6].

The thermal fatigue resistance is improved due to the refinement of the carbide network which reduces the variations in thermal expansion and contraction during service [6]. Apart from the carbide morphology modification, REE has also been found to decrease the carbide content while the alloying elements are consumed by the matrix, which increases the matrix hardness and improves the wear resistance of the steel in general [12, 26], see Figure 2-7.

Cerium (Ce) has been the most widely used REE addition. REE modification has also been combined with the beneficial modification of alkali and alkali earth metals. Magnesium (Mg), Sodium (Na) and Potassium (P) have also been successfully added

11

as complex modifiers such as RE-Al-B-Ti and RE-Mg-Ti [6, 12, 19, 25, 26, 27, 28]. RE-Al-B-Ti also increases the volume fraction of MC carbides while improving the toughness and red hot hardness of the steel [27].
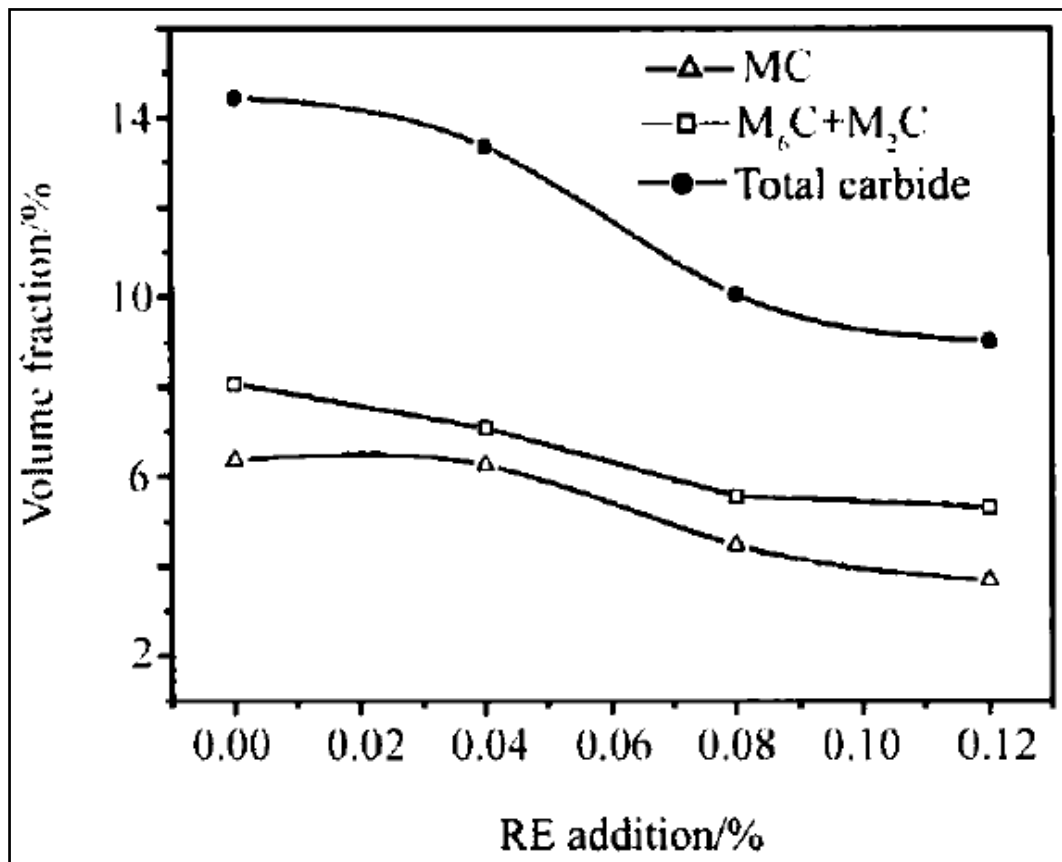
Figure 2-7: Reduction in carbide content with increasing RE additions [12].

2.1.6. Niobium, Cobalt, Aluminium, Nitrogen, and Silicon

Niobium (Nb) behaves similarly to V and promotes the formation of MC carbides and can substitute V [2]. Peak hardness is achieved at Nb levels of approximately 30% of the total V content or 1.0-2.0%Nb [6, 7, 29]. Nb is principally added to reduce MC segregation by increasing the density of MC carbides [6, 7]. Nb also improves the secondary hardening response.

Cobalt (Co) generally increases the matrix hardness, due to secondary hardening during heat treatment, but decreases toughness [30]. The secondary hardening improves both the wear resistance and crack resistance. It is recommended to add 1.0-2.5% Co for optimal results [10].

Aluminium (Al) decreases the decomposition temperature of the M_2C carbides, which reduces the amount of M_2C carbide after the austenitising treatment. This leads to the

12

improvement in toughness. It is recommended to add 0.5-1.2% Al for optimal results [31].

Nitrogen (N) and Silicon (Si) promote the formation of M_6C carbides. Si additions improve the temper hardness by refining the secondary carbides [32]. More significant Si conditions have also been utilised in combination with modification and inoculation procedures to develop graphite containing HSS rolls for the final finishing stands of the HSM [33, 34].

2.1.7. Boron

The addition of Boron (B) to HSS rolls has been investigated by adding minor amounts similar to that typical found in B-containing steels or by substituting some of the carbon in HSS with significant quantities of B. Minor B additions of 0.04% have a cell refining effect due to the increased constitutional supercooling effect associated with the small distribution coefficient of B in Iron (Fe). The refinement also increased the bending strength by 10% and the hardness. B tends to segregate to the grain boundaries (GB's) and improves cohesion while also limiting grain growth during high temperature treatments by lowering the grain boundary's surface energy [35].

The potential of high-boron high speed steels (HBHSS) have also been investigated, but requires significant adjustments in terms of chemical composition, see Table 2-3. The principal change is the reduction in carbon content, which eases the formation of lath martensite and improves the toughness of the matrix. Boron enables the formation of high hardness boro-carbides $M_2(B,C)$, $M_3(B,C)$ and $M_{23}(B,C)_6$, with high wear resistance. The secondary effect is an associated reduction in the Nickel (Ni), Mo and W requirements and hence cost. This makes the possibility of a new generation HBHSS economically attractive as B is inexpensive in comparison to the other carbide forming elements [36].

Table 2-3: Example of the composition of a typical HBHSS [37].

Weight%	C	B	Cr	W	V	Mo	Mn	Si	Ti
HBHSS	1,1-1,3	1,3-1,5	4,8-5,0	0,8-1,0	0,5-0,8	1,2-1,5	0,3-0,6	0,5-0,7	<0,15

Sufficient research and testing on HBHSS has not yet delivered a commercial alloy suitable for service application due to the associated low toughness. However, initial wear testing indicates that the HBHSS could be a more cost effective alternative to traditional HSS in future [36], see Figure 2-8.

13
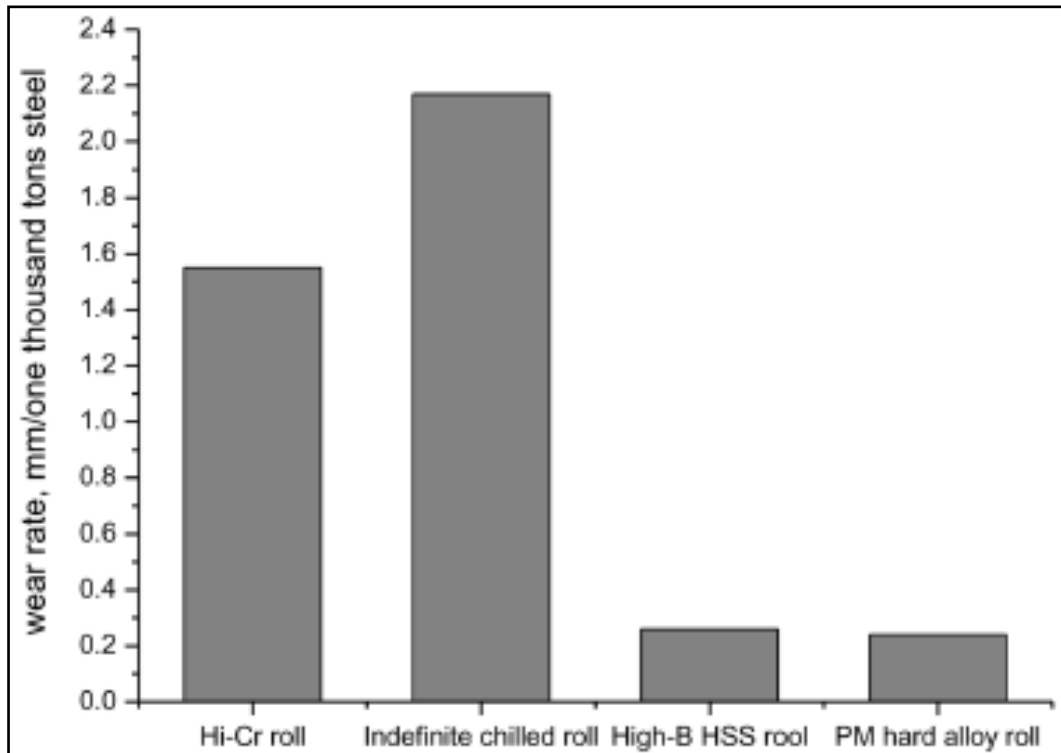
Figure 2-8: Comparison of wear rate of HBHSS with other traditional work rolls [36].

2.2. Microstructures

The as-cast microstructure of HSS rolls typically consist of an austenitic matrix with a variety of carbides including MC, M_2C, M_6C, M_7C_3 and $M_{23}C_6$. The matrix can also contain variable amounts of martensite depending on the chemical composition [8, 11, 38]. There are three types of carbides found within the microstructure. These are primary carbides which form during the initial solidification of the shell and secondary carbides which form mainly during tempering of the shell. The size and distribution of the primary carbides are primarily determined by the solidification conditions (i.e. cooling rate) [2].

The chemical compositions of the carbides in HSS rolls are unique compared to typical HSS material in that significant variation in composition is found within a specific carbide type. This variation is believed to be related to the unique chemical composition and high solidification rates experienced during CC, resulting in highly non-equilibrium solidification conditions. The chemical segregation within the carbides is so severe, that variations in carbide type have been found to occur over the length of the carbides, which is only a couple of microns. The chemical composition of the different carbides as determined by various authors is shown in Table 2-4.

14

Table 2-4: Measured chemical composition of various carbides [4, 8, 19, 22, 39, 40].

Weight %	Cr	W	Mo	V	Fe
MC	2-9	0-21	1-34	31-82	2-24
M_2C	8-23	0-40	18-68	4-14	6-24
M_6C	4-16	3-39	12-27	3-7	13-36
M_7C_3	22-40	1-7	3-8	5-12	27-54

In the as-cast microstructure the M_7C_3 and M_2C carbides are typically located along the cell boundaries of the austenitic matrix while the MC carbides (V rich) are predominantly located within the cells [8, 11, 22, 38, 41], see Figures 2-9 to 2-11.

Figure 2-9: As-cast microstructure etched with Nital, showing MC and M_7C_3 carbides in a 2%W-3%Mo-3.6%V-9%Cr HSS steel [8].

The MC carbides have a rod-like, bulk-like, globular or spherical shape, while the M_2C and M_6C carbides are generally found as needle-like and fishbone-like carbides. The M_7C_3 carbides typically show a brain-like or fishbone-like structure. A lower V content promotes the occurrence of VC carbides at the cell boundaries rather than within the cells [8, 42, 43]. The as-cast microstructure also shows very fine $M_{23}C_6$ carbides within the matrix, which form during the slow cooling after casting [8, 11, 38, 41], see Figure 2-12.

15
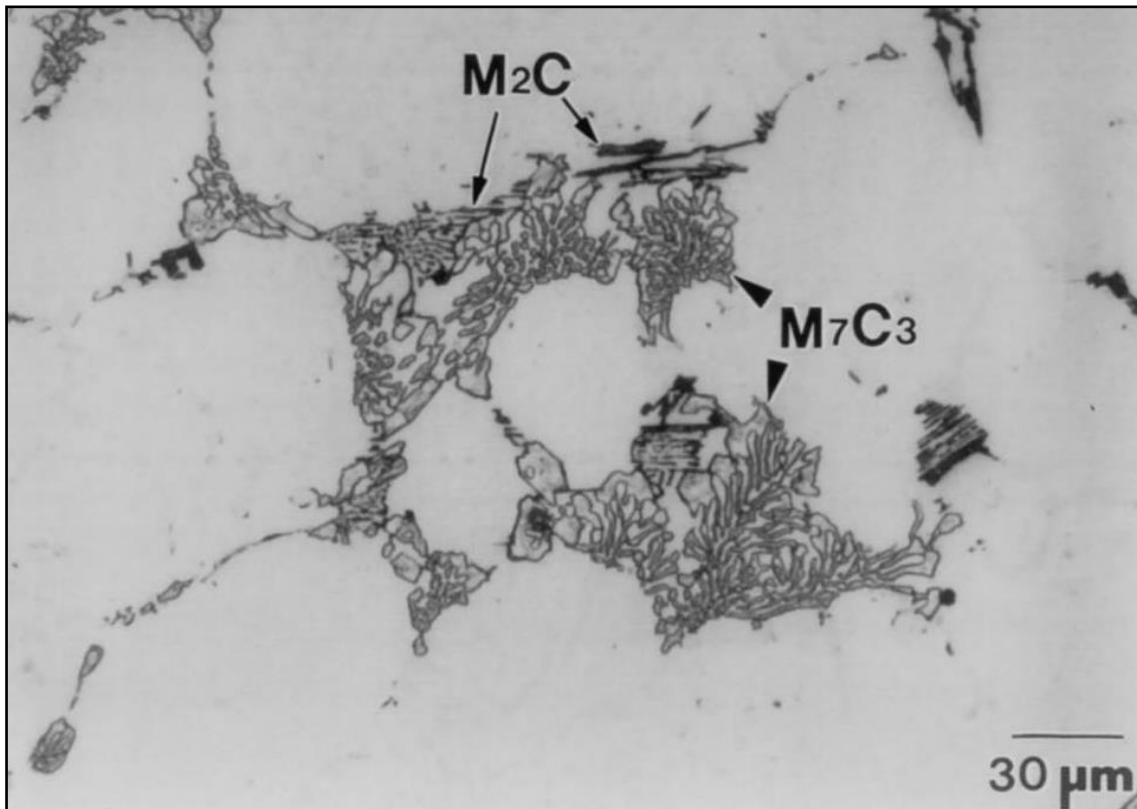
Figure 2-10: As-cast microstructure etched with Murakami's etchant, showing M_2C and M_7C_3 carbides in a 2%W-3%Mo-5%V-9%Cr HSS steel [8].
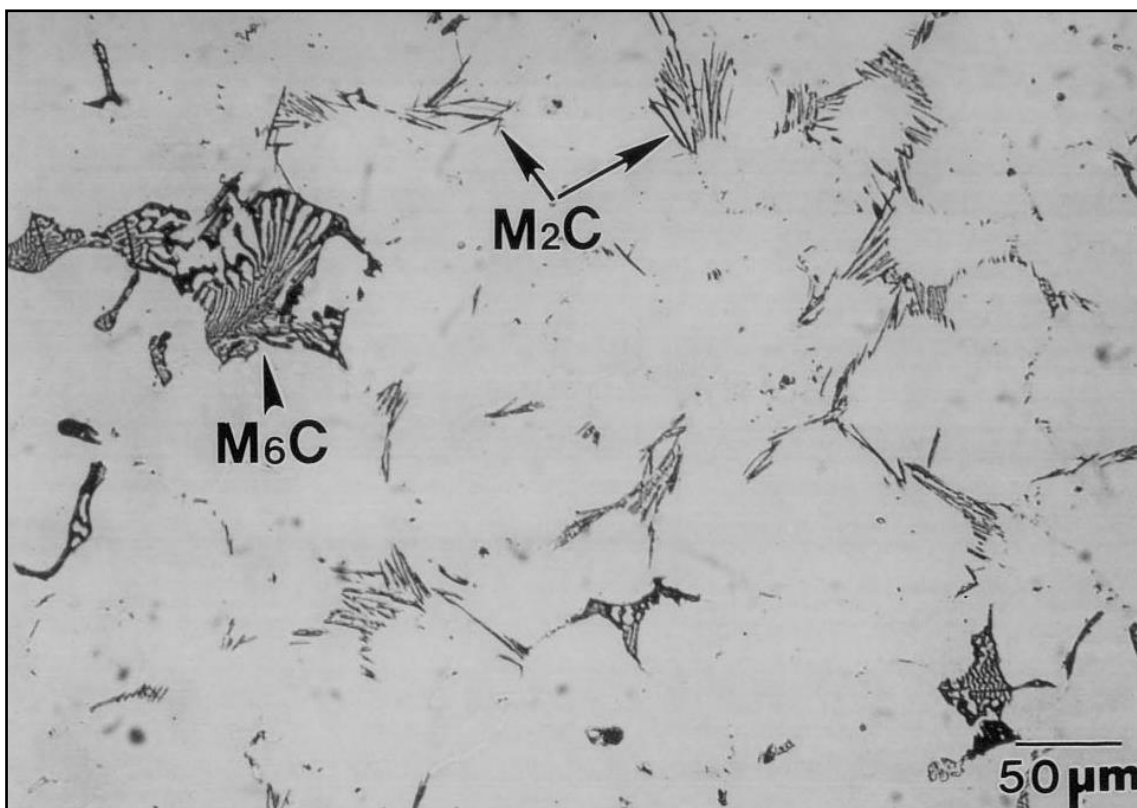
Figure 2-11: As-cast microstructure etched with Murakami's etchant, showing M_2C and M_6C carbides in a 5%W-5%Mo-5%V-5%Cr HSS steel [8].

16
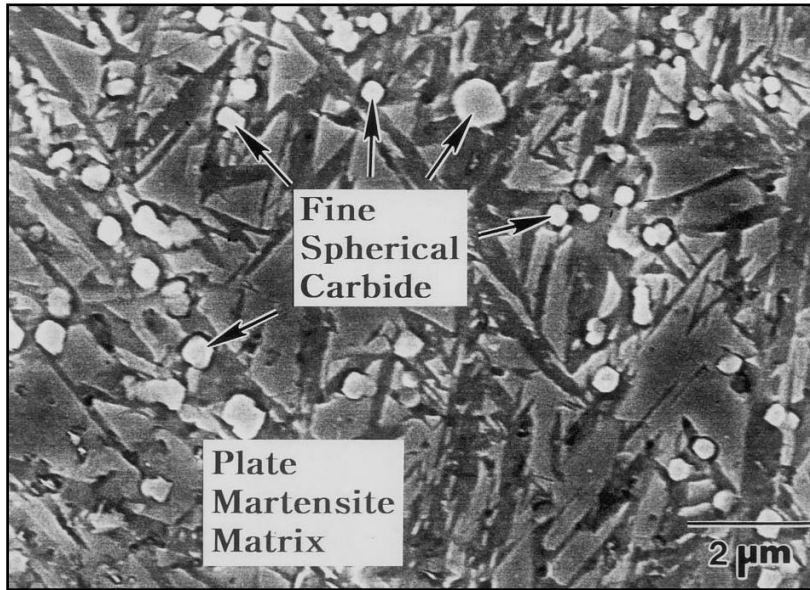
Figure 2-12: As-cast microstructure etched with Nital, showing the $M_{23}C_6$ carbides in a 5%W-5%Mo-5%V-5%Cr HSS steel [8].

The carbide types, quantity, size and morphology have a strong influence on the performance of HSS rolls [2, 8]. The variations in the characteristics of the different carbides are summarised in Figure 2-13.

Carbide type		Morphology	Chemistry	Localization
MC		•Globular •Thick •Isolated or associated	•Mainly V •Secondary Mo, W, Cr	Centre of grains or grain boundaries (in association with M_7C_3)
M_2C		•Acicular (needles) or lamellar •Associated	•Mainly Mo, W •Secondary Cr, Fe, V	Interdendritic areas
M_6C		•Thin lamellae (fish bone) •Associated	•Mainly Mo, W •Secondary Cr, Fe, W, V	Areas of strong cooling (first 5 mm from surface)
M_7C_3		•Thick lamellae (fish bone) •Associated	•Mainly Fe, Cr •Secondary Mo, V, W	Interdendritic areas
$M_{23}C_6$		•Small globules •Isolated	•Mainly Cr, Fe •Secondary Mo, W, V	Homogeneously reparted in matrix

Figure 2-13: Summary of the morphology and occurrence of the different carbide types [41].

17

The major difference between the general microstructure of HSS rolls before and after heat treatment is the matrix which is transformed from being predominantly austenitic to martensitic, see Figures 2-14 and 2-15.
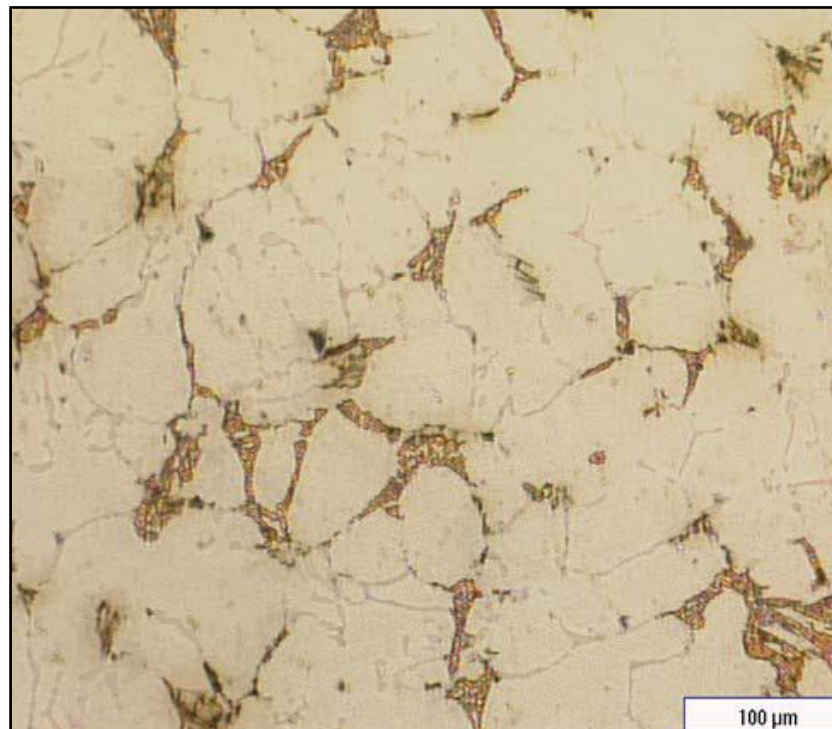
Figure 2-14: General microstructure after heat treatment [45].
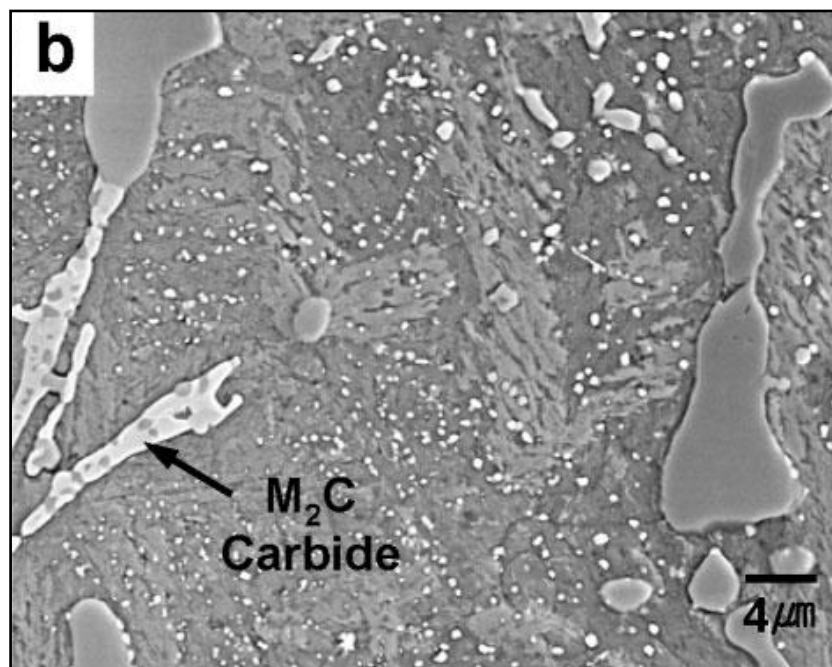
Figure 2-15: General microstructure after heat treatment showing fine $M_{23}C_6$ spheroidal carbides in a 9.8%W_{EQ}-6.3%V HSS steel [46].

18

The changes to the carbides are less severe during heat treatment of HSS rolls compared to typical HSS tool material due to a lower austenitisation temperature in the latter. Higher temperatures are required in order to dissolve the carbides and change the occurrence and morphology in HSS roll material [2]. Lath martensite is typically the dominant matrix structure at carbon concentrations below 0.4% and plate martensite at concentrations above 0.4% [44]. If the carbon content of the matrix is higher than 0.6% it can have a significant embrittling effect on the structure due to large amounts of plate martensite which forms [8]. The type of martensitic microstructure also affects the friction coefficient and wear rate of the roll [2].

The range of volume fraction of the different carbide types as-measured by a variety of authors is shown in Table 2-5.

Table 2-5: Typical volume fractions of carbides found in HSS [9, 14, 15, 16, 35, 41].

Total	MC	$M_7C_3+M_2C+M_6C$
7-22%	3-15%	0-10%

Other than the carbide and matrix type and characteristics, the cell size also has a significant influence on the mechanical properties and performance of the HSS rolls. The cell size generally increases from the outer surface of the shell towards the core as the solidification rate decreases. The typical cell size at the surface is approximately 50µm and can increase to over 100µm below the surface [9, 42], see Figures 2-16 and 2-17.

As previously mentioned, REE modification is an effective method of reducing the cell size and improving the overall characteristics of the HSS rolls, see Figure 2-18. Minor B additions have also been found to show refinement of the cell structure and can enable reductions in cell size of up to 30% [35], see Figure 2-19. Other than modification the cell size can also be reduced by increasing the cooling rate during casting [43], see Figure 2-20.

19
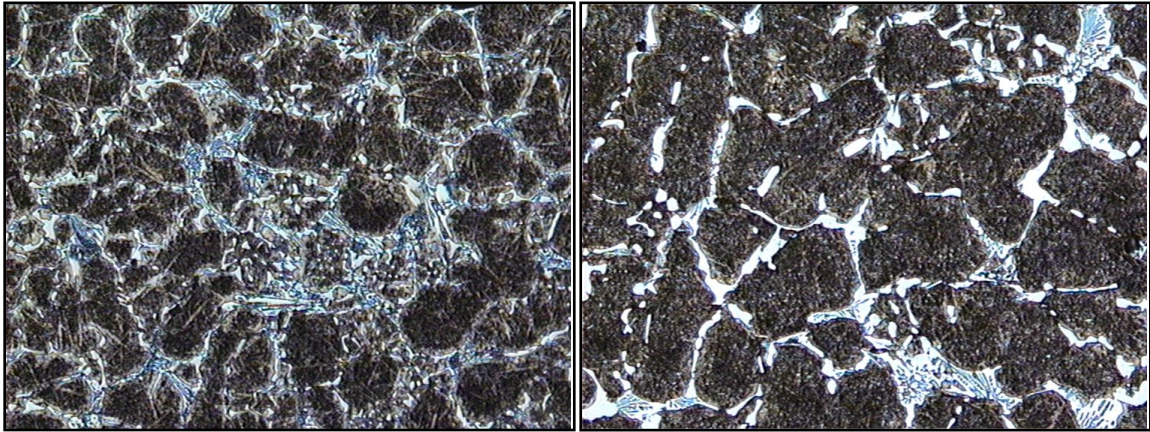
Figure 2-16: HSS microstructure at a depth of 5mm (left) below the surface (left) and 50mm below the surface (right) [42].
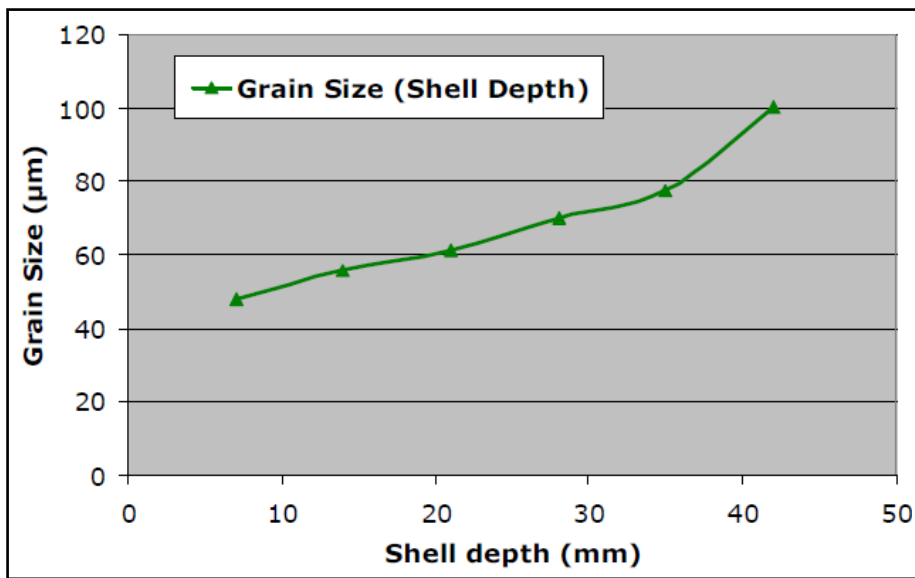
Figure 2-17: Graph showing the increase in grain size with shell depth [42].
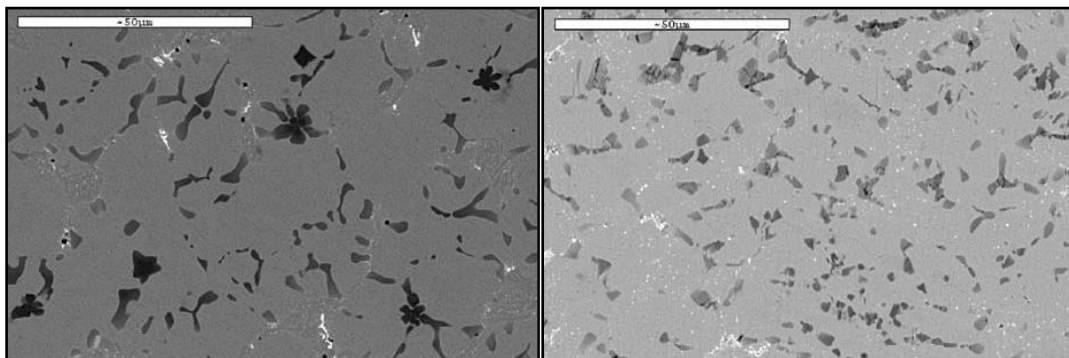
Figure 2-18: Microstructure without REE modification (left) and with REE modification (right) on a 5%V-9%Cr-2.5%Mo-2%W HSS steel [19].

20
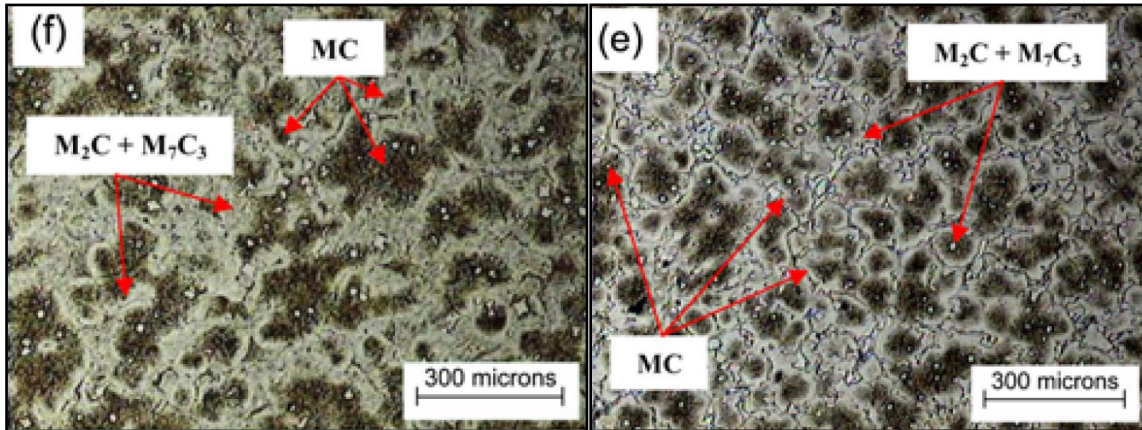
Figure 2-19: Microstructure without B addition (left) and with 0.04%B addition (right) in a 5.9%Cr-3.6%Mo-4.3%W-5.6%V HSS steel [35].
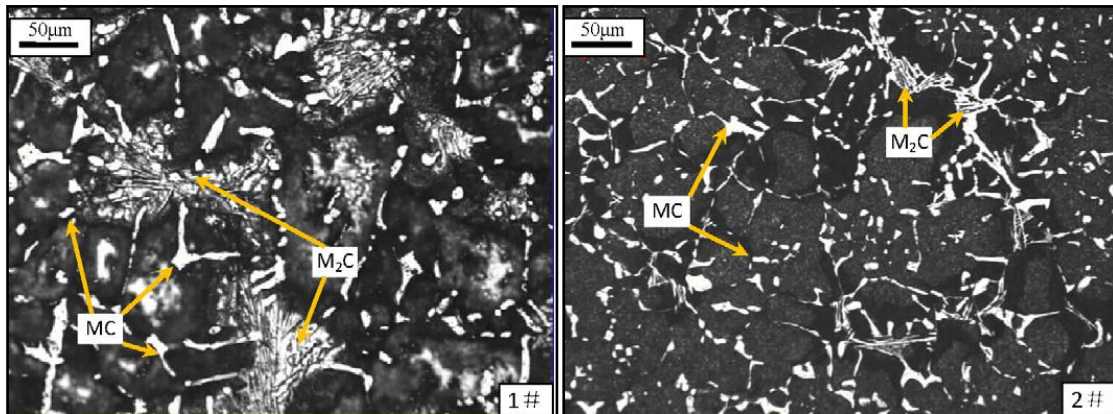
Figure 2-20: Microstructure with a cooling rate of 1.57°C/s during casting (left) and 2.48 °C/s (right) in a 4.1%Cr-5.9%Mo-6%V HSS steel [43].

The microstructures of HSS rolls are typically examined using a variety of etchants, of which Nital (5-10% Nitric acid in ethanol) and Murakami's etchant (10% NaOH, 10% $K_3Fe(CN)_6$ solution) are most common. Nital serves as a good general microstructure etchant while Murakami's etchant is useful for selective carbide identification. Murakami's etchant has been found to colour M_2C carbides black, M_7C_3 carbides light pink, and M_6C carbides pink. Murakami's etchant has no effect on MC carbides or the matrix [8]. Groesbeck's etchant (4% NaOH, 4% $KMnO_4$ solution) has also been used for carbide identification and colours M_2C carbides dark brown, M_6C and M_7C_3 carbides yellow or blue with no effect on MC carbides [42, 47], see Figures 2-21 and 2-22.

21
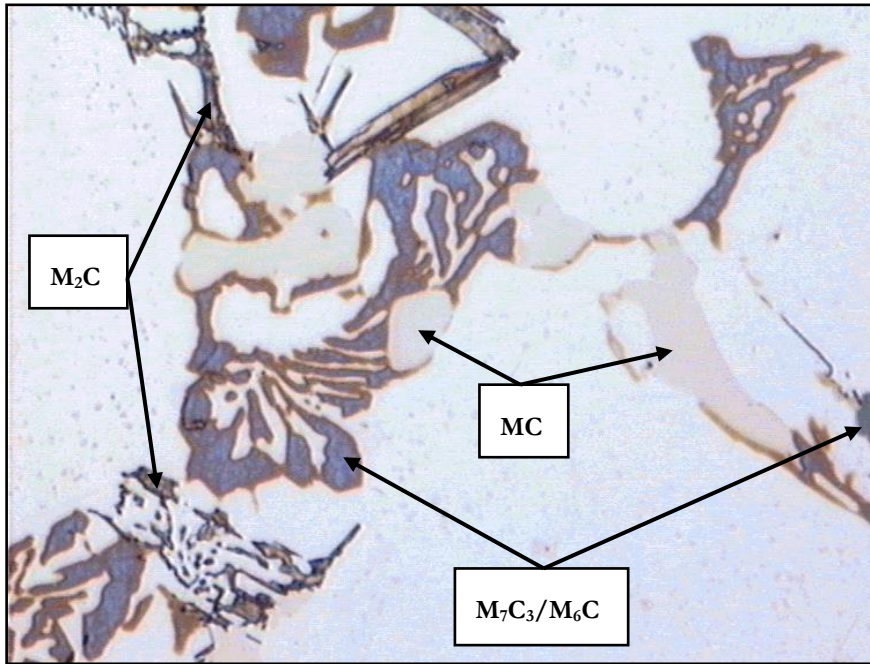
Figure 2-21: HSS microstructure etched with Groesbeck's etchant for 20s [42].
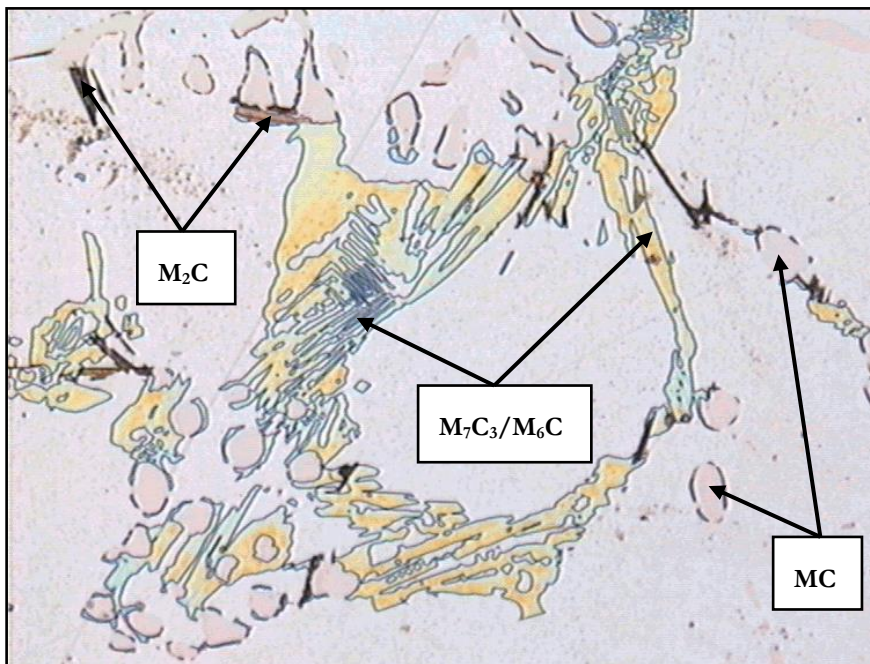
Figure 2-22: HSS microstructure etched with Groesbeck's etchant for 5s [42].

The selective carbide etchants are useful to study the carbide volume fractions and basic shape. However, they do not give a good indication of the three-dimensional morphology. Deep etching followed by SEM analysis is utilised in order to study the carbide's morphology further [43], see Figures 2-23 and 2-24.

22
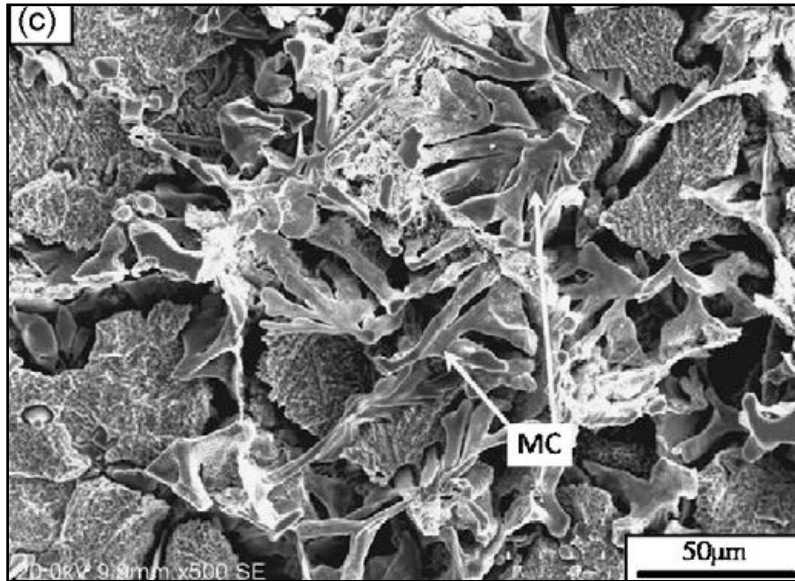
Figure 2-23: SEM image captured in secondary electron mode of MC carbides deep etched with 10% Nital, in a 4.1%Cr-5.9%Mo-6%V HSS steel [43].
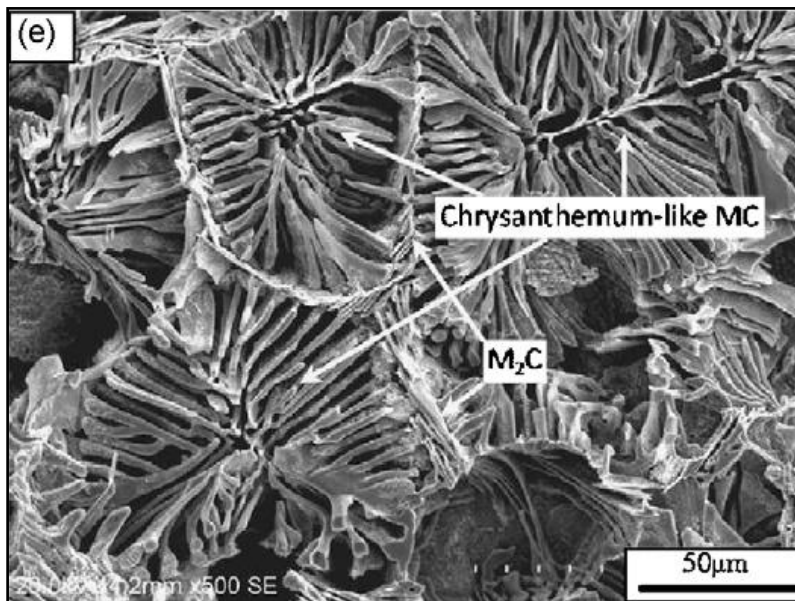
Figure 2-24: SEM image captured in secondary electron mode of MC and M_2C carbides deep etched with 10% Nital, in a 4.1%Cr-5.9%Mo-6%V HSS steel [43].

The microstructure of HBHSS differs significantly from traditional HSS microstructures in that the as-cast structure consists of martensite, $M_2(B,C)$, $M_{23}(N,C)_6$ and little retained austenite [37], see Figures 2-25 and 2-26. This allows for a less strenuous heat treatment procedure, which would typically consist of double tempering and would not require an austenitizing treatment prior to tempering. The carbide volume fraction is also significantly increased and the structure is similar in appearance to HC

23

rolls. This does raise concerns regarding the toughness of the HBHSS as fatigue cracks could propagate along the boro-carbide boundaries.
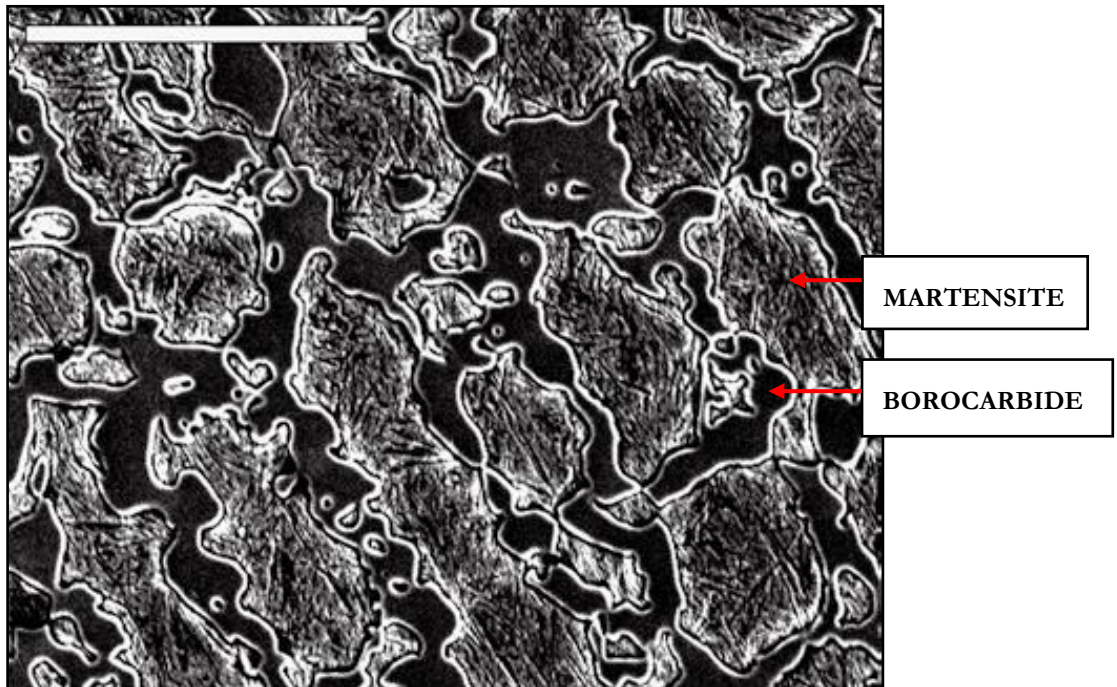
Figure 2-25: General microstructure of a 1.3-1.5%B, HBHSS as-cast and etched with 5% Nital [37].
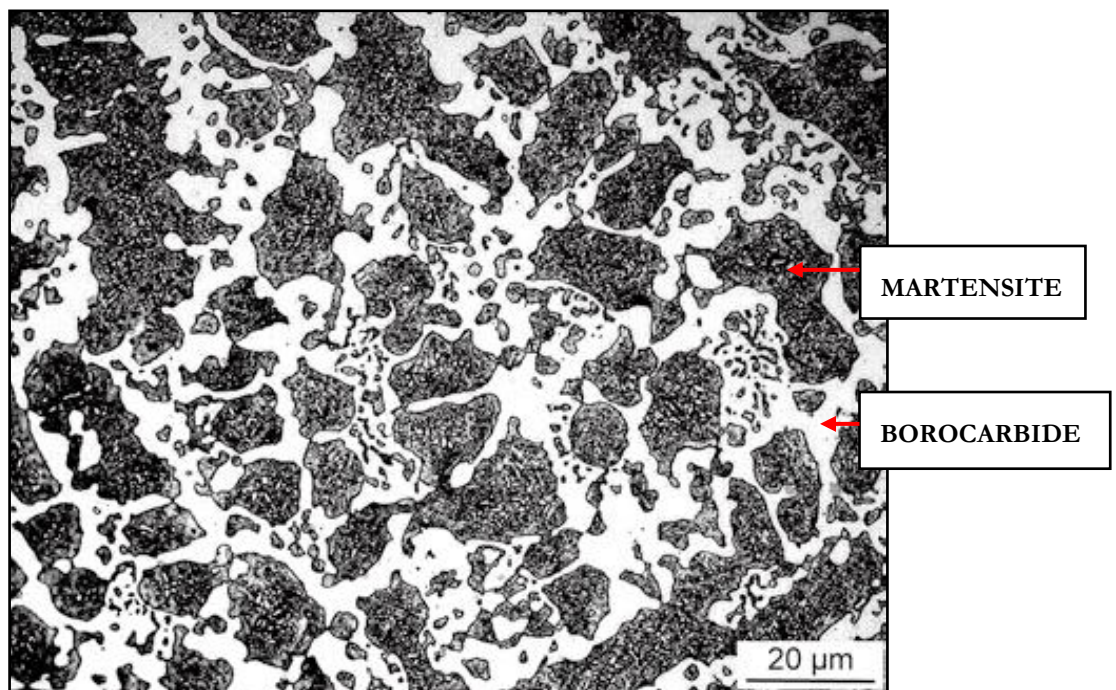
Figure 2-26: Micrograph of a 1.3-1.5%B, HBHSS tempered at 525°C and etched with 5% Nital [37].

The graphite containing HSS is similar to traditional HSS material, except for the nodular/compacted graphite and lower primary carbide volume fractions, see Figure 2-27.
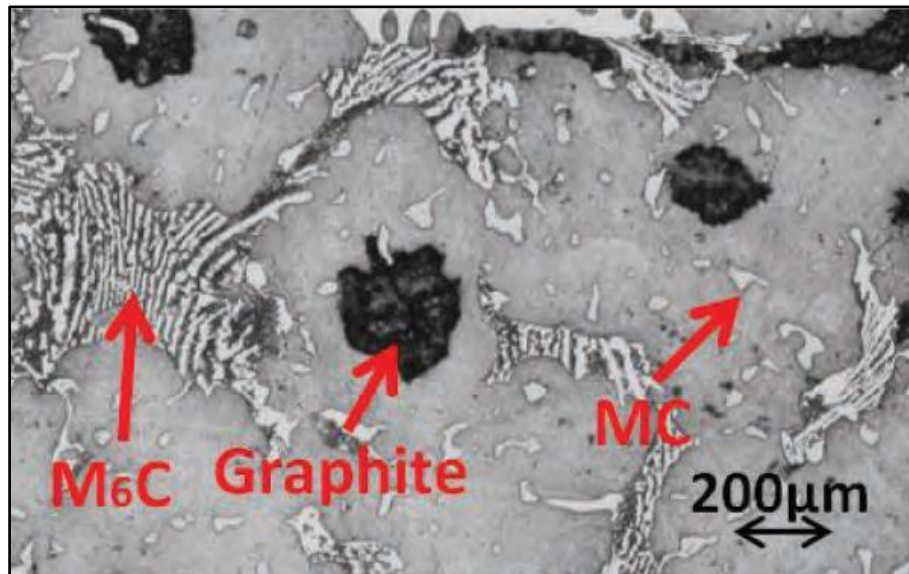
Figure 2-27: Micrograph of a graphite containing HSS alloy under development [33].

2.3. Mechanical Properties of HSS Alloys for Rolls

It is impossible to satisfy all the mill requirements for optimal performance with a single HSS roll, thus the roll properties have to be tailored to the application. In the roughing stands the resistance to oxidation and thermal fatigue should be prioritised over wear resistance, where the contrary is true for the finishing stands. Similar to the chemical composition and prevailing microstructure, significant variations in mechanical properties of HSS are found in order to satisfy the respective mill requirements [8].

HSS roll materials typically have a high Young's modulus in the order of 200-235GPa. This is sufficient for the roughing and initial finishing stands, but is too high for the final finishing stands, which typically require a Young's modulus of 190GPa or less. The low modulus is required in order to achieve sufficient control with more roll flattening for tolerance control during rolling. The low Young's moduli are typically achieved by IC rolls. Hence, graphite containing HSS rolls was developed with improved lubrication and sufficiently reduced Young's modulus in order to be successfully applied in the final finishing stands [33, 34, 48-50].

The mechanical properties of a HSS roll are strongly influenced by the microstructural characteristics [11]. A hardness range of 78-83Sh.C (shore hardness scale C) is used by many roll producers as it provides the best compromise between performance and mill incident resistance [4], see Table 2-6. It has been found that the matrix hardness has a strong influence on the bulk hardness, more so than the volume fraction and

25

hardness of the carbides [11, 14, 46], see Figure 2-28. The hot hardness also generally increases with bulk hardness [3, 4].

Table 2-6: Typical and optimal bulk hardness ranges for HSS rolls [3, 6, 8, 14, 15, 39, 45, 46, 52].

Hardness	Typical	Optimal
HV	540-800	650-720
Sh.C	68-89	78-83
HRC	51.5-64.5	58-61
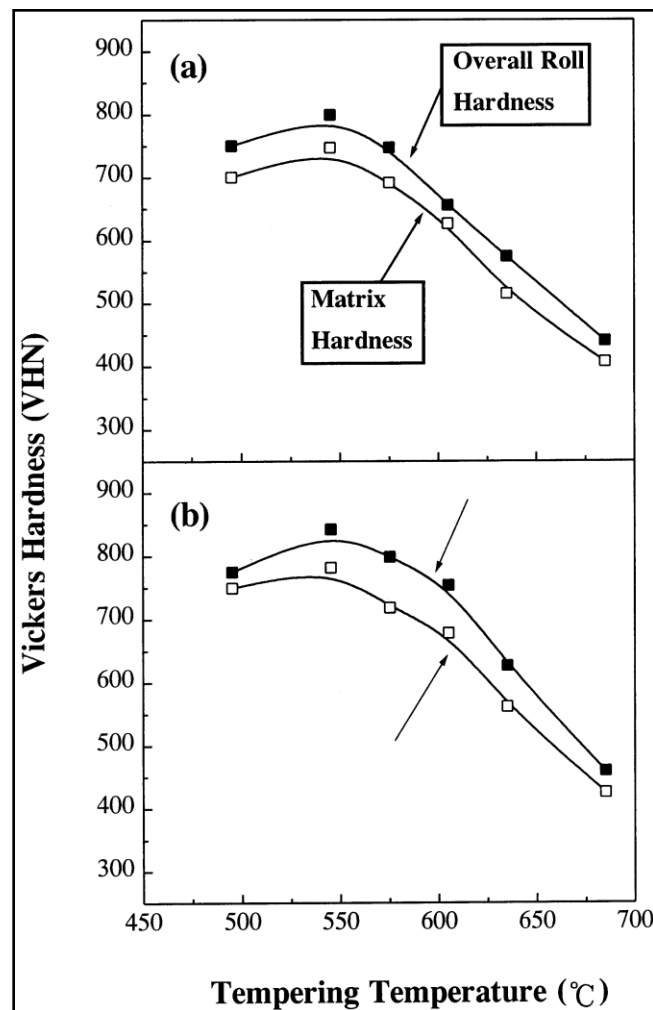
Figure 2-28: Graph showing the relationship between the bulk and matrix hardness in relation to tempering temperature [8].

The carbides present within the microstructure also show a wide range of hardnesses, see Table 2-7. Low hardness M_3C carbides are generally not found in HSS rolls and are typically utilised in IC rolls.

Table 2-7: Typical hardness ranges of carbides found in HSS [2, 8, 9, 14, 39, 41, 43, 46, 54-57].

Carbide type	Carbide Former	Hardness (HV)
M_3C	Fe (Cr, Mo)	850-1350
M_7C_3	Cr (Fe, Mo)	1200-2380
MC	V, Nb, Ti	2200-3400
M_2C	Mo (W, V, Cr, Fe)	1400-2400
M_6C	W (Mo, Fe, Cr)	1200-1890
Matrix	-	500-750

Of the carbides found in HSS rolls the M_7C_3 and M_6C carbides are typically the softer carbides with M_2C carbides slightly harder and MC carbides significantly harder than the other carbides. The wear resistance of HSS is 3 to 4 times higher than for HC rolls, due to the presence of harder carbides (MC) compared to the predominant carbides in HC rolls (M_7C_3) [11, 30, 53]. The matrix can also be produced over a wide hardness range depending on the alloy content and heat treatment. The typical tensile properties of HSS roll material are shown in Table 2-8.

Table 2-8: Typical tensile properties of HSS rolls [4, 45, 54].

Property	UTS	Elongation	Area Reduction	Compressive Strength
Units	MPa	%	%	MPa
Typical values	647-925	0.3-1.0	0.23-0.50	2350-3200

The typical toughness values of HSS rolls are shown in Table 2-9. It is also interesting to compare the impact toughness of HBHSS, which is typically less than 8J, to that of HSS [37].

Table 2-9: Typical toughness values of HSS rolls [6, 12, 45, 46, 58].

Toughness	Fracture toughness K_C	Charpy Impact
Units	MPa√m	J
Typical	14-30	7-16.5

GB carbides are beneficial in HC rolls due to the improved wear resistance. However, in HSS rolls coarse carbides located at the intercellular regions are detrimental, since they serve as preferential fracture locations, see Figure 2-29. This causes a decrease in the toughness of the material and an increase in the susceptibility to thermal fatigue cracking. Thus, the solidification cell structure directly influences the fracture toughness as it determines the carbide distribution. The fine spherical MC carbides,

27

which are typically not associated with the cell boundaries, do not affect the fracture toughness significantly. The fracture toughness can also be improved by increasing the amount of lath martensite rather than plate martensite within the matrix [46].

Fracture in HSS rolls is accelerated by the presence of hard carbides at the GB's. The cracking typically initiates at the interface of the matrix and the carbides by the fracture of the carbide itself. The cracks typically penetrate the matrix and propagate along cell boundaries [11, 58]. Thus, the amount of M_7C_3 and M_2C carbides at the grain boundaries should be limited to improve the toughness. The MC carbides have only a minor effect on the crack propagation once formed as they are isolated within the matrix and do not form networks. The plate martensite matrix also shows preferred crack propagation compared to lath martensite. The fracture surface of HSS rolls are typically characterised by brittle cleavage [58], see Figure 2-30.
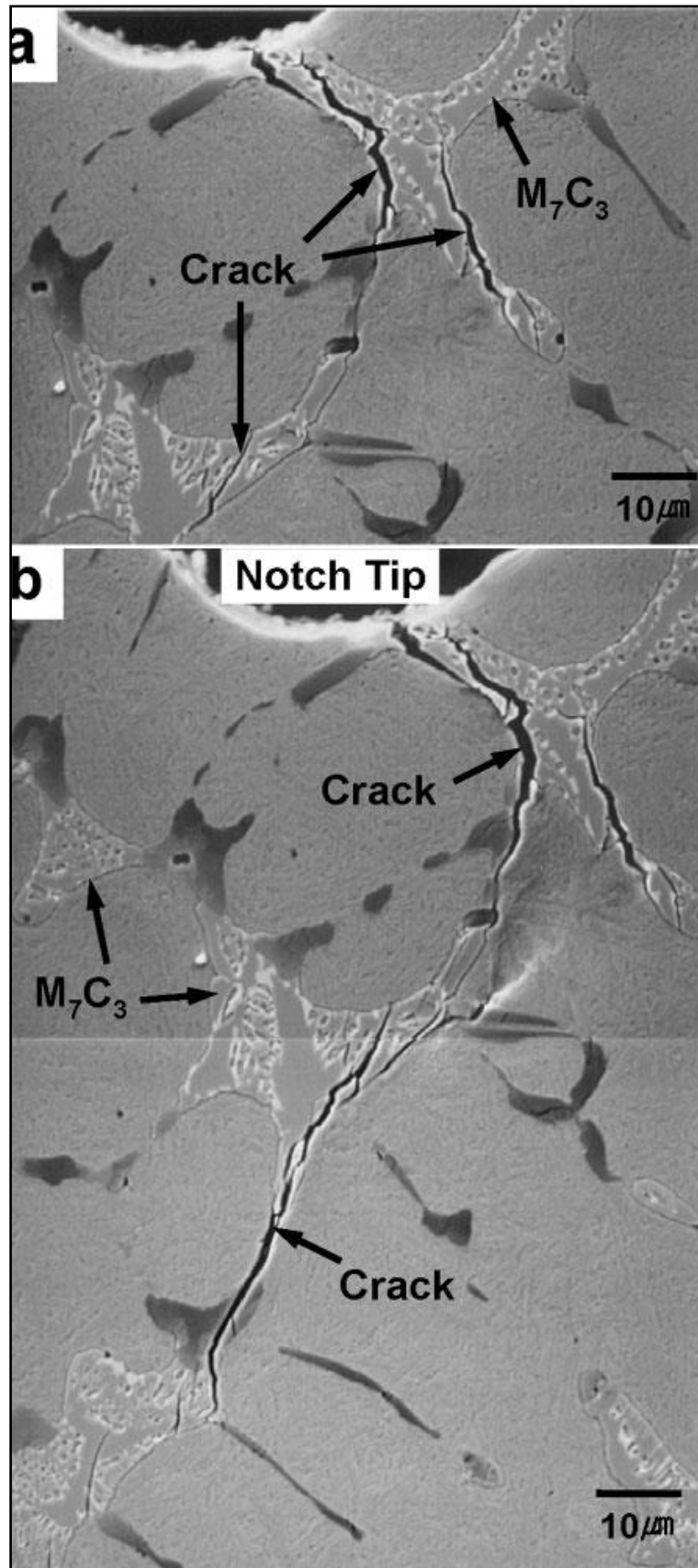
Figure 2-29: Micrograph showing crack propagation along the coarse intercellular carbides [46].
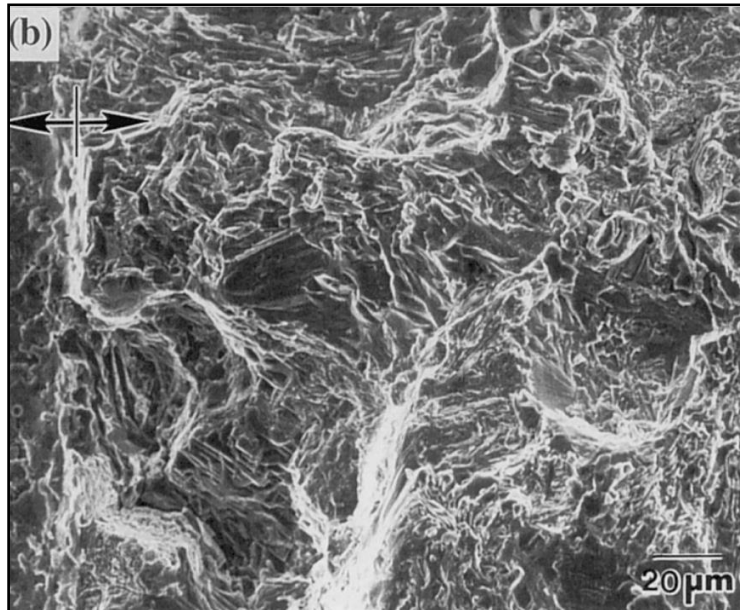
Figure 2-30: Cleavage fracture generally found on HSS roll failures [58].

2.4. Solidification Behaviour

In order to interpret the solidification behaviour of HSS roll material it is useful to consider a representative phase diagram. The most widely used Isopleth which appears to be representative of a wide range of HSS alloys is shown in Figure 2-31.
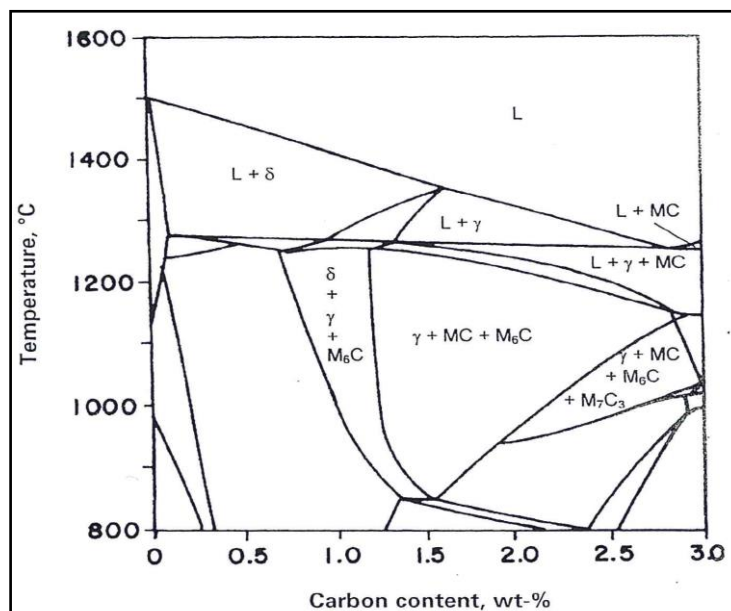
Figure 2-31: Isopleth created with Thermo-Calc™ for Fe-5%Cr-5%W-5%Mo-5%V-C HSS [59].

The isopleth predicts that for typical HSS the first phase to form on solidification is primary austenite from the liquid. The second transformation during solidification is the formation of austenite and MC carbide from the remaining liquid via the eutectic

30

reaction (L = γ + MC). The eutectic forms directly from the liquid independent of the primary austenite. The third phase to form can be either M_2C or M_7C_3 carbides, depending on the chemical composition, and are formed at the cell boundaries (L = γ + M_2C) [8, 18]. The isopleth predicts the formation of M_6C, but it rarely forms due to the non-equilibrium high cooling rate and rather forms metastable M_2C [18]. Thus, the size and distribution of the primary carbides is primarily determined by the chemical composition and the solidification conditions (i.e. cooling rate) [2]. Table 2-10 shows a summary of the transformations during cooling.

Table 2-10: Transformations during solidification upon cooling [3, 6, 9, 16, 20, 22, 43, 59].

Phase	Transformation	Formation Temperatures (°C)
Austenite	L → γ	1240-1375
MC	L → γ + MC	1225-1380
M_7C_3	L → γ + M_7C_3	1090-1210
M_2C	L → γ + M_2C	1090-1180
M_s	γ → martensite	190-285

Although the isopleth is widely used, it should be noted that the tie-lines are unlikely to lie within the isopleth and the isopleth in Figure 2-31 is limited to estimating the melting points of a particular composition. Figures 2-32 and 2-33 show solidification curves measured by differential thermal analysis (DTA) of two HSS alloys at equivalent cooling rates. Note that the formation of M_7C_3 has been completely suppressed in Figure 2-33 due to the selection of the chemical composition [5].
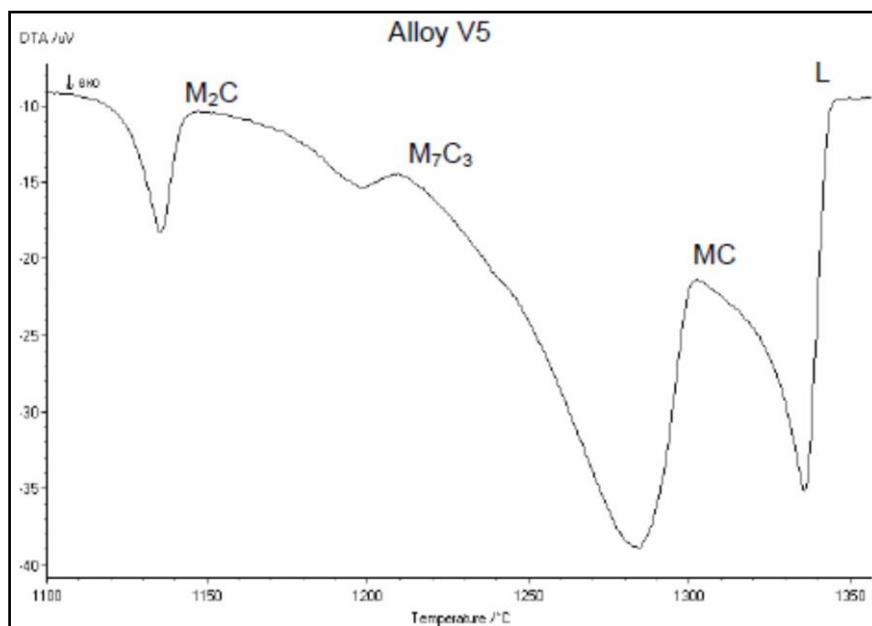
Figure 2-32: Solidification curve measured by DTA for a 5.1%V-3.5%Cr HSS alloy [5].

31
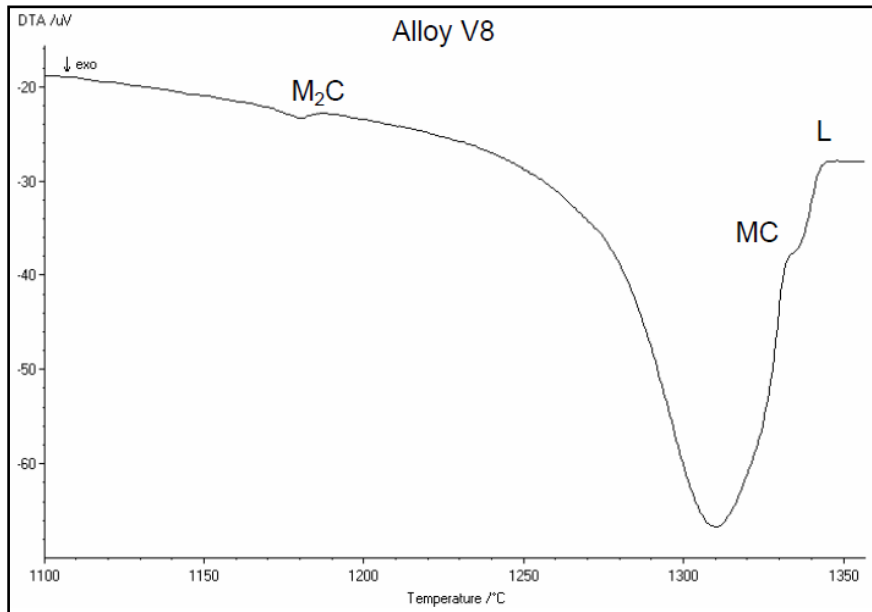
Figure 2-33: Solidification curve measured by DTA for a 8.1%V-3.5%Cr HSS alloy [5].

DTA testing on HSS is typically performed at a cooling rate of 5-10°C/min. The liquidus obtained by DTA is always higher than that predicted by Thermo-Calc^{TM} [3, 9]. V affects the liquidus of various components of the HSS microstructure, see Figure 2-34.
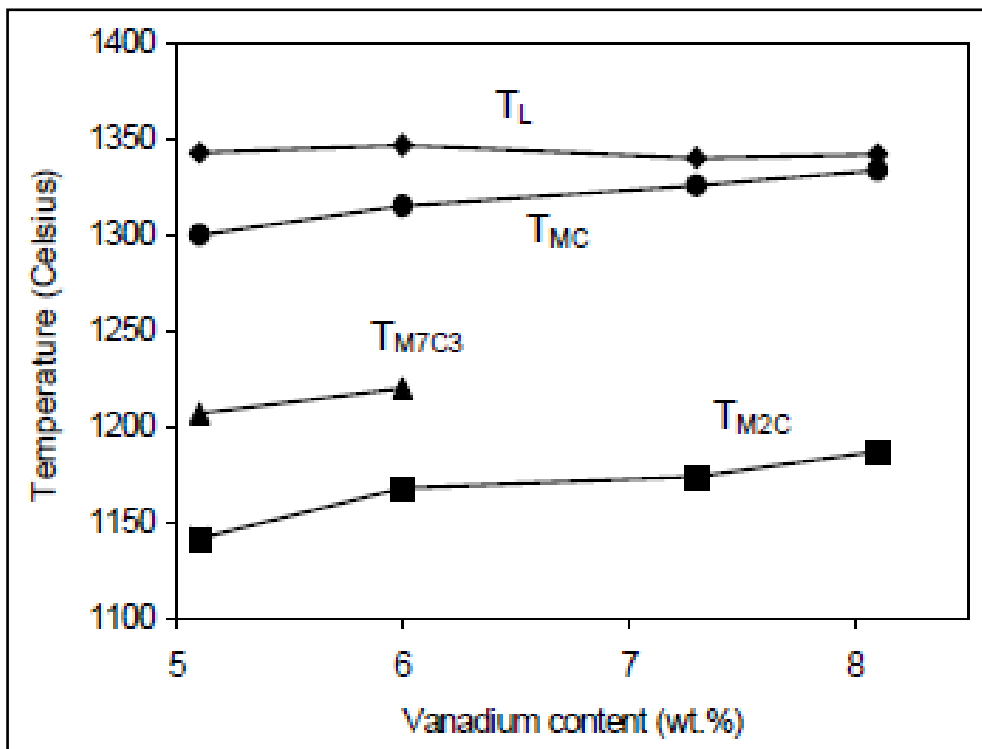
Figure 2-34: Effect of V on the transformation temperatures during solidification [5].

32

At high V contents VC carbides have even been found to precipitate prior to the formation of austenite. The V also decreases the temperature difference between the formation of primary austenite and MC eutectic, allowing less time for grain growth prior to the eutectic transformation and creates a finer structure [5].

2.5. Heat Treatment of HSS Rolls

The typical heat treatment of HSS consists of a three-step treatment. The first step is an austenitising treatment followed by two tempering treatments. The austenising treatment in traditional HSS serves to homogenise the material and dissolves most of the primary carbides within the matrix. This breaks down the carbide networks and improves the overall mechanical properties of the steel. The austenising temperature in conventional HSS is 20-40°C below the solidus temperature, which ensures that sufficient primary/eutectic carbides formed during solidification are dissolved. However, in the case of rolls the maximum austenizing temperature is determined by the lower solidus temperature of the SG iron core. This limits the amount of carbides which can be dissolved into the matrix during heat treatment and the primary carbide networks remain fairly intact [2].

The continuous carbide networks can be reduced during austenitising with the addition of REE when treated at a sufficiently high temperature (>1050°C) [25]. HSS rolls are typically austenitised at 980-1100°C [2]. The general hardness increases with increasing austenising temperature due to the increased dissolution of the $M_{23}C_6$ carbides and enrichment of the austenite matrix, which promotes the formation of plate martensite over lath martensite and increases the hardness of the matrix during tempering [8, 11]. Generally the hardness of the final heat treated microstructure increases with increasing austenising temperature up to a maximum of 1050°C, where after a decrease in hardness is found, see Figure 2-35. Combined with the hardness, the tensile strength, toughness and elongation also appear to increase with increasing austenising temperature [60, 61], see Figures 2-36 and 2-37.
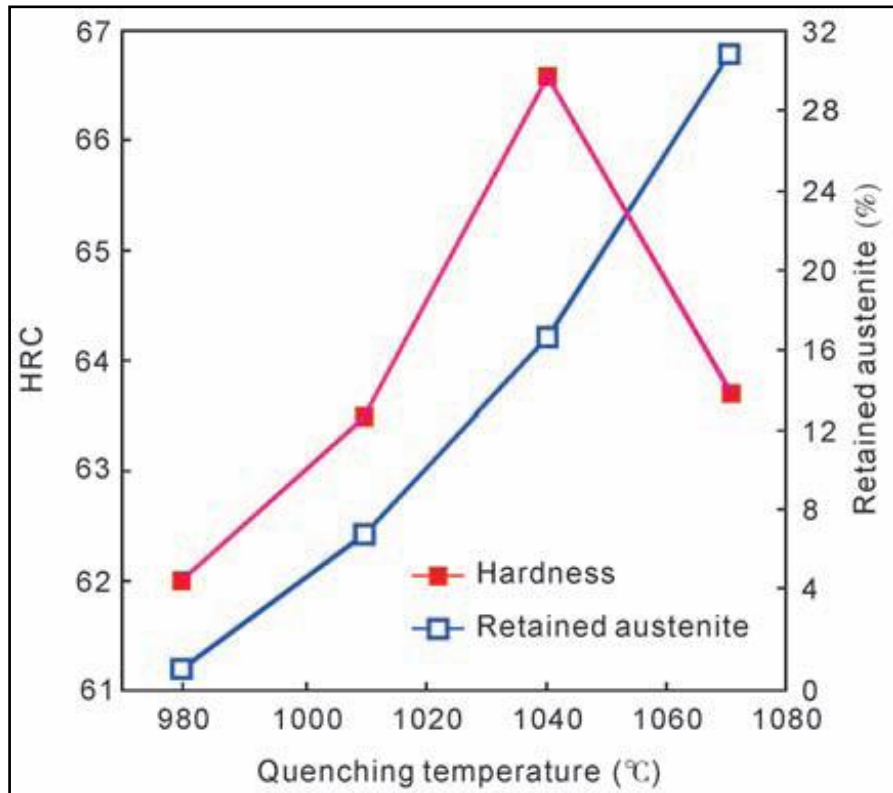
Figure 2-35: Effect of austenising temperature on the bulk hardness and retained austenite of a 4-6.5V, 3-6W, 3-6Mo, 4-8Cr, 0.5-1.5Nb HSS [61].
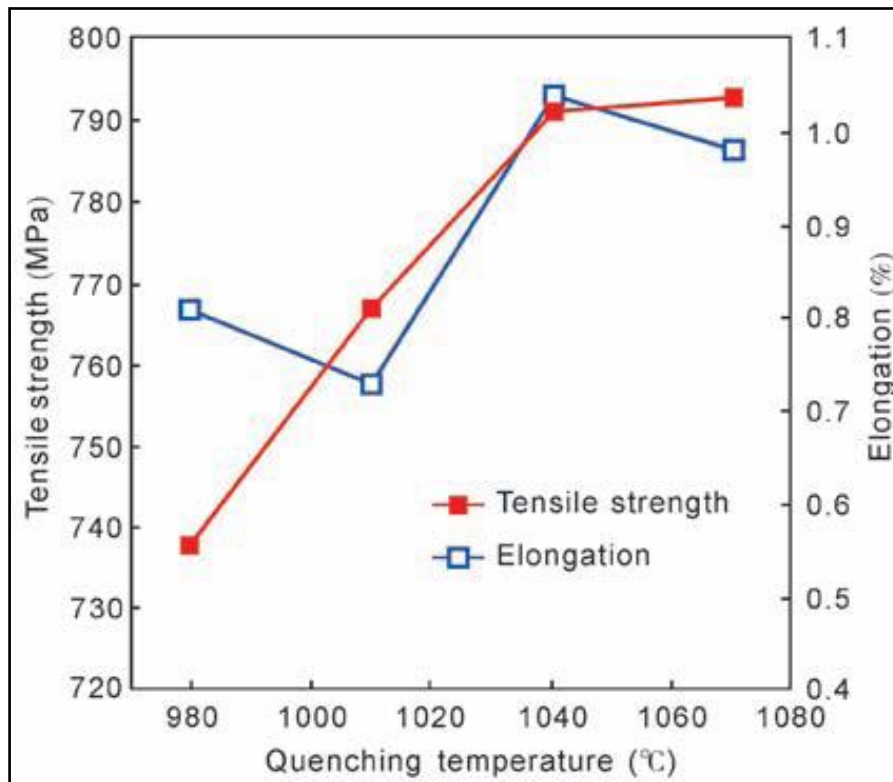
Figure 2-36: Effect of austenising temperature on tensile strength and elongation of a 4-6.5V, 3-6W, 3-6Mo, 4-8Cr, 0.5-1.5Nb HSS [62].

34
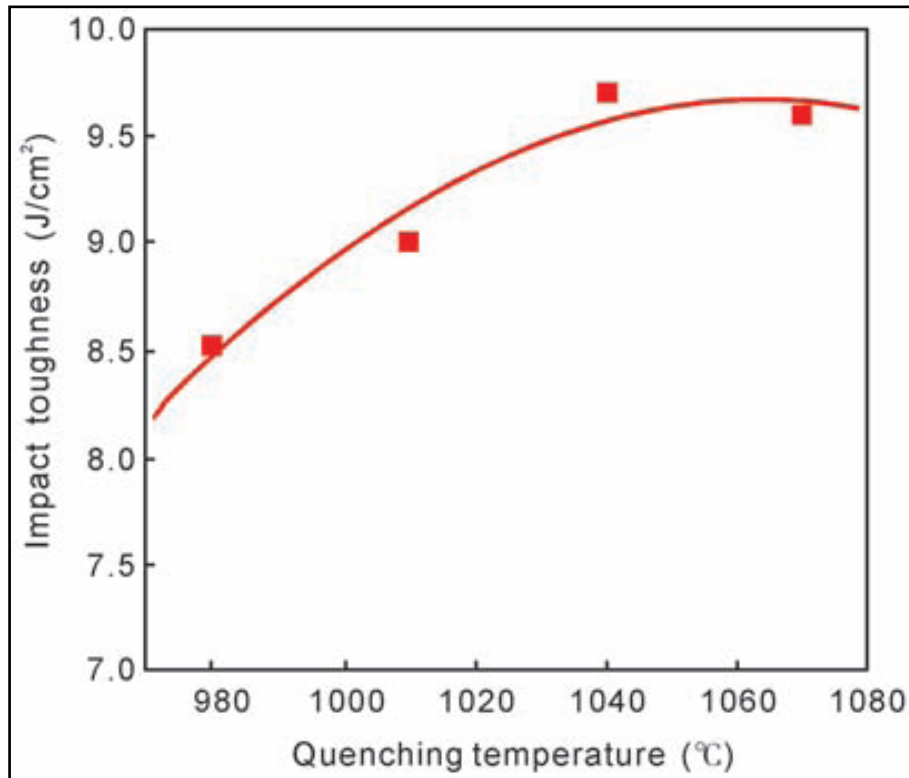
Figure 2-37: Effect of austenising temperature on impact toughness of non-standard Charpy specimens from unspecified grade HSS steel [62].

REE also increase the carbide dissolution and melting temperatures, but this should not pose a problem considering the low austenising temperature [71], see Figure 2-38.
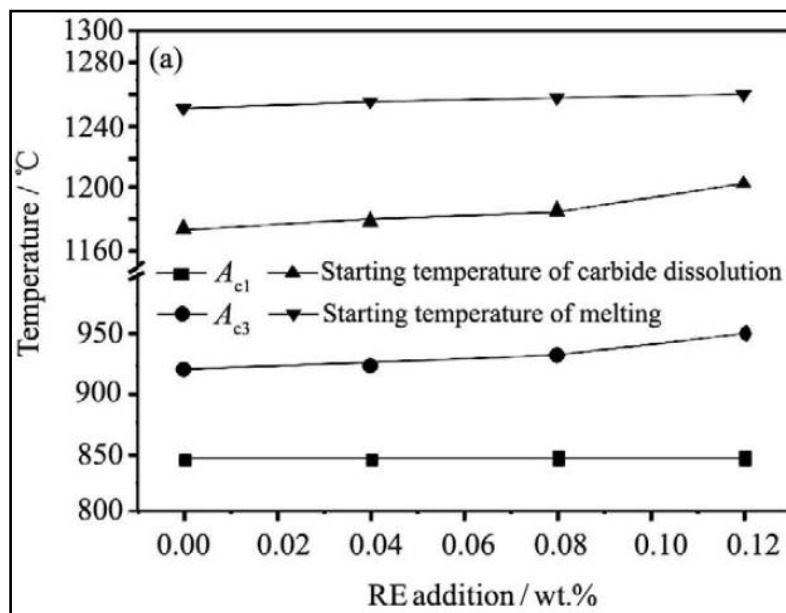
Figure 2-38: Effect of RE addition to the melting and carbide dissolution temperatures [26].

35

The austenising treatment also enables the decomposition of the metastable M_2C carbides to form MC and M_6C carbides, see Figures 2-39 and 2-40. The degree of decomposition was also found to increase with increasing austenitising temperature, as expected [8]. Hence, an increase in austenitisation time decreases the amount of M_2C and an increase in the amount of M_6C, MC and M_7C_3 formed [39].
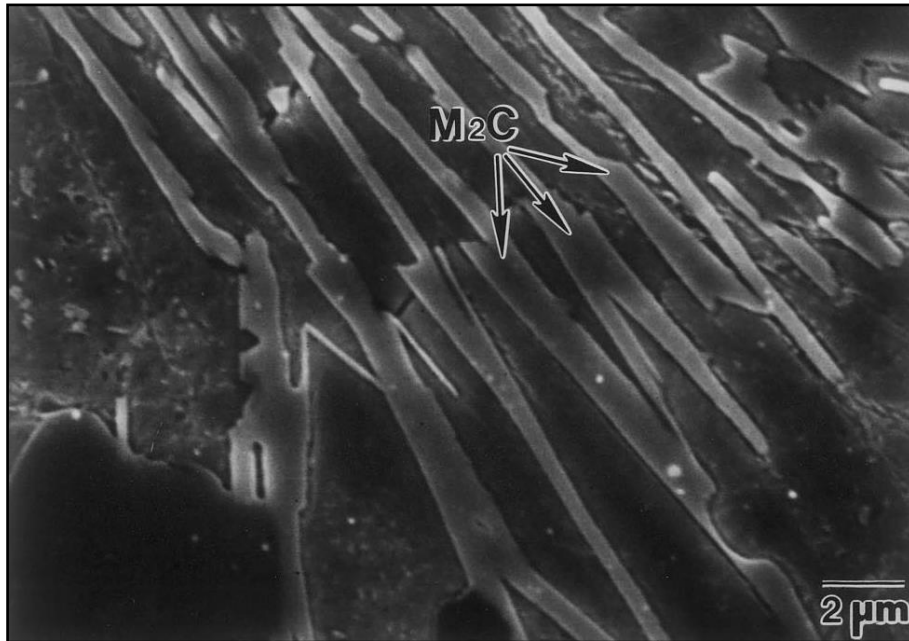
Figure 2-39: M_2C carbide prior to austenitising [8].
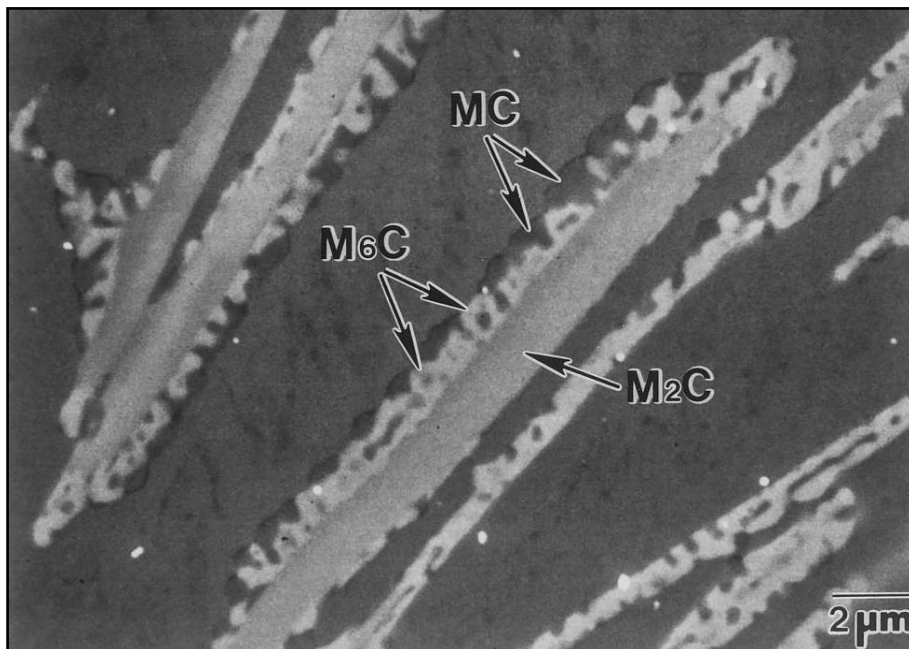
Figure 2-40: Partially transformed M_2C carbide after quenching [8].

36

The austenitising treatment is typically followed by an air cool. In some cases an accelerated air cool, fog spray (water mist) or sodium silicate quench has also been utilised [6, 41, 60]. Continuous cooling transformation (CCT) and time temperature transformation (TTT) diagrams have been constructed by a few authors in order to achieve a fully martensitic microstructure after quenching and avoid bainite formation [20], see Figures 2-41 and 2-42.
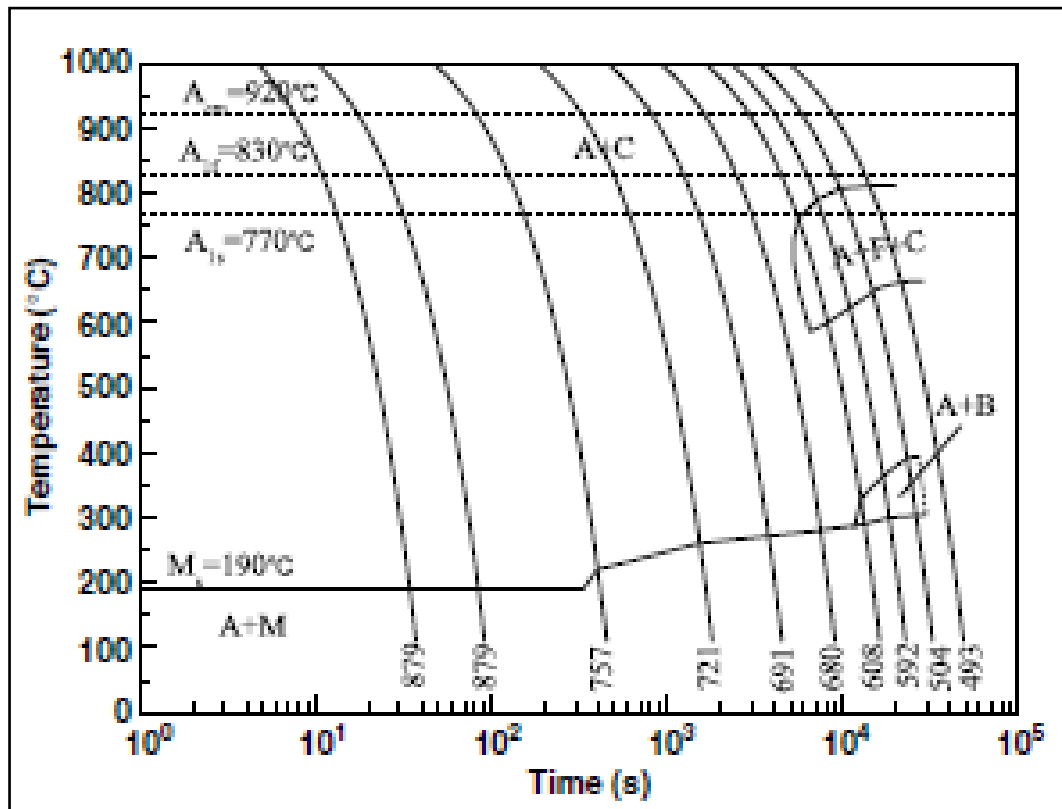
Figure 2-41: CCT diagram for HSS rolls [20].

The first tempering treatment results in the transformation of most of the supersaturated austenite to martensite during cooling, while the second treatment serves to increase the toughness by tempering the transformed martensite [11]. The phase transformation during tempering also results in secondary hardening of the roll [2]. Various authors performed studies to determine the influence of the tempering temperature on the mechanical properties by varying the tempering temperature over a range of 495-635°C. It was shown that peak hardness was achieved when tempered at 520-560°C for most chemical compositions, see Figure 2-43. The hardness showed a sharp decrease if tempered above 550°C.
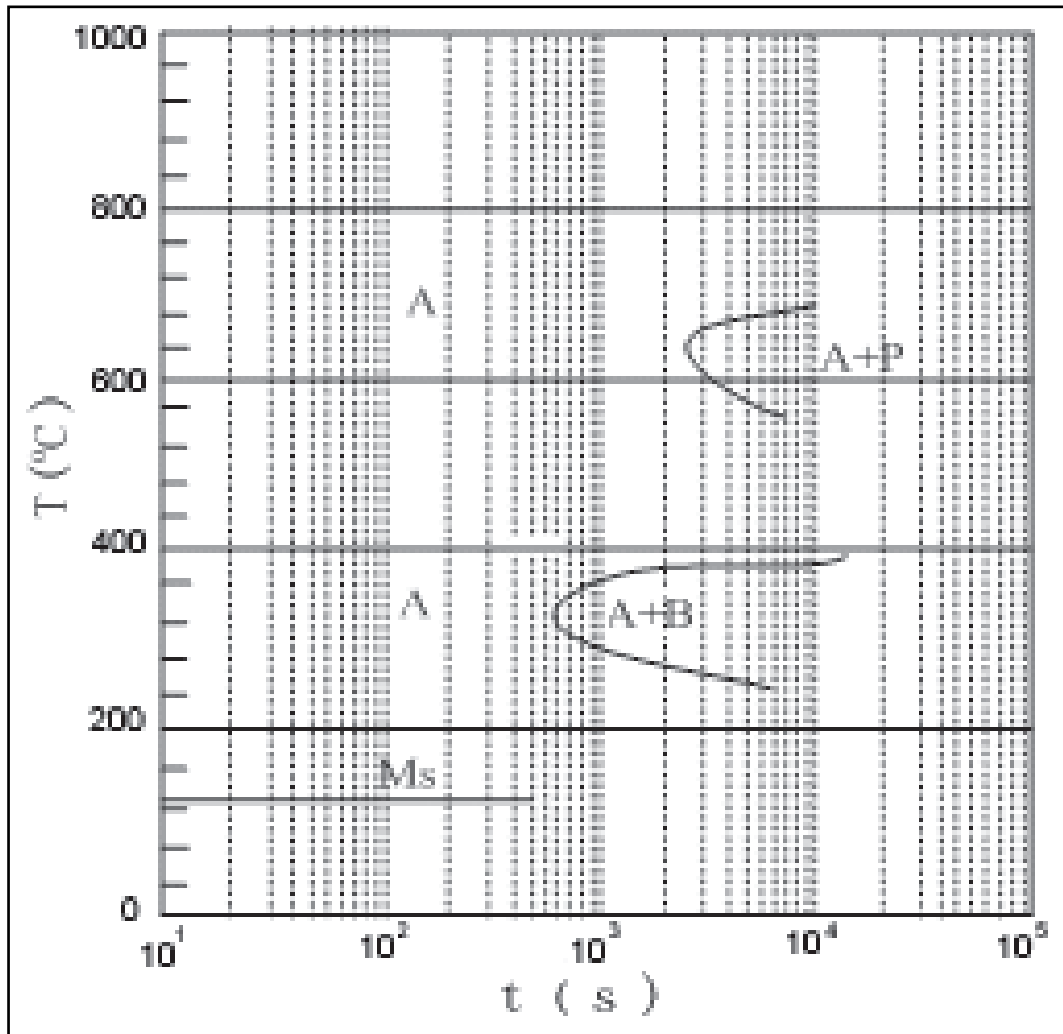
Figure 2-42: TTT curve for HSS rolls [62].

The tensile strength follows a similar trend to the hardness, see Figure 2-44. The variation of the toughness and elongation with tempering temperature showed a toughness and ductility trough at peak hardness, see Figures 2-45 and 2-46. Thus, it is better to temper at higher temperatures to improve the uniformity of the roll microstructure and associated mechanical properties. However, at excessive temperatures the secondary carbides begin to coarsen and softening takes place once more [7, 8, 14, 61]. It was also reported that excellent wear resistance can be achieved when tempered between 500-550°C [60, 61]. Larson Miller Parameter (LMP) diagrams have also been constructed for the HSS alloys, see Figure 2-47.

38
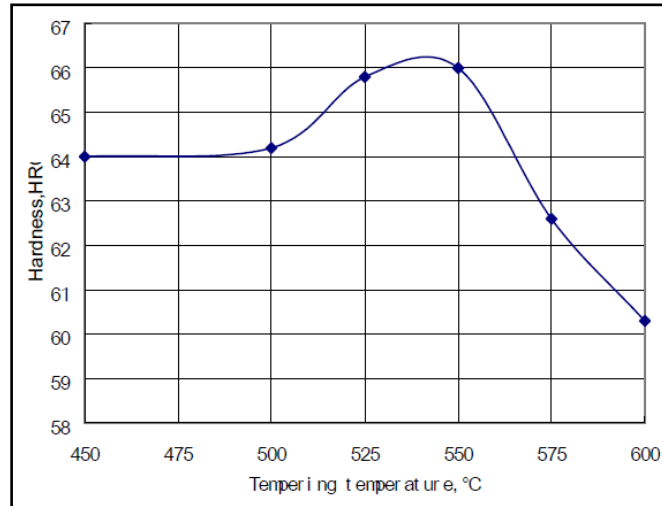
Figure 2-43: Effect of tempering temperature on the bulk hardness of typical HSS for rolls [61].
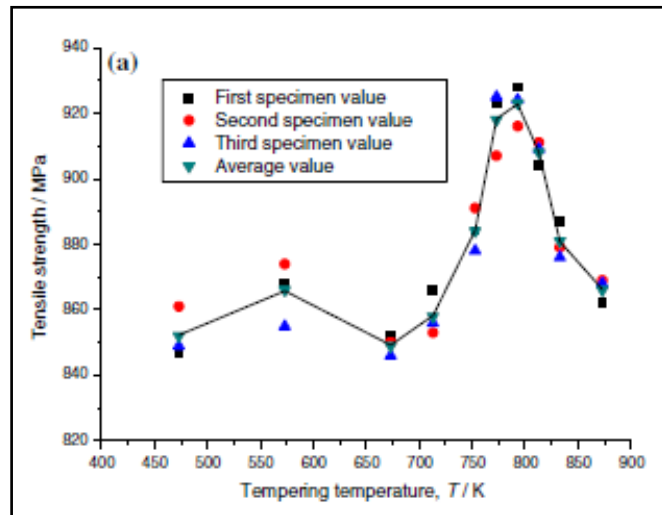
Figure 2-44: Effect of the tempering temperature on the tensile strength of typical HSS for rolls [60].
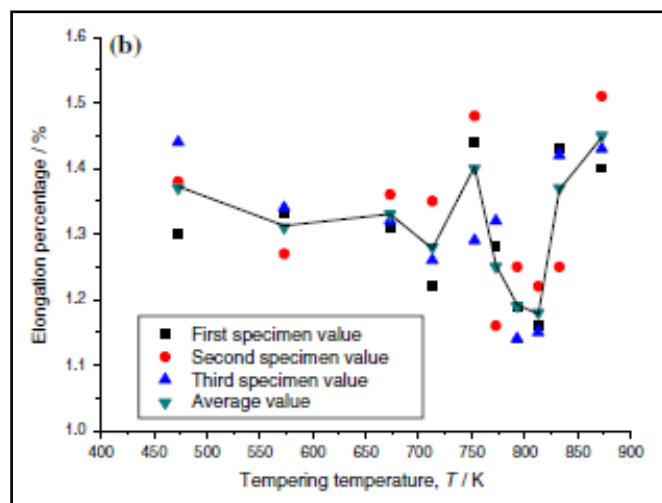
Figure 2-45: Effect of the tempering temperature on the elongation of typical HSS for rolls [60].

39
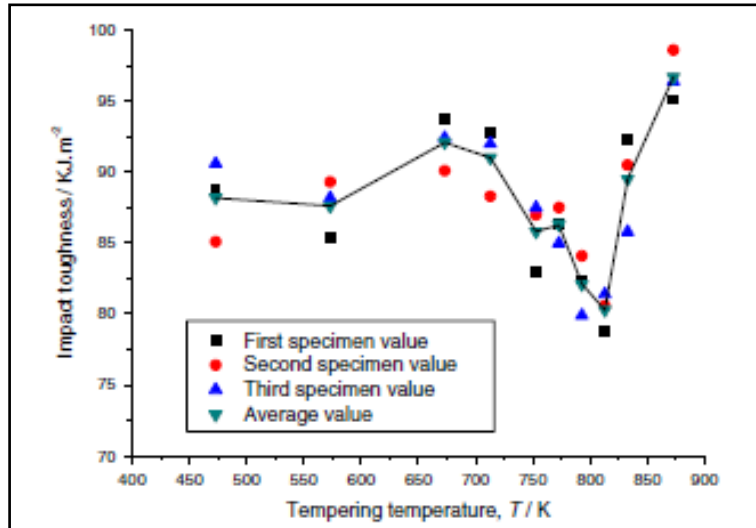
Figure 2-46: Effect of tempering on the impact toughness of typical HSS for rolls [60].
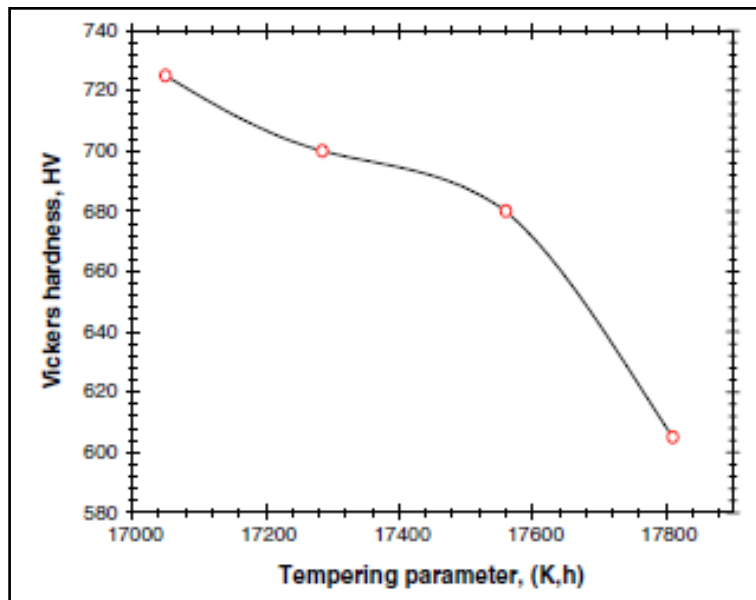
Figure 2-47: LMP diagram for HSS [45].

A summary of the typical heat treatment and peak hardness heat treatment parameters is given in Table 2-11. Modification of the typical heat treatment has also been proposed as a method to strengthen the matrix without deteriorating the toughness. The modification entails a pre-annealing heat treatment prior to austenitising. The modification requires that the roll is heated to ~850°C and soaked for sufficient time before reducing it again to 500-600°C. The austenising treatment and remainder of the typical heat treatment is then followed from the 500-600°C temperature range. The pre-annealing treatment results in the refinement of the prior

40

austenite grains within the carbide islands, which could increase the matrix hardness and the toughness [11], see Figure 2-48.

Table 2-11: Typical and peak hardness heat treatment parameters [2 8, 15, 22, 46, 60, 62, 63].

Heat treatment Process	Typical Temperature (°C)	Peak Hardness Temperature (°C)
Austenising	900-1200	1040-1050
1st Temper	450-635	520-560
2nd Temper	450-635	520-560
M_s	131	-
M_f	<20	-
A_{C1}	796	-

Figure 2-48: Refined microstructure of a 2%C-1.9%W-1.3%Mo-2.8%V-5.4%Cr HSS alloy after the additional pre-annealing treatment [11].

2.6.   Segregation in HSS Roll Materials

The centrifugal forces produced during CC causes segregation across the shell depth due to variable density components within the microstructure [2], see Table 2-12. V forms VC carbides of lower density than the matrix and tends to segregate towards the centre during casting under centrifugal force [8, 64, 65]. The opposite is true for W

41

carbides (W_2C and WC) which have a high density and segregate towards the outer diameter during spin casting. Mo forms carbides similar to W, but the segregation effect is less severe due to the lower density [41, 64]. No clear indications of Cr segregation have been observed as expected, since the density of Cr is similar to that of the steel [64]. The typical segregation is shown in Figure 2-49.

Table 2-12: Relative carbide and element densities [6].

Carbides	W_2C	WC	Mo_2C	NbC	VC	Fe_3C
Density (kg.m^{-3})	17200	15800	9100	7900	5700	7200
Element	**W**	**Mo**	**Nb**	**Fe**	**Cr**	**V**
Density (kg.m^{-3})	19300	10200	8600	7900	7200	6100
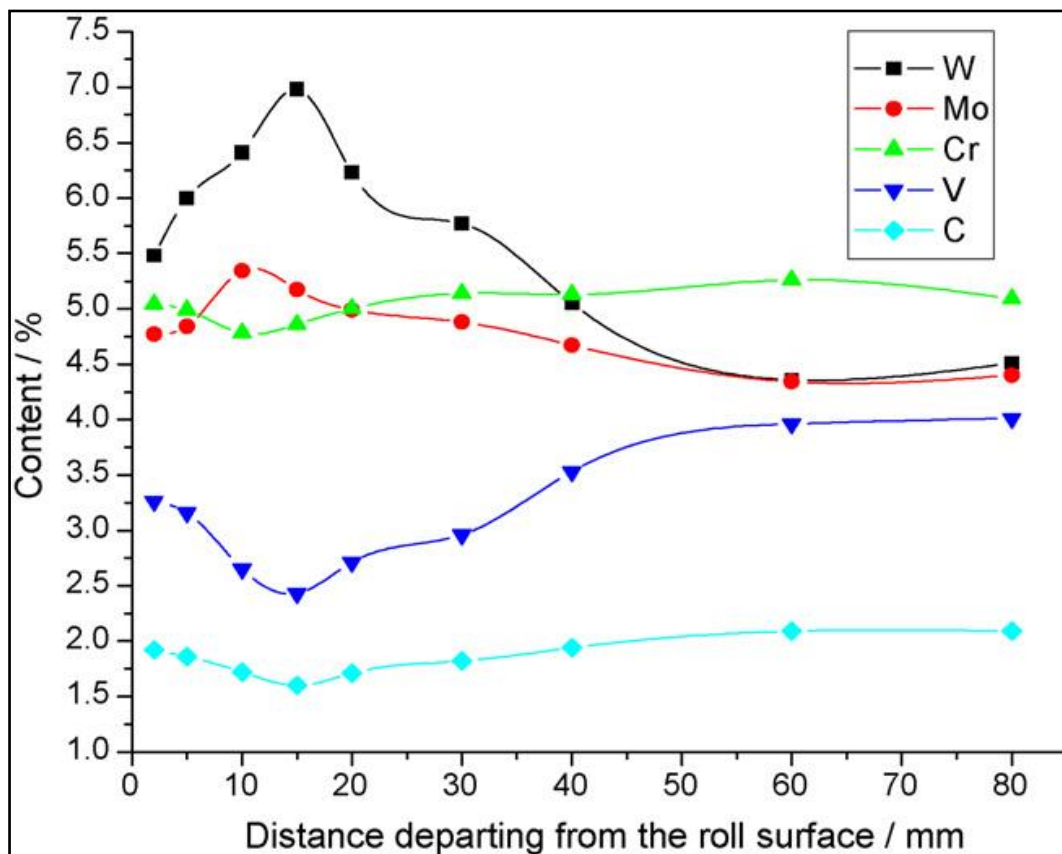
Figure 2-49: Typical segregation of the carbide forming elements over the shell depth [64].

The segregation decreases the mechanical properties and reduces the wear resistance [64], see Figures 2-50 and 2-51. This limits the compositional ranges over which HSS rolls can be produced [2, 66].

42
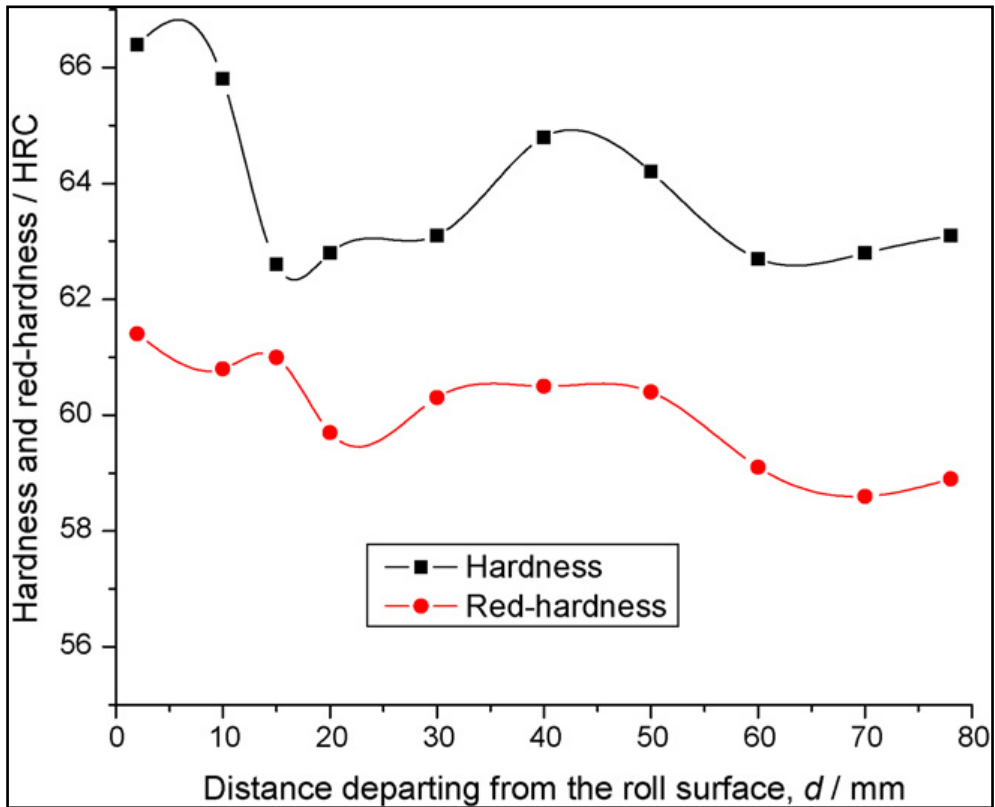
Figure 2-50: Graph showing the effect of segregation on the hardness and red-hot hardness [64].
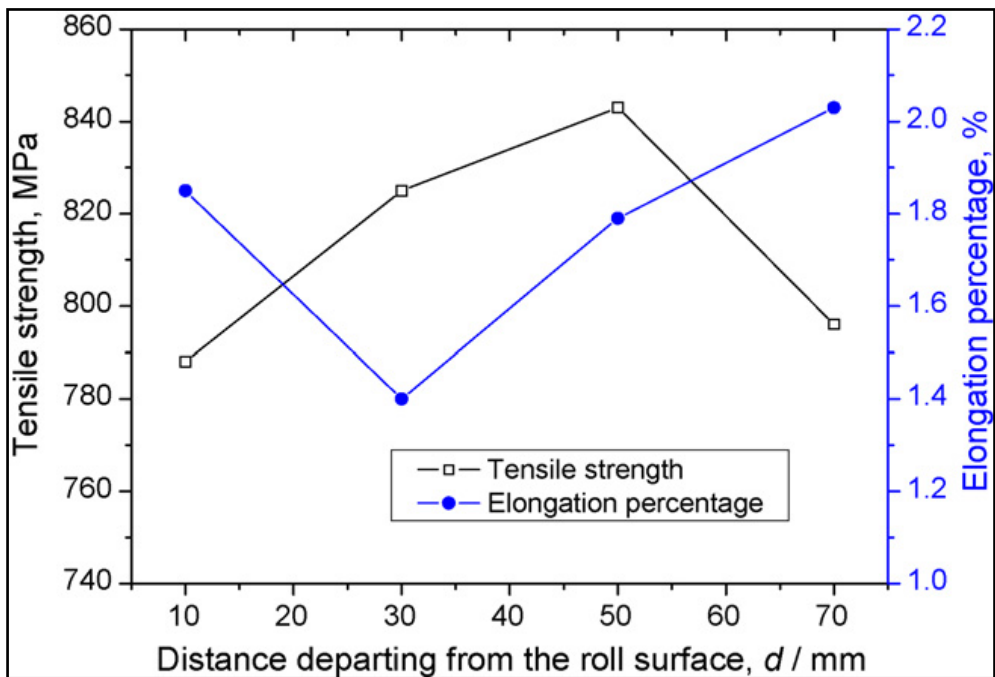
Figure 2-51: Graph showing the effect of segregation on the tensile strength and elongation of the roll [64].

One method of reducing the segregation is by increasing the solidification rate during spin casting. This decreases the time the atom clusters spend in solution and

43

decreases the degree of segregation. Another method of reducing the level of segregation is by reducing the rotational speed, which reduces the centrifugal force, see Figure 2-52 [64].
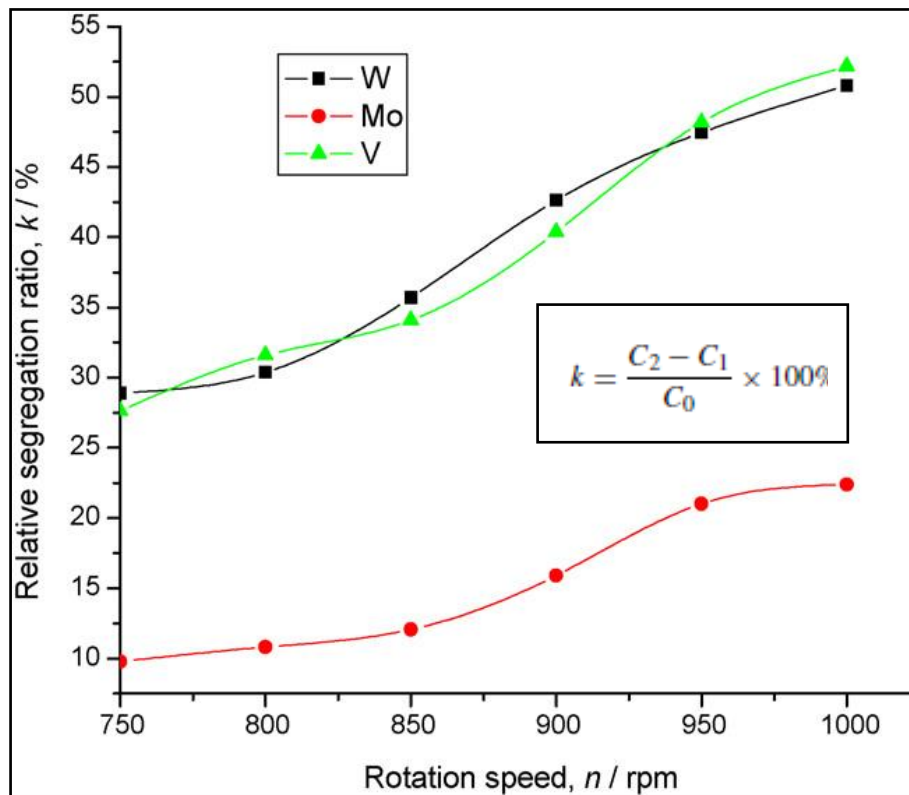
Figure 2-52: Graph showing the influence of rotational speed on the level of segregation [64].

Alloying has also been shown to be effective in reducing the segregation of VC carbides. This is achieved by Nb additions to form (V, Nb) carbides, increasing the specific gravity to be closer to that of the molten steel, see Figure 2-53. There are contrasting indications in the literature whether Nb has a beneficial effect on the segregation of other carbide forming elements [64] or not, see Figure 2-54. Electromagnetic field (EMF) stirring has also been shown to reduce carbide segregation. If applied correctly it can eliminate all segregation completely, see Figures 2-53 and 2-54. EMF stirring also improves solidification and refines the structure [6].

© University of Pretoria
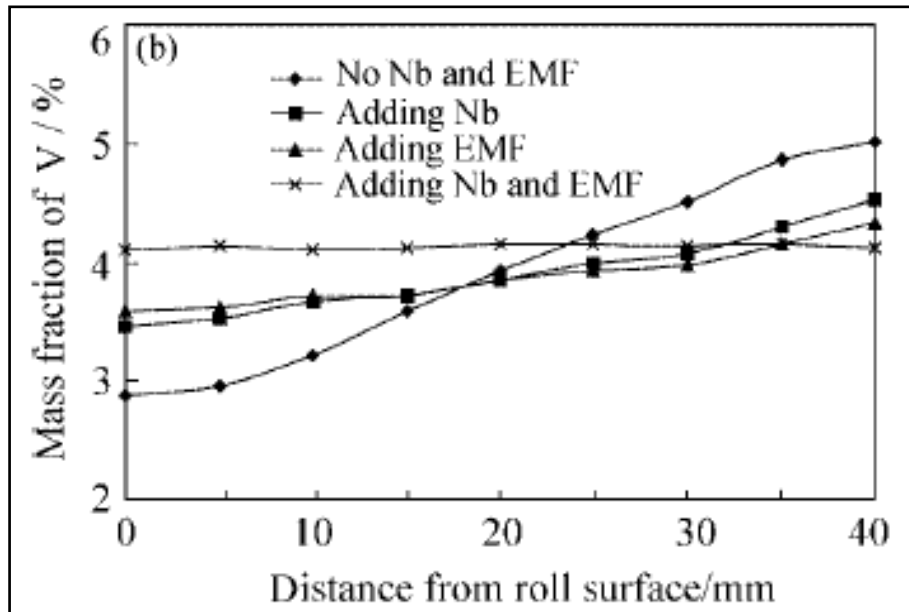
Figure 2-53: Graph showing the beneficial effect of Nb and EMF on V segregation [6].
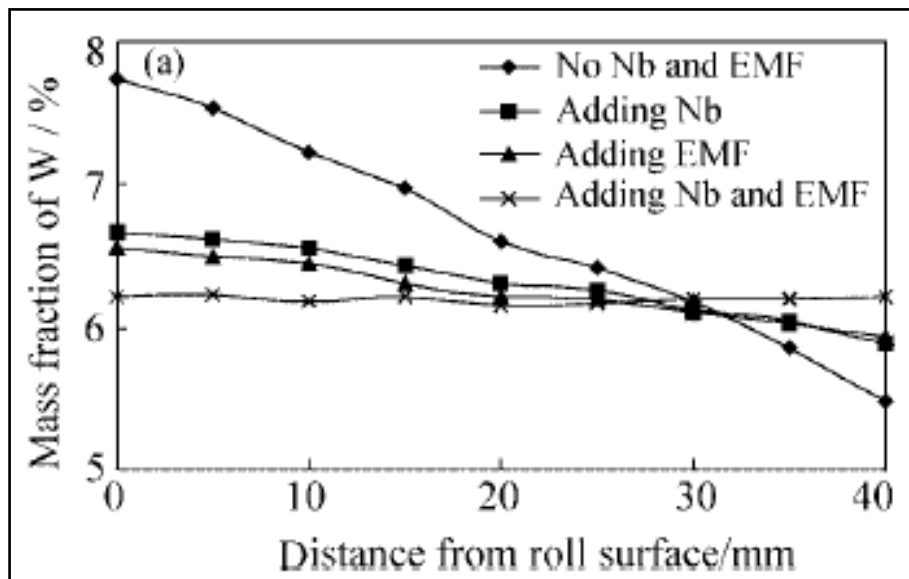
Figure 2-54: Graph showing the beneficial effect of Nb and EMF on W segregation [6].

2.7.   Wear Resistance of HSS Rolls

Wear resistance is inherently related to hardness under rolling conditions. However, spalling from the surface can occur at excessive hardness levels. Generally any metallurgical changes resulting in increased hardness will also lead to an increase in the wear resistance, see Figure 2-55. The wear resistance of some HSS roll alloys is almost eight times higher than that of HC rolls [15, 60, 67].

45

Fig. 4. Influence of the bulk Rockwell-C hardness on the wear rate.
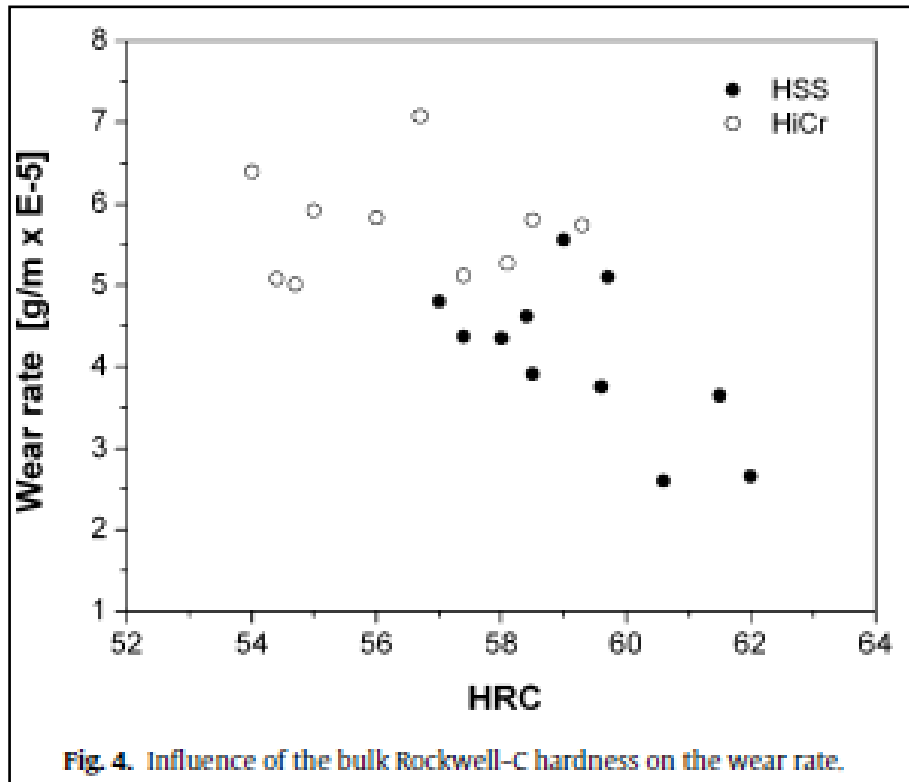
Figure 2-55: Comparison of wear rate with bulk hardness [15].

Wear rate is strongly influenced by the size, amount, distribution and morphology of the V carbides [11, 30, 43], that is the wear resistance increases with increasing V content due to an increase in hard MC carbides. Excessive amounts of V do lead to a rough working surface due to cracking on the cell boundaries, which increases the friction coefficient of the rolling force and can even cause chattering [4, 11, 30]. In terms of the application of HSS rolls in service, the surface roughness overrides the wear resistance, therefore it is recommended to increase the amount of M_7C_3 carbides in order to improve the surface roughness and wear resistance [14]. MC carbides have been shown to be the primary element which affects the friction coefficient and surface roughness, see Figures 2-56 and 2-57 [11, 30]. Reducing the mean carbide size and carbide spacing reduces the friction pick-up. This also reduces the degree of carbide breakage due to the reduction in massive carbides and reduces the matrix exposure to wear due to a reduction in the mean carbide spacing. The wear rate can vary by as much as 40% for a fixed chemistry, depending on the variation in carbide size and morphology [43, 68].

46
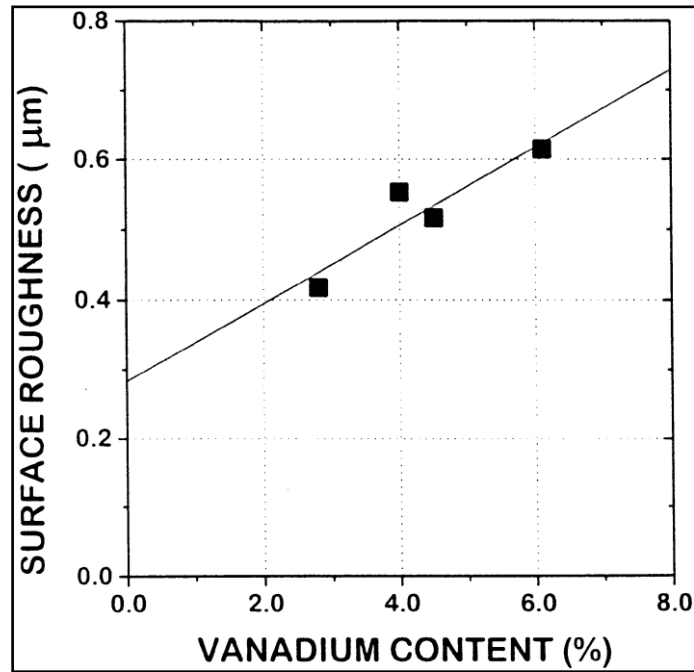
Figure 2-56: Effect of V content on the surface roughness [11].
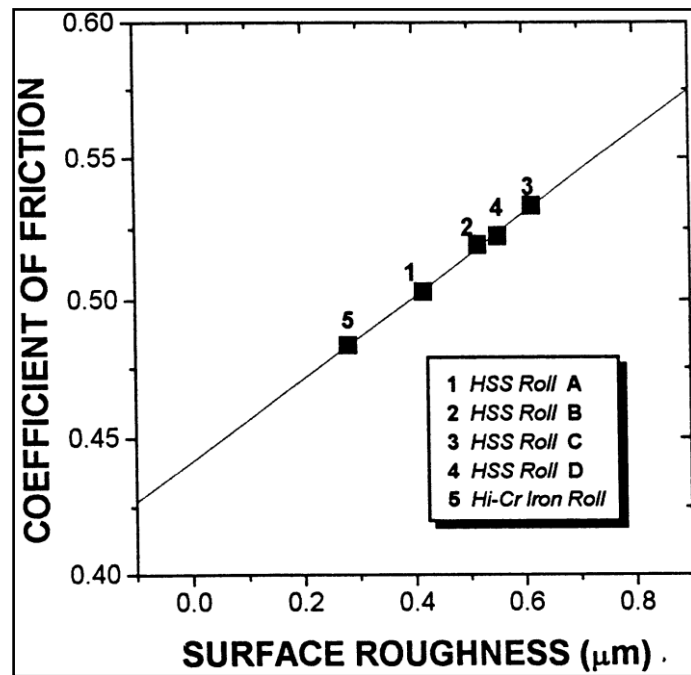
Figure 2-57: Effect of surface roughness on the friction coefficient [11].

The wear rate of a HSS roll is also dominated by the abrasion resistance which is increased by a higher matrix hardness. Thus, a higher matrix hardness results in a lower wear rate [15].

There have been many different types of wear testing performed with varying conditions and simulation types, which have made the comparison of relative wear

47

rates from different authors almost impossible. The different wear tests include pin-on-disc, multi-component wear testing, dry and wet wear testing and service simulated testing [15, 63].

The most popular method of wear testing appears to be the service simulated testing. The testing involves the rotation of a product disc and HSS disc at differential speed to create a rotating friction environment. The product disk (simulated strip material) is heated by an induction heating coil while the HSS disc (work roll) is cooled with water, see Figure 2-58. The friction coefficient (μ) is then calculated using Equation (2.3) after measuring the torque applied to the rotating axis (T) and the load placed on the disc (P). In the equation, R is the radius of the disc [11, 14, 46, 60, 69, 70].

$\mu = T/(PR)$……………………………………………………………………….(2.3)
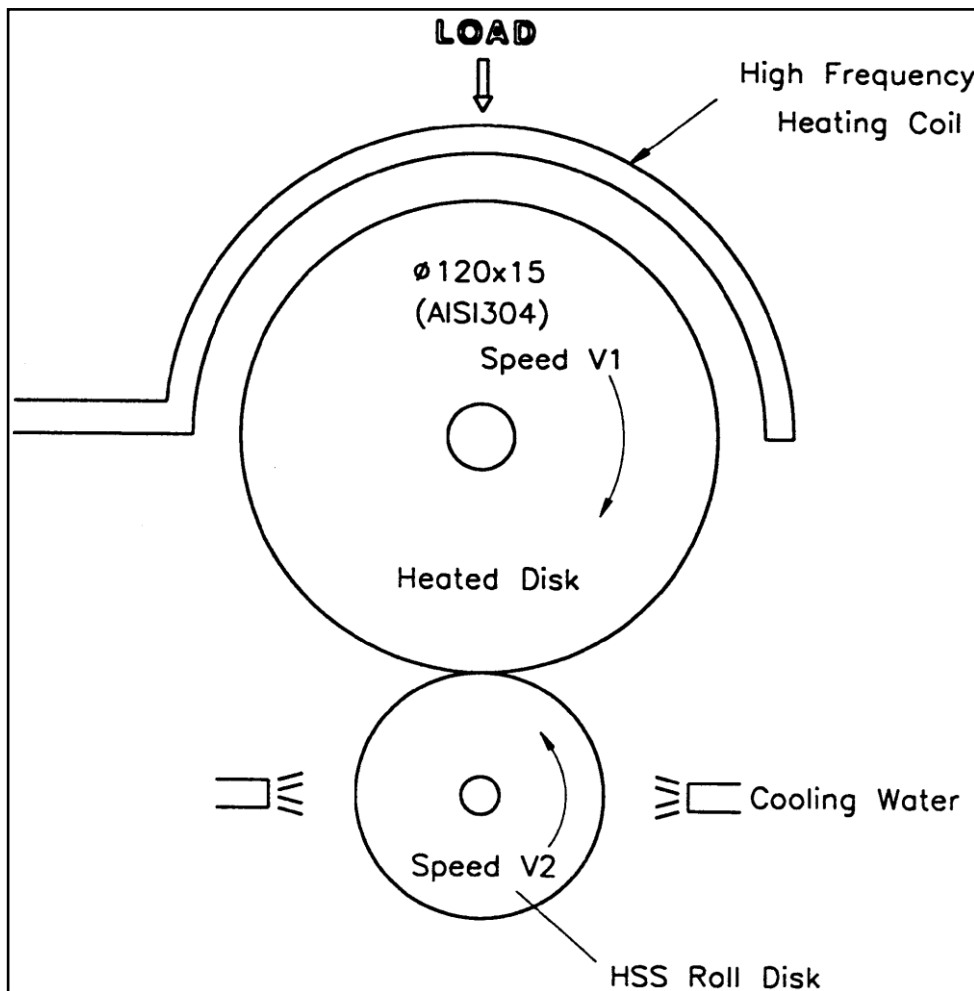
Figure 2-58: Schematic diagram of the service simulated wear testing method [11].

48

2.8.   Oxidation of HSS Roll Materials

HSS rolls are produced over a wide range of chemical compositions, hence it shows a wide range of oxidation characteristics [2]. Chromium has the largest positive influence on the oxidation characteristics, where the rate of oxidation decreases with increasing chromium content [23, 24]. Oxide formation generally decreases the friction during rolling and prolongs roll life. However, this requires the oxide layer to be compact and adherent [24, 55]. The oxidation of HSS rolls has been found to occur at the interface between the carbides and the matrix, and propagates exclusively within the matrix. This leads to non-uniform scale growth [24]. The outer oxide layer typically consists of Fe_2O_3, while the inner layer consists of $(Fe,Cr)_3O_4$ [65].

2.9.   Casting Processes and Procedures

Most of the HSS rolls currently being produced are CC, see Figure 2-59. The HSS rolls are also produced by hot isostatic pressing and cladding methods. Although research and improvement has been made on the HSS rolls, various problems are still encountered and the success rate is generally low [66].
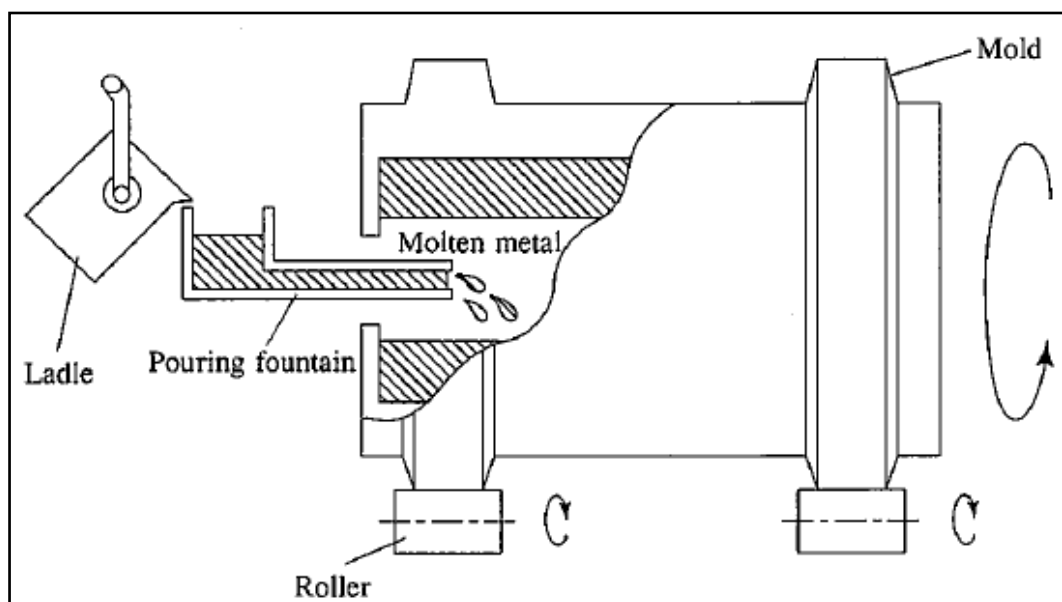
Figure 2-59: Schematic diagram of the CC casting process [66].

The CC process results in a clean and fine structure, free of inclusions. One of the principal problems in the production of HSS rolls via CC is the bonding between the HSS shell and the SG iron core. The combination of the vastly dissimilar metals gives rise to defects at the interface. A buffer/intermediate layer of grey cast iron is spun cast within the shell to decrease the absorption of carbide forming elements by the SG

49

iron core. The HSS shell material at the interface of the bond tends to consume the excess carbon from the buffer causing a layer of brittle carbide to form at the interface. An alternative to the grey iron buffer has not been proposed [2]. Simulation showed that the correct core filling time for a 450x900x2680mm core would be 180-240s. When the core filling temperature exceeds 1550°C the temperature of the outside surface of the intermediate layer is too high and will cause diffusion of the carbon in the core to the intermediate layer and promote the formation of coarse carbides. The best filling temperature for SG iron cores is approximately 1490°C [1].

During CC the solidification interval should be limited, as a wide solidification interval leads to increased absolute shrinkage and higher susceptibility to cracks. Elements expanding the solidification interval promote cracking. The pouring temperature and pouring rate can also be reduced to decrease the solidification interval and cracking susceptibility while improving the structure due to the higher cooling rate [6, 41]. The optimal pouring temperature was determined to be 1450-1520°C. The cooling rate can be increased even further by forced cooling of the chill. This is achieved by cooling water typically sprayed on the top of the mould along the axial direction as it is rotated. Uneven preheating of the mould also leads to variable cooling rates which can accelerate cracking during casting [6].

It has also been recommended that the thickness of the mould paint should be greater than 4mm or the solidification rate will be too fast and cause cracking. However, the thickness should not be excessive either. Paints with good retrogression have lower possibilities of generating cracks. Zircon based powder paints are recommended. Sodium silicate is typically used as a binder with additions of bentonite and sodium carbonate to reduce gas forming. Spraying is also obviously better than painting as this creates a more uniform paint layer [6]. It is also recommended to use a flux addition of 3-5kg/m^2 [7].

It has been suggested that the rotational speed should be altered during casting to achieve optimal properties, see Figure 2-60 [6]. The rotational speed should be systematically reduced during pouring in order to reduce the force on the outer solidified shell to prevent cracking. This will reduce the force exerted by the inner molten steel. However, once the outside of the shell has sufficiently solidified the

© University of Pretoria

rotational speed should be increased once more in order to ensure the compaction at the solidification front [6].
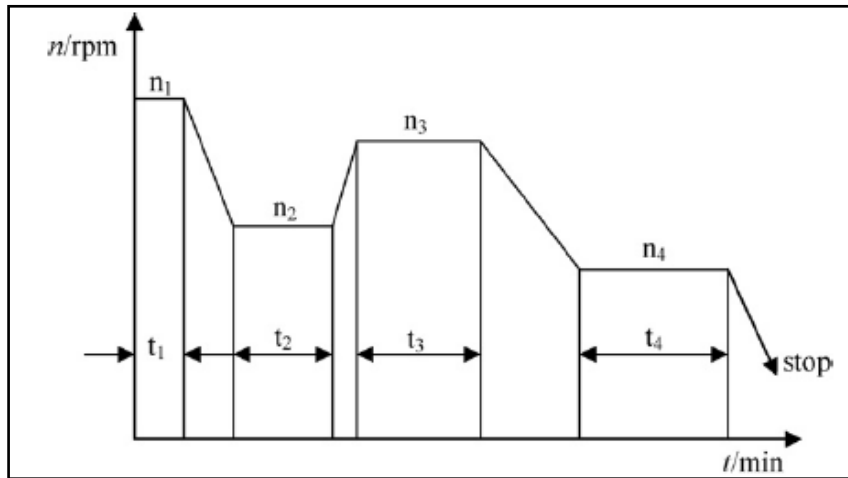
Figure 2-60: Schematic diagram for changing the centrifugal casting rotation speed [6].

It has been proposed that for an outer diameter, internal diameter and length, 330mm, 200mm, and 150mm, that n_1 is optimal at 960-980rpm, for t_1 2-2.5min. If kept at n_1 for too long, cracks could form due to excessive centrifugal force. To prevent excessive force on the external surface and prevent cracks, the optimal n_2 is 800-820rpm, for 3-3.5min. The rotational speed n_3 should be in the range of 880-900rpm for t_3 of 4.5-5min to ensure sufficient compactness. Finally n_4 is recommended to be 720-740rpm to reduce internal stress from the high solidification rate for t_4 of 5.5-6min. The applicable rotational speed can be escalated or reduced based on the following equation [6], where n is the chill rotation speed in rpm, d is the molten metal density in kg/m^3, r is the roll inner radius and β is an adjustment factor:

$$n = \frac{55200}{\sqrt{d*r}} * \beta \dots\dots\dots\dots\dots\dots\dots\dots\dots\dots\dots\dots\dots\dots\dots\dots\dots\dots\dots\dots\dots\dots\dots\dots\dots\dots\dots\dots\dots(2.4)$$

REE additions hold many benefits to the microstructure and performance of HSS rolls, however, these are difficult to absorb into the melt. The difficulty arises in the low boiling points of these elements relative to the high melting point of the HSS. The REE are typically added as modifiers with Fe and have to be baked before they are added to the melt [19].

The use of high strength steel rather than grey cast iron chills have been found to be beneficial to reduce fatigue cracks during long term usage. This is due to the prevention of thermal fatigue cracks on the internal surface of the mould which cause

51

cracking of the rolls [6, 40]. The chill is typically pre-heated for CC to approximately 250°C and should not be below 150°C prior to pouring [6].

The combination of REE modification, variable speed spin casting and controlled cooling has been shown to reduce the crack rate during casting from approximately 30% to less than 3% [6].

2.10. Operational Considerations and Modifications

HSS rolls show a higher friction coefficient compared to HC rolls and as such pose greater difficulty in mill control during rolling [2]. Some operational modifications have been found essential in order to integrate and gain the most benefit from HSS rolls for mills previously utilising HC rolls. Figure 2-61 shows the areas of milling where HSS rolls are currently being applied.

The friction effects can be reduced by improved lubrication. This will also reduce scale defects (banding and peeling) commonly found on HSS rolls operated under HC roll practises. The scale defects are encountered due to the lower Cr content of HSS rolls resulting in a higher rate of oxidation if compared to HC rolls [66]. If the additional cooling results in low temperature strip edges, induction edge heaters are proposed to homogenise the strip temperature [2].

The thermal expansion coefficient of HSS rolls is 20% more than those of other typical work rolls leading to more expansion during rolling. The mill operation needs to be adjusted to compensate for the increased thermal expansion. HSS also requires changes to non-destructive testing (NDT) practises, grinding practises, mill automation, mill operation and equipment [72].
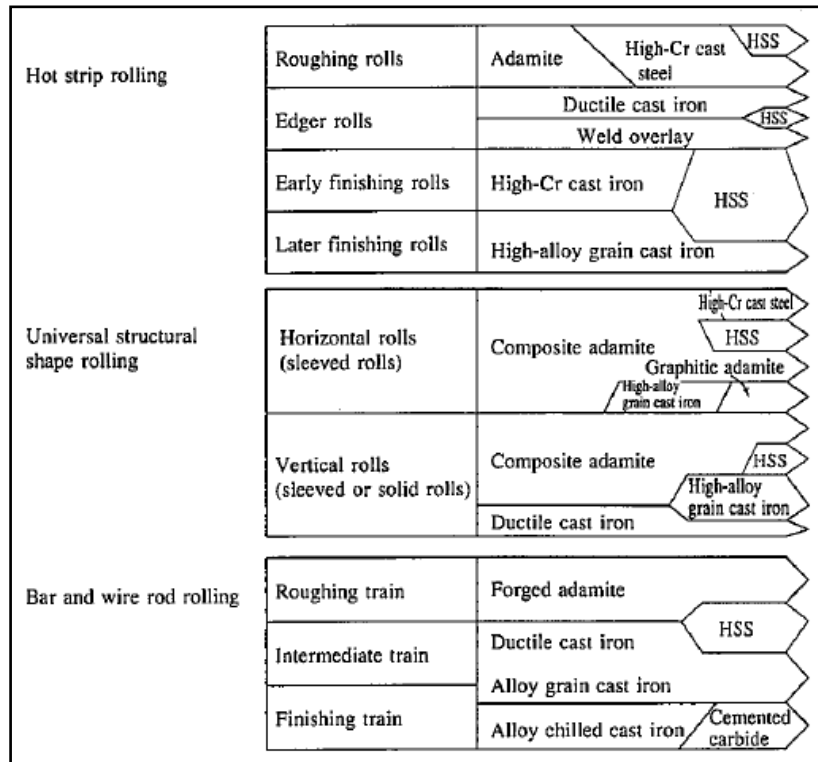
Figure 2-61: Areas where HSS rolls are utilised [66].

It is clear that HSS rolls have to be tailored to a specific location of a mill in order to gain the optimal benefit from using HSS rolls over other work rolls. This has led to a wide range of chemical compositions, mechanical properties and other characteristics of industrial HSS rolls. It is also clear that there is significantly more skill required to achieve a sound CC HSS roll compared to HC or IC work rolls. It is also clear that roll users will have to make sufficient alterations to gain the most benefit from using HSS rolls to make it more cost effective.

53

3. CHAPTER 3: EXPERIMENTAL DETAILS

3.1. Benchmarking

The roll material identified for characterisation in this study consisted of four sets of samples. The first set consisted of as-cast, first temper and final temper samples that were sectioned systematically from the shells of two rolls, which were intended for operation. The samples were sectioned from the shoulders of the shell material, which was intended to be machined away during further production. The as-cast samples, first temper samples and final temper samples were labelled AC1, AC2, T1-1, T2-1, T1-2 and T2-2 respectively, see Figures 3-1 to 3-3.

The second sample set originated from a roll which fractured in service after a mill incident occurred. The roll samples were labelled T3, see Figure 3-4. The third and fourth sample set consisted of as-cast samples from a scrapped roll which spalled during initial machining, and as-cast samples from two bond defect investigations. The samples from the third and fourth set were labelled AC3 and AC4 to AC5 respectively, see Figures 3-5 to 3-7. Table 3-1 shows a summary of the samples included in the characterisation.

The samples were subjected to intensive characterisation, which included chemical analysis, ferit scope measurements, metallography, hardness testing, scanning electron microscopy (SEM) analysis, X-ray diffraction (XRD) analysis and wear testing. Although it was intended to perform impact toughness testing, the sample sizes rendered the testing unfeasible.

Figure 3-1: Photograph of samples AC1 and AC2 as received.

54

Figure 3-2: Photograph of samples T1-1 and T2-1 as received.

Figure 3-3: Photograph of samples T1-2 and T2-2 as received.
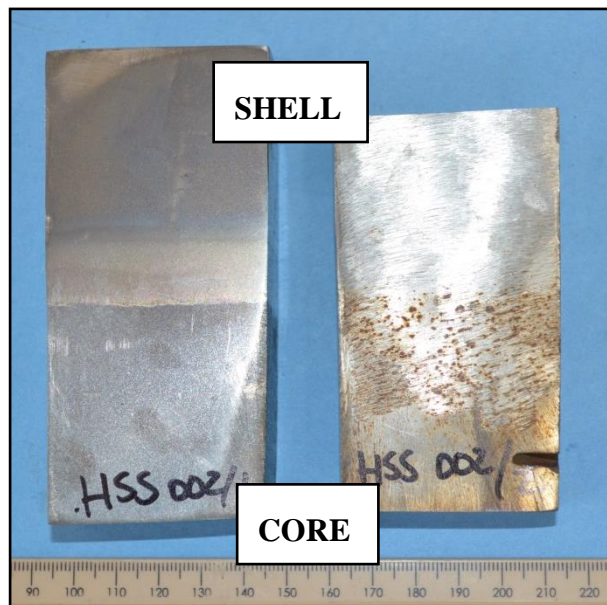
Figure 3-4: Photograph of sample T3 as received.

55
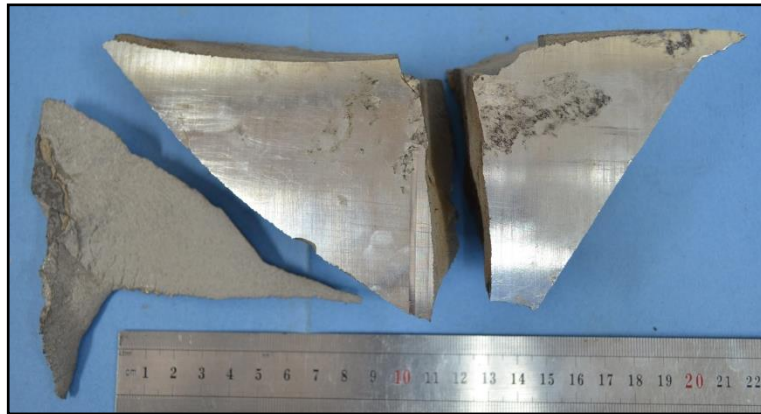
Figure 3-5: Photograph of samples AC3 as received.

Figure 3-6: Photograph of samples AC4 as received.
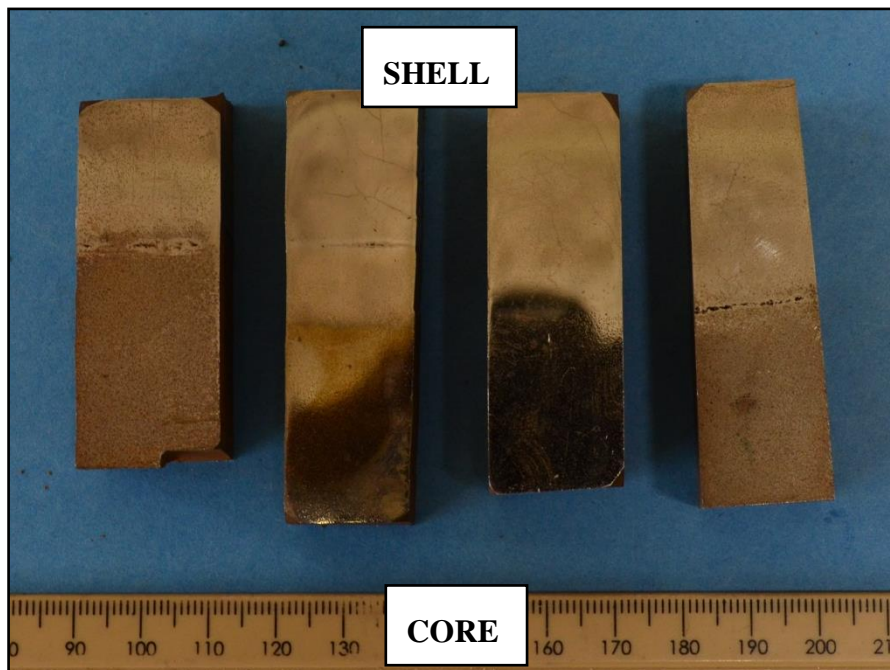
Figure 3-7: Photograph of samples AC5 as received.

56

Table 3-1: Summary of samples included in the characterisation.

Sample identification	Condition
AC1	As-Cast
AC2	As-Cast
AC3	As-Cast
AC4	As-Cast
AC5	As-Cast
T1-1	First Temper
T2-1	First Temper
T1-2	Final Temper
T2-2	Final Temper
T3	Final Temper

3.1.1. Chemical Analysis

The chemical analyses of the samples were performed using spark emission spectroscopy in order to confirm the chemical composition. This was done using a SPECTRO MAXx spectrometer with numerous reference standards, including HSS, high chromium white cast iron (HCWCI) and high V standards, see Figure 3-8. It was attempted to analyse the samples at different depth levels if they showed sufficient shell depth, in order to identify any segregation. The chemical composition at each position was determined from an average of at least three measurements.

It was also attempted to determine the composition of the samples by analytical techniques. Chemical dissolution proved ineffective on bulk samples as complete dissolution was not achieved. This was most likely due to the presence of the large network of carbides in the samples which would require different acids to dissolve than that used for the matrices. It was concluded that fines were necessary to enable complete dissolution. It was first attempted to immerse a sample in liquid nitrogen followed by impact or compression loading. The HSS material could not be crushed in order to generate fines. It was also attempted do drill and mill the HSS material, which also proved to be unsuccessful. In an attempt to generate fines, samples were atomized. The atomization consisted of flushing the chamber with argon gas to remove all the air, before inducing a vacuum and heating to 1450°C and gas atomizing the molten material. The high temperatures required in order to pour the molten metal caused melting of the adjacent protection screens, causing contamination and

blockage during pouring. Hence, the atomization was also not effective in producing fines sufficient for analytical chemical analysis.

Figure 3-8: Photograph showing the SPECTRO MAXx utilised.

3.1.2. Feritscope Analysis

Feritscope measurements were performed using a Fischer Feritscope$_®$ MP30 to determine the amount of magnetic and non-magnetic phases on the specimen surfaces, see Figure 3-9. The equipment was calibrated prior to the analysis using the high ferrite containing reference standards ranging from 0-84.1% ferrite. The device measures the percentage of magnetic phases such as the ferrite matrix, while the remainder consists of non-magnetic phases such as carbides and retained austenite. The average values were calculated from at least five measurements per sample.

Figure 3-9: Photograph showing the Fischer Feritscope® MP30 utilised.

3.1.3. Hardness Testing

Vickers hardness testing was performed to determine the bulk hardness and predict the relative wear resistance of the samples. The testing was performed using an EMCOTEST Duravision universal hardness testing machine, see Figure 3-10. A load of 50kg was used with a dwell time of 15s. The calibration was verified with two reference materials in order to attain a calibrated range of approximately 500-750VHN. The hardness was measured over the shell depth at intervals of 15mm. Ten measurements were performed on all the samples at each depth interval.

It was envisaged to also perform Micro-Vickers hardness tests to characterise the hardness of the matrix and carbides at the different locations. However, due to the refined nature of the carbide's cell size as compared to traditional IC and HC rolls,

59

suitable matrix and carbide regions were not present in order to perform the evaluation.

Figure 3-10: Photograph of the Emcotest Duravision universal hardness tester.

3.1.4. Metallography

The microstructural characterisation of the samples consisted of an extensive examination procedure. The sample preparation entailed sectioning with both a JOEMARS AZ75DR electrical discharge machine (EDM) and water cooled abrasive cutting machines. The samples were mounted in conductive resin using a Struers Labopress-3 hot mounting machine, with a temperature of $180°C$, force of 30kN, total heating time of 6 min and total cooling time of 8 min. After mounting, the samples were prepared for metallography as detailed in Table 3-2. During grinding progressively finer grit silicon carbide embedded paper was used to remove deformation effects, which had been induced by cutting and rendering a surface amenable to polishing.

60

Table 3-2: General metallography preparation procedure [73].

Step	1	2	3	4	5
Type	Grinding	Polishing	Polishing	Polishing	Polishing
Abrasive	SiC	Diamond			Colloidal silica
Grit	120-1200	6μm	3μm	1μm	0.04μm
Speed (rpm)	300	150	150	150	150
Force (N)	35	35	35	30	30
Time (min)	Until planar	3	3	3	2

Each sample was prepared in a number of mountings in order to analyse them with a variety of etchants as detailed in Table 3-3. The etchants were utilised to distinguish various features of interest. Etchants 2 and 7 in Table 3-3 were also combined serially for some of the carbide volume fraction measurements. The metallography was performed using an Olympus BX61 optical microscope, see Figure 3-11. The microscope was complemented with the Stream® image analysis software, which includes volume fraction and particle analysis functions. The software was utilised to perform various volume fraction measurements under different etching conditions. Polarisation filters and dark field illumination was also used to highlight specific features during the analysis.

Figure 3-11: Photograph showing the Olympus BX61 microscope utilised.

61

Table 3-3: Etchants used for the metallography analysis [74, 75].

Etchant	Composition	Procedure	Significance
1. Nital	5% Nitric acid	Swab for up to 2min	General microstructure etchant
	95% Ethanol		
2. Groesbeck's etchant	4g $KMnO_4$	Immerse for 30s	M_6C outlined and coloured brown, M_7C_3 faint effect
	4g NaOH		
	100ml H_2O		
3. Murakami's etchant	10g NaOH	Immerse at 20°C for 30s	Outline and colour M_7C_3 and M_6C, faint effect on
	10g $K_3Fe(CN)_6$		
	100ml H_2O		
4. APS	10g $(NH_4)_2S_2O_8$	Electrolytic, 6V DC for 11s	Attacks MC and $M_{23}C_6$
	100ml H_2O		
5. ASP	2g Picric acid	Immerse 90-100°C for 5min	Colour M_6C and M_3C
	25g NaOH		
	100ml H_2O		
6. Bechet	Saturated Picric acid	Immerse 1min	Grain boundary etchant
	1% Teepol		
	1% HCl		
7. Beraha's etchant	3g PMB	Immerse for 90s	Austenite coloured blue and brown
	1g Sulfamic acid		
	100ml H_2O		

3.1.5. Scanning Electron Microscope (SEM) Analysis

SEM analysis was performed using a FEI Nova NanoSEM 230 high-resolution scanning electron microscope (HRSEM) fitted with an EDAX energy dispersive x-ray (EDX) detector in order to characterise the chemical composition of both the matrix and carbides and any variations over the shell depth, see Figure 3-12. Backscatter electron mode was used throughout the analysis. The average chemical compositions were determined from at least 5 measurements in each case, except for the M_2C carbide needles, which were averaged from at least 3 measurements. An accelerating voltage of 30kV was used during the analysis.

Figure 3-12: Photograph of the FEI NOVA NanoSEM 230 FEG used for analysis.

3.1.6. X-Ray Diffraction (XRD) Analysis

XRD analysis was performed to identify the presence of retained austenite and any minor phases present, which may not be identifiable by metallography. Sample preparation followed the same procedure utilised during metallography. The samples received a brief final electro polish using chromic-acetic acid at 15V (induced current was typically 1.5A) using a stainless steel cathode. The samples were examined prior to testing to ensure no pitting of the surface had occurred [76, 77]. The samples were prepared using a zero background holder. They were analysed with a Bruker D8 Advance X-ray diffractometer, with a Co X-ray source, see Figure 3-13. The phases were identified using Topas complemented by the ICDS database. The relative phase amounts (weight %) were estimated using the reference intensity ratio method.

63

Figure 3-13: Photograph of the Bruker D8 Advance X-ray diffractometer used for analysis.

3.1.7. Wear Testing

The testing was aimed at predicting the relative wear resistance of the various samples after heat treatments, which is related to in-service performance. The only method of testing amenable to the sample size and availability was tribology testing. The testing utilised wire cut samples, which were 18x8x4mm in size. The testing utilised a tungsten carbide ball, with the highest load of 25N and a scanning motion. The test was performed in both dry and wet conditions. Used rolling fluid originating from the Steckel mill at Columbus Stainless Steel was used for the wet testing. The degree of wear was determined by the mass loss.

3.1.8. Statistical Analysis

Statistical analysis of all the results was performed where applicable to test the influence of all the parameters evaluated, including any deviations. The statistical

analysis also indicates the reliability and repeatability of the results. The Standard Deviation (S) of all measurements was calculated as shown in Equation 3.1 [78]:

$$S = \sqrt{\frac{\sum(Xi-X)^2}{N-1}}$$ ……………………………………………………………….(3.1)

where X is the mean of the individual measurements, Xi the individual measured value and N the total number of measurements. Unfortunately, standard deviations cannot be compared directly with each other, thus the Coefficient of Variance (CV) was calculated to serve as a relative deviation, as shown in Equation 3.2 [78]:

$$CV = \frac{S}{X} * 100\%$$ ……………………………………………………………..(3.2)

Additionally, the 95% confidence limit (95%CL) and percentage relative accuracy (%RA) were calculated as shown in Equations 3.3 and 3.4 [78]:

$$95\% \, CL = \frac{t*S}{\sqrt{N-1}}$$ ……………………………………………………………….(3.3)

$$\%RA = \frac{95\% \, CL}{X} * 100\%$$ ……………………………………………………………..(3.4)

In Equations (3.3) and (3.4) t varies with N. The 95%CL value indicates a range in which 95% of all measurements should be contained. The %RA is a measure of the relative confidence limit and should be below 10% in order to ensure sufficient repeatability.

3.2. Heat Treatment

As-cast HSS and HC material was utilised for the heat treatment study, see Table 3-4. HC material was included in order to compare the properties with HSS, although it did not form part of the main aim of this work. Samples were sectioned for the study using wire cutting to dimensions of 10x10x25mm. The 25mm sections of the samples represented the shell depth from approximately 5mm to a depth of 30mm.

The schedule was divided into four sections. The first set of 8 samples (designated LT) were utilised to determine the temper curve with reference to hardness under laboratory conditions. The second set of samples No. 9 to 15 (designated ST) were used to determine the temper curve with reference to hardness under simulated production conditions. Longer holding times were used to simulate the slower ramping rates and longer holding times required for the large rolls.

Table 3-4: Heat treatment schedule.

Heat	Designation	Annealing Temp (°C)	Annealing Time	Austenitising Temp (°C)	Austenitising Time	1st Temper Temp (°C)	1st Temper Time	2nd Temper Temp (°C)	2nd Temper Time	Cooling
1	LT0	-	-	1050	2h	-	-	-	-	Air
2	LT48	-	-	1050	2h	425	2h	475	2h	
3	LT50	-	-	1050	2h	450	2h	500	2h	
4	LT53	-	-	1050	2h	475	2h	525	2h	
5	LT55	-	-	1050	2h	500	2h	550	2h	
6	LT58	-	-	1050	2h	525	2h	575	2h	
7	LT58	-	-	1050	2h	525	2h	575	2h	
8	LT58	-	-	1050	2h	550	2h	600	2h	
9	ST0	-	-	1050	12h	-	-	-	-	Furnace
10	ST43	-	-	1050	12h	375	10h	425	10h	
11	ST45	-	-	1050	12h	400	10h	450	10h	
12	ST48	-	-	1050	12h	425	10h	475	10h	
13	ST50	-	-	1050	12h	450	10h	500	10h	
14	ST53	-	-	1050	12h	475	10h	525	10h	
15	ST55	-		1050	12h	500	10h	550	10h	
16	LA85	850	2h	-	-	-	-	-	-	Air
17	LA55	850-550	2h	-	-	-	-	-	-	
18	LA85T0	850	2h	1050	2h	-	-	-	-	
19	LA85T48	850	2h	1050	2h	425	2h	475	2h	
20	LA85T50	850	2h	1050	2h	450	2h	500	2h	
21	LA85T53	850	2h	1050	2h	475	2h	525	2h	
22	LA85T55	850	2h	1050	2h	500	2h	550	2h	
23	LA85T58	850	2h	1050	2h	525	2h	575	2h	
24	LA85T60	850	2h	1050	2h	550	2h	600	2h	
25	SA85T0	850	10h	1050	12h	-	-	-	-	Furnace
26	ST85T40	850	10h	1050	12h	375	10h	425	10h	
27	ST85T43	850	10h	1050	12h	400	10h	450	10h	
28	ST85T45	850	10h	1050	12h	425	10h	475	10h	
29	ST85T48	850	10h	1050	12h	450	10h	500	10h	
30	ST85T50	850	10h	1050	12h	475	10h	525	10h	
31	ST85T53	850	10h	1050	12h	500	10h	550	10h	

The third set of samples, No. 16 to 24 (designated LA), were used to determine the effect of pre-annealing on the temper curve with reference to hardness under laboratory conditions. The treatment included pre-annealing at 850°C for 2 hours and reducing the temperature to 550°C, holding for an additional 2 hours, before ramping up to 1050°C in order to perform the remainder of the typical heat treatment similar to that applied for the LT sample set. LA85 was annealed at 850°C only with no further

processing, while LA55 was annealed at 850°C, followed by holding at 550°C for 2 hours, but without performing the austenitisation. The fourth set of samples No. 25 to 31 was used to determine the effect of pre-annealing on the temper curve with reference to hardness under simulated production conditions. HSS material was utilised for all four sets, while the HC material was only included in the first and second sample sets for comparison to the HSS material.

The austenitising temperature of 1050°C was selected based on the literature indications that this temperature typically yields the highest hardness levels. The second tempering temperature was selected to be 50°C above the first tempering temperature to achieve a more uniform hardness within the matrix microstructure. This originated from the observation that the HSS material contains significant amounts of retained austenite upon cooling after austenitising. The retained austenite is transformed to martensite during cooling after the first temper. If the second tempering temperature is selected to be in excess of the first tempering temperature, this could result in the newly formed martensite to be significantly under-tempered relative to the martensite formed after austenitising.

The laboratory simulated samples were removed from the furnace and cooled in still air after each treatment, while the production simulated samples were allowed to furnace cool to represent a much slower cooling rate in practice from a more massive roll. The heat treatment was performed using a Lenton laboratory furnace and a Lenton Elite tube furnace, see Figures 3-14 and 3-15. The tube furnace was utilised for the annealing and austenitising treatments under simulated conditions, since it can be performed under a controlled atmosphere. Inert, high purity argon gas was utilised for the tube furnace treatments. The need for a controlled atmosphere during the simulated conditions arises from the need to eliminate excessive oxidation, which on these smaller sized samples, may results in significant compositional changes. The extended time at high temperatures increases the level of oxidation, which was found to influence the test results. Under industrial conditions some oxidation can be tolerated at these levels, but proved to be excessive given the small samples used for the study.

Figure 3-14: Photograph of the Lenton laboratory furnace used for heat treatment.
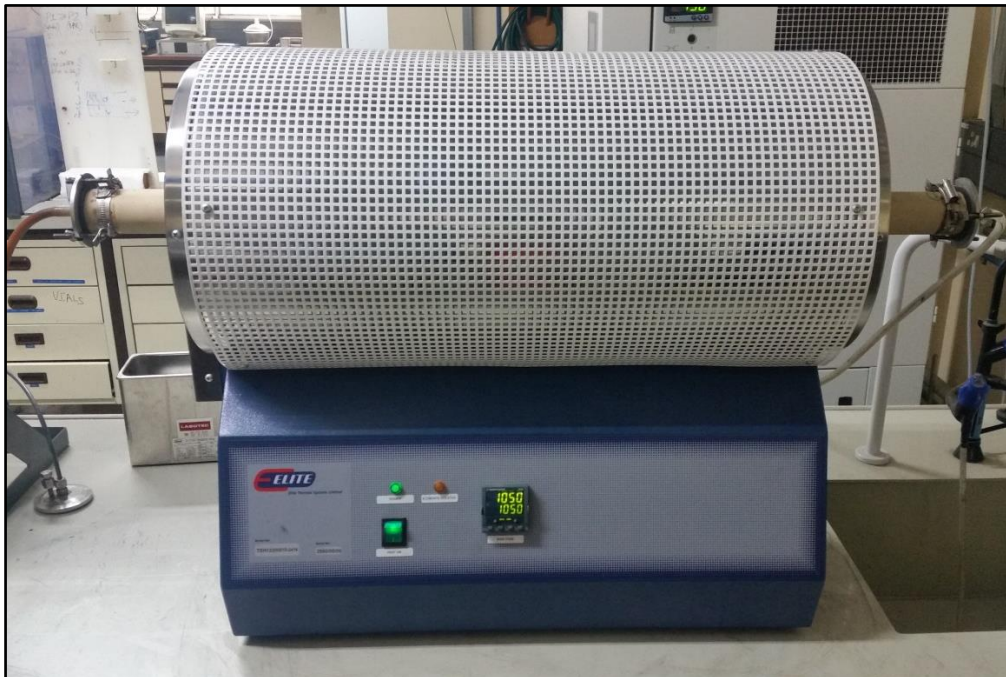
Figure 3-15: Photograph of the Lenton Elite tube furnace used for heat treatment.

The heat treated materials were subjected to similar characterisation as the benchmarked material including metallography, hardness testing, XRD, SEM and statistical analysis. In addition it was also attempted to do simultaneous thermal analysis (STA), tensile and impact testing as detailed below.

68

3.2.1. Metallography

Each of the samples was prepared in a number of mountings in order to analyse them with a variety of etchants as detailed in Table 3-5. The etchants were utilised to distinguish various features of interest. The etching procedure deviated from the benchmarked material. The selective carbide etchants were applied in sequence without re-preparing the samples, in order to systematically reveal the respective carbides.

Table 3-5: Etchants used for the metallography analysis [74, 75].

Etchant	Composition	Procedure	Significance
1. Nital	5% Nitric acid	Swab for up to 2min	General microstructure etchant
	95% Ethanol		
2. Groesbeck's etchant	4g $KMnO_4$	Immerse for 30s	M_6C outlined and coloured brown, M_7C_3 faint effect
	4g NaOH		
	100ml H_2O		
3. Murakami's etchant	10g NaOH	Immerse at 20°C for 30s	Outline and colour M_7C_3 and M_6C, faint effect on $M_{23}C_6$
	10g $K_3Fe(CN)_6$		
	100ml H_2O		
4. ASP	2g Picric acid	Immerse 90-100°C for 5min	Colour M_6C and M_3C
	25g NaOH		
	100ml H_2O		
5. Chromic	1g CrO3	Electrolytic, 2-3V DC for 10s	Attacks M_2C, outlines M_7C_3 and $M_{23}C_6$ and colours MC
	100ml H_2O		
6. Beraha's etchant	3g PMB	Immerse for 90s	Austenite coloured blue and brown
	1g Sulfamic		
	100ml H_2O		

3.2.2. Tensile Testing

Tensile testing was performed to determine the yield strength, ultimate tensile strength (UTS) and elongation to fracture. The testing was performed using an Instron 1175 static testing machine and BlueHill2 software, see Figure 3-16. The displacement rate used was 2mm/min for the testing. The testing was performed in triplicate.

Figure 3-16: Photograph of the Instron 1175 used for tensile testing.

The HSS roll material cannot be machined by conventional means and is only amenable to wire cutting utilising plate specimens. The ruling section of the available material was small, which limited the specimen size to the shell depth. This necessitated the use of a smaller size specimen than specified under the sub-size specifications of ASTM E8. The specimens were machined according to the drawing shown in Figure 3-17.
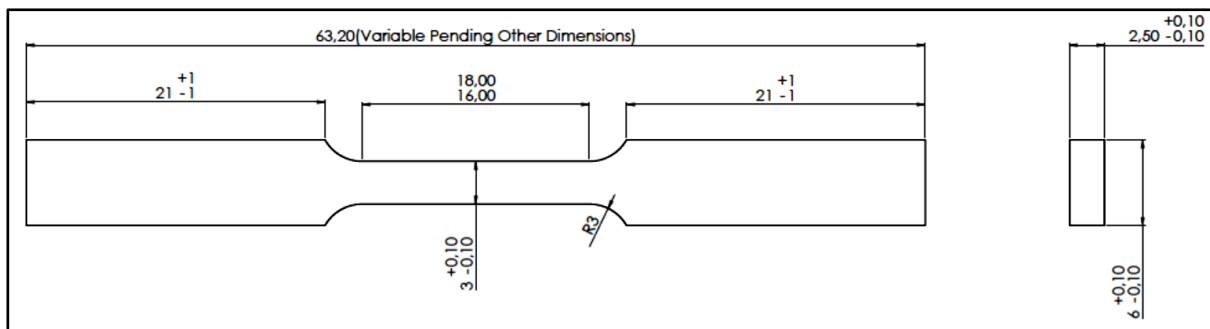
Figure 3-17: Drawing of the tensile specimen dimensions utilised.

70

3.2.3. Impact Testing

Charpy V-Notch (CVN) impact testing was performed to determine the impact toughness of the material and the variation with applicable heat treatment. The testing was performed using an Instron SI-1M instrumented impact testing machine, see Figure 3-18. It was opted to use an instrumented impact testing machine, due to the HSS material being inherently brittle with expected low impact energy values. The instrumented CVN test would ensure accurate comparison and supply additional information regarding both the crack initiation and propagation energy and not only the overall characteristics. The testing was performed in triplicate, and in accordance with the ASTM E23 specification.

Figure 3-18: Photograph of the Instron SI-1M used for CVN impact testing.

3.2.4. Simultaneous Thermal Analysis (STA)

STA analysis was applied to characterise the formation temperatures and sequence during solidification. It was intended to use small chippings from the samples as the

71

HSS material could not be successfully milled or drilled for shavings. However, the chippings showed poor consistency of results and inconsistent sample weight for comparison. To improve the results and consistency, wire cutting was utilised in order to section 1.5mm cubes. The analysis was performed using a Netzsch STA 429 CD in an inert Argon atmosphere (at a flow rate of 20ml/min) utilizing a rate of 5°C/min for both the heating and cooling cycles, see Figure 3-19. A holding time of 20min was utilised between the heating and cooling cycles to stabilise the sample. A peak temperature of 1500°C was utilised for the testing. The analysis was performed within 6.8mm diameter Al_2O_3 crucibles.

Figure 3-19: Photograph of the Netzsch STA 429 CD used for analysis.

The interpretation of the STA curves necessitated the construction of a baseline at each deviation from the straight line endotherm/exotherm. The area under the endotherm/exotherm was calculated in order to compare the enthalpy of formation or dissolution.

4. CHAPTER 4: RESULTS

4.1. Benchmarking

4.1.1. Chemical Analysis

The chemical compositions of the respective samples were generally very similar, see Table 4-1. Due to proprietary reasons the exact composition may not be reported. The minimum and maximum values does not represent the tested minimum and maximum values but merely the range all test results conformed to. The chemical composition of samples AC1, T1-1 and T1-2 was near identical, as expected, since they were sectioned from the same roll at different stages of production. Similarly samples AC2, T2-1 and T2-2 were also very similar in composition. Sample AC3 showed the lowest average W content. Sample AC4 showed the highest Mo and Cr content. Sample T3 showed the lowest average V and highest Ni contents. Thus, sample T3 is expected to show a lower average vanadium carbide content compared to the other samples. No measurable indication of chemical segregation over the shell depth was observed for V, W or Mo between the samples measured.

Table 4-1: Spark emission spectrometry results (wt%).

Sample		C	V	Cr	Mo	W	Ni	Si	Mn
All*	Minimum	1.0	1.0	1.0	1.0	1.0	0.0	0.0	0.0
	Maximum	2.5	7.0	8.0	5.0	5.0	3.0	2.0	2.0
Optimal		1,9-2,0	4,0-6,0	5,0-7,0	3,0-4,0	3,0-4,0	0,7-0,9	-	-

The chemical composition of the samples generally compared well with the optimal composition proposed in the literature. The total content of carbide-formers was similar for all the samples with samples AC3 and T3 showing lower values, at 17.36% and 17.21% respectively, compared to the other samples; see Figure 4-1 and Table 4-2.

73

Table 4-2: Comparison of Carbide-former content.

Sample	Surface depth	Carbide formers	W_{eq}
AC1	10 mm	16.79	9.85
	20 mm	16.29	9.49
	Average	16.54	9.67
AC2	10 mm	16.71	9.67
	20 mm	16.64	9.58
	Average	16.68	9.63
AC3	10 mm	15.79	8.81
	20 mm	15.90	9.01
	30 mm	15.65	8.96
	Average	15.78	8.93
AC4	Average	16.91	10.79
AC5	10 mm	15.80	9.85
	20 mm	16.52	10.29
	30 mm	17.19	10.76
	Average	16.50	10.30
T1-1	10 mm	16.74	9.81
	20 mm	16.96	9.98
	Average	16.85	9.90
T1-2	10 mm	16.77	9.86
	20 mm	16.54	9.62
	Average	16.66	9.74
T2-1	10 mm	16.95	10.01
	20 mm	16.29	9.48
	Average	16.62	9.75
T2-2	10 mm	16.99	9.97
	20 mm	16.32	9.46
	Average	16.66	9.72
T3	10 mm	16.18	10.22
	20 mm	15.25	9.48
	30 mm	15.75	10.00
	Average	15.73	9.90
AC1, T1-1, T1-2	Average	16.68	9.77
AC2, T2-1, T2-2	Average	16.65	9.70
All	Minimum	15.25	8.81
	Maximum	17.19	10.79
	Average	16.49	9.83

74
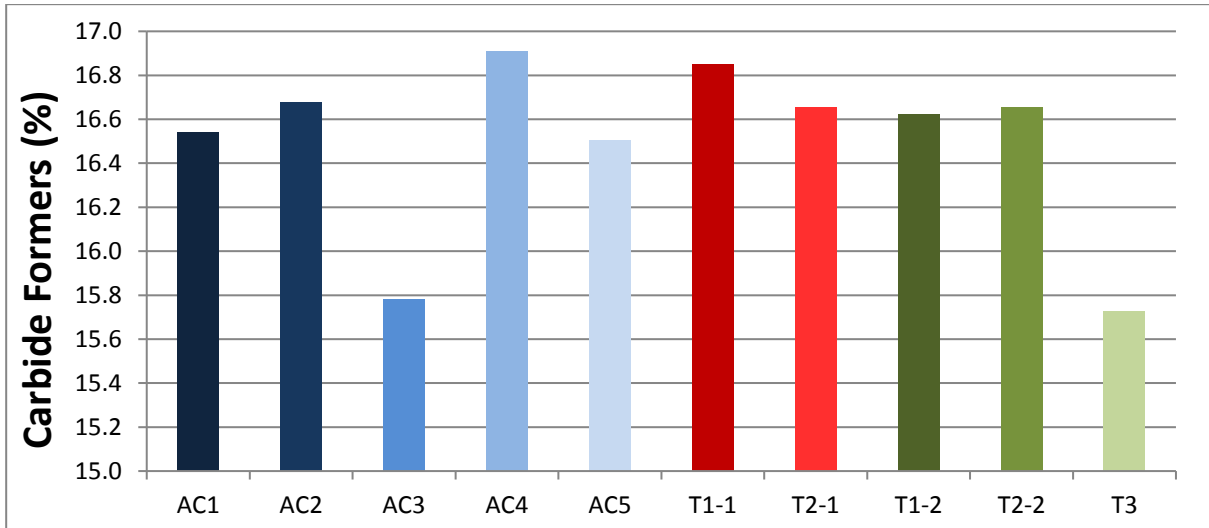
Figure 4-1: Comparison of the total carbide-former content.

4.1.2. Feritscope Analysis

The results from the Feritscope analysis are detailed in Table 4-3 and Figure 4-2. The black lines on the graph indicate the highest and lowest individual values measured. The average values were calculated from 5 individual measurements.

Table 4-3: Results of Feritscope analysis.

Sample	Ferrite (%)			Statistical Analysis			
	Minimum	Maximum	Average	S	CV	95%CL	RA
AC1	41.3	43.8	42.6	1.0	2.3%	1.4	3.2%
AC2	40.9	43.5	42.3	1.0	2.4%	1.4	3.4%
AC3	36.6	38.2	37.4	0.6	1.5%	0.8	2.1%
AC4	37.5	40.6	39.1	1.2	3.1%	1.7	4.3%
AC5	37.8	39.5	38.5	0.7	1.8%	1.0	2.5%
T1-1	48.3	49.9	49.1	0.6	1.2%	0.8	1.7%
T2-1	48.5	51.6	49.8	1.1	2.3%	1.6	3.2%
T1-2	60.7	64.7	62.1	1.7	2.7%	2.3	3.7%
T2-2	59.9	61.7	60.6	0.7	1.1%	0.9	1.5%
T3	74.5	78.1	77.0	1.5	1.9%	2.1	2.7%

The as-cast specimens showed the lowest values as expected, since they should contain the highest amount of retained austenite. The first temper specimens (T1-1 and T2-1) showed a slight increase in ferrite percentage value compared to the as-cast specimens, which is probably attributed to the transformation of some of the austenite to martensite. The final tempered specimens (T1-2, T2-2 and T3) showed the highest ferrite values as expected, since most or all of the austenite is expected to

75

have transformed to martensite. Specimen T3 showed a higher value compared to samples T1-2 and T2-2. This is expected as T3 showed a much lower total content of carbide formers compared to samples T1-2 and T2-2. Hence, the difference could be due to lower quantities of carbides in the structure.
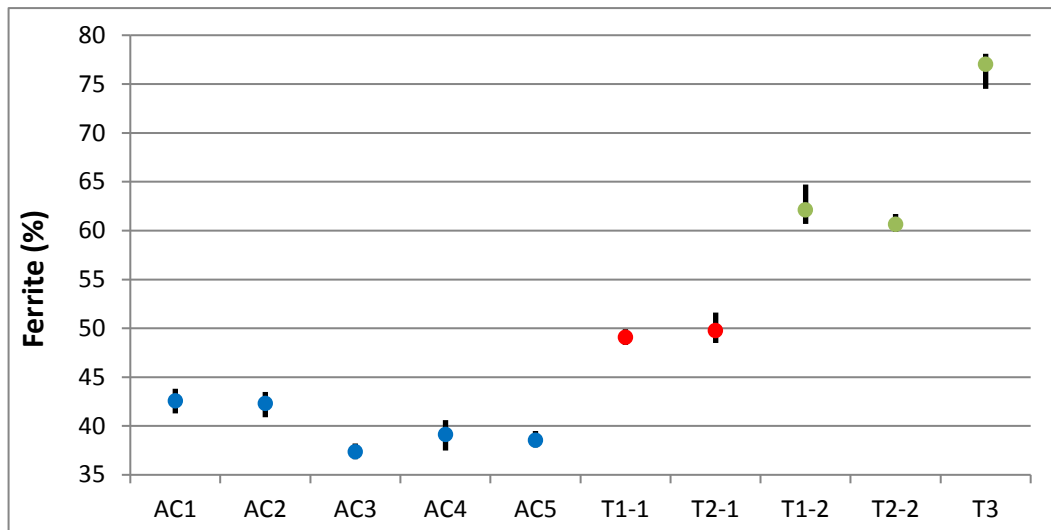
Figure 4-2: Average ferrite content of the tested samples as determined by the Feritscope.

The low standard deviations (S) and coefficient of variance (CV) suggests limited variation between the test results. The small 95% confidence limits also confirm that the variations in average ferrite measurement between the as-cast, first temper and final temper samples are definite and are not attributed to variations in measurements. The low relative accuracy values also indicate sufficient repeatability.

4.1.3. Hardness Testing

The results from the hardness testing are detailed in Figure 4-3 and Table 4-4. The average hardness values were calculated from at least 10 measurements on each sample. The as-cast samples generally showed the lowest overall hardness values, with the final temper samples (T1-2, T2-2 and T3) showing intermediate hardness values and the first temper samples (T1-2, T2-1) showing the highest hardness values. This is as expected since the matrix of the as-cast samples contain significant quantities of soft austenite, thereby reducing the matrix hardness and hence also the bulk hardness, while the matrix of the first temper samples contained large quantities of high hardness, un-tempered martensite. The reduced hardness of the final tempered samples compared to the first temper samples is due to the tempering (softening) of the fresh martensite during the second temper.
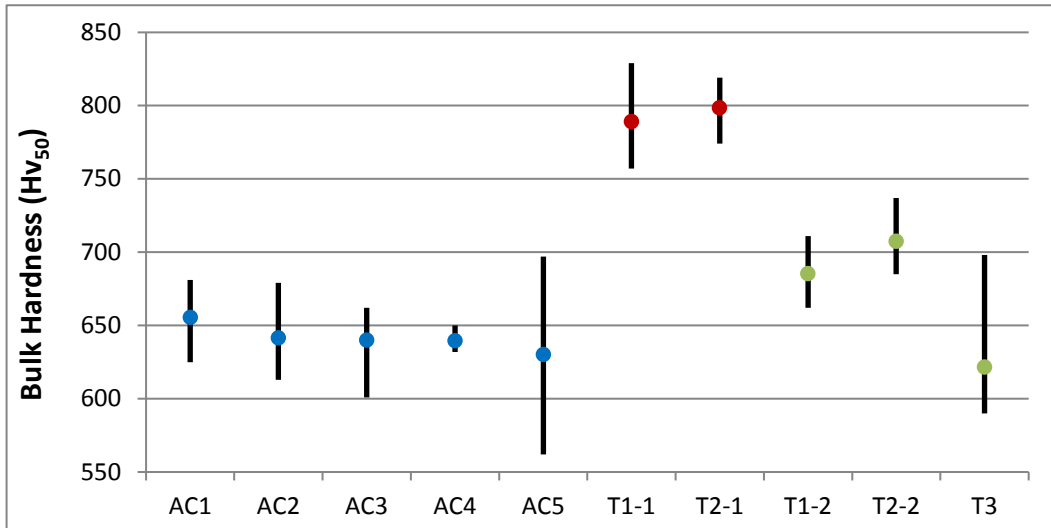
Figure 4-3: Overall average Vickers hardness values and hardness range as tested.

The exception to the general trend was sample T3, which showed a hardness more than 60HV lower than the other final temper samples (T1-2 and T2-2) and even lower than any of the as-cast samples. The lower bulk hardness could be attributed to lower quantities of carbides present in the structure as suggested by the chemical analysis and the feritscope analysis. The bulk hardness of the final tempered samples compared well with the rolls manufactured by other roll producers, see Table 2-6 [48-51, 78-82].

The bulk hardness remained fairly constant over the first 30mm depth on all the samples, showing no consistent trend or decrease in hardness, see Figure 4-4. This is unusual as the literature typically reports a consistent decrease in hardness with increasing shell depth due to the variations in centrifugal force during casting which causes segregation effects [48-51, 64]. Sample T3 even showed an increase in hardness at a depth of 45mm from the surface.

Table 4-4: Hardness testing results.

Sample		Hardness (Hv$_{50}$)			Statistical Analysis			
Description	Depth	Minimum	Maximum	Average	S	CV	95%CL	RA
AC1	Surface	625	651	641	8.7	1.4%	6.5	1.0%
	15mm	636	667	655	9.5	1.4%	7.1	1.1%
	30mm	663	681	670	5.1	0.8%	3.9	0.6%
	Overall	625	681	656	14.5	2.2%	5.5	0.8%
AC2	Surface	613	654	633	13.4	2.1%	10.1	1.6%
	15mm	626	679	647	14.6	2.3%	11.0	1.7%
	30mm	631	665	645	9.1	1.4%	6.9	1.1%
	Overall	613	679	641	13.7	2.1%	5.2	0.8%
AC3	Surface	604	662	633	14.7	2.3%	11.1	1.8%
	15mm	601	657	634	17.5	2.8%	13.2	2.1%
	30mm	620	641	634	17.5	2.8%	13.2	2.1%
	45mm	639	692	664	15.1	2.3%	11.4	1.7%
	Overall	601	662	640	19.7	3.1%	6.4	1.0%
AC4	Overall	632	650	640	5.9	0.9%	4.5	0.7%
AC5	Surface	587	671	639	23.5	3.7%	17.7	2.8%
	15mm	605	697	629	28.3	4.5%	21.4	3.4%
	30mm	562	668	622	29.9	4.8%	22.6	3.6%
	Overall	562	697	630	27.4	4.4%	10.4	1.7%
T1-1	Surface	757	793	774	12.0	1.6%	9.0	1.2%
	15mm	766	814	792	15.8	2.0%	11.9	1.5%
	30mm	790	829	802	12.3	1.5%	9.3	1.2%
	Overall	757	829	789	17.6	2.2%	6.7	0.9%
T2-1	Surface	788	819	800	11.1	1.4%	8.4	1.1%
	15mm	774	804	793	8.9	1.1%	6.7	0.9%
	30mm	794	814	803	7.5	0.9%	5.6	0.7%
	Overall	774	819	799	9.9	1.2%	3.8	0.5%
T1-2	Surface	673	702	689	9.6	1.4%	7.2	1.1%
	15mm	662	696	678	11.2	1.7%	8.4	1.3%
	30mm	671	711	690	11.8	1.7%	8.9	1.3%
	Overall	662	711	685	11.9	1.7%	4.5	0.7%
T2-2	Surface	694	724	709	8.4	1.2%	6.3	0.9%
	15mm	697	721	710	6.9	1.0%	5.2	0.7%
	30mm	685	737	703	16.5	2.3%	12.4	1.8%
	Overall	685	737	707	11.3	1.6%	4.3	0.6%
T3	Surface	590	623	606	9.7	1.6%	7.3	1.2%
	15mm	597	614	606	4.9	0.8%	3.7	0.6%
	30mm	590	633	606	11.7	1.9%	8.8	1.5%
	40mm	656	698	669	11.9	1.8%	9.0	1.3%
	Overall	590	698	622	29.3	4.7%	9.5	1.5%
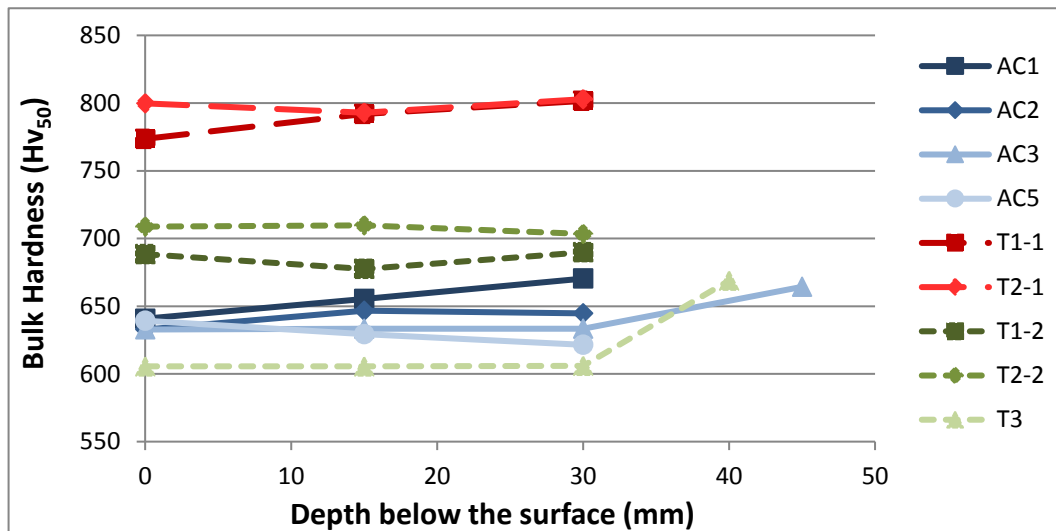
Figure 4-4: Variation in Vickers hardness over shell depth.

The standard deviation values were fairly high for some of the samples tested with a peak SD value of 29.9HV. However, this corresponded to a peak coefficient of variance of 4.8%, which is acceptable. The relative accuracy values were low with a peak value of 3.6% and indicate sufficient repeatability.

4.1.4. Metallography

4.1.4.1. Nital Etch

The general microstructure of all the as-cast samples, as revealed with 5% Nital, consisted of networks of carbides located in a matrix consisting predominantly of un-tempered martensite and some pearlite, see Figures 4-5. Isolated globular primary carbides were present within the interior of the matrix cells. Fine secondary carbides were observed within the matrix, but could not be quantified, see Figure 4-6. The pearlite appeared to be associated with the primary carbide networks and was never present at the centre of the cells.
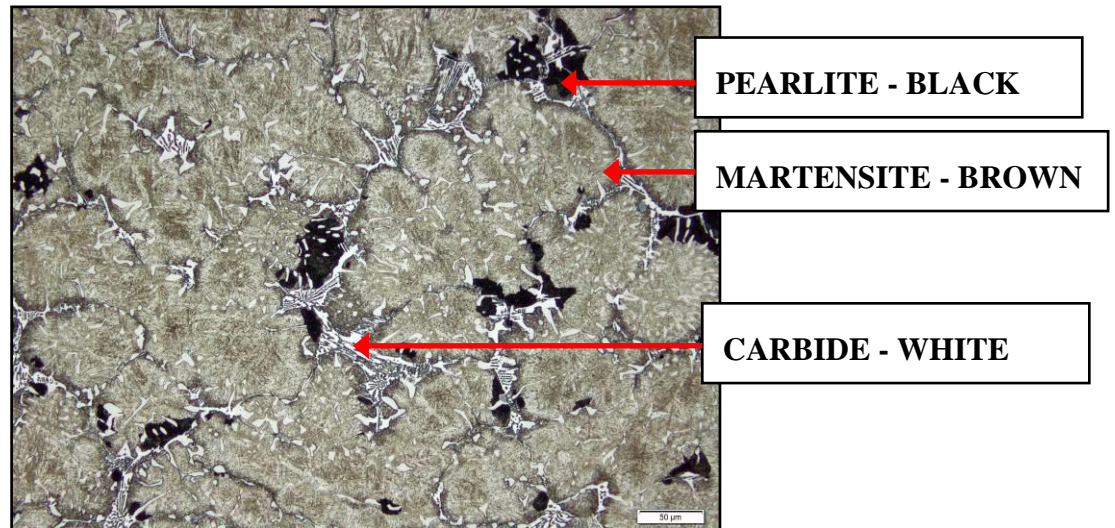
Figure 4-5: Sample AC2 etched with Nital, 15mm below the surface.
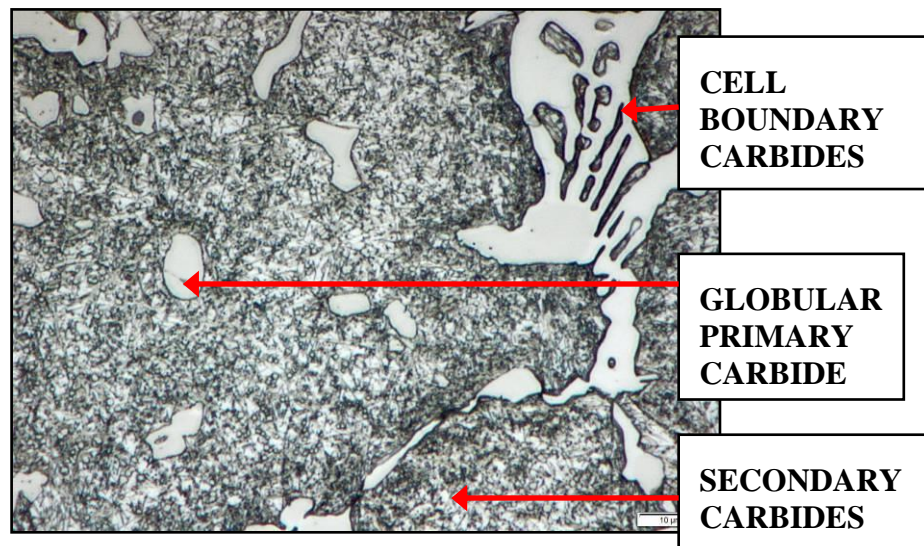
Figure 4-6: Sample AC4 at high magnification, showing secondary carbides.

Image analysis was performed to measure the volume fraction of pearlite within the microstructures. The results are shown in Table 4-5. The average pearlite content was calculated from at least ten measurements. The average pearlite content showed significant variation between the as-cast samples with sample AC2 and AC4 showing the highest and lowest pearlite content at 3.58% and 0.03% respectively, see Figure 4-7. The analysis was also characterised by large variations between individual measurements as shown by the high relative accuracy values which varied between 16.5% and 42.2%. A general trend in pearlite content over shell depth was not clear as samples AC1 and AC2 showed a decrease in pearlite content with increasing depth below the surface while the other samples did not, see Figure 4-8.

80
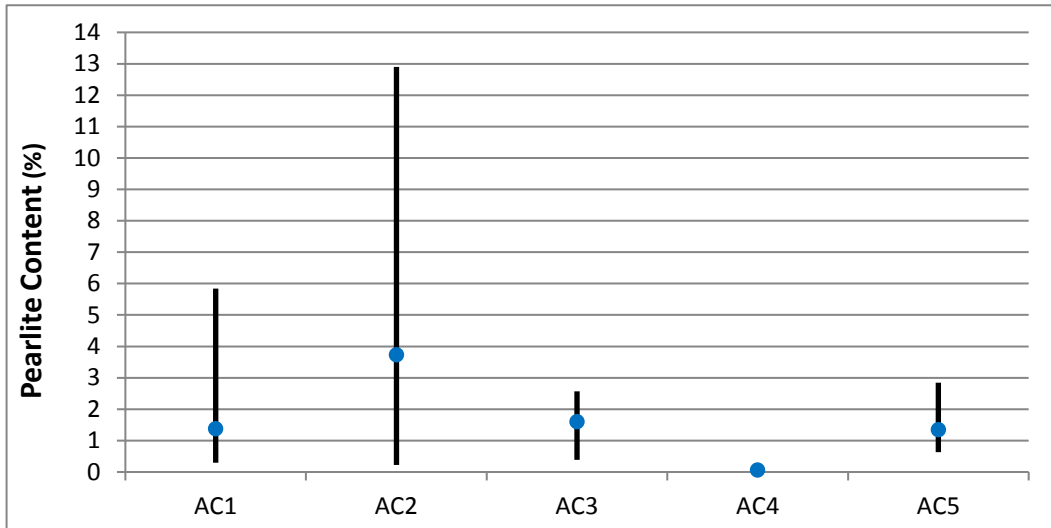
Figure 4-7: Range and average pearlite content of the as-cast samples.
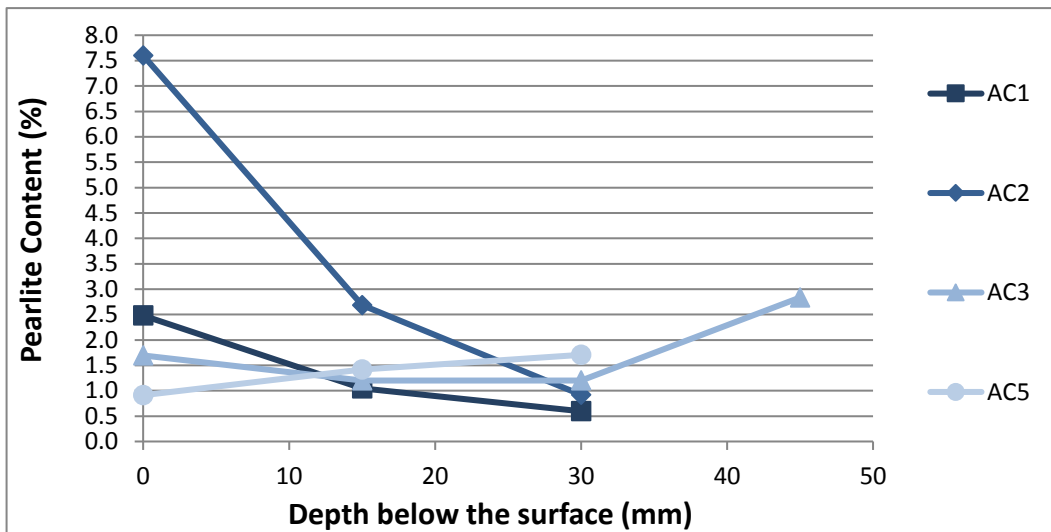
Figure 4-8: Variation in pearlite content with shell depth.

The cell size generally appeared to increase slightly in size with increasing shell depth. The largest increase appeared to occur within the first 10mm from the surface, see Figure 4-9. The martensite found in the matrix's microstructure of the as-cast samples appeared to show a mixture of plate and lath martensite, see Figure 4-10. The plate martensite is highlighted when viewed under polarised light, see Figure 4-11. Polarised light also showed that the plate martensite is concentrated at the centre of the cells. This is in agreement with the response to etching of the samples showing coring (microstructure etched darker at the centre of the cells than at the cell boundaries). The coring indicates micro-segregation during solidification leaving the matrix adjacent to the cell boundaries enriched in alloying elements compared to the

81

centre of the cells. The enrichment should cause the retained austenite to be concentrated at the cell boundaries.

Table 4-5: Pearlite volume fraction results.

Sample		Pearlite (%)			Statistical Analysis			
Description	Depth	Minimum	Maximum	Average	S	CV	95%CL	RA
AC1	Surface	1.01	5.84	2.48	1.39	56.0%	1.05	42.2%
	15mm	0.70	1.46	1.05	0.27	25.4%	0.20	19.2%
	30mm	0.30	1.04	0.60	0.28	46.7%	0.21	35.2%
	Overall	0.30	5.84	1.37	1.15	83.3%	0.43	31.7%
AC2	Surface	3.12	12.90	7.60	3.59	47.2%	2.71	35.6%
	15mm	0.53	4.43	2.69	1.25	46.4%	0.94	35.0%
	30mm	0.22	1.49	0.92	0.42	46.2%	0.32	34.8%
	Overall	0.22	12.90	3.74	3.58	95.8%	1.36	36.4%
AC3	Surface	1.28	2.57	1.70	0.40	23.6%	0.30	17.8%
	15mm	0.78	1.97	1.20	0.37	30.6%	0.28	23.1%
	30mm	0.39	1.03	1.20	0.37	30.6%	0.28	23.1%
	45mm	1.96	3.86	2.84	0.62	21.9%	0.47	16.5%
	Overall	0.39	2.57	1.60	0.91	56.7%	0.29	18.4%
AC4	Overall	0.02	0.11	0.06	0.03	56.7%	0.03	42.7%
AC5	Surface	0.63	1.18	0.91	0.17	18.5%	0.13	13.9%
	15mm	0.77	1.82	1.42	0.34	23.9%	0.26	18.0%
	30mm	1.12	2.84	1.71	0.56	32.8%	0.42	24.7%
	Overall	0.63	2.84	1.35	0.50	37.4%	0.19	14.2%
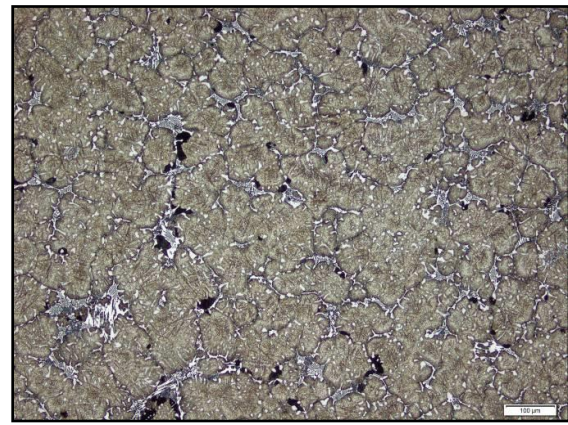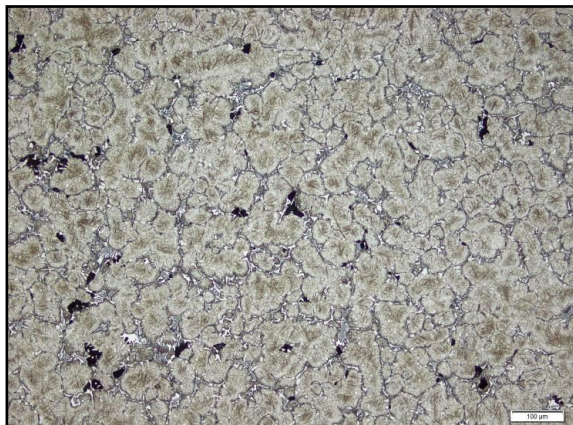
Figure 4-9: Sample AC1 etched with 5% Nital, 15mm below the surace (left) and 30mm below the surface (right).

82
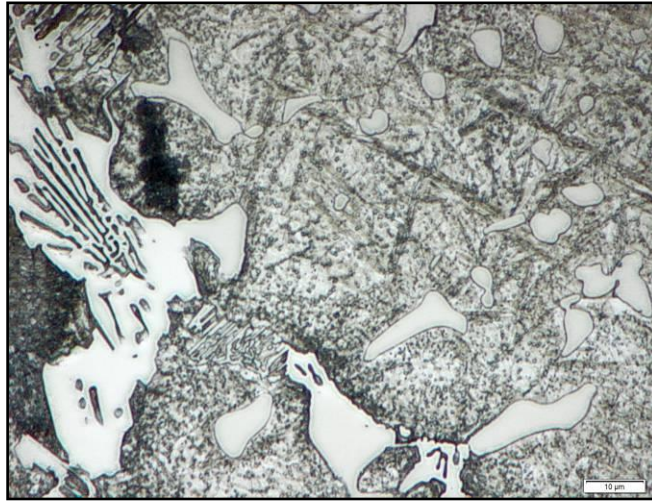
Figure 4-10: Sample AC1 etched with Nital, 30mm below the surface showing both plate and lath martensite.
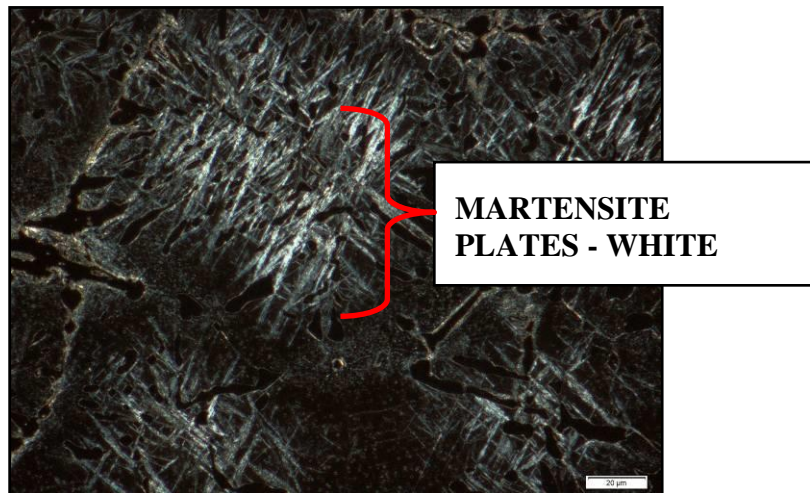
Figure 4-11: Sample AC3 etched with Nital, 45mm below the surface and viewed under polarised light.

Regions showing clustered carbides were found on samples AC2 and AC3 at depths of 25 and 36mm respectively, see Figures 4-12 and 4-13. The carbide clusters appeared to show higher volume fractions of carbide compared to the surrounding microstructure. The shapes of carbides within the clusters ranged from needle-like to irregular in shape. The presence of the clusters are a concern as they may lead to variations in roll properties (hardness, wear resistance) over the surface and cause surface defects such as hard spots during rolling. The matrix associated with the carbide clusters appeared to consist of pearlite and plate martensite, see Figure 4-14.

83
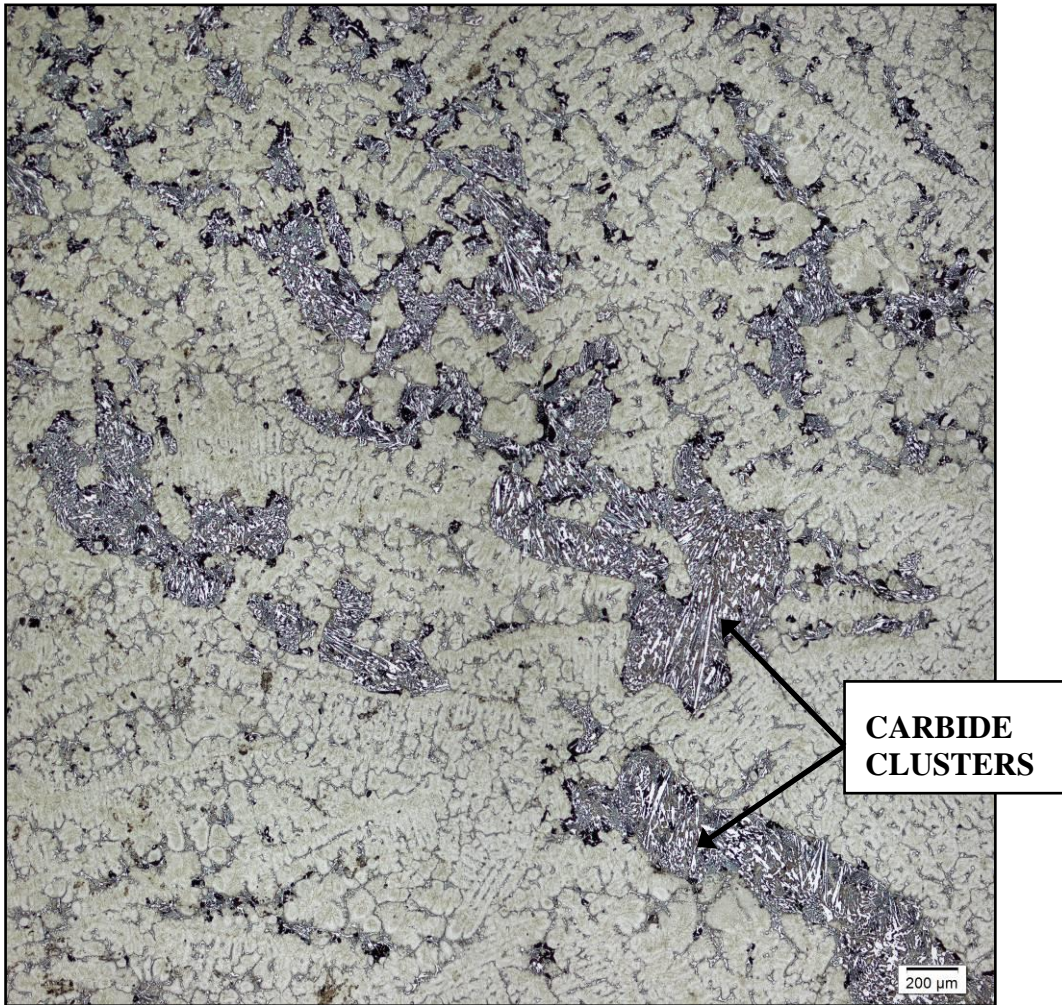
Figure 4-12: Sample AC2 etched with Nital, showing carbide clusters at a depth of 25mm.
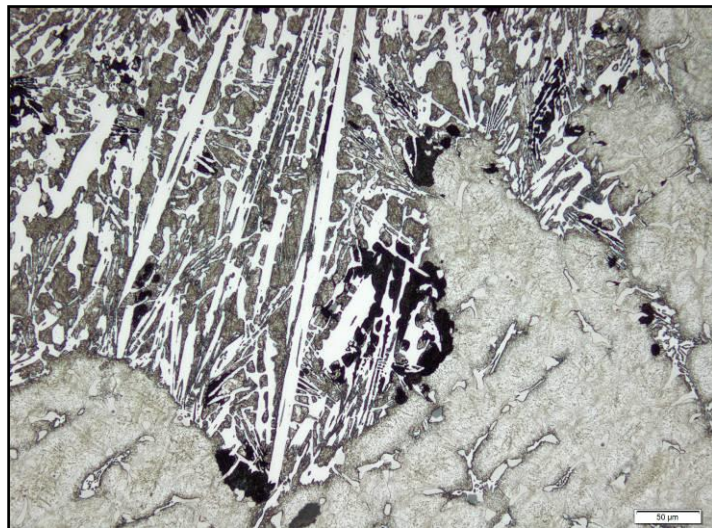
Figure 4-13: Carbide clusters found on sample AC2 at higher magnification.

84
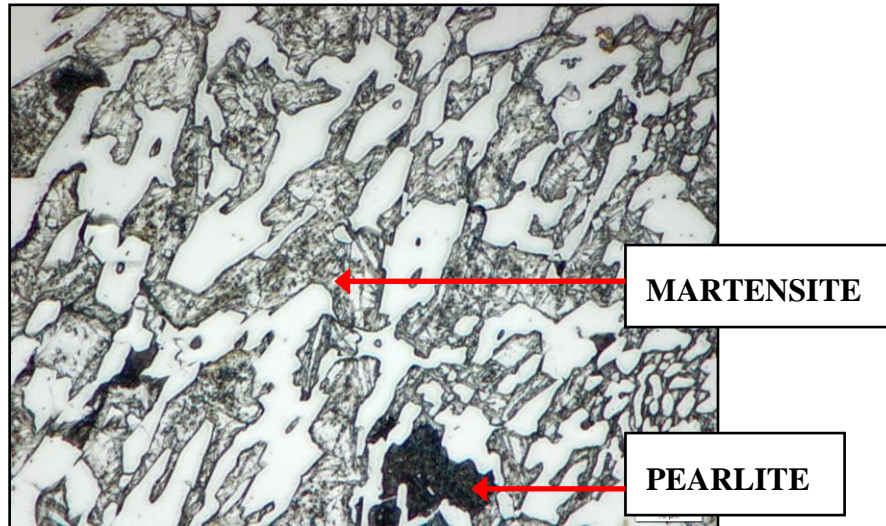
Figure 4-14: Carbide clusters found on sample AC3 at higher magnification.

The general microstructure of the first temper samples (T1-1 and T2-1), as revealed with 5% Nital, were similar to the as-cast samples and consisted of networks of carbides located in a matrix consisting predominantly of un-tempered martensite, see Figure 4-15. However, unlike the as-cast samples the matrix consisted exclusively of plate martensite with no traces of pearlite or lath martensite. The martensite plates also appeared to have two distinct size distributions, with larger plates occurring at the centre of the cell regions and smaller sized plates associated with the carbide networks, see Figure 2-16.
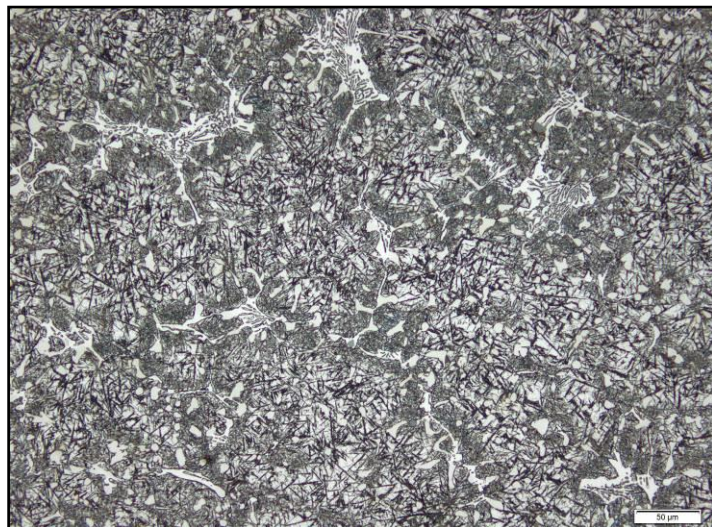
Figure 4-15: Sample T1-1 etched with Nital, 30mm below the surface.

85
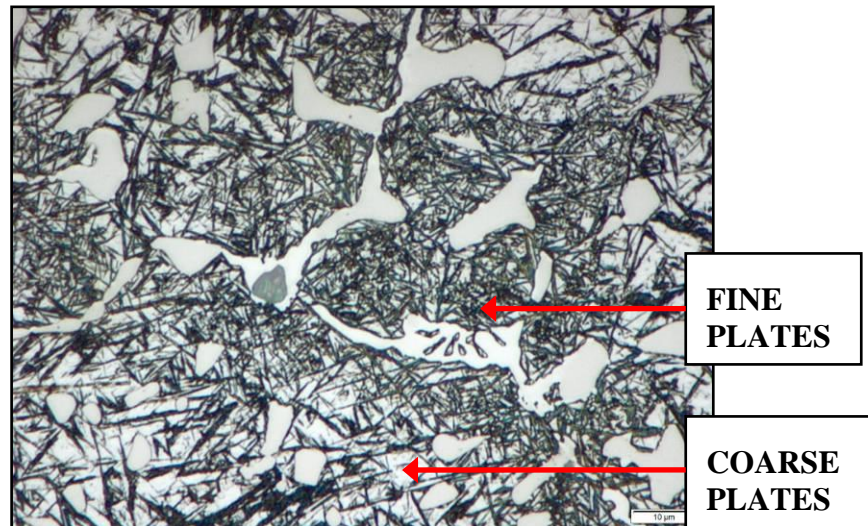
Figure 4-16: Sample T1-1 etched with Nital, 30mm below the surface at higher magnification.

The different martensite plate sizes are probably related to the coring identified on the as-cast samples. The small secondary carbides which appeared to be fairly evenly distributed within the matrix of the as-cast samples were now limited to the regions containing the finer martensite plates. The carbide clusters previously identified on sample AC2, were not found on sample T2-1.

The general microstructure of the final temper samples (T1-2, T2-2 and T3), as revealed with 5% Nital, consisted of networks of carbides located in a matrix consisting predominantly of tempered martensite and fine secondary carbides, see Figures 4-17 to 4-20. The dendritic nature is also clearly evident in Figure 4-17.
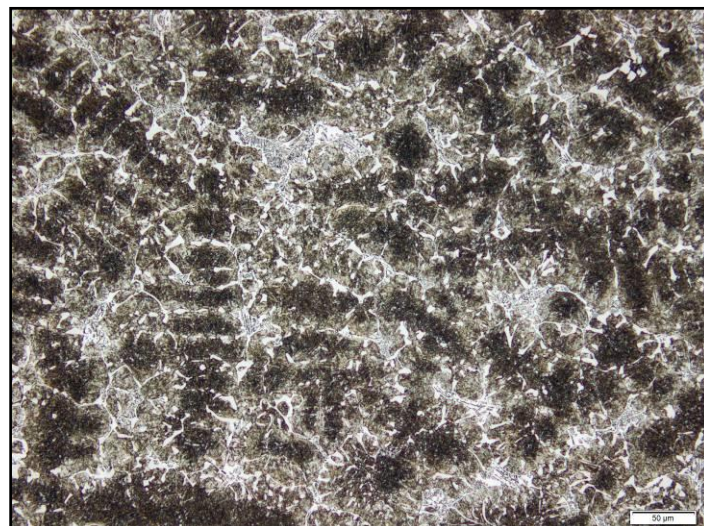
Figure 4-17: Sample T2-2 etched with Nital, at the shell surface.
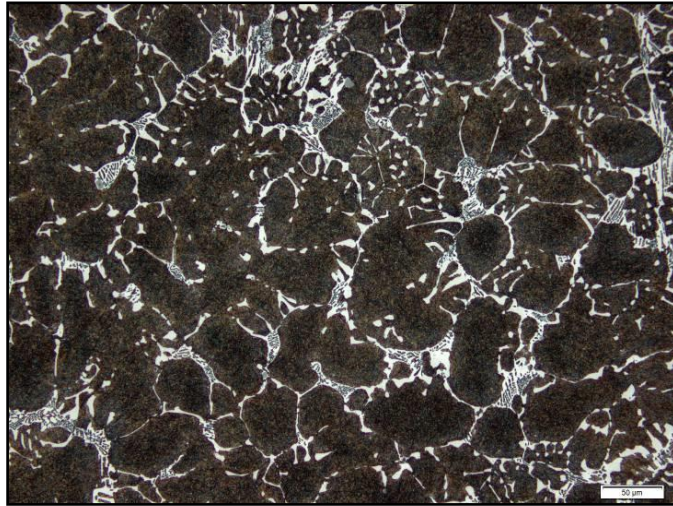
Figure 4-18: Sample T3 etched with Nital, at the shell surface
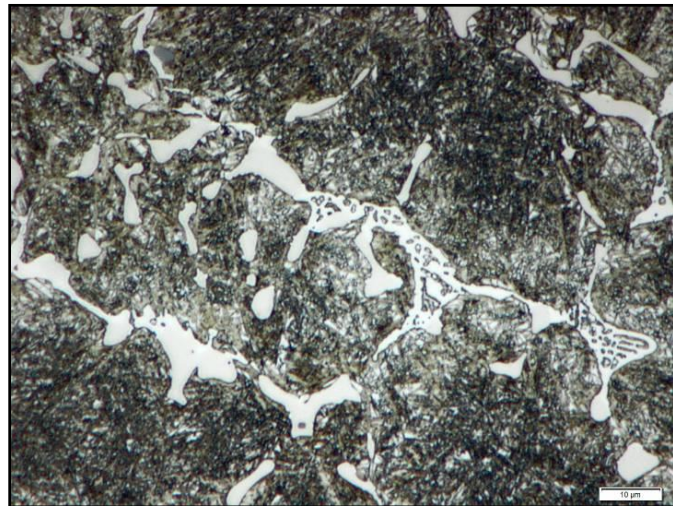
Figure 4-19: Sample T2-2, at the shell surface captured at higher magnification.
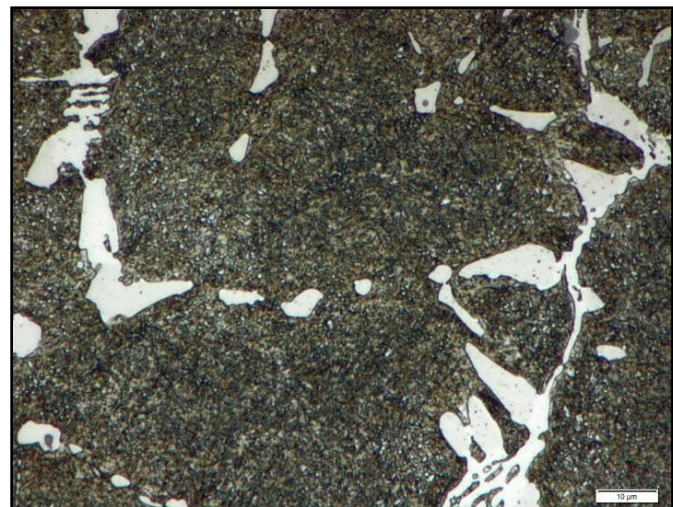
Figure 4-20: Sample T3, at the shell surface captured at higher magnification.

Sample T3 appeared to be more tempered than samples T1-2 and T2-2, as indicated by the absence of any remaining martensite plates within the matrix of sample T3. This could be due to the difference in C, V and W content of sample T3 compared to T1-2 and T2-2. Alternatively sample T3 may have been tempered at higher temperatures or tempered for longer times compared to the other two final temper samples.

The microstructure is also in agreement with the lower hardness and higher ferrite percentage values of sample T3 compared to T1-2 and T2-2. The difference in composition could have resulted in the formation of less retained austenite and more transformation upon tempering. Alternatively higher tempering temperatures and/or longer tempering times will also lead to additional tempering of the martensite, resulting in the decreased hardness observed. The higher tempering temperatures and/or longer tempering times will also cause more retained austenite to transform to martensite, decreasing the amount of non-magnetic material within the microstructure and increasing the ferrite percentage values.

Sample T3 showed a marked increase in the amount and size of the secondary carbides at a depth of 40mm, see Figure 4-21.
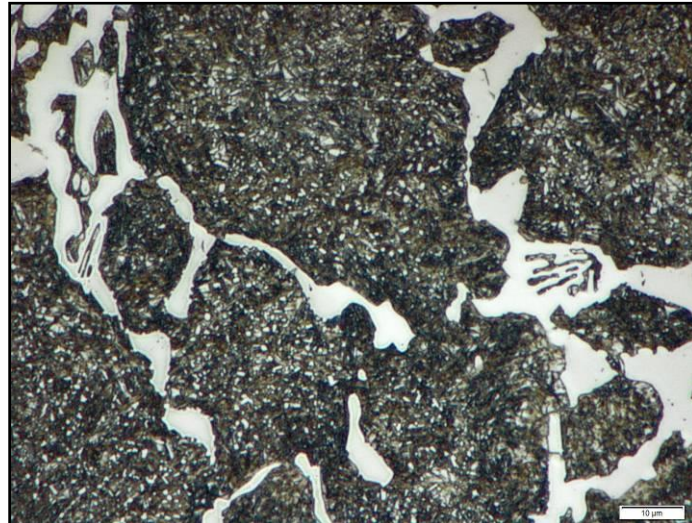
Figure 4-21: Sample T3, at a depth of 40mm captured at higher magnification.

Samples AC5 and T3 had sufficient depth to include the bond zone and core microstructure, where the other samples showed shell material only. The core microstructure of both AC5 and T3 samples consisted of graphite nodules intermittently surrounded by some ferrite, in a matrix consisting of pearlite (bull's eye structure), see Figures 4-22 and 4-23. In addition to the traditional bull's eye structure

88

the matrix also contained carbides, which appeared to be associated with the intercellular regions.
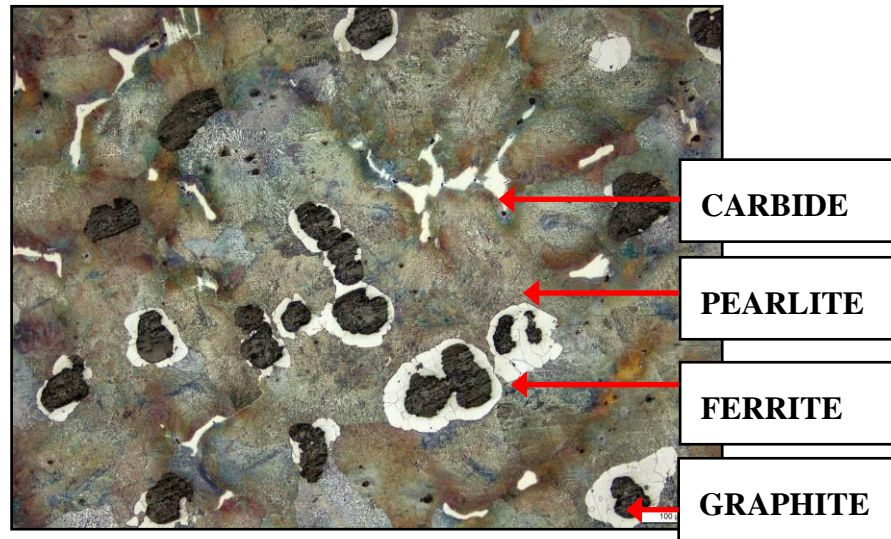
Figure 4-22: Sample AC5 etched with Nital, showing the core microstructure.

Figure 4-23: Sample AC5 showing the core microstructure at higher magnification.

Sample AC5 showed a transition from a martensitic to a pearlitic matrix when the bond zone is approached, see Figures 4-24 and 4-25. The bond zone appeared to show an increase in the carbide content of the matrix as it transitioned to the core's microstructure, see Figure 4-26. Some clustered carbides were also found within this region of sample AC5, which was often associated with defects related to shrinkage porosity, see Figures 4-27 and 4-28. The transition microstructure varied in thickness from 2mm on some of the AC5 samples to 12mm on others, see Figure 4-29 to 4-31.
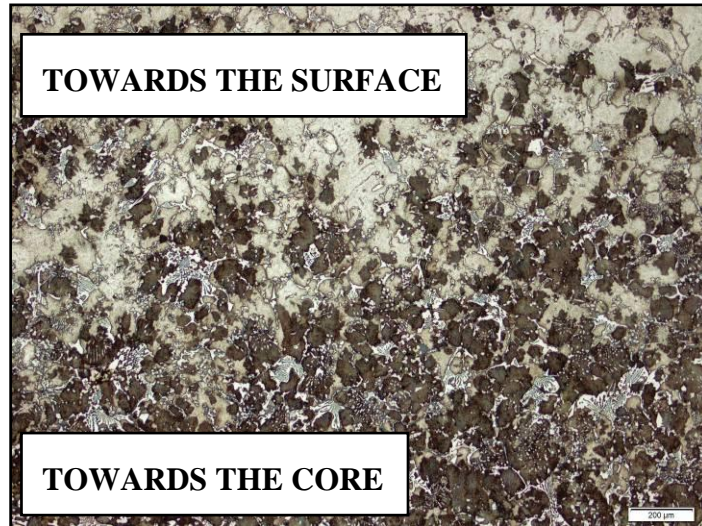
Figure 4-24: Sample AC5 etched with Nital, showing the matrix transition at the bond zone.
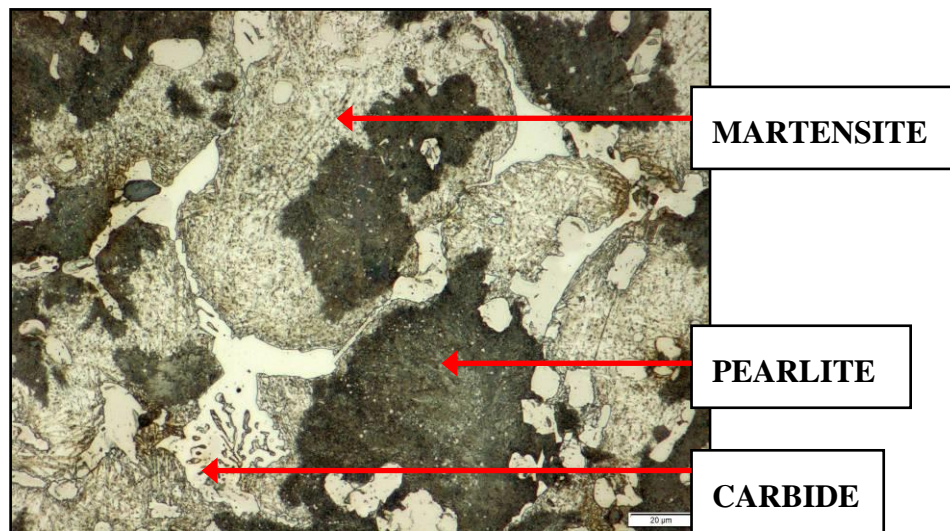
Figure 4-25: Sample AC5 showing the bond zone at higher magnification.

.

90

Figure 4-26: Sample AC5 etched with Nital, showing the transition from shell to core at the bond zone.
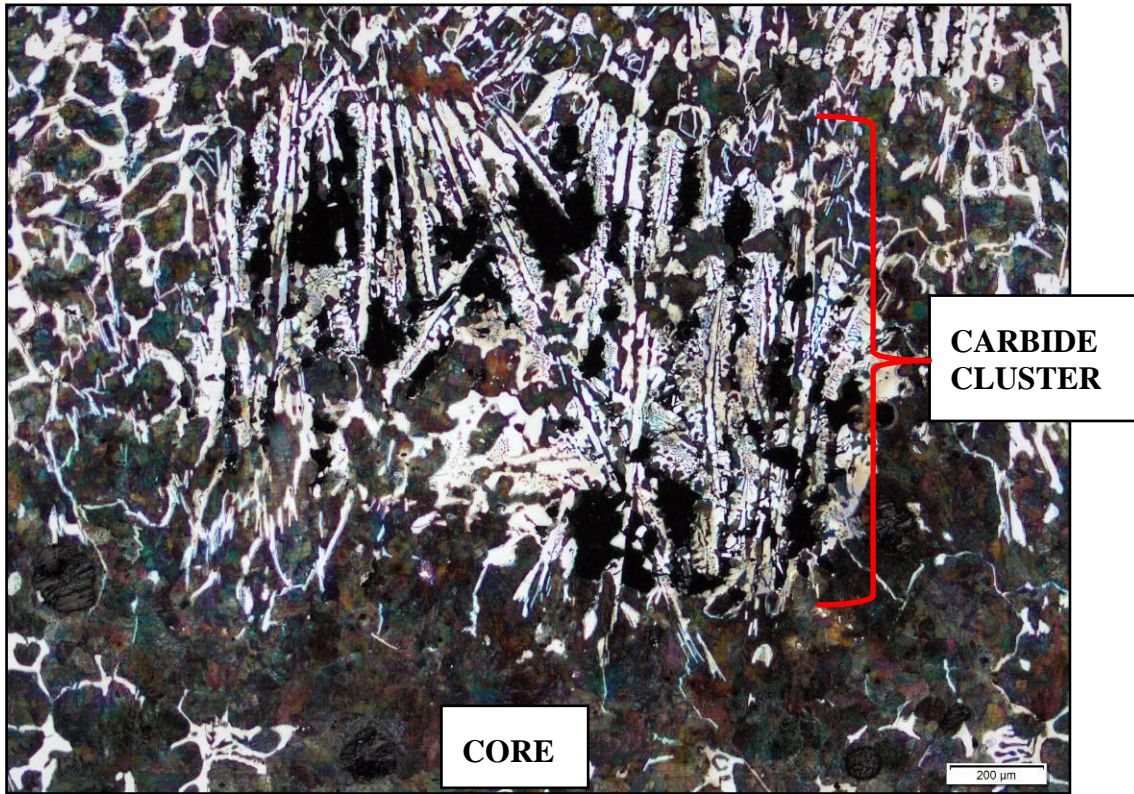
Figure 4-27: Defect riddled carbide cluster at the bond zone of sample AC5.
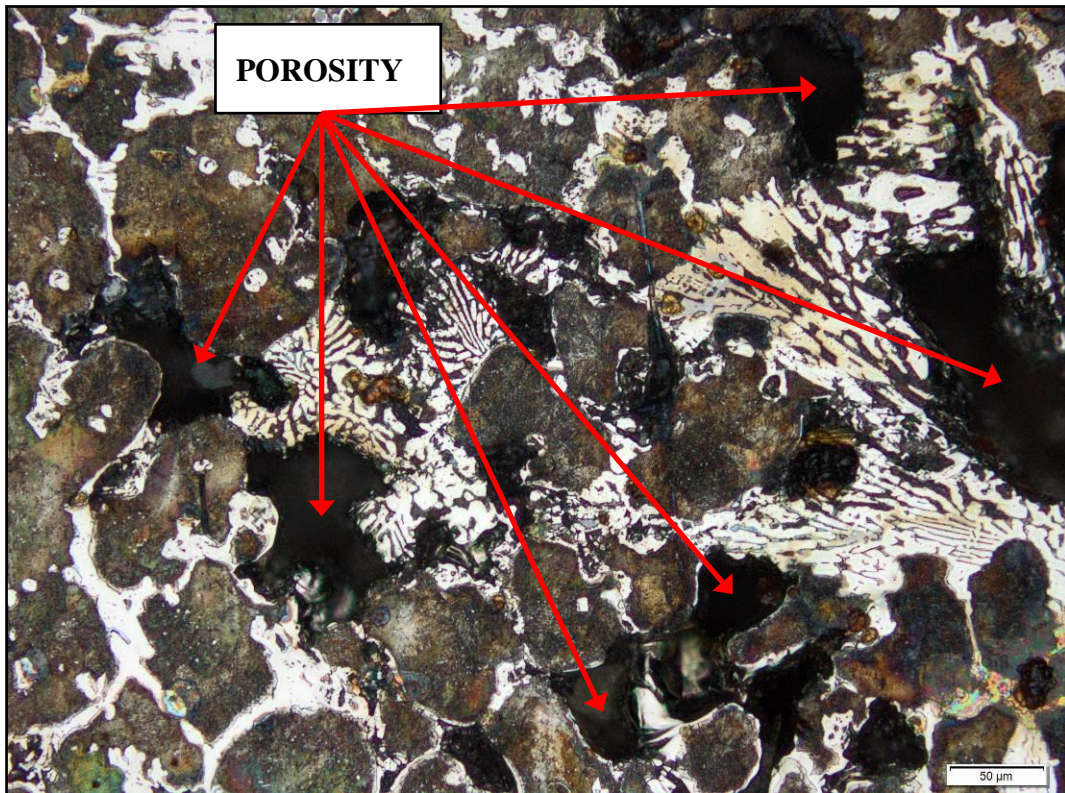
Figure 4-28: Porosity associated with the carbide clusters on sample AC5 at higher magnification.

92
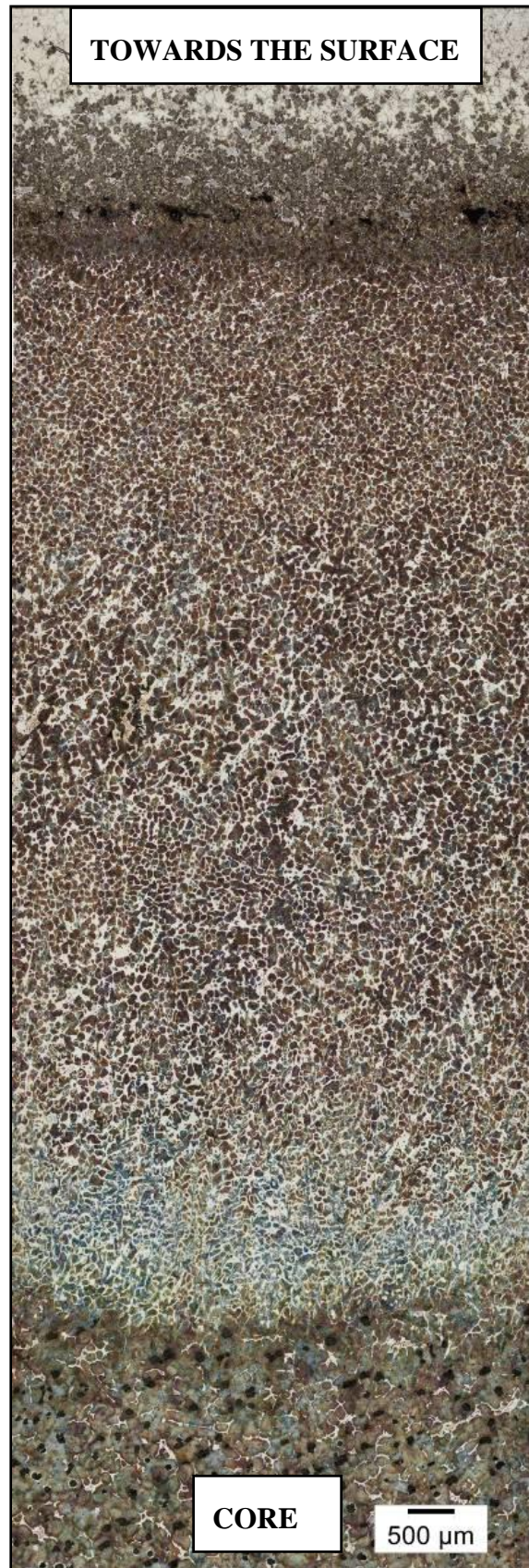
Figure 4-29: Bond zone of sample AC5, showing a large transition region.
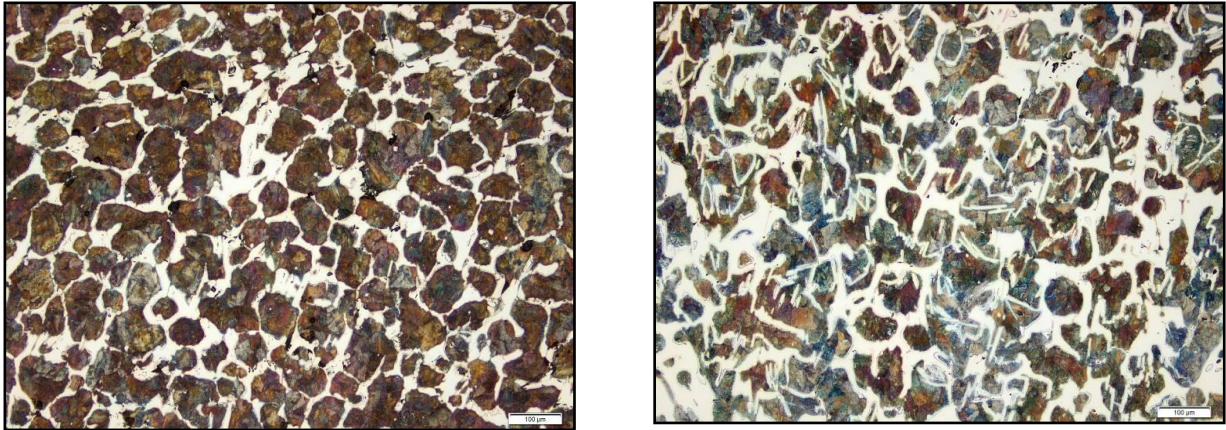
Figure 4-30: Bond zone of sample AC5 near the shell (left) and near the core (right).
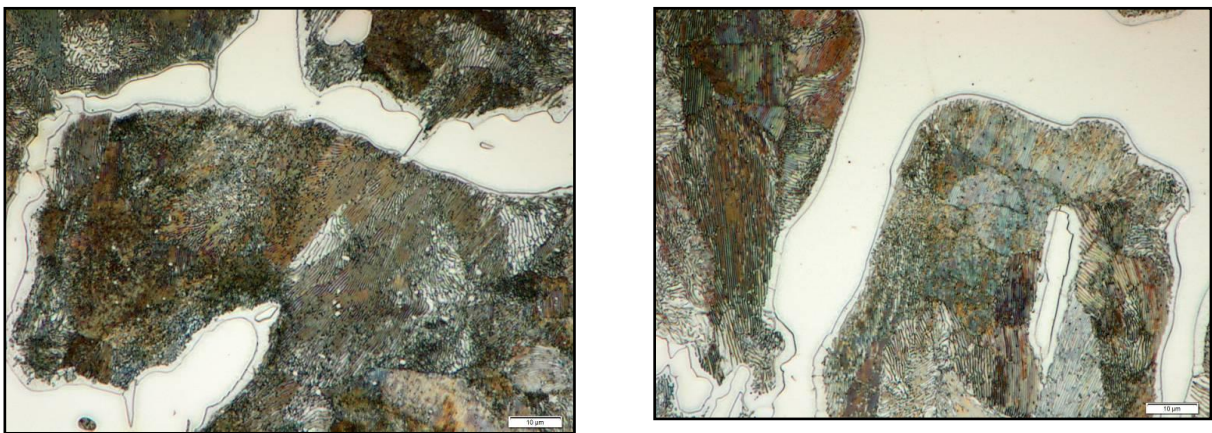
Figure 4-31: Bond zone of sample AC5 near the shell (left) and near the core (right) at higher magnification.

Figures 4-32 to 4-34 show the microstructures of the bond zone near the shell and near the core. The carbide volume fraction appeared to increase notably from the shell towards the core. The bond zone of Sample T3 showed a marked change in microstructure at a depth of approximately 45mm. The matrix microstructure changed from martensitic to pearlitic while the secondary carbides appeared more abundant and significantly larger in size. The transition continued to a depth of 50mm before transitioning to the SG iron core. Similarly to sample AC5, sample T3 also showed some clustered carbides before transitioning to the SG microstructure, which was also associated with defects related to shrinkage porosity, see Figures 4-35 to 4-37.

94

Figure 4-32: Bond zone of sample T3, showing the transition region.
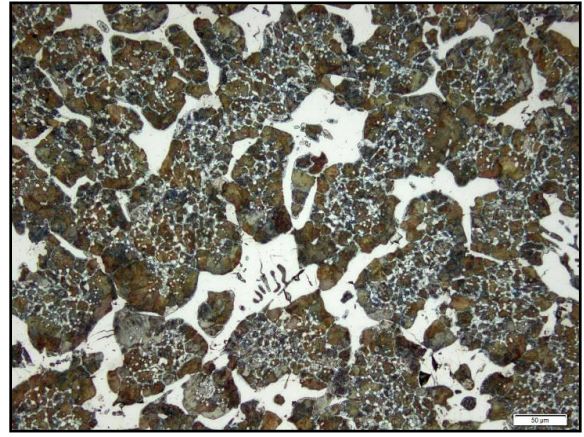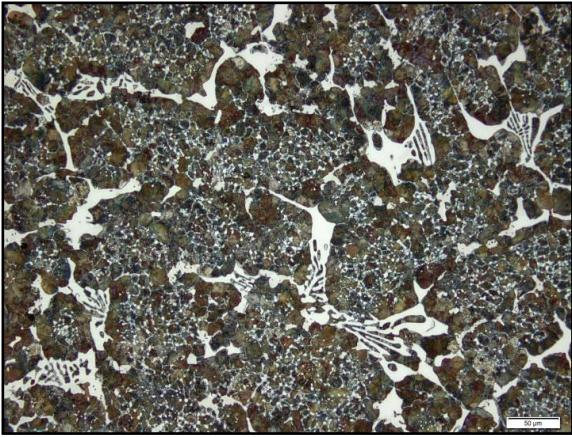
Figure 4-33: Sample T3, 45mm (left) and 50mm (right) below the surface.
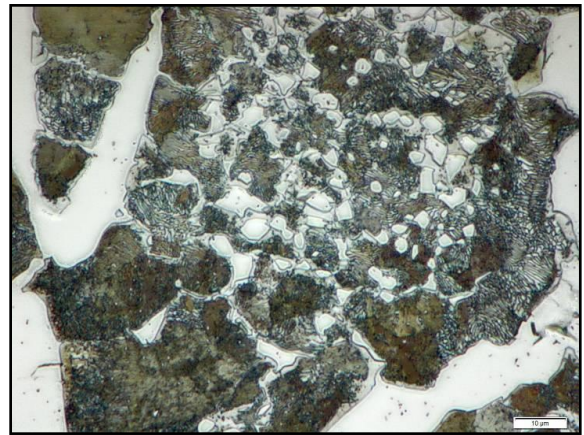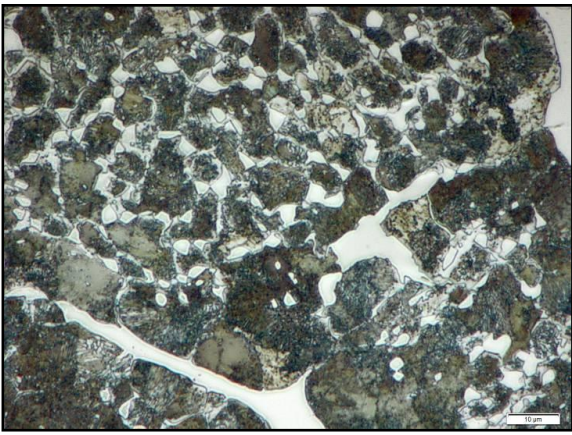
Figure 4-34: Sample T3, 45mm (left) and 50mm (right) below the surface captured at higher magnification.
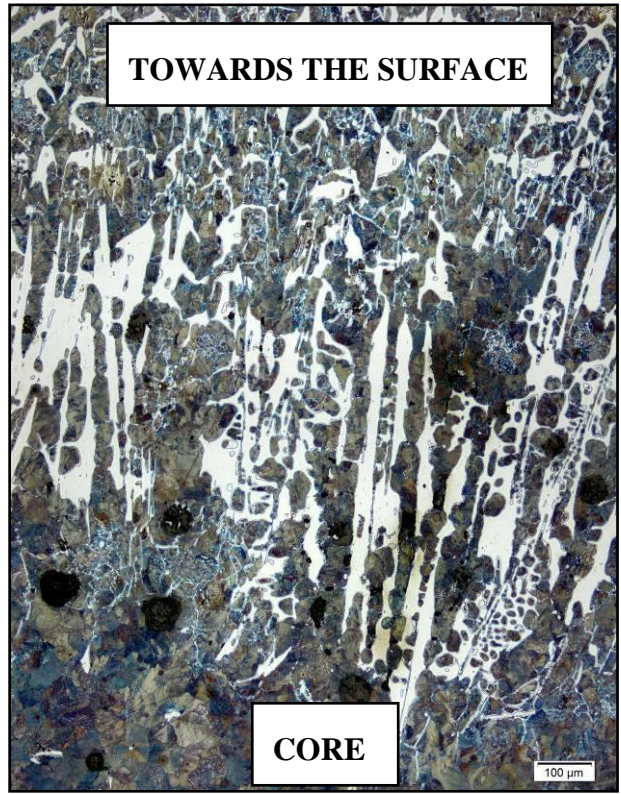
Figure 4-35: Large primary carbides at the bond zone of sample T3.
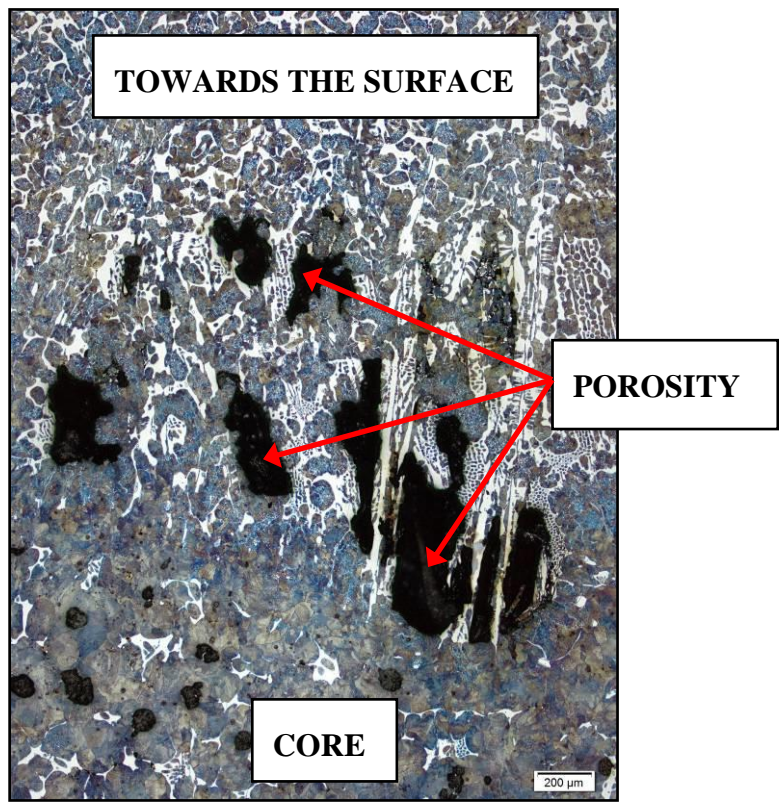
Figure 4-36: Defect riddled carbide cluster at the bond zone of sample T3.

97
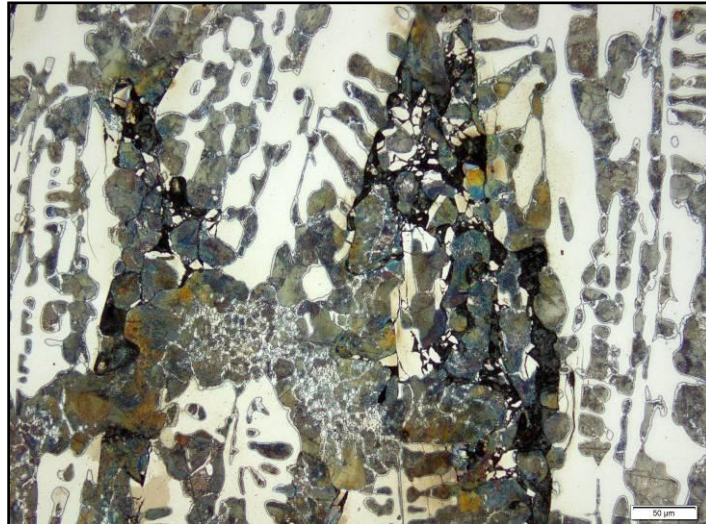
Figure 4-37: Porosity associated with the carbide clusters on sample T3 at higher magnification.

4.1.4.2. Groesbeck's Etchant

Groesbeck's etchant selectively etched some of the primary carbides, see Figures 4-38 to 4-40. The etchant identified three distinct carbides associated with the as-cast samples, see Figures 4-41 and 4-42. The most abundant of the three etched carbides showed a coarse fish bone structure and was located at the interdendritic areas, which was assumed to consist of M_7C_3 carbides. Groesbeck's etchant outlined and attacked the M_7C_3 carbides on the as-cast samples, with the colour ranging from pink to light brown. The second most abundant of the three etched carbides showed a thinner fish bone structure and was located at the interdendritic areas, which was assumed to be either M_2C or M_6C carbides. Groesbeck's etchant etched the M_6C carbides dark brown on the as-cast samples. The third carbide type affected by Groesbeck's etchant occurred as sharp needles at the interdendritic regions, which was assumed to be M_2C carbides. Groesbeck's etched the M_2C carbides black on the as-cast samples. Groesbeck's etchant had no clear effect on globular, isolated carbides which were located both at the interdendritic regions and interiors of the dendrites, which was assumed to be MC carbides. In some regions the MC carbides appeared to be surrounded by thin films of M_7C_3 carbide which gave the appearance of haloes, see Figure 4-43.

98

Figure 4-38: Sample AC3 etched with Groesbeck's, at the shell surface.
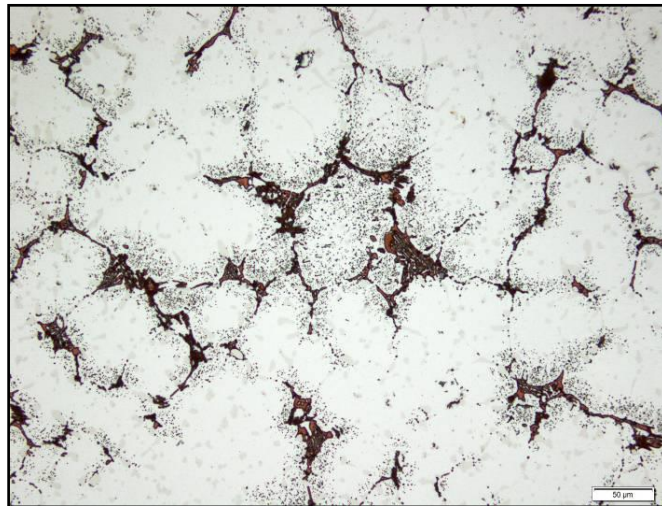
Figure 4-39: Sample T1-1 etched with Groesbeck's, 30mm below the surface.

Figure 4-40: Sample T3 etched with Groesbeck's, 15mm below the surface.
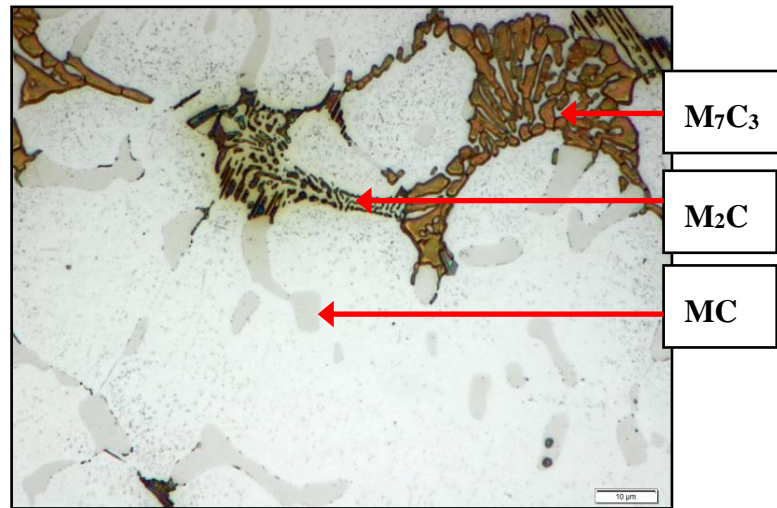
Figure 4-41: Sample AC2 etched with Groesbeck's, 15mm below the surface at higher magnification.
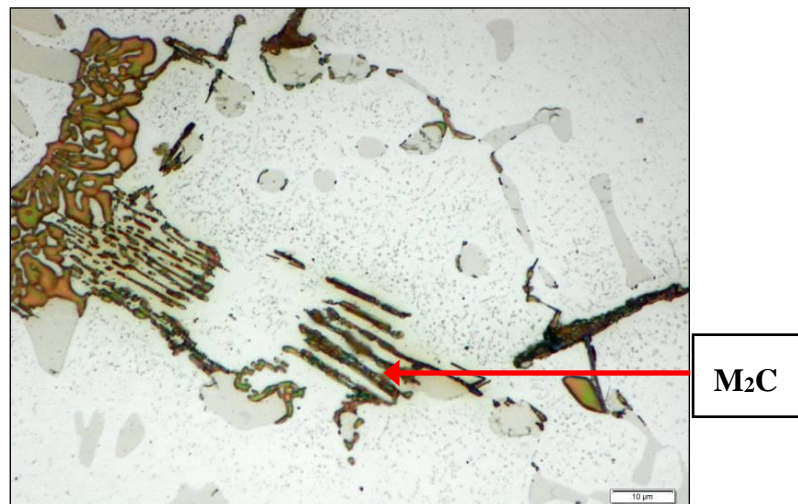
Figure 4-42: Sample AC3 etched with Groesbeck's, 15mm below the surface at higher magnification.
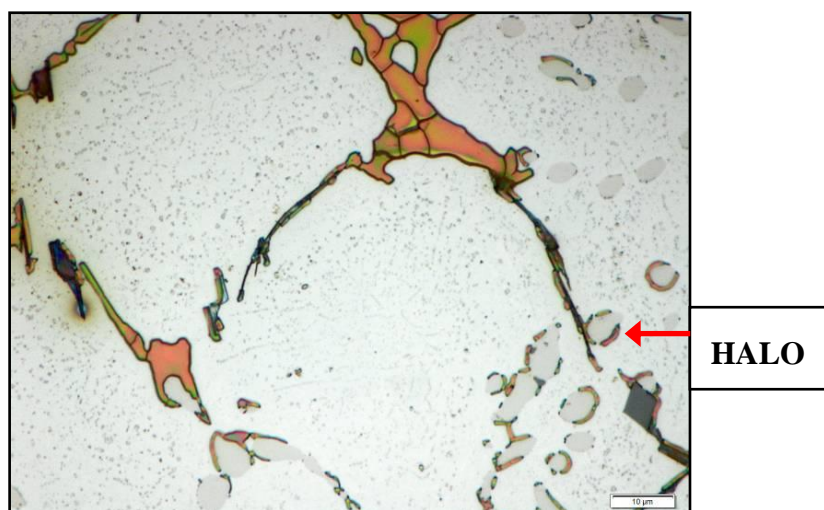
Figure 4-43: Sample AC3 etched with Groesbeck's, 45mm below the surface at higher magnification.

100

Groesbeck's etchant also highlighted three distinct carbides associated with the first temper and final temper samples, but slightly different from those identified on the as-cast samples. Thick and thinner fish bone structures located at the interdendritic areas were identified similar to the as-cast samples, which were assumed to be M_7C_3 and M_6C carbides respectively, see Figures 4-44 to 4-46. Groesbeck's etchant outlined and etched the M_7C_3 carbides on the as-cast samples, with the colour ranging from pink to green. Groesbeck's etched the M_6C carbides dark brown on the tempered samples, showing a thick film build-up. The M_6C carbides appeared to be more abundant on the tempered samples compared to the as-cast samples. No M_2C carbide needles were identified on the tempered samples as expected, since the M_2C carbides have been found to decompose and transform to M_6C during heat treatment.
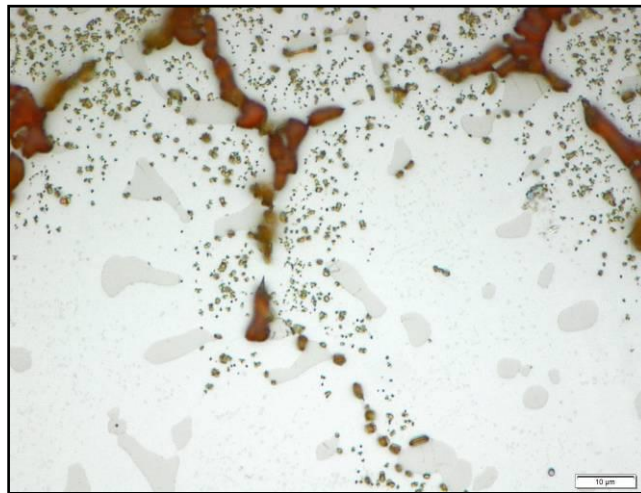
Figure 4-44: Sample T1-1 etched with Groesbeck's, 30mm below the surface at higher magnification.
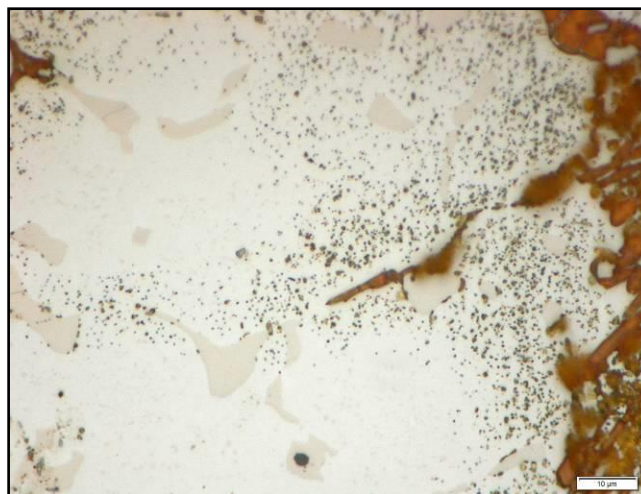
Figure 4-45: Sample T2-2 etched with Groesbeck's, 30mm below the surface at higher magnification.
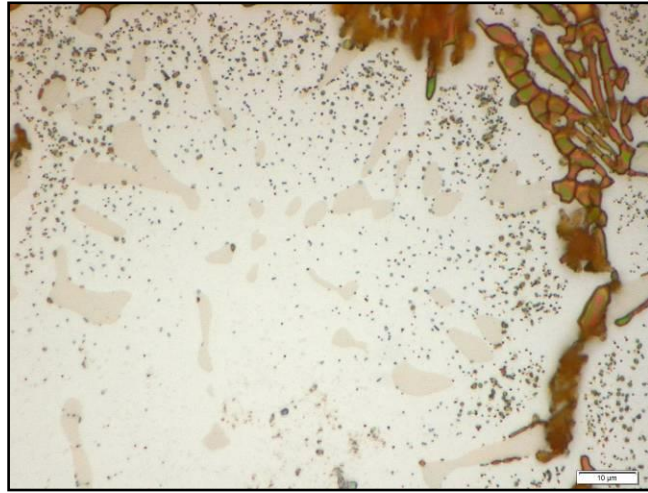
Figure 4-46: Sample T3 etched with Groesbeck's, 30mm below the surface at higher magnification.

The third carbide type affected by Groesbeck's etchant occurred as fine secondary carbides associated with the primary carbides at the interdendritic regions. It is not clear what the structure of the carbides were, since Groesbeck's etchant does not affect $M_{23}C_6$ secondary carbides according to Vander Voort et al. [74]. Groesbeck's etchant had no clear effect on globular, isolated carbides which were located both at the interdendritic regions and interiors of the dendrites, which were assumed to be MC carbides. However, remnants of the thin films of M_7C_3 carbide haloes surrounding the MC carbides were still visible, but the haloes appeared to be broken down into isolated carbide particles.

Groesbeck's etchant also identified that the carbide clusters previously identified on samples AC2 and AC3, consisted primarily of M_7C_3 carbides etched pink and green, while the second carbide type is expected to be M_6C and/or M_2C carbides, see Figures 4-47 to 4-49. No MC carbides were associated with the clusters. Additional carbide clusters were also identified on sample AC3 at a depth of 40-45mm.

102
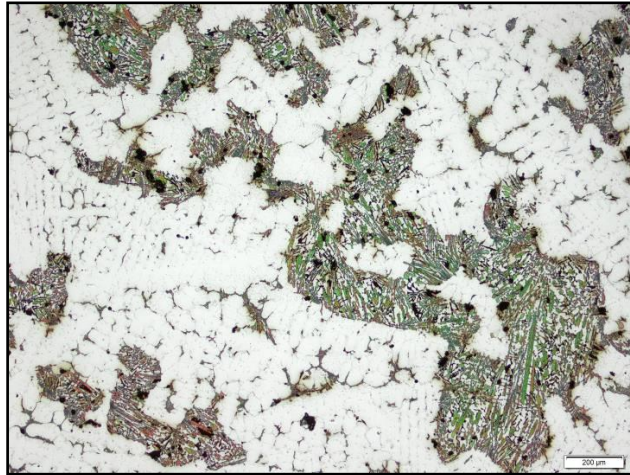
Figure 4-47: Sample AC2 etched with Groesbeck's, showing carbide clusters at a depth of 25mm.
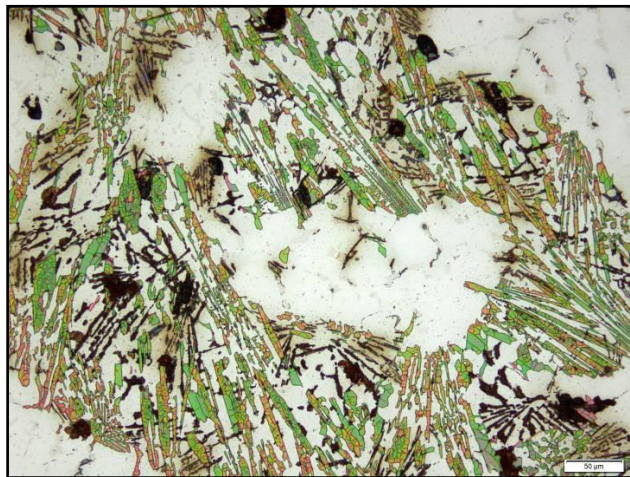
Figure 4-48: Carbide clusters found on sample AC2, etched with Groesbeck's and viewed at higher magnification.

M₂C/M₆C

M₇C₃
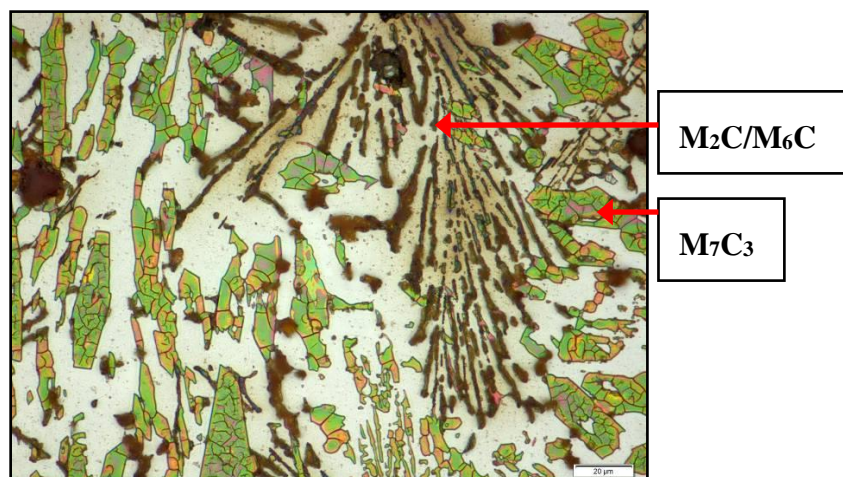
Figure 4-49: Sample AC2 etched with Groesbeck's showing the two carbide types associated with the carbide clusters.

103

Sample T3 showed a gradual transition in the carbide type near the bond zone at a depth of 45mm when etched with Groesbeck's, see Figures 4-50 and 4-51. The transition is marked by a reduction in the affinity of the etchant indicated by the colour change. The transition also marked the reduction in the volume fraction of the thinner M_6C carbides, which were eliminated completely when entering the bond zone. The carbides at the bond zone of sample AC5 were unaffected by Groesbeck's etchant.
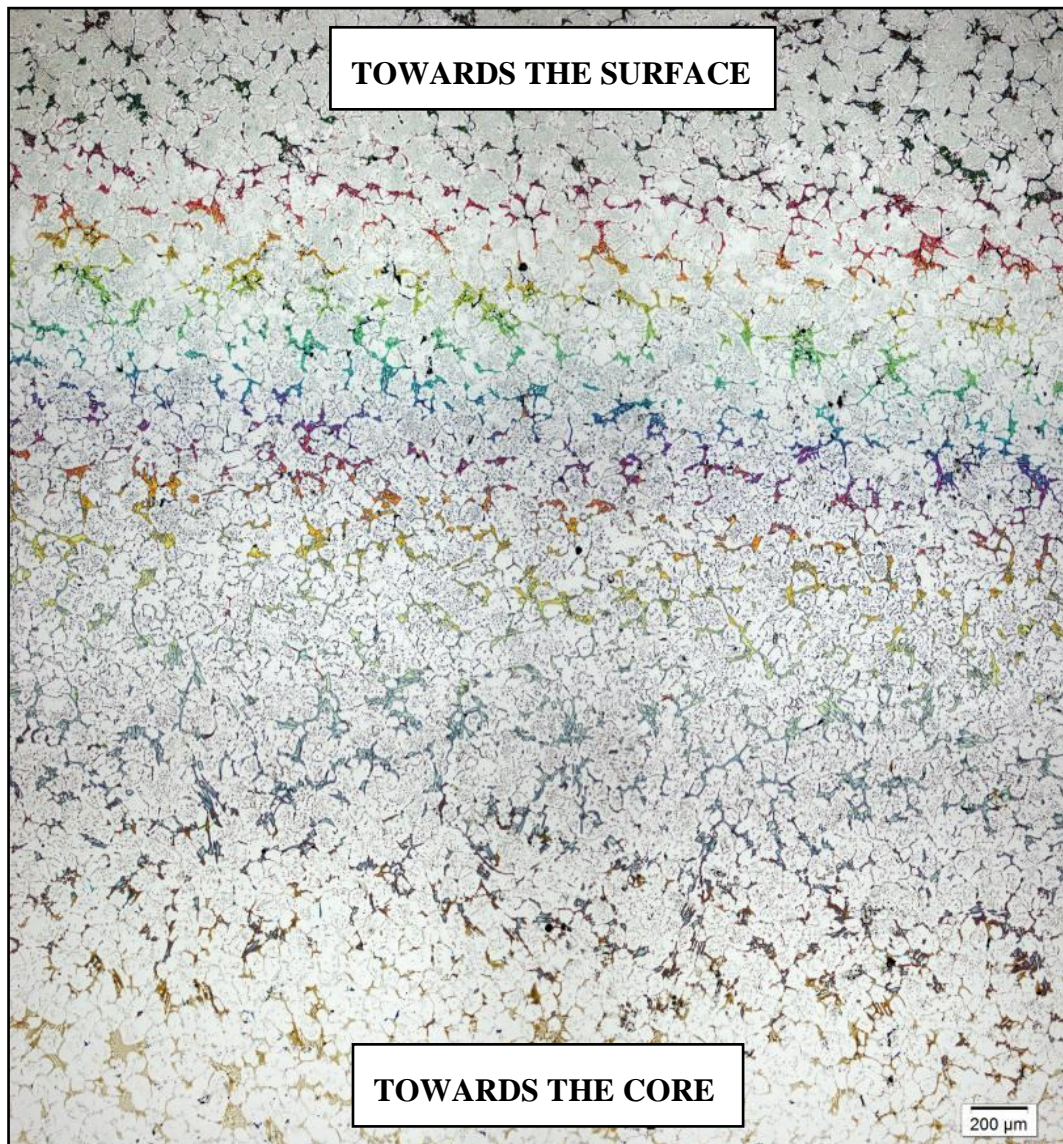
Figure 4-50: Sample T3 etched with Greosbeck's, showing the carbide type transition at a depth of 45mm.
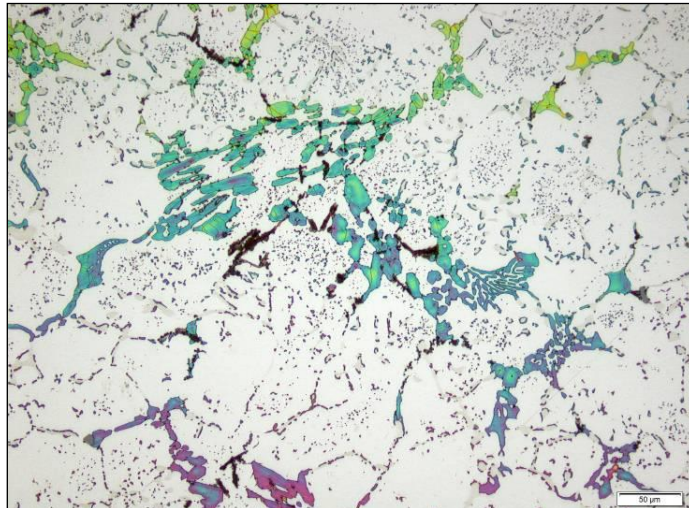
Figure 4-51: Sample T3 etched with Greosbeck's, showing the reduction in volume fraction of M_6C carbides at the transition.

4.1.4.3. Ammonium Persulphate (APS)

APS selectively etched some of the primary carbides, see Figures 4-52 to 4-55. The etchant attacked the suspected globular MC carbides while showing no effect on the thick fish bone M_7C_3 carbides, thinner fish bone M_6C carbides or M_2C needle carbides. APS also etched fine secondary carbides and differed from Groesbeck's etch as the carbides were not associated with the primary carbides, but appeared fairly uniform over the matrix. APS confirmed that MC carbides were not associated with the carbide clusters found on AC2 and AC3. The carbides at the bond zone of samples AC5 and T3 were unaffected by APS.

Figure 4-52: Sample T1-1 etched with APS, 15mm below the surface.
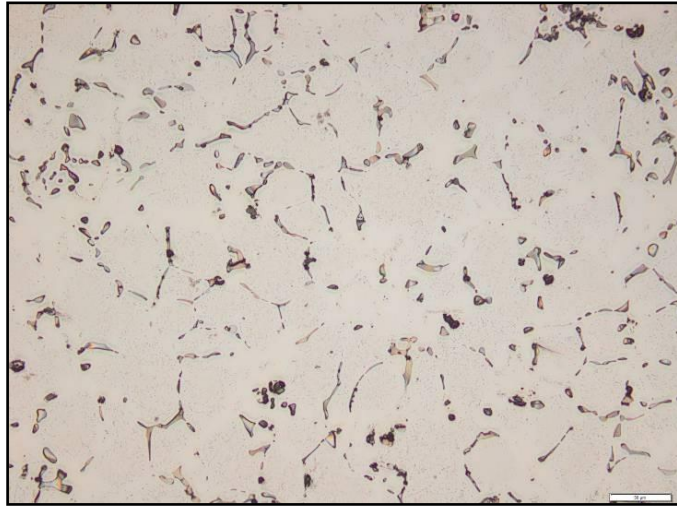
Figure 4-53: Sample T3 etched with APS, at the shell surface.

Figure 4-54: Sample T1-1 etched with APS, 30mm below the surface at higher magnification.
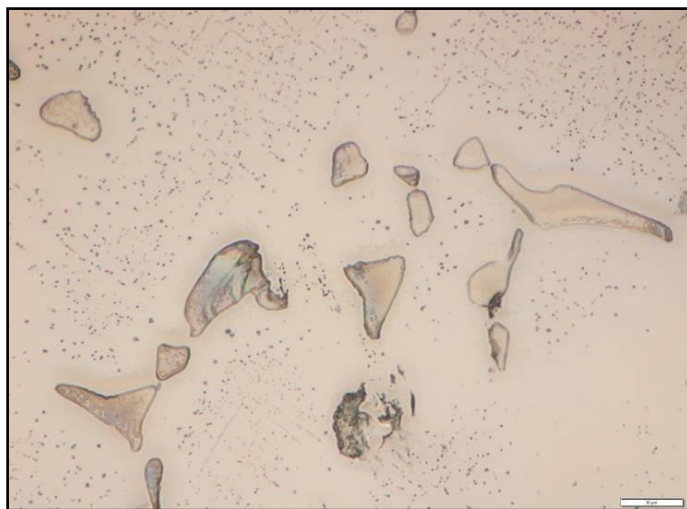
Figure 4-55: Sample T3 etched with APS, at higher magnification near the surface.

### 4.1.4.4. Murakami's Etchant

Murakami's etchant showed similar results to that of Groesbeck's etchant as expected, see Figures 4-56 to 4-58. Murakami's etchant also etched the M_7C_3 carbides in the as-cast samples, with the colour ranging from orange to light brown. The M_6C/M_2C carbides were etched dark brown in the as-cast samples. The sharp needle like M_2C carbides were etched black on the as-cast samples, similar to Groesbeck's etchant. Murakami's etchant also had no clear effect on the MC carbides, while some of the MC carbides still appeared to be associated with carbide films at its borders.

Figure 4-56: Sample AC2 etched with Murakami's, at the shell surface.
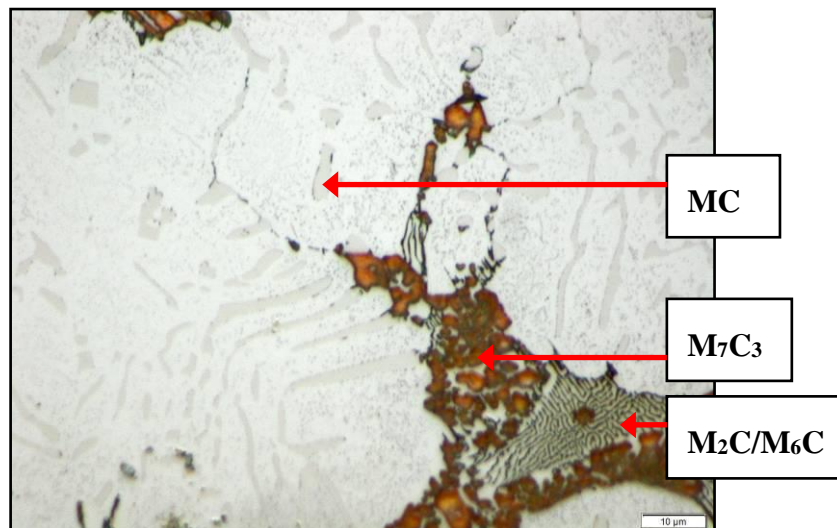
Figure 4-57: Sample AC1 etched with Murakami's, at higher magnification near the shell surface.

107
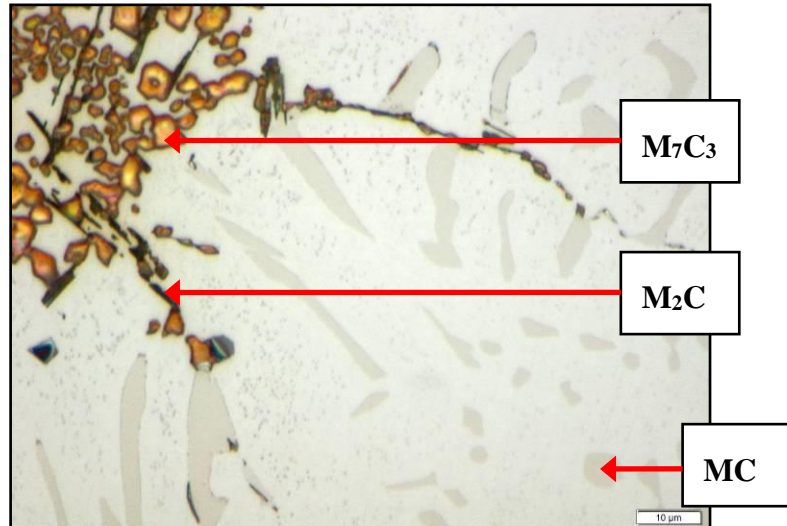
Figure 4-58: Sample AC3 etched with Murakami's, 30mm below the surface at higher magnification.

The Murakami's etchant also highlighted three distinct carbides associated with the first temper and final temper samples, see Figures 4-59 to 4-64. Groesbeck's etchant outlined and etched the M_7C_3 carbides in the as-cast samples, with the colour ranging from orange to dark brown. Groesbeck's etched the M_6C carbides dark brown in the tempered samples, showing a thicker film build-up. The M_6C carbides appeared to be more abundant on the tempered samples compared to the as-cast samples, based on the visual appearance as the volume fractions could not be accurately quantified. No M_2C carbides were identified in the tempered samples as expected. The third carbide type affected by Groesbeck's etchant occurred as fine secondary carbides associated with the primary carbides at the interdendritic regions. Murakami's etchant had no effect on the globular MC carbides. However, remnants of the thin films of carbide at the perimeters of the MC carbides were still visible, but the films appeared to be broken down into isolated carbide particles.

Murakami's etch also highlighted the carbide clusters previously identified on samples AC2 and AC3, see Figures 4-65 and 4-66.

Figure 4-59: Sample T1-1 etched with Murakami's, at the shell surface.
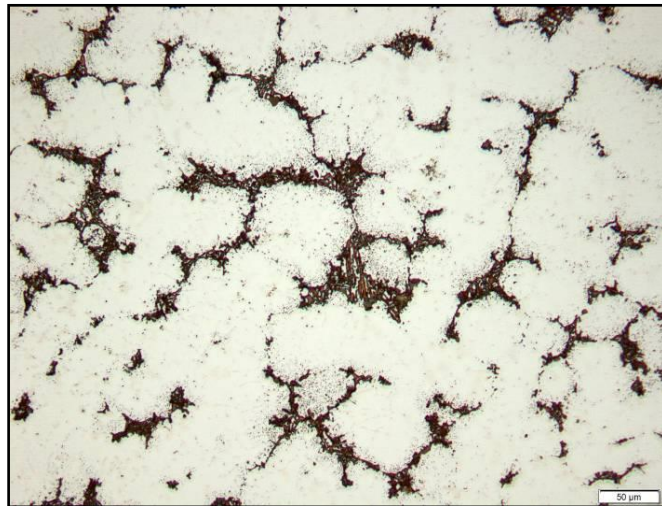
Figure 4-60: Sample T1-2 etched with Murakami's, at the shell surface.
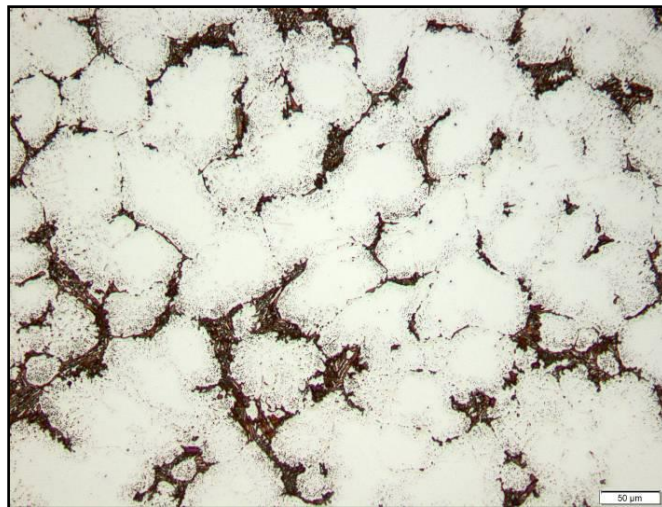
Figure 4-61: Sample T3 etched with Murakami's, at the shell surface.

109
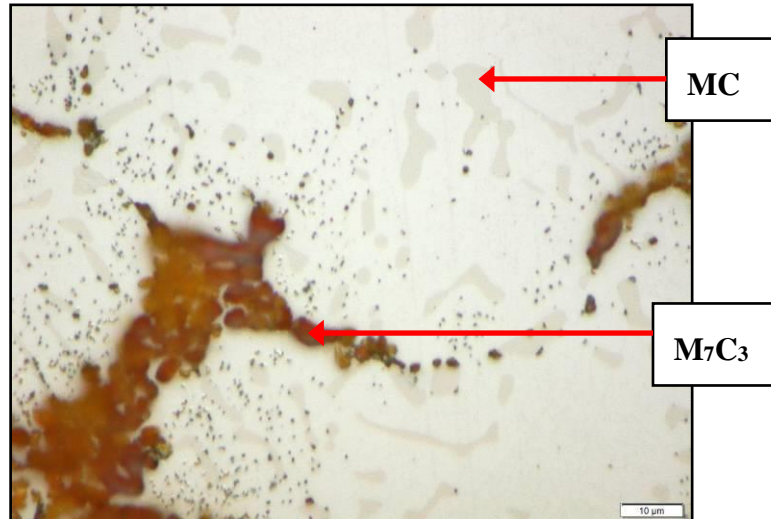
Figure 4-62: Sample T1-1 etched with Murakami's, 15mm below the surface at higher magnification.
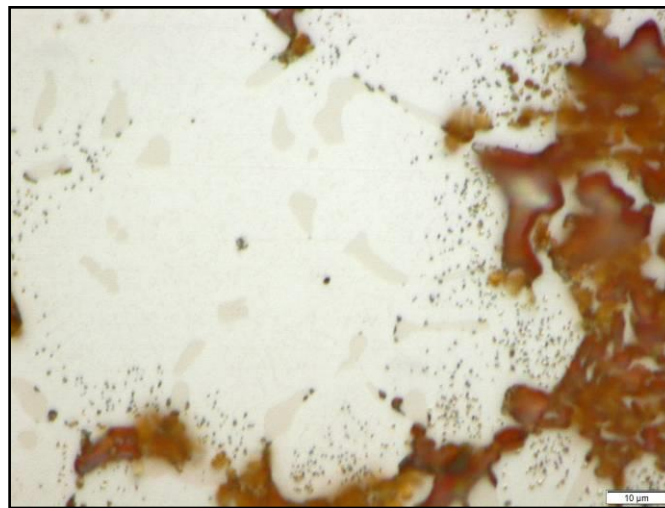
Figure 4-63: Sample T1-2 etched with Murakami's, 15mm below the surface at higher magnification.
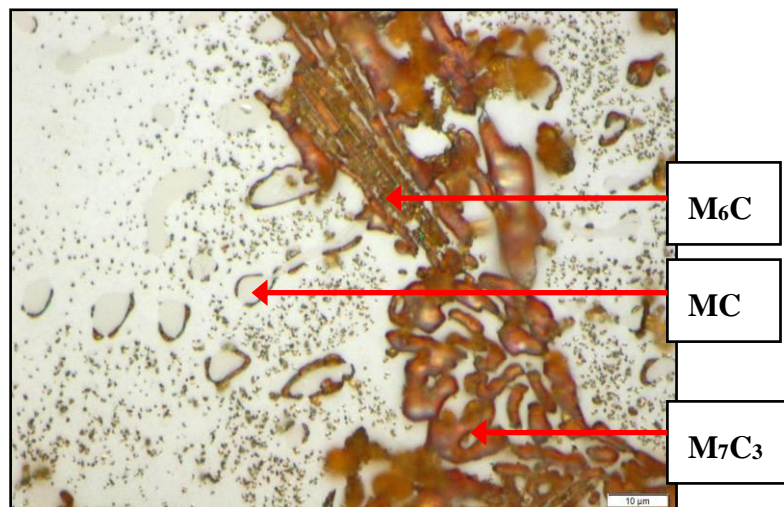
Figure 4-64: Sample T3 etched with Murakami's, 30mm below the surface at higher magnification.

110
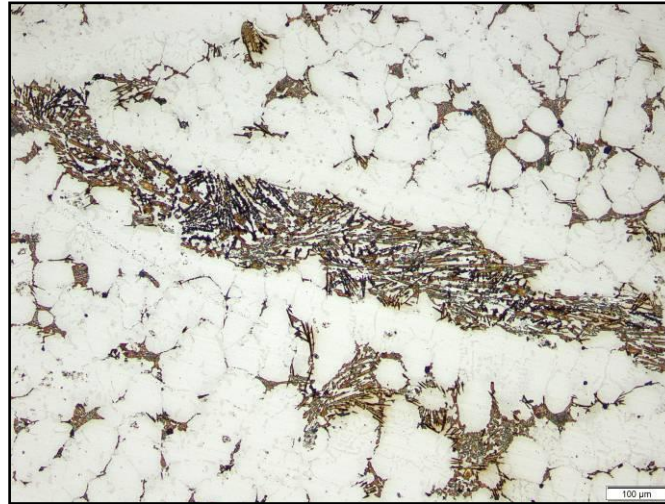
Figure 4-65: Sample AC2 showing carbide clusters at a depth of 25mm below the surface, etched with Murakami's.
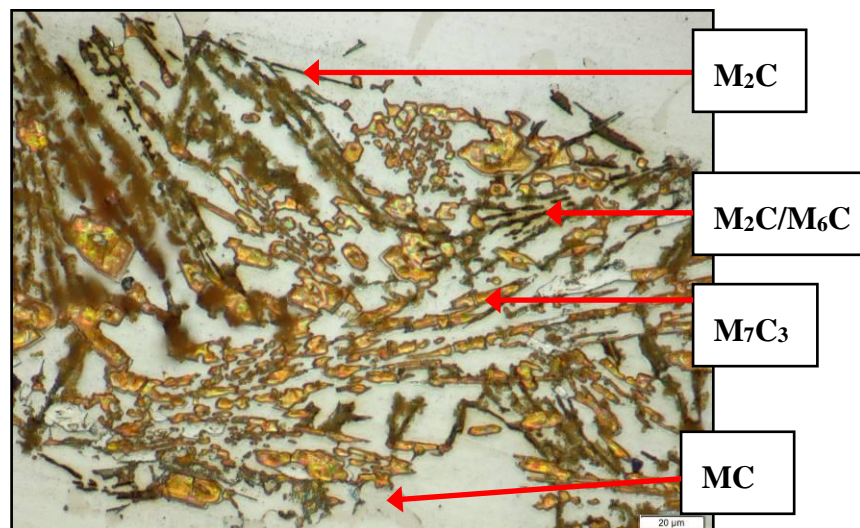
Figure 4-66: Sample AC2 showing carbide clusters at a depth of 25mm below the surface, etched with Murakami's.

4.1.4.5.   Alkaline Sodium Picrate (ASP)

The ASP etchant did not etch any of the carbides in the as-cast samples. However, ASP did etch the M_6C carbides black on the first and final temper samples, see Figures 4-67 to 4-72. Both the thin fish bone structure and remnants from the M_2C needles showed a mottled appearance, suggesting that the initial thin fish bone carbides forming on solidification are also of the M_2C type and not M_6C. ASP did not affect any of the other primary carbides in the shell other than M_6C on the tempered materials. ASP also etched fine secondary carbides associated with the primary carbides at the interdendritic regions. This suggests that the likely structure is also M_6C.

ASP also identified that the carbides present within the core's microstructure of both the AC5 and T3 samples consisted of M_3C carbides, see Figures 4-73 and 4-74. The colour of the ferrite varied from white to tan while the carbides varied from orange to pink.
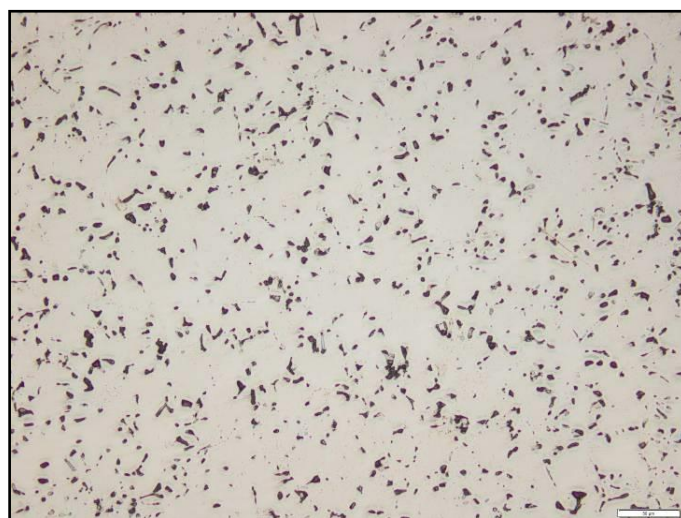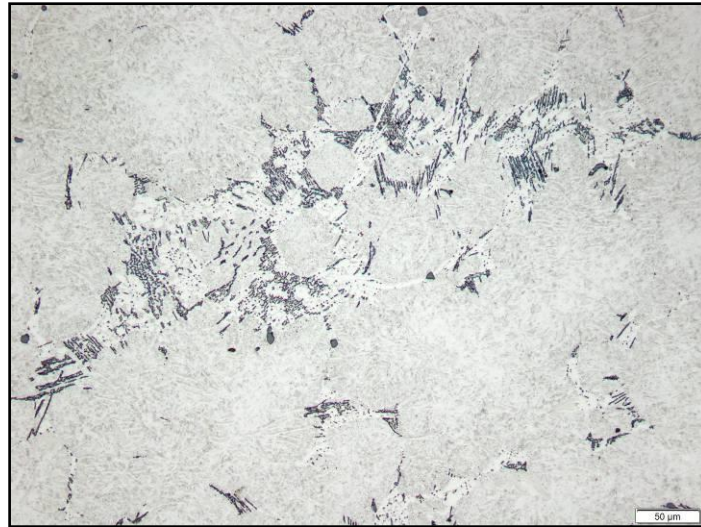

Figure 4-67: Sample T2-1 etched with ASP, 15mm below the surface.
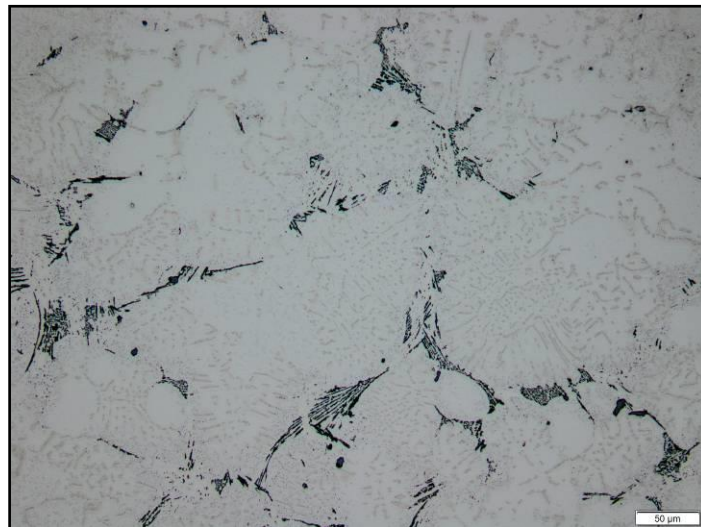
Figure 4-68: Sample T2-2 etched with ASP, 15mm below the surface.
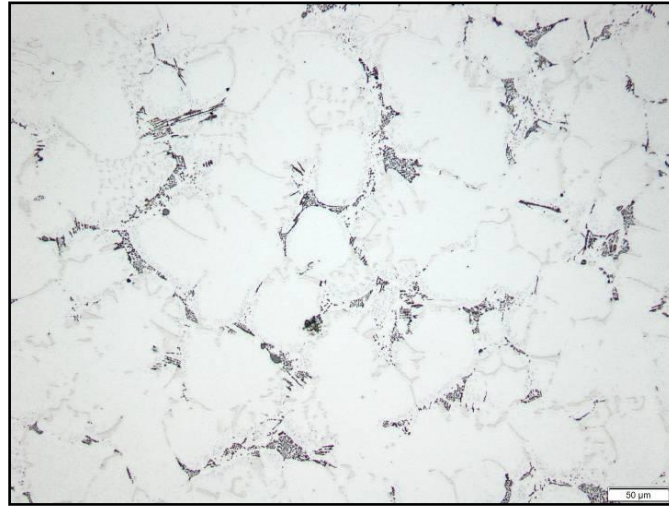
Figure 4-69: Sample T3 etched with ASP, at the surface.
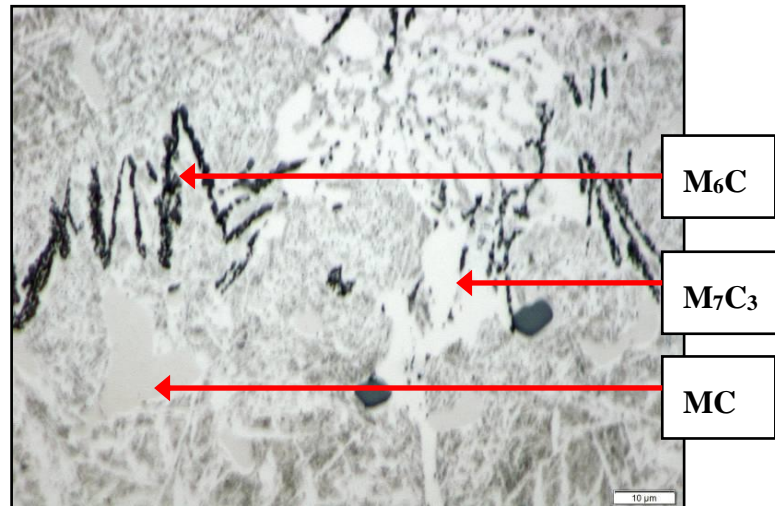
Figure 4-70: Sample T1-1 etched with ASP, 30mm below the surface at higher magnification.
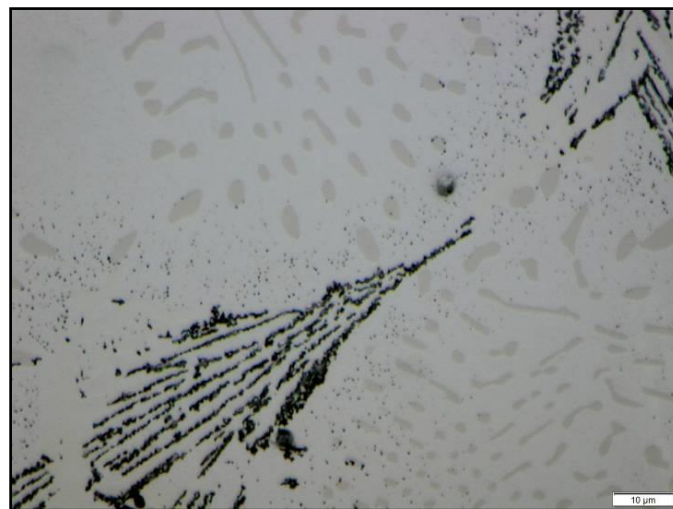
Figure 4-71: Sample T2-2 etched with ASP, 15mm below the surface at higher magnification.

113
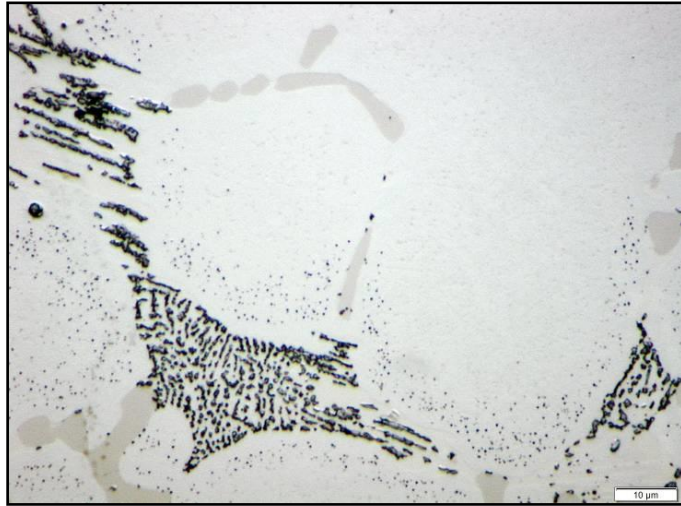
Figure 4-72: Sample T3 etched with ASP, 15mm below the surface at higher magnification.
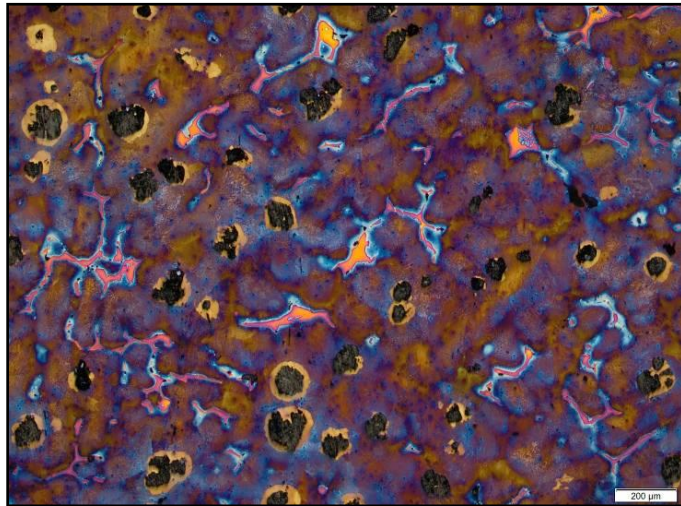
Figure 4-73: Sample AC5 etched with ASP, showing the core microstructure.
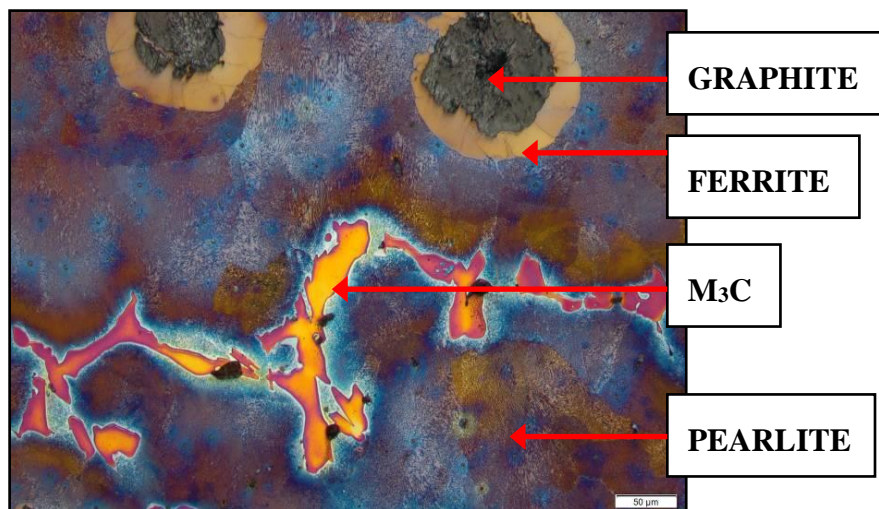
Figure 4-74: Sample AC5 etched with ASP, showing the core microstructure at higher magnification.

114

The increase in carbide content observed with the bond zone of sample AC5 was associated with the transition in carbide type to predominantly M_3C, as indicated by the etch response to ASP, see Figures 4-75 and 4-76. The bond defect associated with the clustered carbides of sample AC5 consisted exclusively of M_3C carbides. Figures 4-77 and 4-78 show the microstructures of the bond zone near the shell and near the core.
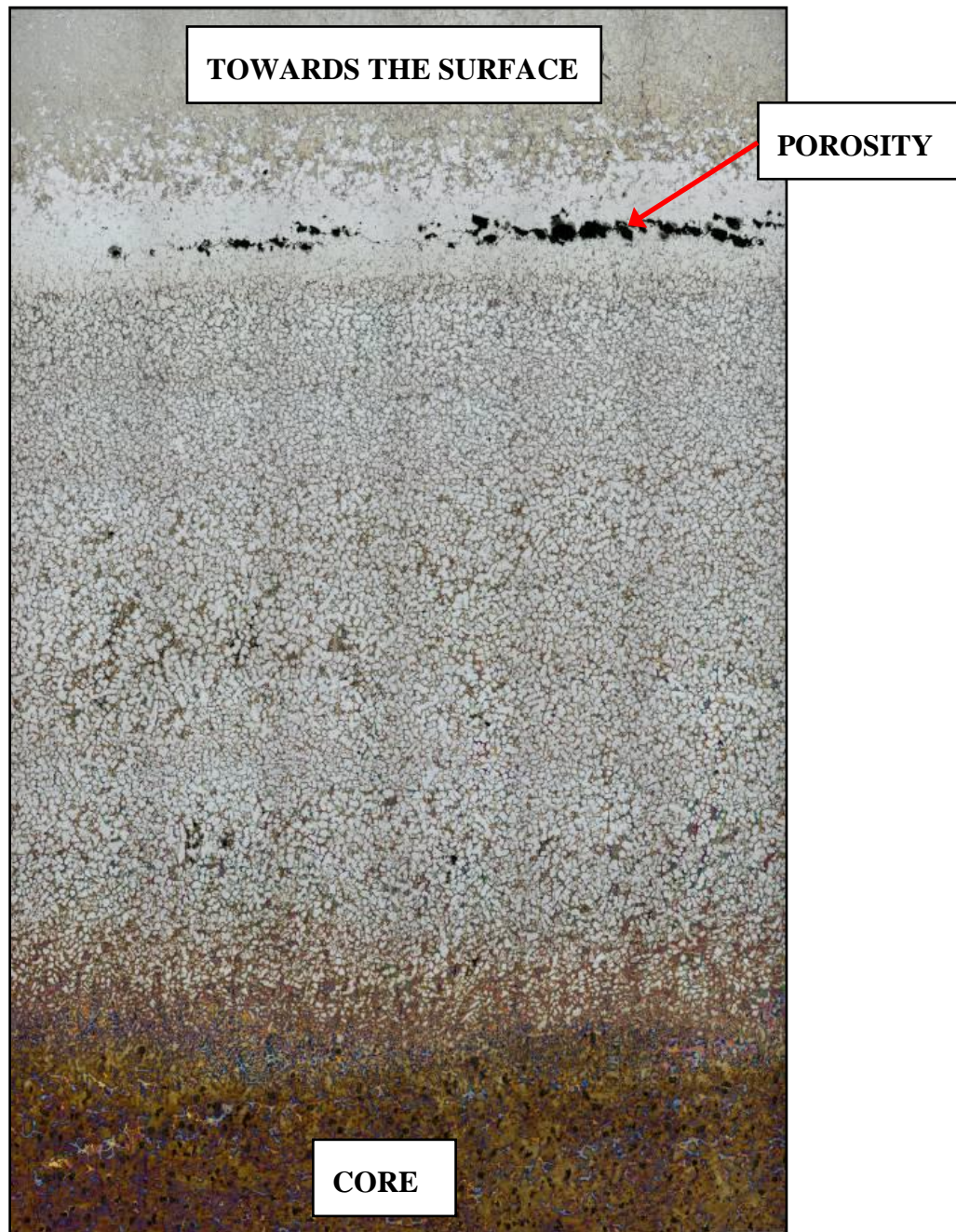
Figure 4-75: Sample AC5 etched with ASP, showing the transition from shell to core at the bond zone.
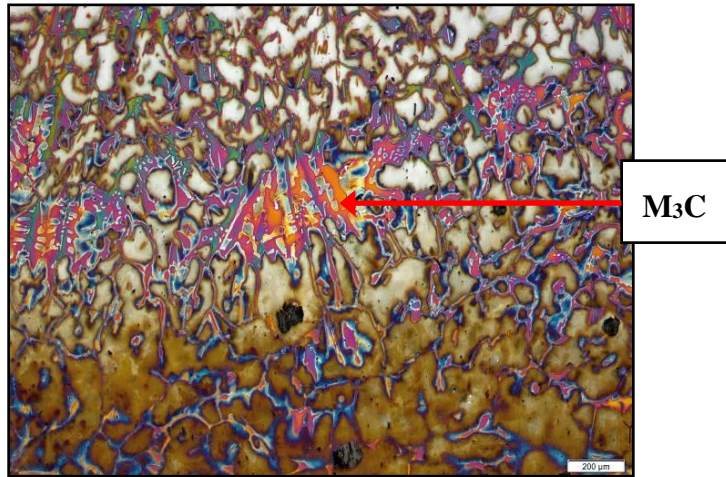
Figure 4-76: Sample AC5 etched with ASP, showing the clustered carbides at the bond zone.
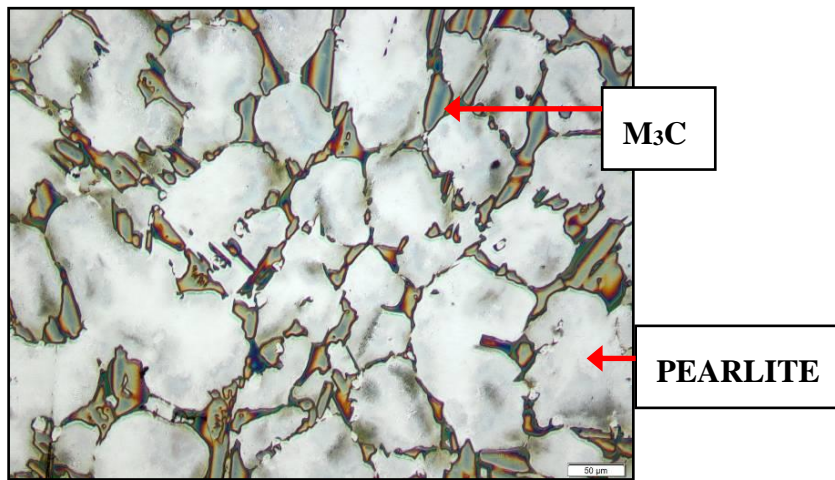
Figure 4-77: Sample AC5 etched with ASP, showing the microstructure at the bond zone near the shell.
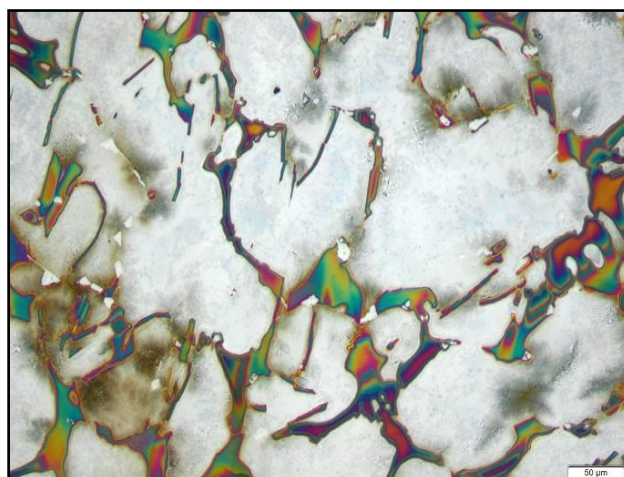
Figure 4-78: Sample AC5 etched with ASP, showing the microstructure at the bond zone near the core.

116

The carbide volume fraction within the bond zone appeared to increase notably from the shell towards the core. The gradual transition of Sample T3 in carbide type near the bond zone was also associated with the transition to M_3C carbides, see Figures 4-79 to 4-82.
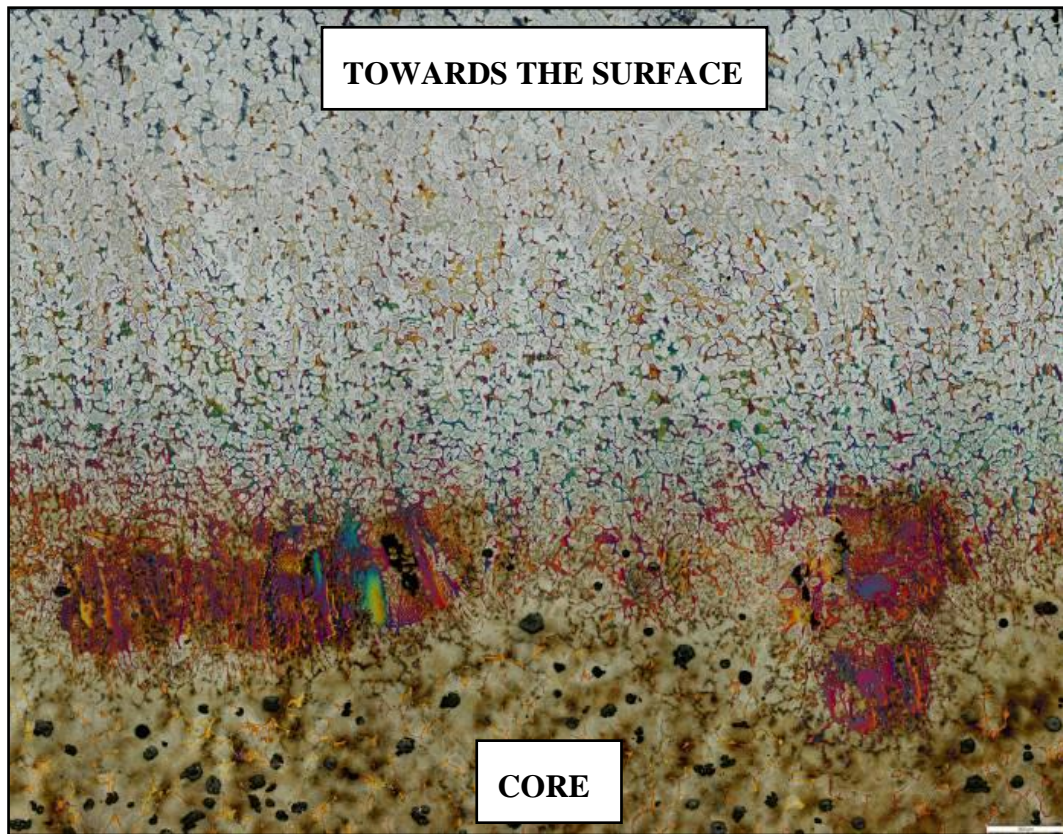
Figure 4-79: Sample T3 etched with ASP, showing the transition from shell to core at the bond zone.
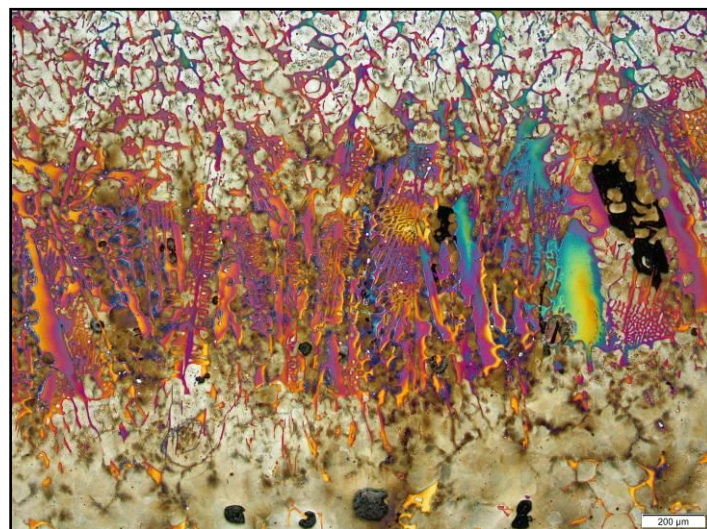
Figure 4-80: Sample T3 etched with ASP, showing the clustered carbides at the bond zone.

117
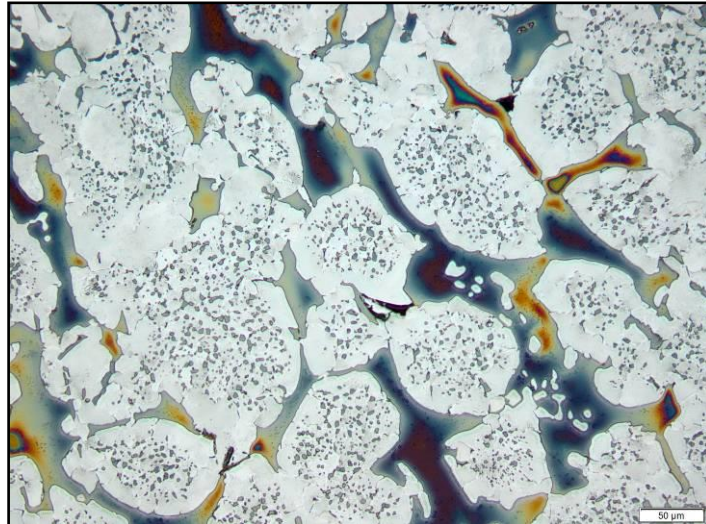
Figure 4-81: Sample T3 etched with ASP, showing the microstructure at the bond zone.
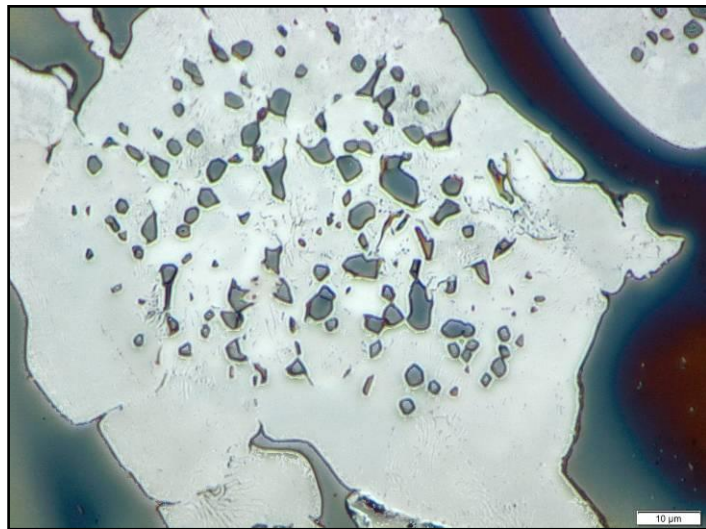
Figure 4-82: Sample T3 etched with ASP, showing the microstructure at the bond zone.

4.1.4.6.   Beraha's Etchant

Beraha's etchant was used to identify chemical segregation and the presence of retained austenite. The as-cast samples showed significant coring around the carbide cell boundaries, see Figures 4-83 to 4-85. This indicates the presence of chemical segregation. This also identified the presence of significant quantities of retained austenite, which was primarily associated with the carbide networks. The coring also clearly showed that the carbide clusters found in sample AC2 were associated with a region of dendritic solidification, see Figure 4-86. The tempered samples showed limited chemical segregation and no retained austenite could be positively identified, see Figures 4-87 to 4-91.

118
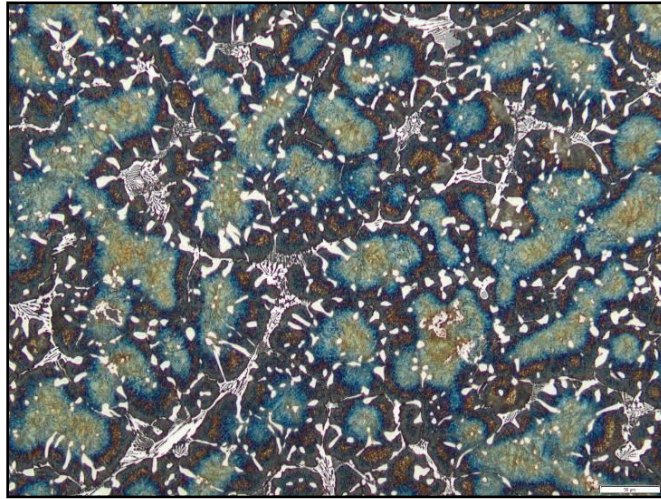
Figure 4-83: Sample AC1 etched with Beraha's, 30mm below the surface.
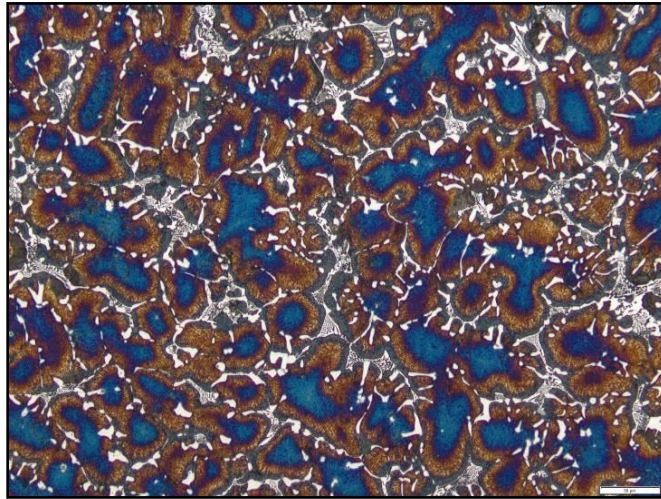
Figure 4-84: Sample AC2 etched with Beraha's, 15mm below the surface.
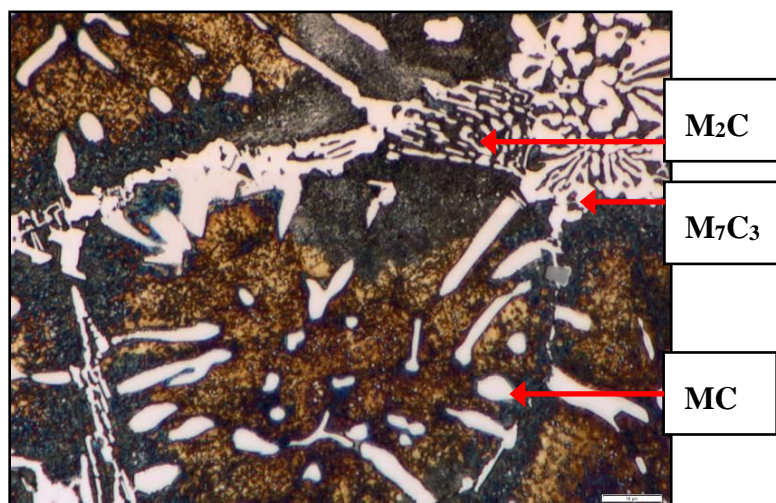
Figure 4-85: Sample AC2 etched with Beraha's, 15mm below the surface at higher magnification.
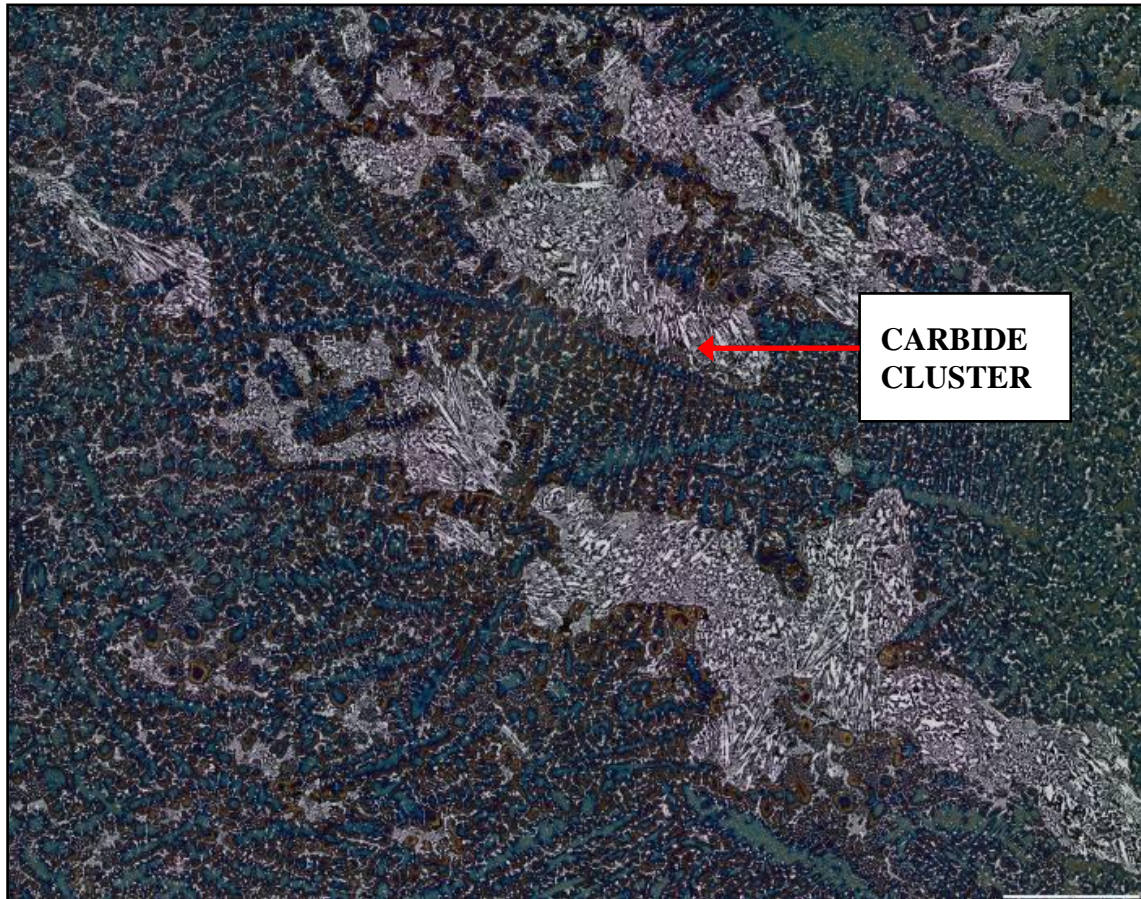
Figure 4-86: Sample AC2 etched with Beraha's etchant, showing the dendritic nature of the microstructure associated with the Carbide clusters.
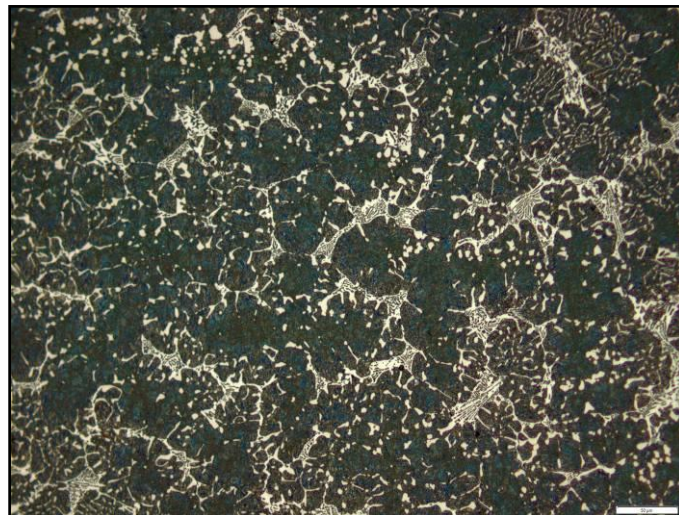
Figure 4-87: Sample T1-1 etched with Beraha's etchant, at the surface.

120
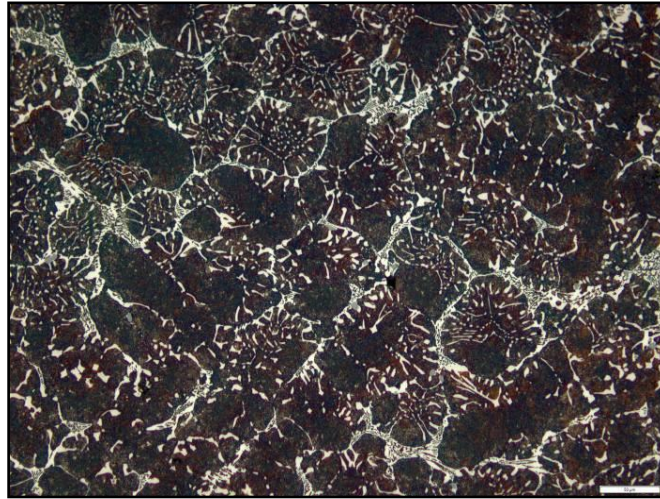
Figure 4-88: Sample T2-2 etched with Beraha's etchant, at the surface.

Figure 4-89: Sample T3 etched with Beraha's etchant, at the surface.
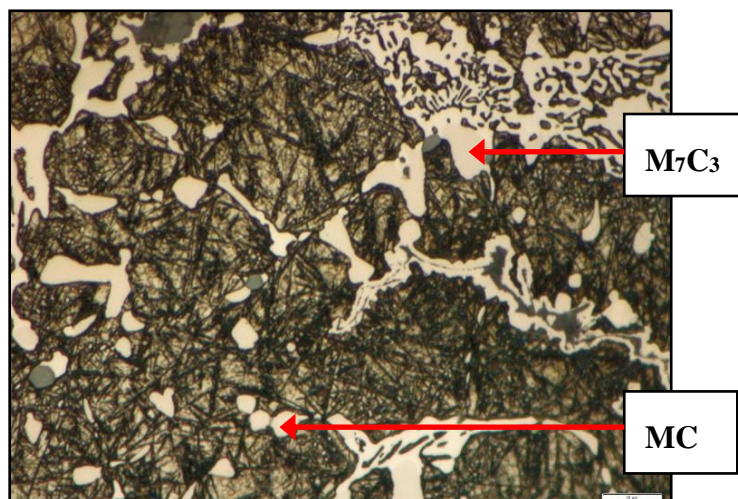
Figure 4-90: Sample T1-1 etched with Beraha's etchant, 15mm below the surface at higher magnification.

121
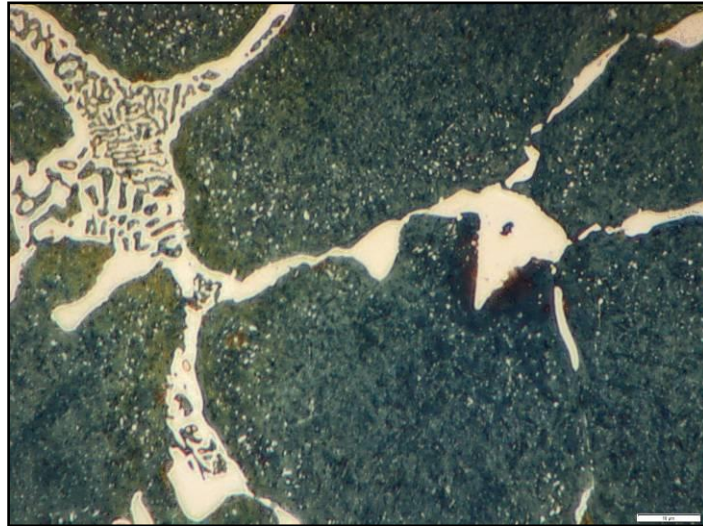
Figure 4-91: Sample T3 etched with Beraha's etchant, at the surface at higher magnification.

Since Beraha's etchant attacks all the matrix phases and leaves the carbides unaffected, the etched samples were used in order to determine the total carbide volume fraction using automated phase analysis. The total carbide content showed large variations between the measured values, especially sample AC5, see Figure 4-92 and Table 4-6. The total carbide volume fraction was similar for all samples over the shell depth, see Figure 4-93.
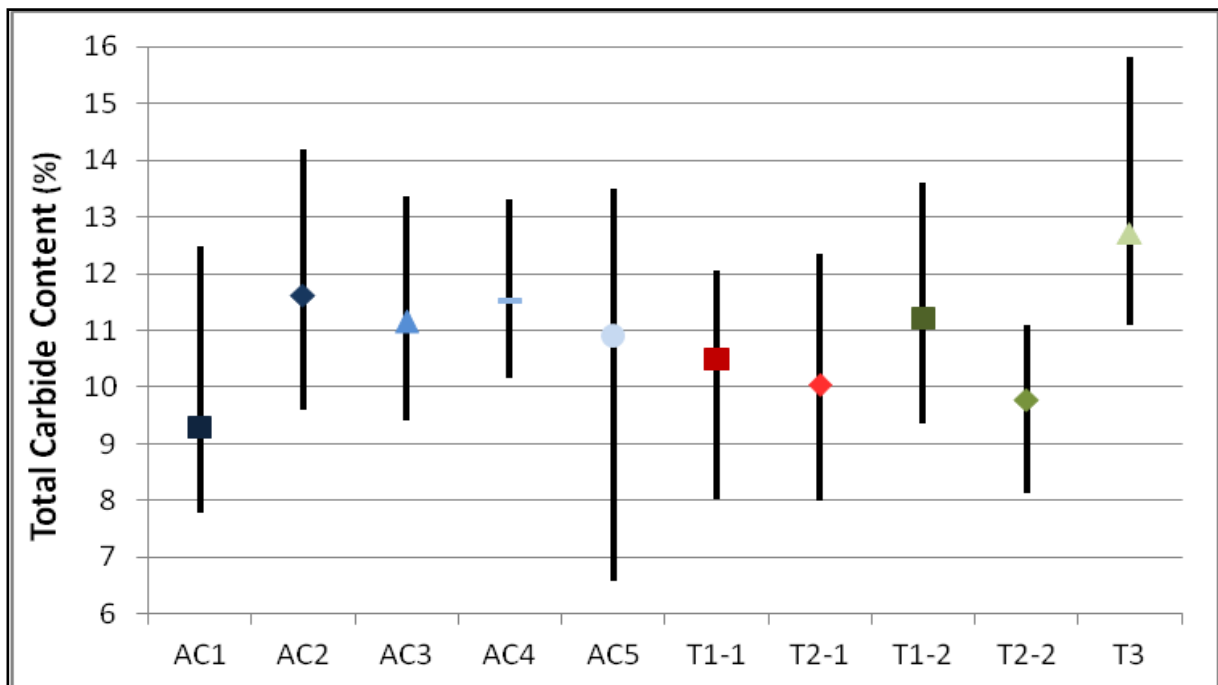
Figure 4-92: Average total carbide content measurement results and range of individual measurements for the benchmark samples.

Table 4-6: Phase analysis results for total carbide content.

Sample		Carbide Content (%)			Statistics			
Description	Depth	Minimum	Maximum	Average	S	CV	95%CL	RA
AC1	Surface	8.5	9.8	8.9	0.36	4.1%	0.28	3.1%
	15mm	7.8	9.1	8.7	0.38	4.4%	0.29	3.3%
	30mm	9.6	12.5	10.3	0.82	8.0%	0.62	6.0%
	Overall	7.8	12.5	9.3	0.90	9.7%	0.34	3.7%
AC2	Surface	9.6	14.2	13.2	1.30	9.8%	0.98	7.4%
	15mm	10.2	11.2	10.7	0.31	2.9%	0.23	2.2%
	30mm	10.6	11.5	10.9	0.29	2.6%	0.22	2.0%
	Overall	9.6	14.2	11.6	1.36	11.7%	0.52	4.5%
AC3	Surface	9.6	12.8	11.7	0.86	7.3%	0.65	5.5%
	15mm	9.6	11.1	10.4	0.49	4.8%	0.37	3.6%
	30mm	10.1	12.3	11.4	0.49	4.3%	0.37	3.3%
	45mm	9.4	13.4	11.2	1.15	10.3%	0.87	7.8%
	Overall	9.4	13.4	11.2	0.94	8.4%	0.30	2.7%
AC4	Overall	10.2	13.3	11.5	1.19	10.4%	0.90	7.8%
AC5	Surface	6.6	9.6	8.6	0.90	10.5%	0.68	7.9%
	15mm	10.7	12.3	11.4	0.50	4.4%	0.38	3.3%
	30mm	11.6	13.5	12.7	0.59	4.6%	0.44	3.5%
	Overall	6.6	13.5	10.9	1.89	17.3%	0.72	6.6%
T1-1	Surface	8.0	10.5	9.6	0.71	7.4%	0.53	5.5%
	15mm	9.7	10.7	10.4	0.31	3.0%	0.23	2.2%
	30mm	10.6	12.1	11.5	0.46	4.0%	0.35	3.0%
	Overall	8.0	12.1	10.5	0.92	8.7%	0.35	3.3%
T2-1	Surface	9.0	12.3	10.5	0.90	8.5%	0.68	6.4%
	15mm	9.4	10.8	10.3	0.43	4.2%	0.32	3.1%
	30mm	8.0	9.9	9.2	0.53	5.8%	0.40	4.3%
	Overall	8.0	12.3	10.0	0.85	8.5%	0.32	3.2%
T1-2	Surface	11.5	13.6	12.4	0.59	4.8%	0.47	3.8%
	15mm	9.4	10.5	10.1	0.34	3.4%	0.26	2.5%
	30mm	10.8	12.0	11.3	0.37	3.3%	0.28	2.5%
	Overall	9.4	13.6	11.2	1.03	9.2%	0.40	3.6%
T2-2	Surface	8.1	9.9	8.8	0.57	6.4%	0.43	4.9%
	15mm	9.3	10.9	10.1	0.53	5.3%	0.40	4.0%
	30mm	9.1	11.1	10.5	0.60	5.7%	0.45	4.3%
	Overall	8.1	11.1	9.8	0.92	9.4%	0.35	3.6%
T3	Surface	11.1	13.5	12.3	0.72	5.9%	0.55	4.4%
	15mm	11.3	12.5	11.9	0.47	3.9%	0.35	2.9%
	30mm	11.8	13.3	12.4	0.49	3.9%	0.37	3.0%
	40mm	13.4	15.8	14.2	0.74	5.2%	0.56	3.9%
	Overall	11.1	15.8	12.7	1.09	8.5%	0.35	2.8%
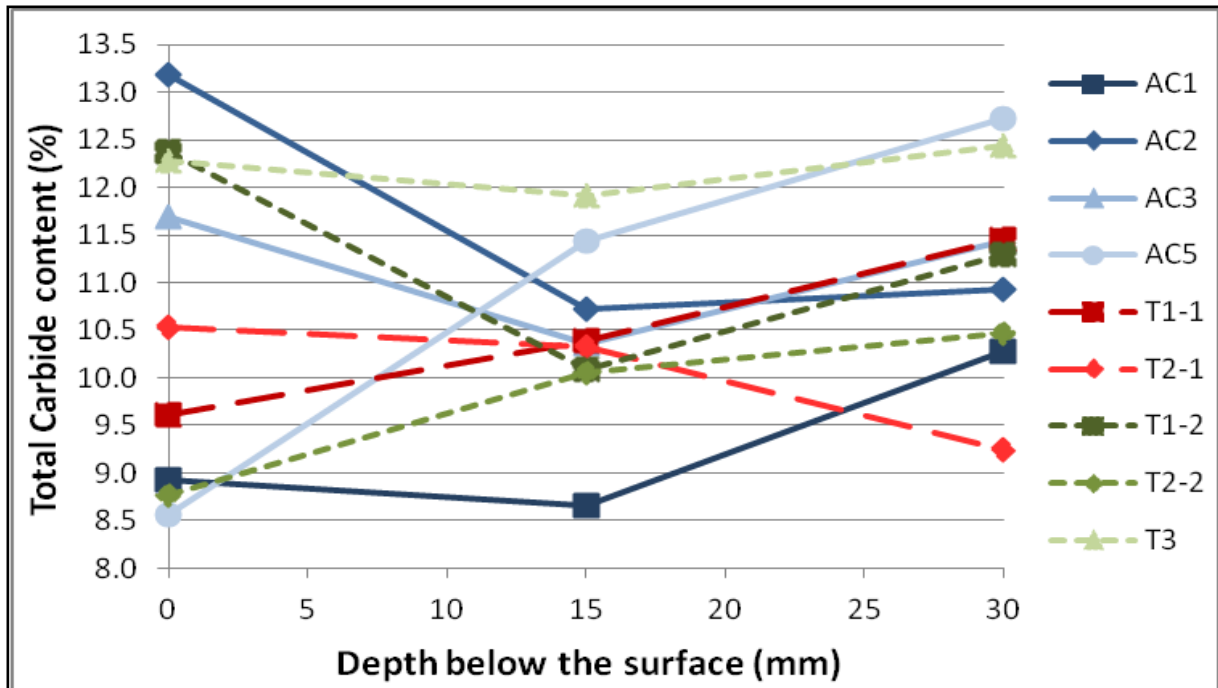
Figure 4-93: Total carbide content versus shell depth.

4.1.4.7. Combined Beraha's and Groesbeck's Etchants

In order to determine the total MC carbide volume fraction a combination of Groesbeck's and Beraha's etchant was used to achieve sufficient contrast for image analysis, see Figures 4-94 to 4-101.
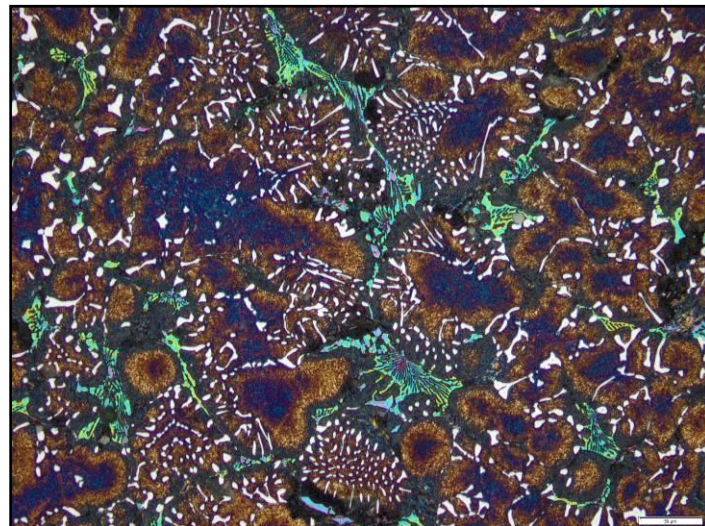
Figure 4-94: Sample AC2 etched with Beraha's and Groesbeck's etchants, 15mm below the surface.
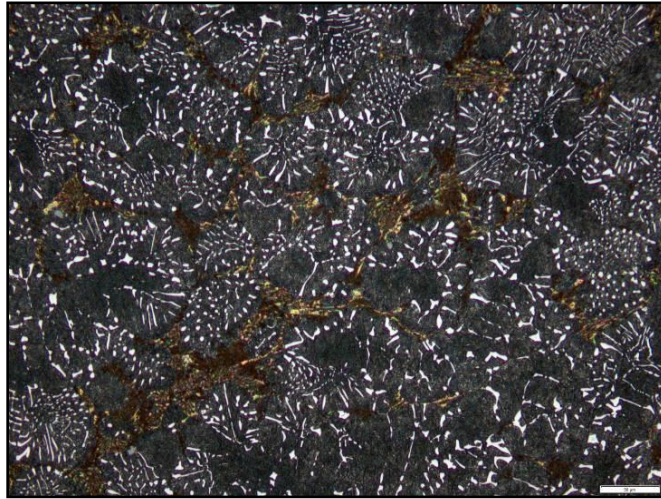
Figure 4-95: Sample T2-1 etched with Beraha's and Groesbeck's etchants, at the surface.
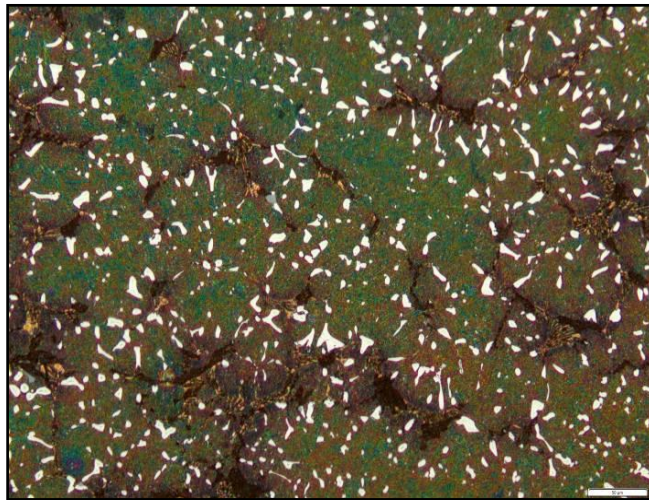
Figure 4-96: Sample T1-2 etched with Beraha's and Groesbeck's etchants, 30mm below the surface.
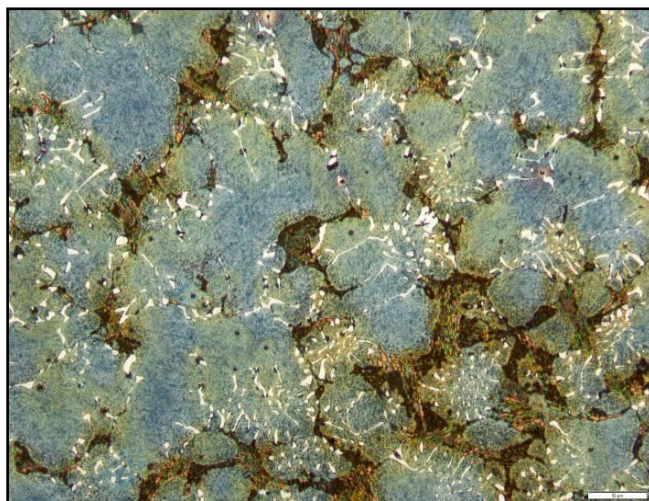
Figure 4-97: Sample T3 etched with Beraha's and Groesbeck's etchants, at the surface.

125
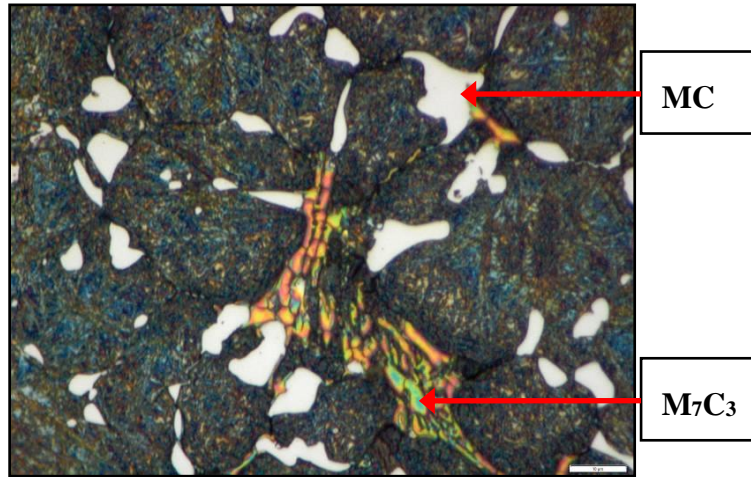
Figure 4-98: Sample AC1 etched with Beraha's and Groesbeck's etchants, 15mm below the surface at higher magnification.
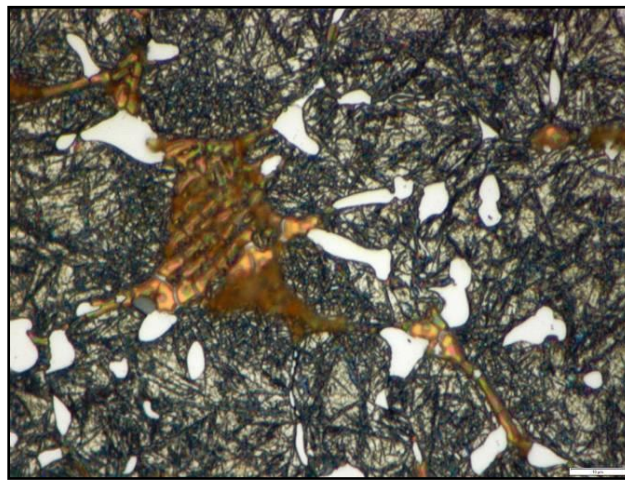
Figure 4-99: Sample T1-1 etched with Beraha's and Groesbeck's etchants, 15mm below the surface at higher magnification.
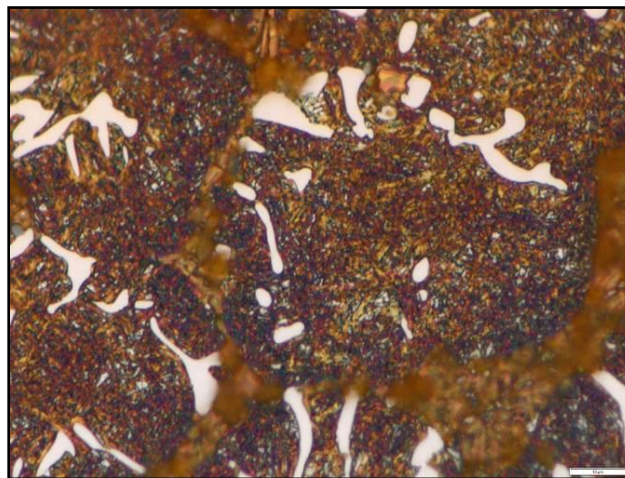
Figure 4-100: T1-2 etched with Beraha's and Groesbeck's etchants, higher magnification image at the surface.

126
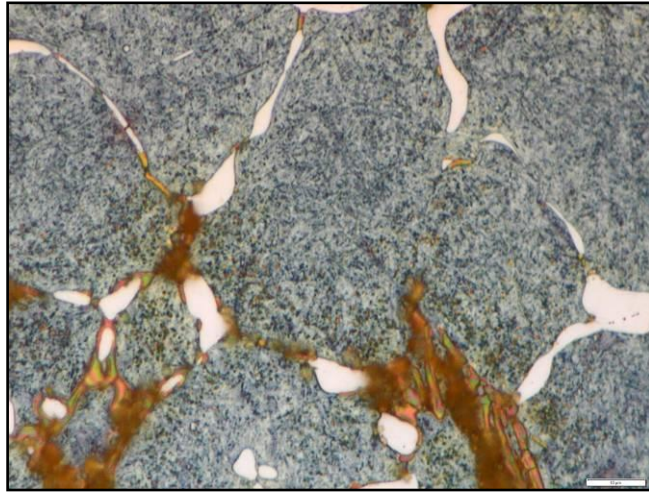
Figure 4-101: Sample T3 etched with Beraha's and Groesbeck's etchants, 15mm below the surface at higher magnification.

The phase analysis results showed large variation between individual measurements, especially in sample AC5, see Table 4-7 and Figure 4-102. The average MC carbide content of the samples were similar, except for sample T3, which showed the lowest MC carbide content of 3.6%. However, this is expected as sample T3 also showed a lower V content compared to the other samples.
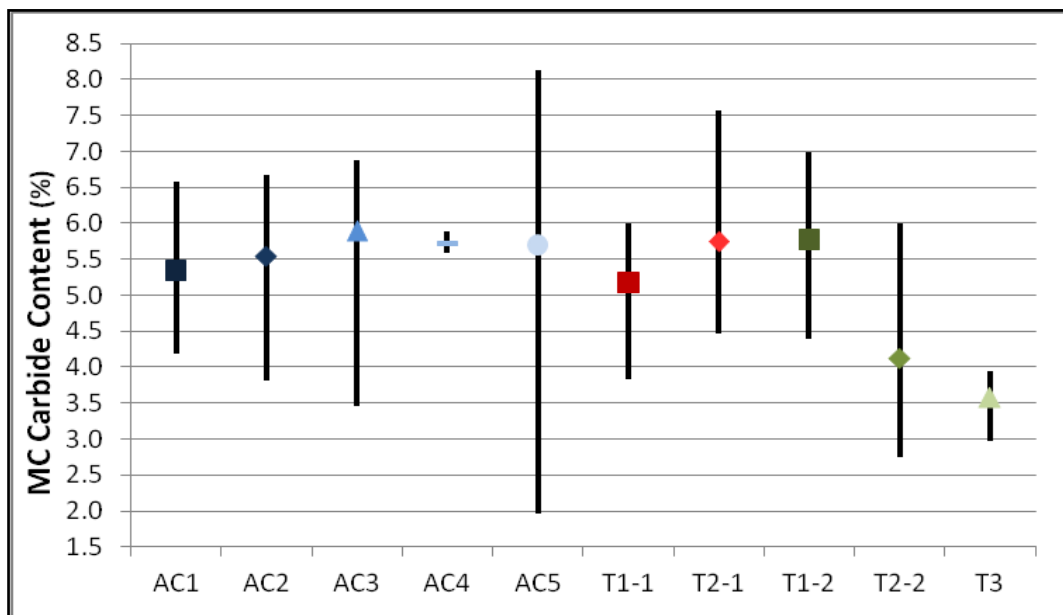
Figure 4-102: Average MC carbide content and range of individual measurements for the benchmark samples.

127

Table 4-7: MC carbide phase analysis results.

Sample		Carbide Content (%)			Statistics			
Description	Depth	Minimum	Maximum	Average	S	CV	95%CL	RA
AC1	Surface	4.2	5.2	4.6	0.29	6.2%	0.22	4.7%
	15mm	4.9	5.5	5.2	0.22	4.2%	0.17	3.2%
	30mm	5.5	6.6	6.2	0.40	6.4%	0.30	4.8%
	Overall	4.2	6.6	5.3	0.74	13.9%	0.28	5.3%
AC2	Surface	3.8	5.1	4.6	0.33	7.3%	0.25	5.5%
	15mm	5.0	6.3	5.6	0.36	6.3%	0.27	4.8%
	30mm	5.7	6.7	6.4	0.28	4.3%	0.21	3.3%
	Overall	3.8	6.7	5.5	0.84	15.2%	0.32	5.8%
AC3	Surface	3.5	6.9	5.0	1.45	28.9%	1.10	21.8%
	15mm	5.0	6.5	5.8	0.42	7.2%	0.32	5.5%
	30mm	5.7	6.9	6.3	0.42	6.6%	0.32	5.0%
	45mm	5.9	6.9	6.4	0.35	5.5%	0.27	4.1%
	Overall	3.5	6.9	5.9	0.95	16.2%	0.31	5.2%
AC4	Overall	5.6	5.9	5.7	0.12	2.1%	0.09	1.6%
AC5	Surface	2.0	3.7	3.2	0.47	14.9%	0.36	11.2%
	15mm	6.0	6.9	6.4	0.26	4.1%	0.20	3.1%
	30mm	6.8	8.1	7.5	0.39	5.1%	0.29	3.9%
	Overall	2.0	8.1	5.7	1.91	33.6%	0.73	12.7%
T1-1	Surface	3.8	4.6	4.3	0.25	6.0%	0.19	4.5%
	15mm	4.8	5.7	5.4	0.31	5.7%	0.23	4.3%
	30mm	5.5	6.0	5.8	0.13	2.3%	0.10	1.7%
	Overall	3.8	6.0	5.2	0.71	13.7%	0.27	5.2%
T2-1	Surface	4.5	5.5	4.9	0.29	5.9%	0.22	4.5%
	15mm	5.1	5.6	5.4	0.21	3.9%	0.16	2.9%
	30mm	6.1	7.6	6.9	0.48	6.9%	0.36	5.2%
	Overall	4.5	7.6	5.7	0.93	16.1%	0.35	6.1%
T1-2	Surface	4.4	4.9	4.7	0.19	4.1%	0.15	3.1%
	15mm	5.7	6.6	6.1	0.32	5.2%	0.24	3.9%
	30mm	6.2	7.0	6.6	0.28	4.3%	0.21	3.2%
	Overall	4.4	7.0	5.8	0.86	14.8%	0.33	5.6%
T2-2	Surface	2.8	3.2	3.1	0.15	5.0%	0.12	3.7%
	15mm	3.4	4.0	3.7	0.18	4.7%	0.13	3.6%
	30mm	5.2	6.0	5.5	0.27	4.8%	0.20	3.6%
	Overall	2.8	6.0	4.1	1.07	26.1%	0.41	9.9%
T3	Surface	3.0	3.5	3.2	0.16	5.1%	0.12	3.8%
	15mm	3.7	3.9	3.8	0.10	2.5%	0.07	1.9%
	30mm	3.5	3.9	3.7	0.13	3.4%	0.09	2.6%
	Overall	3.0	3.9	3.6	0.29	8.2%	0.11	3.1%

All the samples showed a clear increase in MC carbide content with shell depth, except for sample T3, which showed an increase from the surface to 15mm below the surface followed by a slight decrease to 30mm below the surface, see Figure 4-103. The increase in MC carbide content with shell depth is typically attributed to segregation due to the lower centrifugal force on the MC carbide during CC.
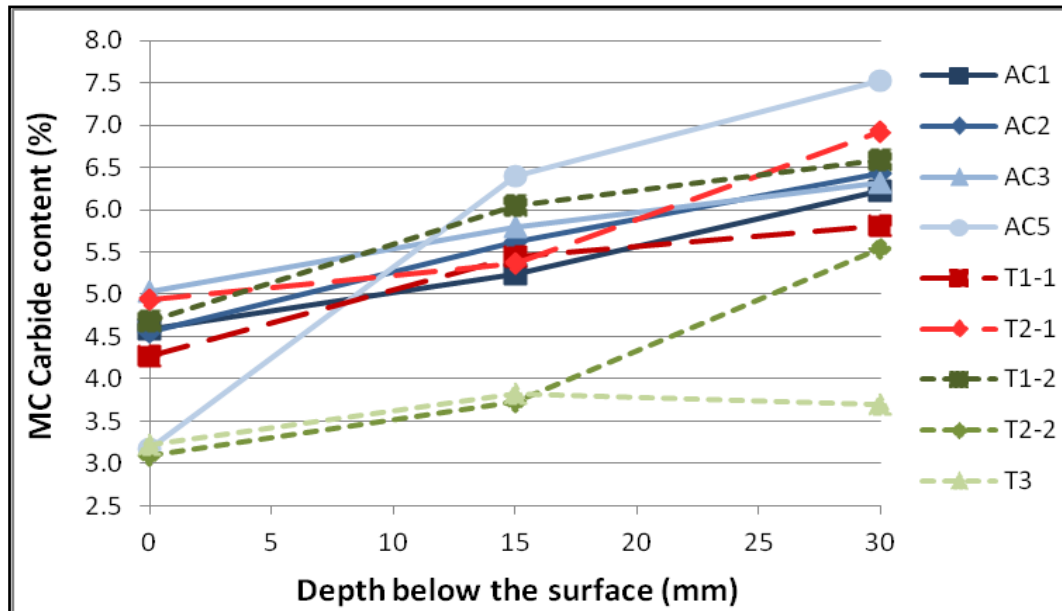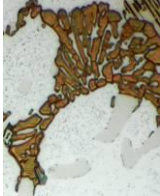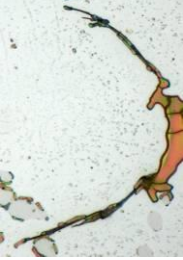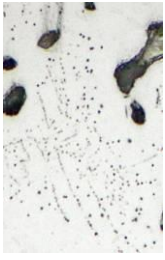
Figure 4-103: MC carbide content versus shell depth.

4.1.4.8. Summary - Carbide Etching
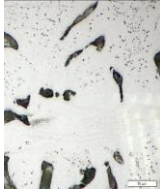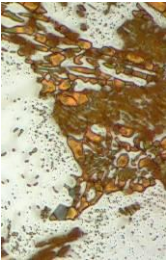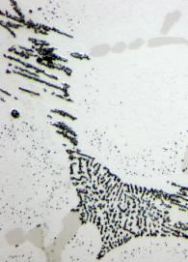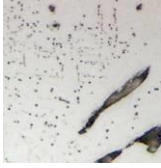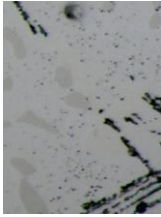
The carbide etchants revealed some key differences in the carbide structure between the as-cast and tempered samples. The as-cast samples contained only three primary carbide types and one secondary carbide type, see Table 4-8. The tempered samples contained three primary carbide types and two secondary carbide types, see Table 4-9. Two of the three primary carbide types were identified as MC and M_7C_3 on both the as-cast and tempered samples and did not show any significant changes in morphology between the two conditions. The third primary carbide type associated with the as-cast samples was M_2C while the tempered samples showed only M_6C. The M_2C found in the as-cast samples occurred in the interdendritic regions as both thin lamellae and acicular needles. The M_2C carbide is metastable and appears to transform to M_6C during heat treatment, retaining the thin lamellar structure but not the needles. The needles appeared to be divided into globules.

129

Table 4-8: Carbide characterisation summary for the as-cast samples.

Carbide Type	MC	M$_7$C$_3$	M$_2$C	M$_{23}$C$_6$
Formation	Primary	Primary	Primary	Secondary
Typical Morphology	Globular	Thick lamellae	Thin Lamellae	Small
			Acicular Needles	Globules
Localization	Matrix	Interdendritic	Interdendritic	Matrix
	Interdendritic			Homogenous
Typical Micrograph				
ASP	NA	NA	NA	NA
Murakami	NA	Colour	Colour	Faint
Groesbeck	NA	Colour	Colour	NA
APS	Attacked	NA	NA	Attacked

The second key difference between the carbide structures of the as-cast and tempered samples was found in the secondary carbides. Both conditions showed homogenously distributed M$_{23}$C$_6$ carbides within the matrix, while only the tempered samples showed another secondary carbide type. The tempered samples showed fine M$_6$C and secondary carbides located within the matrix, but limited to regions adjacent to the larger primary M$_6$C carbides. From the occurrence of the carbides it is assumed that the formation of the M$_6$C secondary carbides is associated with the Mo and W enrichment of the surrounding matrix during austenitising. It is probable that the enrichment is also associated with the decomposition of the M$_2$C carbides to M$_6$C.

Table 4-9: Carbide characterisation summary for the tempered samples.

Carbide Type	MC	M_7C_3	M_6C	$M_{23}C_6$	M_6C
Formation	Primary	Primary	Primary	Secondary	Secondary
Typical Morphology	Globular	Thick lamellae	Thin Lamellae / Acicular Needles	Small / Globules	Small / Globules
Localization	Matrix / Interdendritic	Interdendritic	Interdendritic	Matrix / Homogenous	Interdendritic
Typical Micrograph					
ASP	NA	NA	Colour	NA	Colour
Murakami	NA	Colour	Colour	Faint	Colour
Groesbeck	NA	Colour	Colour	NA	Colour
APS	Attacked	NA	NA	Attacked	NA

4.1.5. Scanning Electron Microscope (SEM) Analysis

The general structures of the samples examined by SEM were similar to the optical metallographic observations and showed a matrix containing four distinct types of primary carbide, see Figures 4-104 to 4-106. The most abundant type was black in colour and was found predominantly within the matrix and not on the grain boundaries. These carbides are assumed to be MC carbides based on the size, shape and abundance shown during metallography. The second/third type was white in appearance and was limited to the grain boundaries. These carbides are assumed to be M_6C/M_2C carbides based on the shape and occurrence shown during metallography. The M_6C and M_2C carbides are distinguished based on morphology, due to lack of contrast difference between the two carbide types. The carbides occurred as both thin lamellae and needles. The fourth type was grey in appearance similar to the matrix, which made them difficult to positively distinguish from the matrix on some of the samples, despite showing clear boundaries between the carbide and the matrix. The grey carbides were also limited to the grain boundaries, but were generally coarser than the white carbides with similar morphology. These carbides are

131

assumed to be M$_7$C$_3$ carbides based on the shape and occurrence shown during metallography.
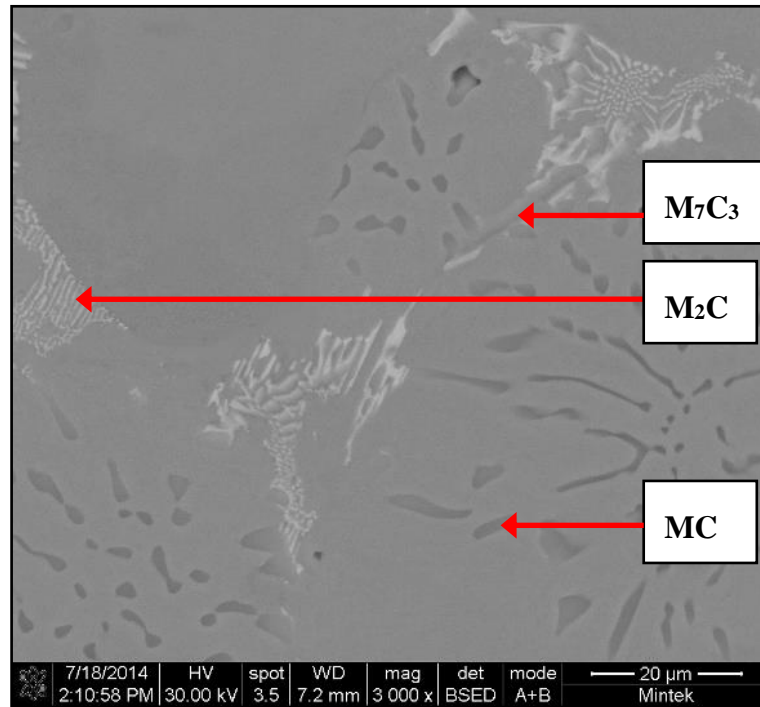
Figure 4-104: SEM image of sample AC1, showing the different carbide types.
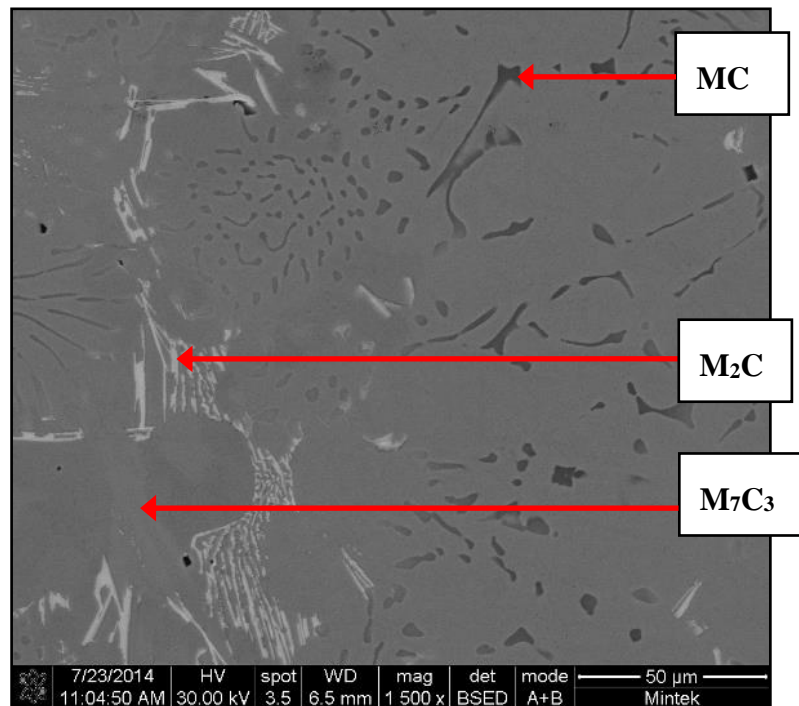
Figure 4-105: SEM image of sample AC2, showing the different carbide types.

132
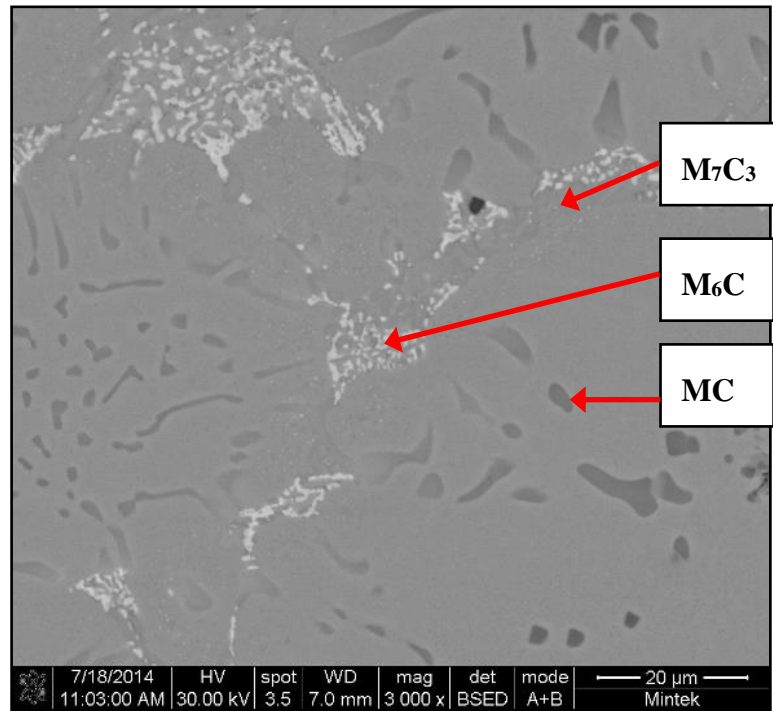
Figure 4-106: SEM image of sample T1-1, showing the different carbide types.

Energy dispersive spectrometry (EDS) analysis showed that the most abundant carbide former associated with the MC carbides is V, as expected from the literature [4, 8, 19, 22, 39, 40]; see Table 4-10 and Figure 4-107. The table reports the normalised average. The amounts of other carbide forming elements associated with the MC carbides also compared well to the reported literature values [4, 8, 19, 22, 39, 40]. The ratio of carbide formers to carbon (M:C) varied between 0.9 and 1.3, with an average of 1.03, which compared well with the ideal ratio of 1:1.

133

Table 4-10: EDS analysis results for the dark MC carbides (wt%).

Sample	C	W	Mo	Ti	V	Cr	Fe	M:C
AC1	14.1	7.1	5.0	1.8	53.9	3.3	14.8	1.3
AC2	16.0	5.5	4.1	4.0	61.0	2.6	6.8	1.2
AC3	17.8	4.6	4.4	1.9	59.6	3.0	8.8	1.0
T1-1	19.4	5.4	4.6	2.2	52.0	3.1	13.3	0.9
T2-1	19.1	6.2	4.5	2.1	54.3	2.7	11.1	0.9
T1-2	17.5	5.8	4.8	1.3	52.2	3.4	15.2	1.0
T2-2	17.7	5.3	4.2	3.2	56.7	3.1	9.9	1.0
T3	18.5	5.6	4.7	3.8	55.8	3.3	8.3	1.0
Minimum	14.1	4.6	4.1	1.3	52.0	2.6	6.8	0.9
Maximum	19.4	7.1	5.0	4.0	61.0	3.4	15.2	1.3
Average	17.5	5.7	4.5	2.5	55.7	3.1	11.0	1.0
Literature	-	0-21	1-34	-	31-82	2-9	2-24	1:1
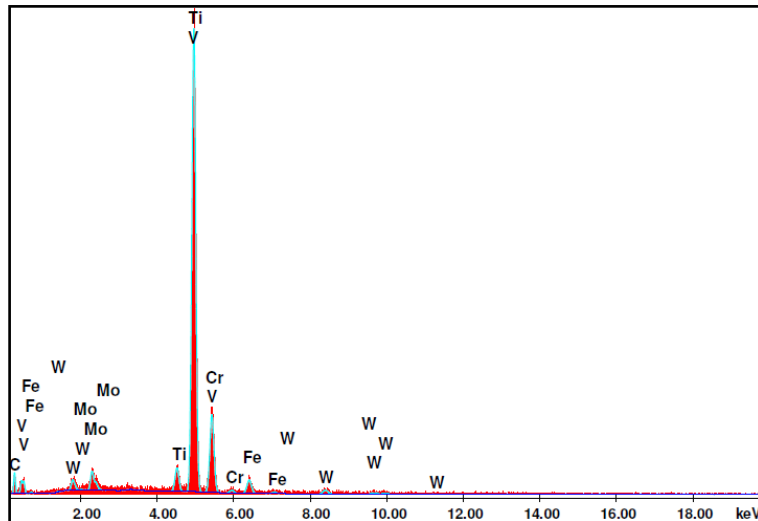
Figure 4-107: Representative spectra of a MC carbide analyses for sample AC3.

EDS analysis also showed that the most abundant carbide former associated with the white lamellar carbides was Mo, followed by Fe and W, see Table 4-11 and Figure 4-108. The lighter colouring of the carbides is attributed to the higher atomic weights associated with the Mo and W. The table reports the normalised average. The amounts of carbide forming elements associated with the white carbides did not compare well with the reported literature values for either M_2C or M_6C [4, 8, 19, 22, 39, 40]. The ratio of carbide formers to carbon (M:C) varied between 1.3 and 2.0, with

134

an average of 1.6, which did not compare well with the expected ideal ratio of 6:1 for the tempered or 2:1 for the as-cast samples.

Table 4-11: EDS analysis results for the white, lamellar M_2C/M_6C carbides (wt%).

Sample	C	W	Mo	V	Cr	Fe	M:C
AC1	7.6	11.5	39.0	7.5	10.2	24.3	2.0
AC2	10.6	12.9	35.7	7.0	10.5	23.3	1.5
AC3	10.4	11.1	43.1	8.0	10.0	17.4	1.4
T1-1	10.7	14.3	33.6	6.0	5.7	29.7	1.5
T2-1	9.9	14.4	31.8	6.7	6.2	31.0	1.5
T1-2	8.0	14.0	30.1	4.3	6.4	37.2	2.0
T2-2	11.9	12.7	29.9	6.7	7.1	31.6	1.3
T3	8.6	12.4	31.9	4.1	6.2	36.8	1.8
Minimum	7.6	11.1	29.9	4.1	5.7	17.4	1.3
Maximum	11.9	14.4	43.1	8.0	10.5	37.2	2.0
Average	9.7	12.9	34.4	6.3	7.8	28.9	1.6
Literature M_6C	-	3-39	12-27	3-7	4-16	13-36	6.0
Literature M_2C	-	0-40	18-68	4-14	8-23	6-24	2.0
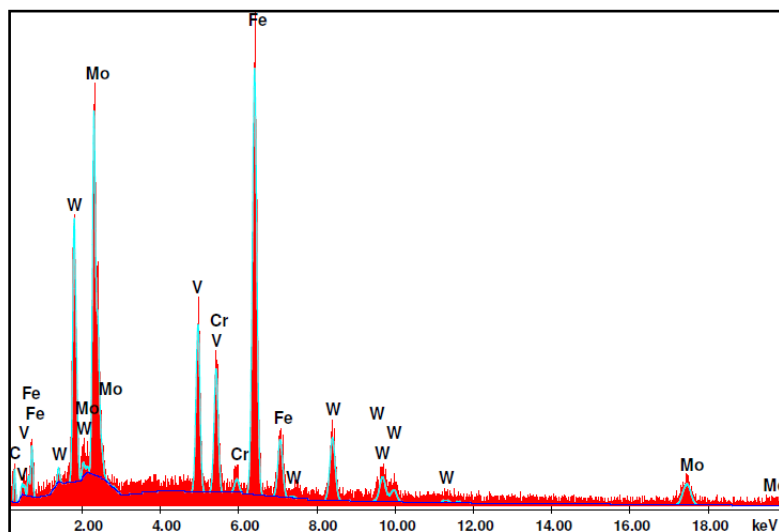
Figure 4-108: Representative spectrum of a thin lamellar M_6C carbide analyses for sample T1-1.

EDS analysis could not be performed on the grey M_7C_3 carbides on all of the samples, due to a lack in contrast, see Table 4-12 and Figures 4-104 to 4-1-6 and 4-109. EDS analysis showed that the most abundant carbide-former associated with the M_7C_3 carbides is Fe followed by Cr, as expected from the literature [4, 8, 19, 22, 39, 40]. The table reports the normalised average. The amounts of other carbide forming elements associated with the M_7C_3 carbides also compared well to the reported

135

literature values, except for Mo and Cr, which showed lower average contents than typically reported [4, 8, 19, 22, 39, 40]. The ratio of carbide formers to carbon (M:C) varied between 1.3 and 2.0, with an average of 1.7, which was similar to the ideal ratio of 7:3 (2.3).

Table 4-12: EDS analysis results for the grey M_7C_3 carbides.

Sample	C	W	Mo	V	Cr	Fe	M:C
AC3	10.9	4.4	8.2	4.7	20.6	51.2	1.7
T1-1	13.0	5.4	8.3	6.4	23.2	43.8	1.4
T2-1	13.7	3.6	10.1	7.2	25.3	40.1	1.3
T1-2	10.0	4.0	5.8	4.9	18.9	56.4	2.0
T2-2	10.6	4.4	6.9	5.2	19.3	53.7	1.8
T3	10.2	3.9	6.9	4.8	19.7	54.5	1.8
Minimum	10.0	3.6	5.8	4.7	18.9	40.1	1.3
Maximum	13.7	5.4	10.1	7.2	25.3	56.4	2.0
Average	11.4	4.3	7.7	5.5	21.2	49.9	1.7
Literature	-	1-7	3-8	5-12	22-40	27-54	2.3
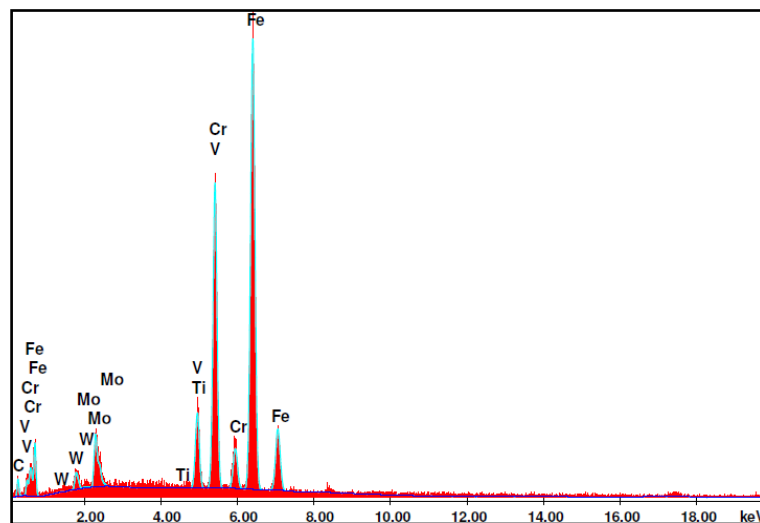
Figure 4-109: Representative spectrum of a M_7C_3 carbide analyses for sample T3.

The smallest region applicable to the EDS analysis was generally found to be slightly larger than the thickness of the white coloured M_2C carbide needles found in the as-cast samples. Hence it was anticipated that the analysis of the needles would inherently include the chemical composition of a portion of the surrounding matrix. The needles could also not be positively distinguished from the white lamellar carbides on some of the samples for the analysis. The most abundant carbide former associated

136

with the M$_2$C carbides was Fe followed by Mo and W, see Table 4-13 and Figure 4-110.

The table reports the normalised average. The higher than expected Fe content is attributed to the surrounding matrix areas. The amounts of other carbide forming elements associated with the M$_2$C carbides compared well to the reported literature values [4, 8, 19, 22, 39, 40]. The ratio of carbide formers to carbon (M:C) varied between 1.7 and 2.7, with an average of 2.0, which compared well with the ideal ratio of 2:1.

Table 4-13: EDS analysis results for the white M$_2$C carbide needles (wt%).

Sample	C	W	Mo	V	Cr	Fe	M:C
AC2	9.1	7.3	24.7	4.2	8.7	45.9	1.8
AC3	9.4	5.4	27.0	5.1	10.2	42.9	1.8
Minimum	9.1	5.4	24.7	4.2	8.7	42.9	1.8
Maximum	9.4	7.3	27.0	5.1	10.2	45.9	1.8
Average	9.3	6.4	25.9	4.6	9.4	44.4	1.8
Literature M$_2$C	-	0-40	18-68	4-14	8-23	6-24	2.0
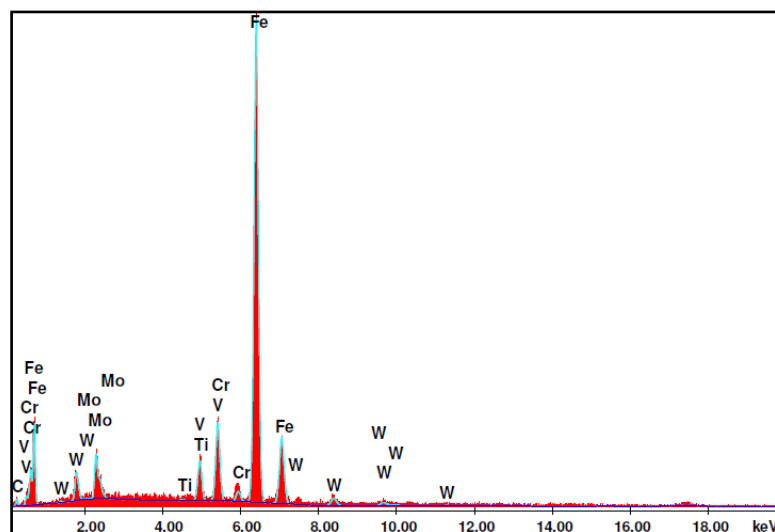
Figure 4-110: Representative spectrum of a M$_2$C carbide needle analyses for sample AC3.

EDS analysis of the bulk of the material generally compared well with the spark emission spectrometry analysis, except for the C and W content, which was significantly higher, see Figure 4-111. Due to proprietary reasons the exact bulk analyses may not be reported. EDS is not able to quantify elements of low atomic weight accurately. EDS analysis of the matrix showed predominantly Fe, see Figure

4-112. All of the carbide forming elements were also present within the matrix, with Fe and W showing the highest within the matrix with reference to the measured bulk.

Comparative EDS analysis of the matrix containing white secondary carbides in the tempered samples, was also performed. These matrix regions showed a significant increase in the Mo, Cr and C content compared to the bulk of the matrix, see Figure 4-113. The strong increase in Mo and C is in accordance with the metallography observations, where the carbide type was identified as M_6C, see Figures 4-114 to 4-116.

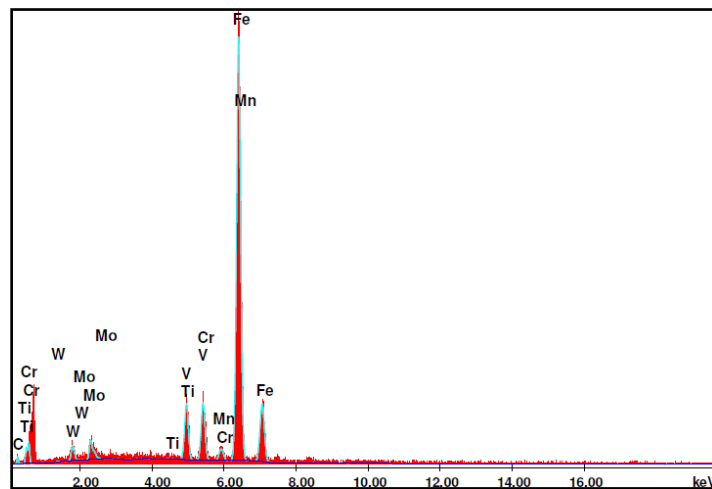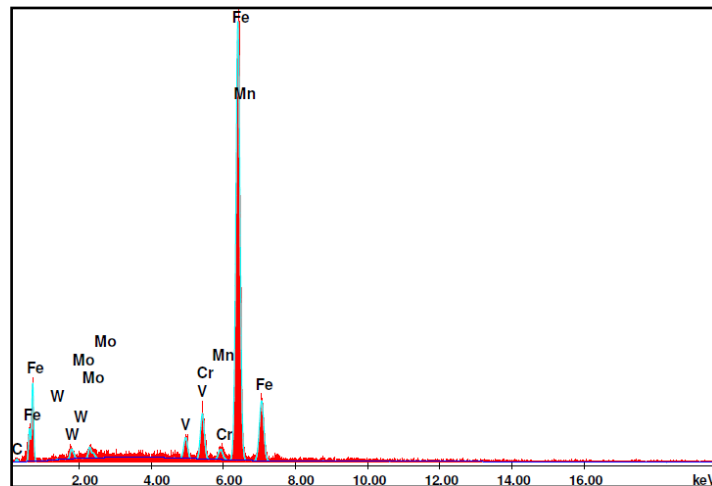Figure 4-111: Representative spectrum of the bulk analyses for sample AC2.

Figure 4-112: Representative spectrum of the matrix analyses for sample T2-1.

Table 4-14: EDS analysis results for the matrix cell centres and white secondary carbide regions (wt%).

| Location	Sample	C	W	Mo	V	Cr	Fe
Matrix Cell centre	AC1	3.3	4.5	1.9	2.5	4.2	83.6
	AC2	4.0	4.9	2.6	2.5	5.2	80.8
	AC3	3.9	4.5	2.5	2.3	4.9	81.9
	T1-1	3.5	4.7	2.4	2.3	4.5	82.6
	T2-1	3.8	5.1	2.5	2.5	4.6	81.5
	T1-2	4.5	4.3	2.2	2.4	4.4	82.2
	T2-2	3.6	4.6	2.3	2.3	4.3	82.9
	T3	3.6	4.3	2.3	1.9	4.5	83.3
	Minimum	3.3	4.3	1.9	1.9	4.2	80.8
	Maximum	4.5	5.1	2.6	2.5	5.2	83.6
	Average	3.8	4.6	2.3	2.3	4.6	82.3
	% of bulk	70.7%	81.1%	59.3%	44.0%	82.8%	-
Matrix white carbide	T1-1	3.8	5.1	3.4	1.3	5.7	80.7
	T2-1	3.7	5.3	3.4	1.3	5.9	80.5
	T1-2	4.1	4.6	3.1	1.3	5.6	81.3
	T2-2	4.9	5.0	3.2	1.3	5.7	80.0
	T3	4.4	4.2	3.3	1.1	5.8	81.2
	Minimum	3.7	4.2	3.1	1.1	5.6	80.0
	Maximum	4.9	5.3	3.4	1.3	5.9	81.3
	Average	4.2	4.9	3.3	1.3	5.7	80.7
	% Increase	10.8%	4.8%	38.9%	-	25.1%	-
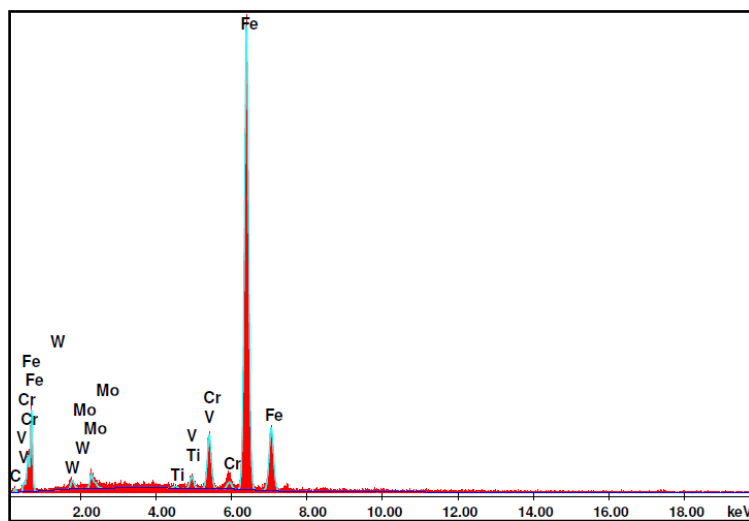
Figure 4-113: Representative spectrum of the matrix analysis containing white secondary carbides for sample T1-2.
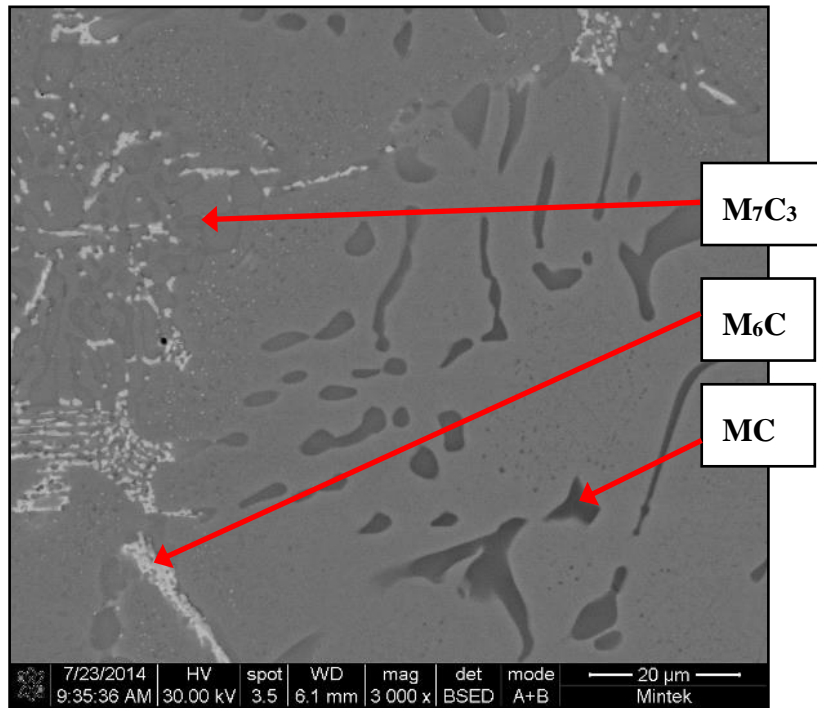
139

Figure 4-114: SEM image of sample T2-1, showing the different carbide types.
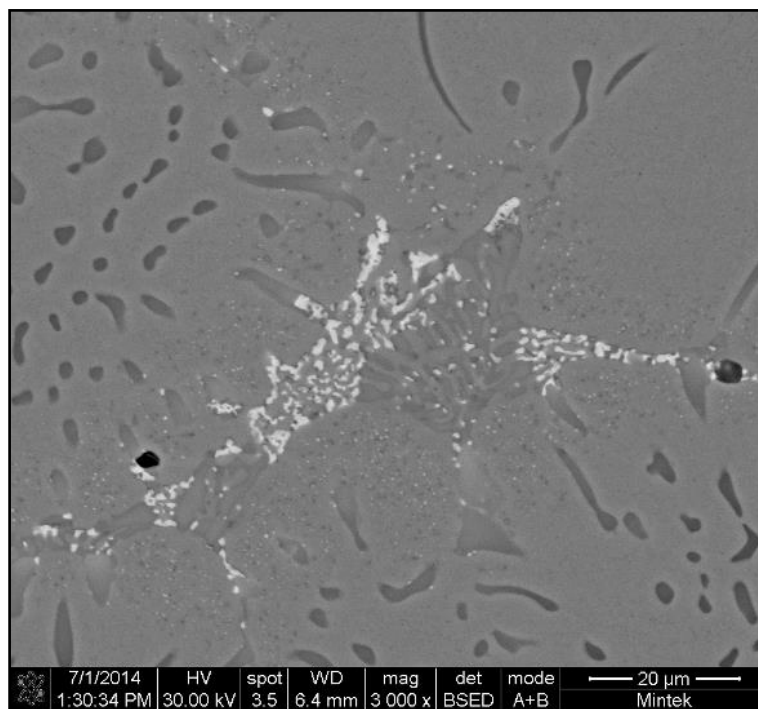

Figure 4-115: SEM image of sample T1-2, showing the fine white secondary carbides.
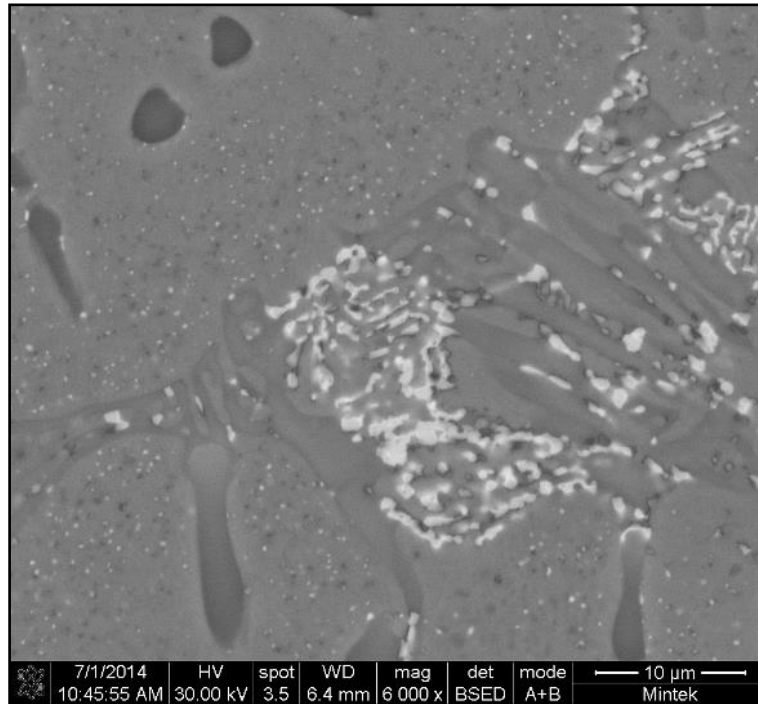
140

Figure 4-116: SEM image of sample T2-2, showing the fine white secondary carbides.

Numerous examples were also found where the dark carbides showed significant change in appearance, from black to grey over the length of the carbides, see Figure 4-117 and Table 4-15. Comparative EDS analysis of opposing carbide ends showed an enrichment of V in the dark region, which was counteracted by an enrichment of both W and Mo in the lighter end of the MC carbide.
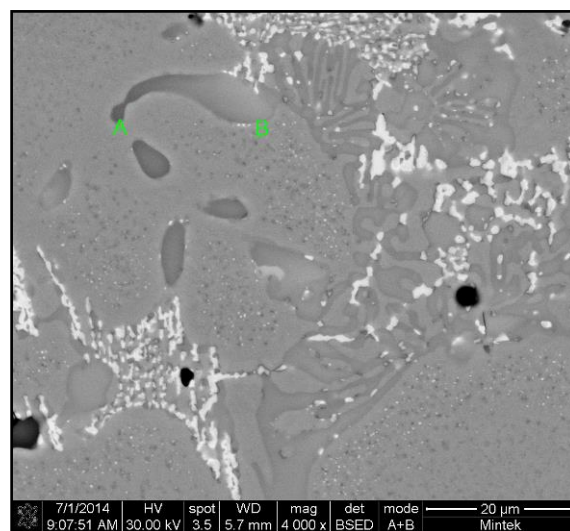

Figure 4-117: SEM image of sample T3, showing the variation in appearance across the length of an MC carbide.

141

Table 4-15: EDS analysis results at opposing ends of a MC carbide on sample T3.

Region	C	W	Mo	Ti	V	Cr	Fe
Dark (A)	16.8	6.5	13.1	0.0	36.4	4.1	23.0
Light (B)	18.0	9.7	23.5	0.2	33.5	8.8	6.2
Average	17.4	8.1	18.3	0.1	35.0	6.5	14.6

4.1.6. X-Ray Diffraction Analysis

The XRD analysis identified five distinct phases within the as-cast, first temper and final temper samples, which included alpha iron, austenite, MC carbide, M_7C_3 carbide and M_2C/M_6C carbide, see Table 4-16 and Figures 2-118 to 2-126. No indications of $M_{23}C_6$ carbides were found, despite being identified during metallographic and SEM analysis. There appeared to be a potential overlap of the peak identification of the $M_{23}C_6$ and M_7C_3 carbides, which is suspected to be the cause of the lack of $M_{23}C_6$ identification.

A slight shift in the M_2C/M_6C peak was also identified when comparing the as-cast samples to the tempered ones. This was assumed to be due to the transformation of the M_2C carbides to M_6C carbides during heat treatment as identified by metallography.

Table 4-16: XRD analysis results (vol%).

Volume %	Iron	Austenite	MC	M_2C/M_6C	M_7C_3
AC1	57.9	32.7	6.6	0.9	1.9
AC2	61.7	26.5	7.2	0.9	3.6
AC3	60.3	30.5	5.7	0.8	2.7
AC4	49.2	40.3	5.2	0.7	4.5
Average	57.3	32.5	6.2	0.8	3.2
T1-1	63.7	22.5	5.2	1.4	7.2
T2-1	67.3	19.9	5.2	1.4	6.2
Average	65.5	21.2	5.2	1.4	6.7
T1-2	82.3	4.5	5.4	1.3	6.5
T2-2	80.0	9.3	7.8	1.5	1.4
T3	81.0	5.6	3.8	1.4	8.2
Average	81.1	6.5	5.6	1.4	5.4

The austenite content of the as-cast samples showed a range of 26.5% to 40.3%, which was significantly higher than the first temper samples as expected. The final

142

tempered samples showed the lowest austenite content as expected. The difference in austenite content between the heat treatment conditions was offset by the change in Fe content. This is expected since the bulk of the austenite is transformed to martensite during heat treatment.

The MC carbide content was significantly higher than the M_2C/M_6C content, which is in agreement with the metallographic observations. The MC carbide content showed a fair degree of variation between the heat treatment conditions and is likely to have inaccuracies. The M_2C/M_6C carbide content appeared to increase from the as-cast state to the tempered condition, which could be due to the precipitation of the fine M_6C secondary carbides during tempering.
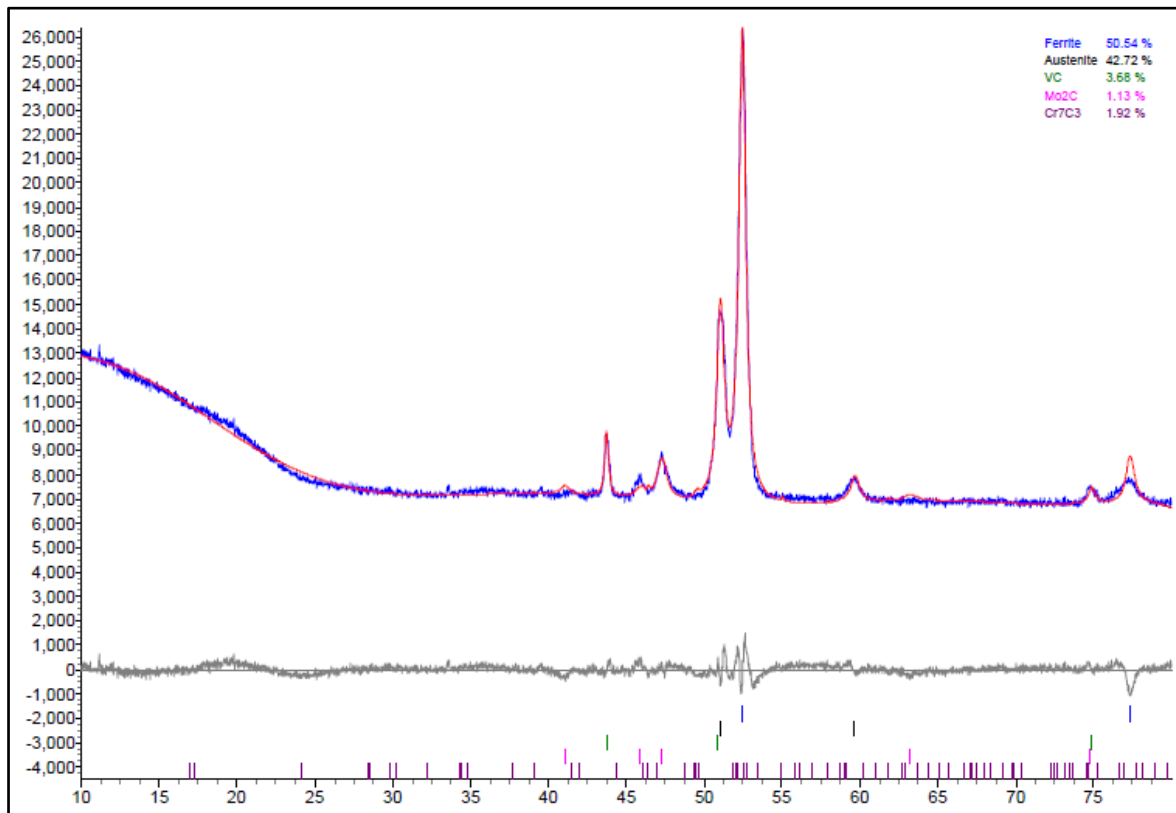

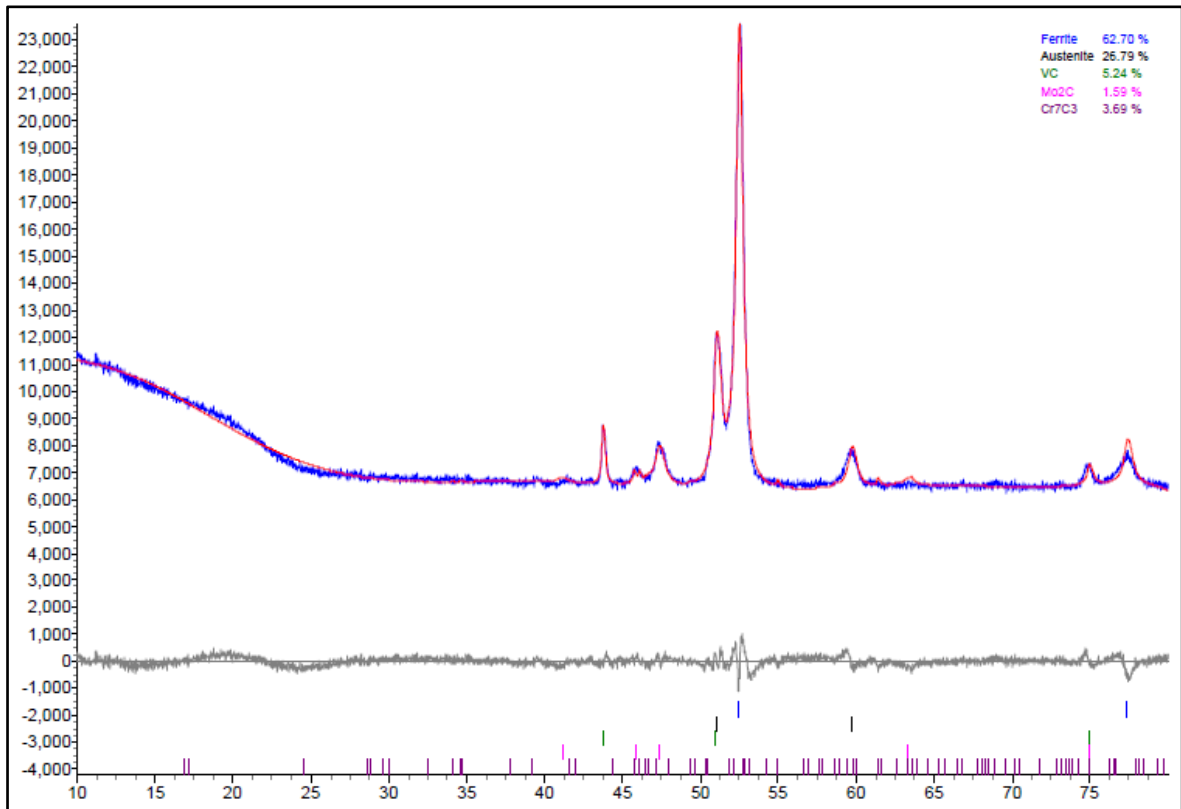Figure 4-118: XRD spectrum for sample AC1.

143
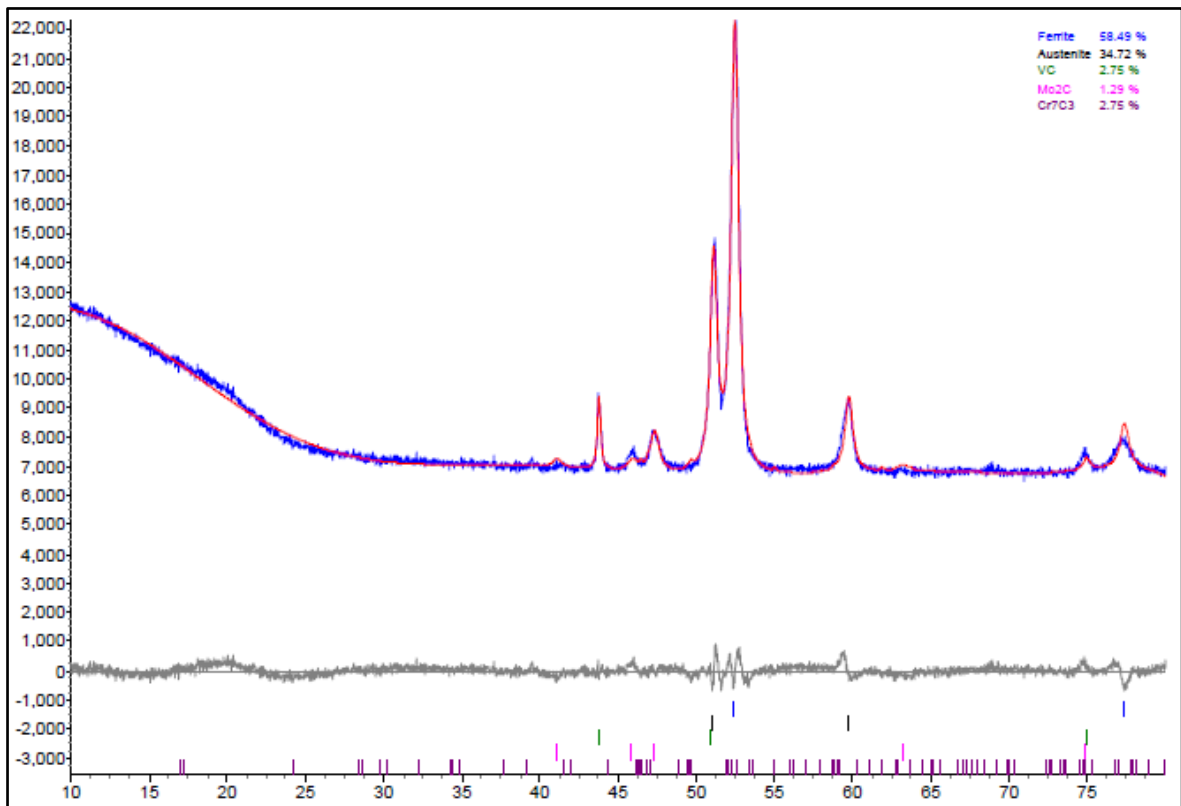
Figure 4-119: XRD spectrum for sample AC2.

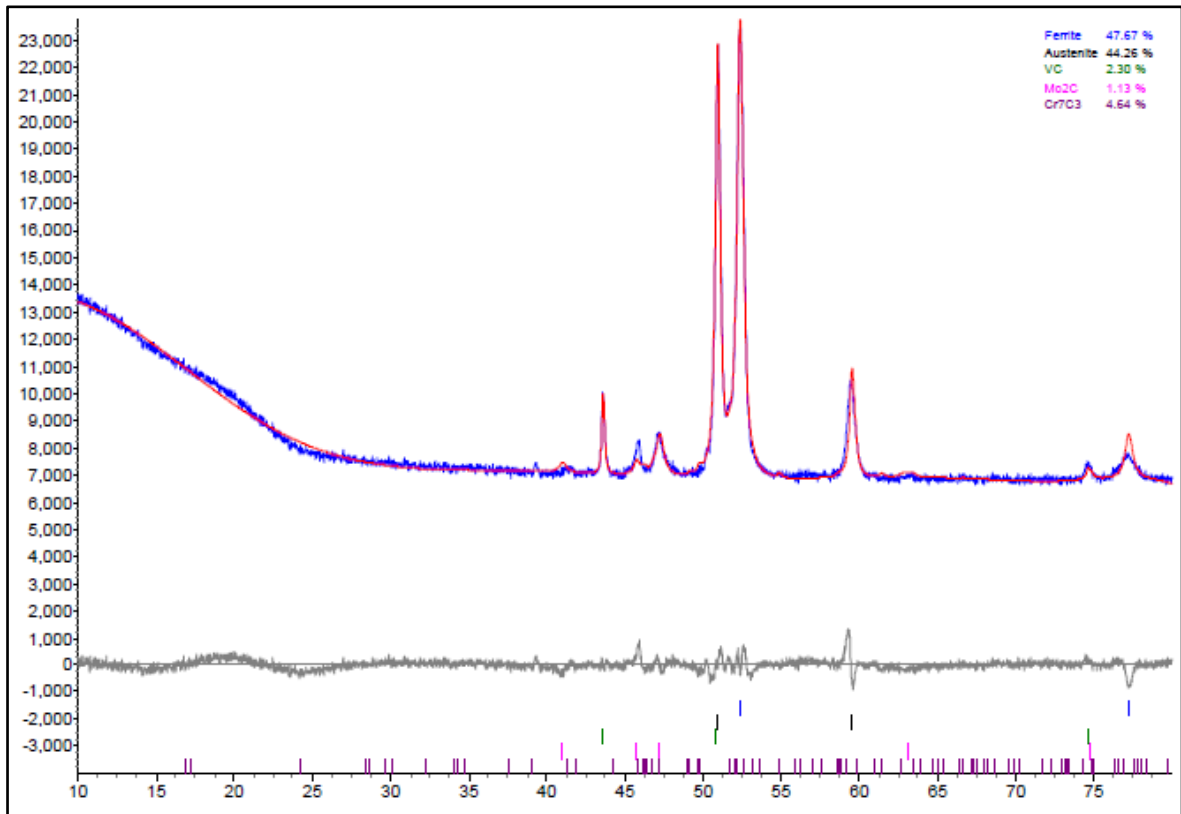Figure 4-120: XRD spectrum for sample AC3.
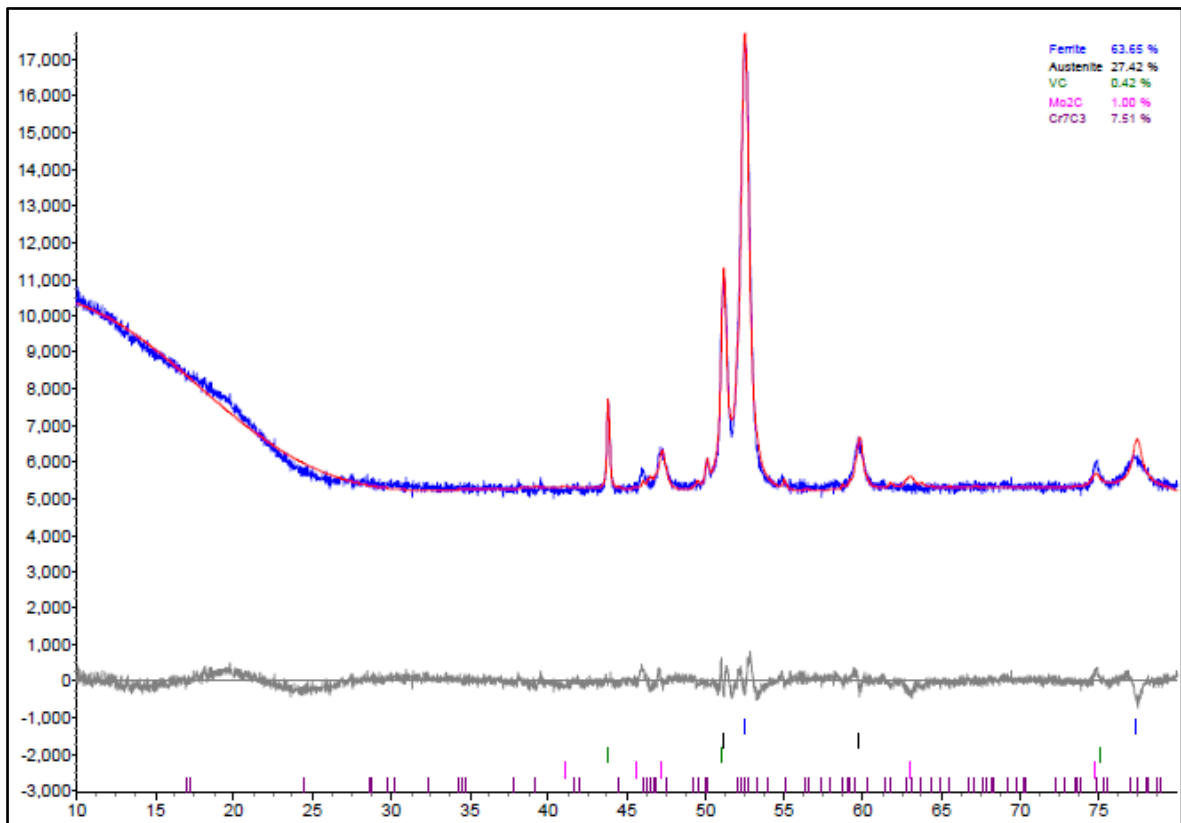
Figure 4-121: XRD spectrum for sample AC4.

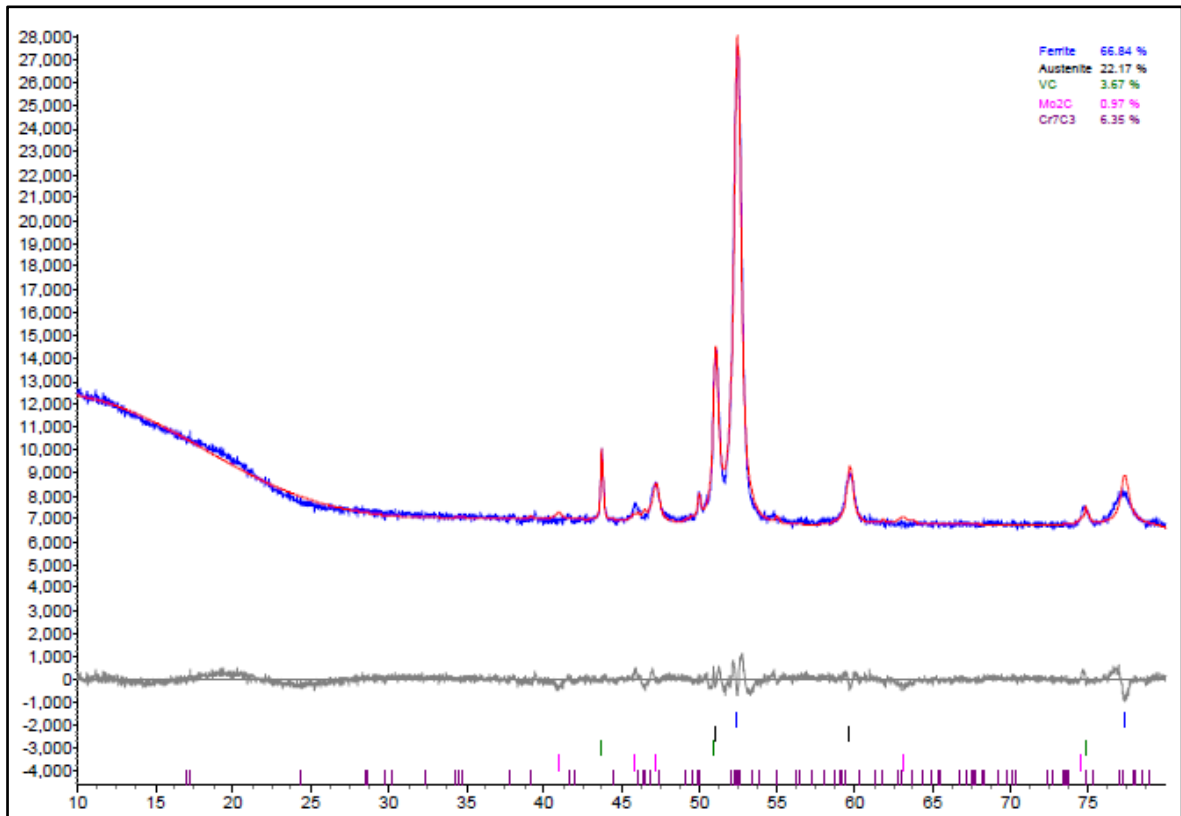Figure 4-122: XRD spectrum for sample T1-1.

145

Figure 4-123: XRD spectrum for sample T2-1.

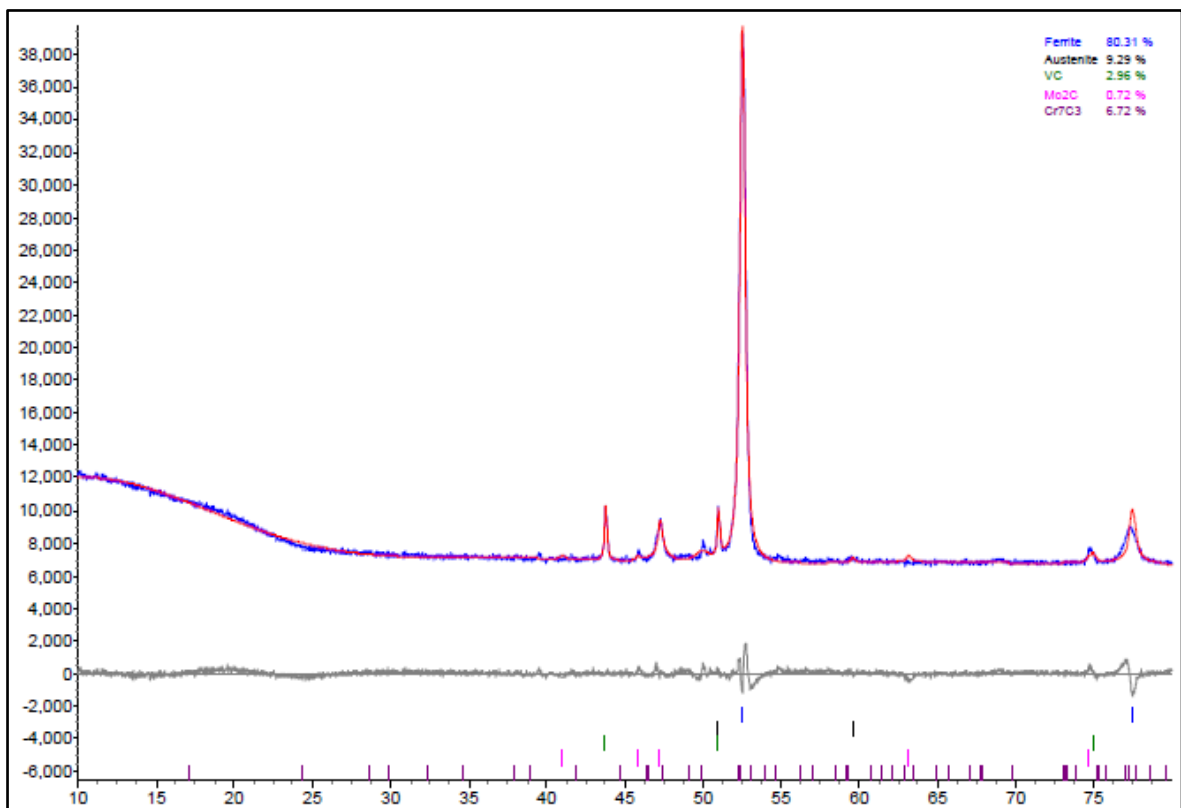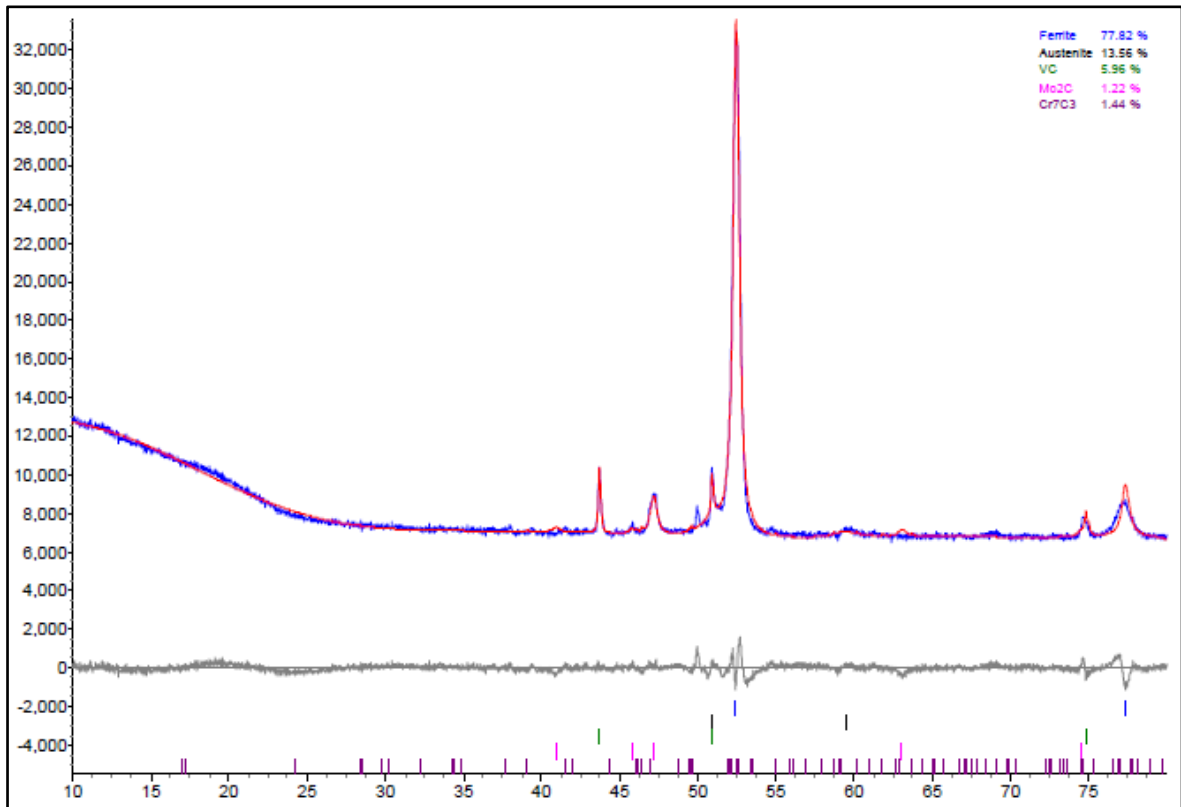Figure 4-124: XRD spectrum for sample T1-2.

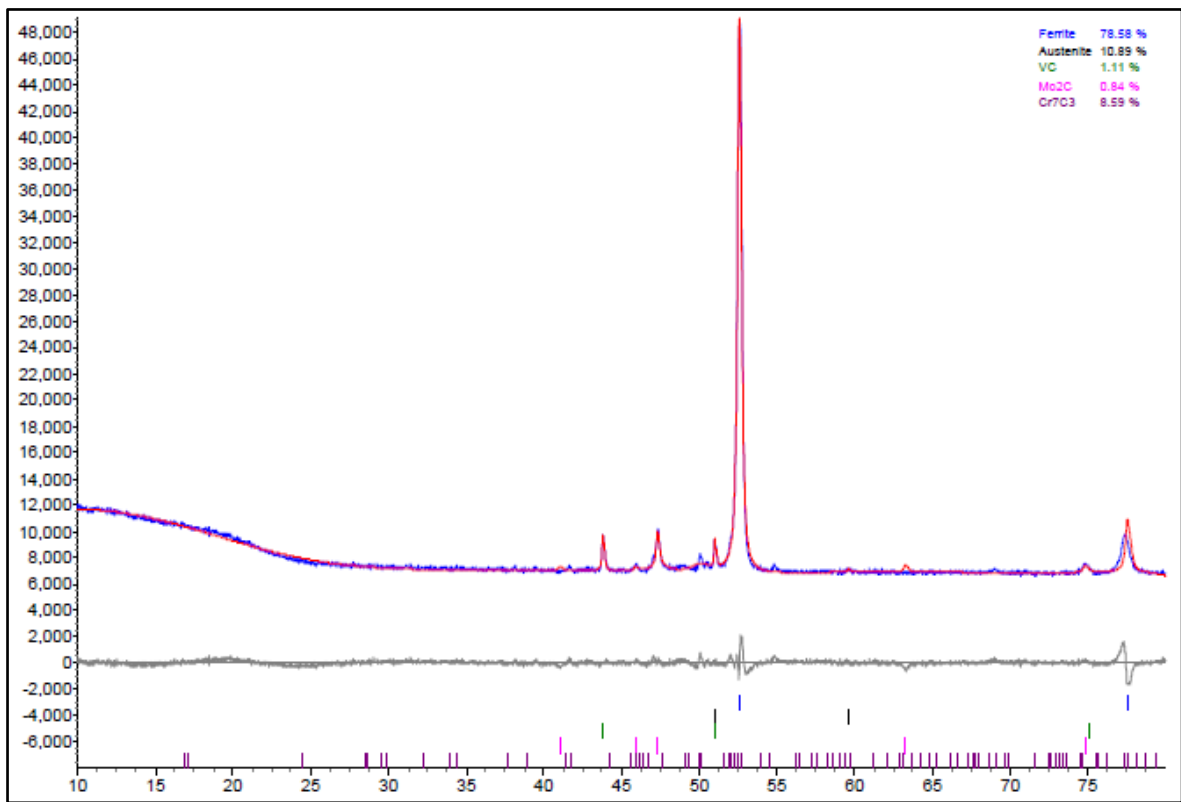146

Figure 4-125: XRD spectrum for sample T2-2.

Figure 4-126: XRD spectrum for sample T3.

147

4.2. Heat Treatment

4.2.1. Chemical Analysis

The chemical composition of the HSS material compared well with the optimal composition proposed in the literature and the benchmark samples [8], see Table 4-17. Due to proprietary reasons, generic composition ranges are given in Table 4-17 as the exact composition may not be reported. The composition of the HC roll was also determined.

Table 4-17: Spark emission spectrometry results.

Sample	C	V	Cr	Mo	W	Ni	Si	Mn
HC	1.5-3.0	0-2	10-20	0-3	0-1	0-3	0-2	0-2
HSS	1.0-2.5	1-7	1-8	1-5	1-5	0-3	0-2	0-2
HSS Optimal	1.9-2.0	4.0-6.0	5.0-7.0	3.0-4.0	3.0-4.0	0.7-0.9	-	-

4.2.2. Hardness Testing

The results from the hardness testing are detailed in Figures 4-127 to 4-129 and Tables 4-18 and 4-19. The average hardness values were calculated from at least 8 measurements. Figure 4-127 shows the summary of all the temper curves generated from the heat treatments. Figure 4-128 shows the combination of the laboratory and simulated heat treatment sample sets for HSS and HC (i.e. LT and ST).

The HSS material showed similar hardness profiles under both laboratory (LT) and simulated (ST) conditions. The peak hardness of the HSS material was recorded at 500°C as 744HV and 739HV for the LT and ST sets, respectively. The temperature of 500°C is slightly lower than for most HSS materials, but the hardness levels compare well [61]. The LT set also showed a more gradual decrease in hardness once peak hardness is achieved.

In contrast to the HSS, the HC material showed a significant difference in both peak hardness and the temperature at which peak hardness is achieved for the LT and ST sample sets. The tempering temperature at which peak hardness occurs decreased from 550°C for LT ($780HV_{50}$) to 475°C for ST ($657HV_{50}$).

The trend suggests that the peak hardness is reduced with increasing tempering time, while also reducing the temperature at which peak hardness occurs. It should also be noted that the HC hardness was slightly higher than that of the HSS under LT

148

conditions, while being significantly lower under ST conditions. In addition the peak hardness for the HC material occurred at a higher temperature than that for the HSS under laboratory conditions (550°C for HC and 500°C for HSS), while occurring at a lower temperature under simulated conditions (475°C for HC and 500°C for HSS).

Table 4-18: Heat treatment hardness testing results for the HC material.

Sample	Hardness (HV_{50})			Statistical Analysis			
	Minimum	Maximum	Average	S	CV	95%CL	RA
Reference 1	502	546	527	16.4	3.1%	14.6	2.8%
LT0	694	722	709	9.6	1.4%	8.6	1.2%
LT48	598	627	618	10.0	1.6%	8.9	1.4%
LT50	651	673	660	7.6	1.2%	6.8	1.0%
LT53	742	769	754	7.8	1.0%	6.9	0.9%
LT55	769	785	780	6.0	0.8%	5.4	0.7%
LT58	666	686	677	6.5	1.0%	5.9	0.9%
LT60	560	577	568	7.1	1.2%	6.3	1.1%
ST0	644	678	664	12.3	1.9%	11.0	1.7%
ST45	600	639	614	12.1	2.0%	10.8	1.8%
ST48	644	668	657	8.9	1.4%	8.0	1.2%
ST50	616	673	642	21.0	3.3%	18.8	2.9%
ST53	539	571	553	11.7	2.1%	10.5	1.9%
ST55	480	516	498	11.9	2.4%	10.7	2.1%
ST58	428	449	436	6.6	1.5%	5.9	1.3%
ST60	397	414	404	5.9	1.5%	5.3	1.3%

Figure 4-129 shows the combination of the laboratory and simulated sample sets with pre-annealing (LA and SA) and without pre-annealing (LT and ST). The pre-annealing increased the peak hardness from $744HV_{50}$ to $798HV_{50}$ under laboratory conditions (LT and LA), while also increasing the temperature of the peak hardness from 500°C to 525°C. The pre-annealing also appeared to yield a more gradual decrease in hardness once over the peak hardness. Hence, the pre-annealing did yield an increase in bulk hardness under laboratory conditions as expected from the indications noted in the literature [11]. The higher hardness is expected to yield improved wear resistance and superior performance in service.

Table 4-19: Heat treatment hardness testing results for the HSS material.

Sample	Hardness (HV$_{50}$)			Statistics			
	Minimum	Maximum	Average	S	CV	95%CL	RA
Reference 1	639	666	656	8.5	1.3%	7.6	1.2%
Reference 3	646	676	656	9.5	1.4%	8.4	1.3%
LT0	716	739	725	8.0	1.1%	7.1	1.0%
LT45	694	719	703	9.7	1.4%	8.7	1.2%
LT48	708	748	722	15.4	2.1%	13.8	1.9%
LT50	724	766	744	15.8	2.1%	14.1	1.9%
LT53	661	697	676	12.4	1.8%	11.1	1.6%
LT55	614	676	643	22.6	3.5%	20.2	3.1%
LT58	611	639	622	10.6	1.7%	9.5	1.5%
ST0	713	795	757	29.4	3.9%	26.2	3.5%
ST43	691	710	705	6.1	0.9%	5.5	0.8%
ST45	708	727	716	5.7	0.8%	5.1	0.7%
ST48	671	745	721	25.9	3.6%	23.1	3.2%
ST50	730	757	739	8.8	1.2%	7.9	1.1%
ST53	571	611	594	15.6	2.6%	14.0	2.4%
ST55	575	592	585	6.6	1.1%	5.9	1.0%
LA85	719	751	735	12.0	1.6%	10.7	1.5%
LA55	705	742	725	11.9	1.6%	10.6	1.5%
LA85T0	760	785	774	8.4	1.1%	7.5	1.0%
LA85T48	719	754	741	12.9	1.7%	11.5	1.5%
LA85T50	754	785	772	10.4	1.3%	9.3	1.2%
LA85T53	788	808	798	8.0	1.0%	7.1	0.9%
LA85T55	772	801	785	10.1	1.3%	9.1	1.2%
LA85T58	739	798	764	20.2	2.6%	18.1	2.4%
LA85T60	719	769	742	15.3	2.1%	13.7	1.8%
LA85T63	560	575	567	4.8	0.8%	4.3	0.8%
SA85T0	751	775	761	10.4	1.4%	9.3	1.2%
SA85T40	694	705	699	3.7	0.5%	3.3	0.5%
SA85T43	724	748	737	9.0	1.2%	8.1	1.1%
SA85T45	713	760	739	15.4	2.1%	13.8	1.9%
SA85T48	733	760	745	8.1	1.1%	7.2	1.0%
SA85T50	611	668	638	21.2	3.3%	18.9	3.0%
SA85T53	575	673	636	31.0	4.9%	27.7	4.3%
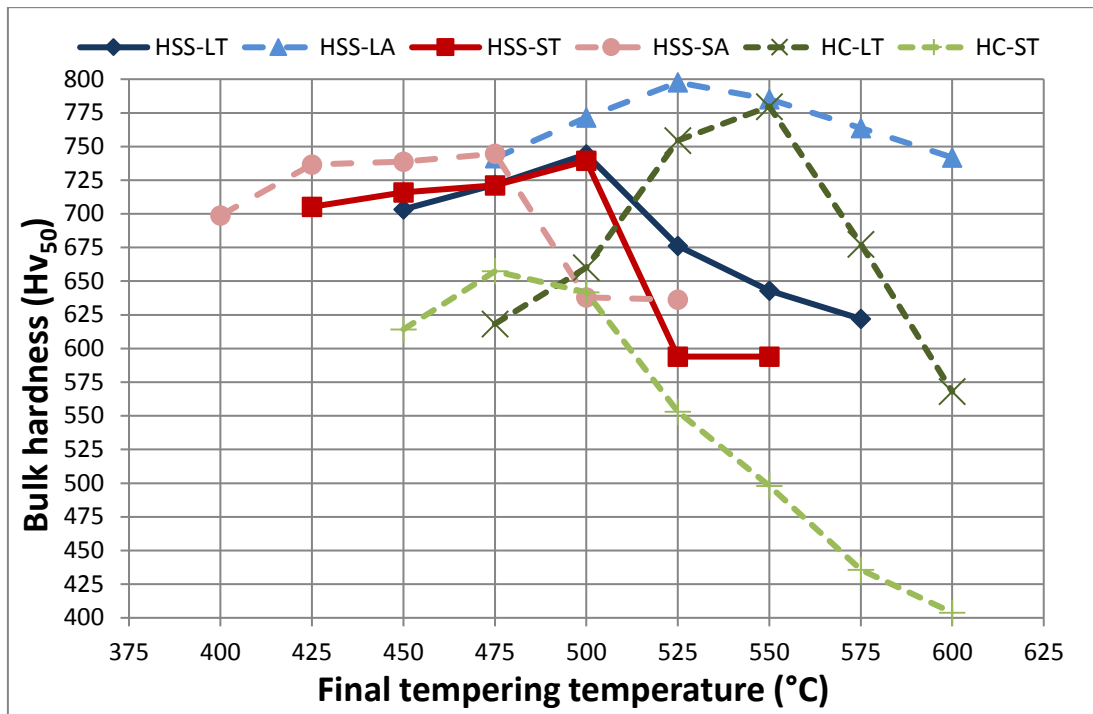
Figure 4-127: Tempering curves for all heat treatments.

The pre-annealing showed no significant increase in the peak hardness under simulated conditions (ST and SA). In contrast to the laboratory conditions, the temperature at the peak hardness was reduced from 500°C to 475°C by pre-annealing. Both ST and SA sample sets showed a significantly more abrupt decrease in hardness over peak hardness compared to the LT and LA sample sets. However, the degree in hardness reduction was more severe for the ST sample set compared to that for the SA sample set. The standard deviation, coefficient of variance and relative accuracy values were acceptable indicating sufficient accuracy and repeatability.
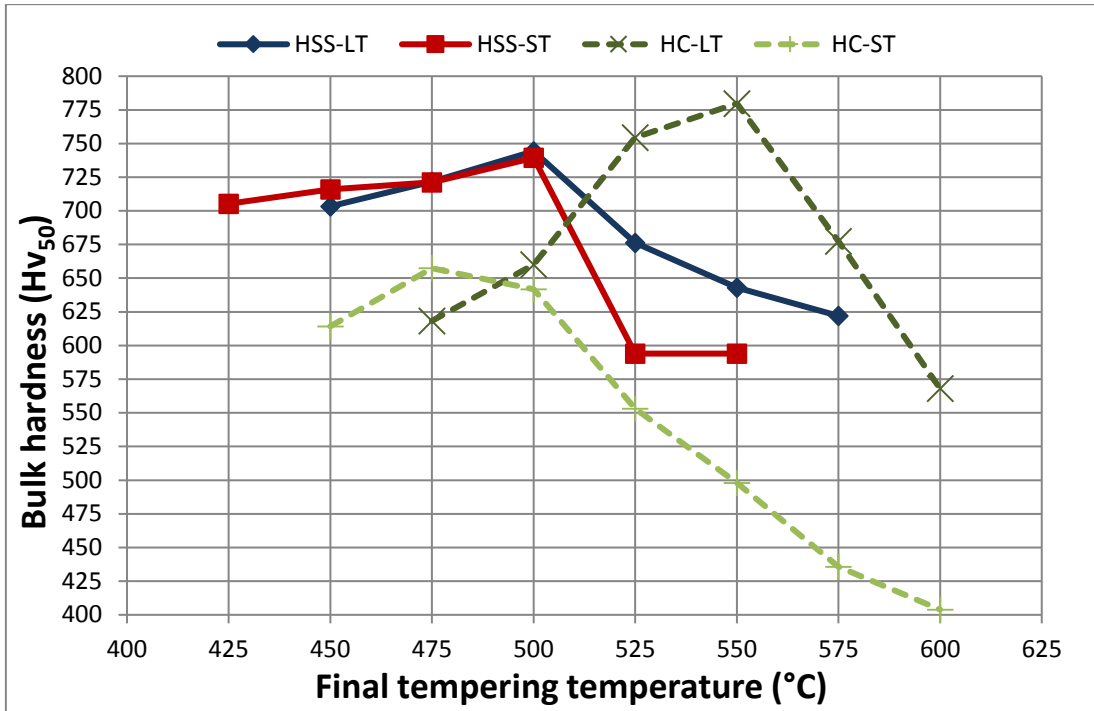
Figure 4-128: Tempering curves showing the effect of tempering time.
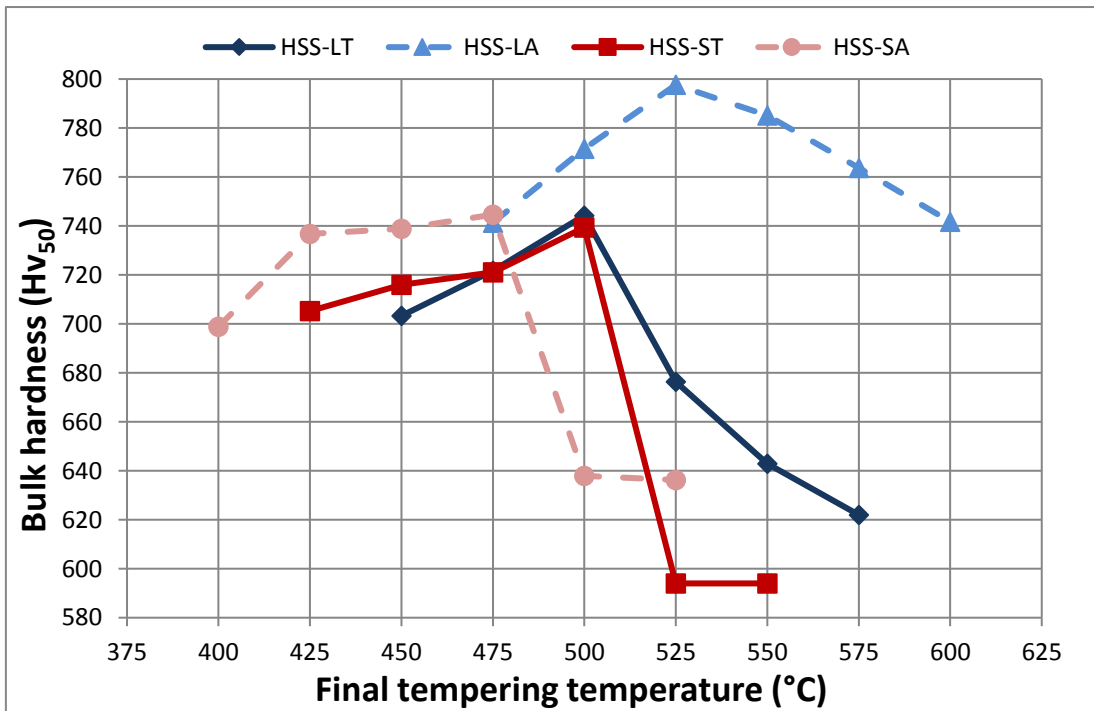
Figure 4-129: Tempering curves showing the effect of pre-annealing.

152

4.2.3. Metallography

4.2.3.1. Nital Etch

The general microstructure of all the laboratory HC austenitised and tempered samples, as revealed with 5% Nital, consisted of networks of carbides located in a matrix consisting of martensite and retained austenite. The retained austenite content varied with the degree of tempering, which decreased with increasing tempering temperature, see Figures 4-130 to 4-134. Fine secondary carbides were observed within the matrix, but could only be clearly identified once the retained austenite had been largely eliminated. The peak hardness of the LT samples appeared to be achieved once the majority of the retained austenite had been eliminated.

Figure 4-130: HC sample Reference1 etched with Nital.
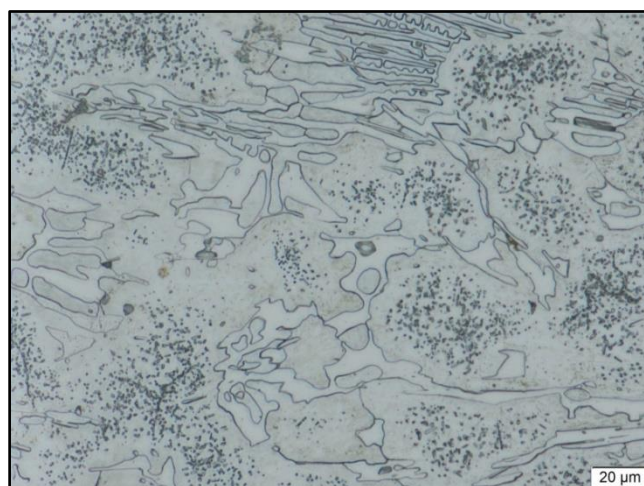
Figure 4-131: HC sample LT0 etched with Nital.

153
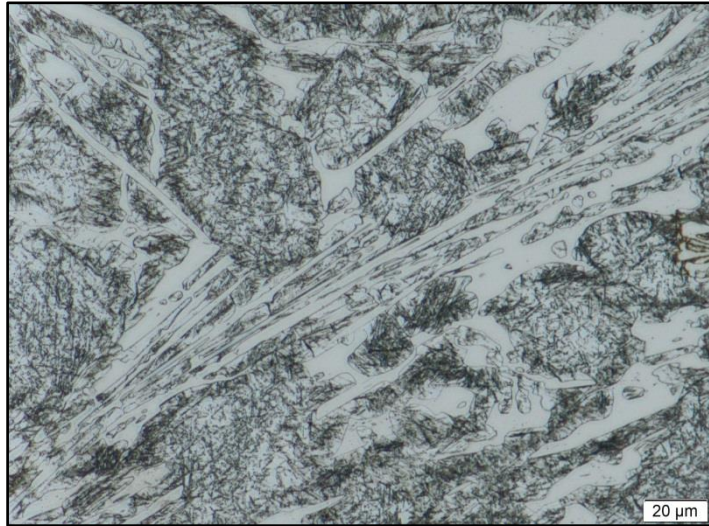
Figure 4-132: HC sample LT48 etched with Nital.
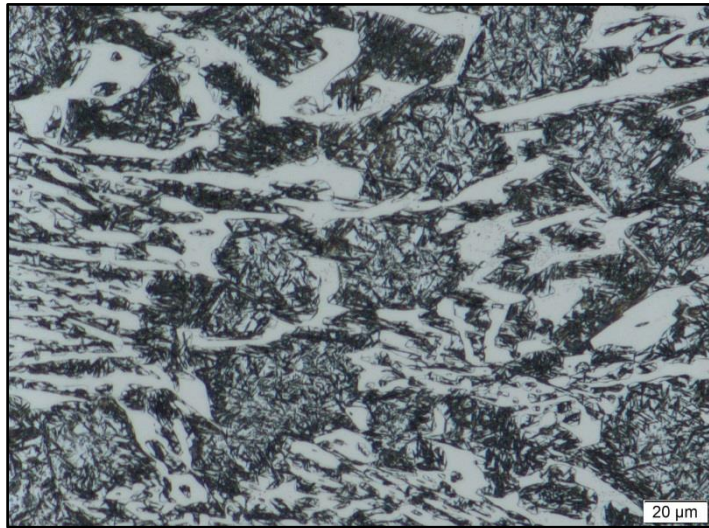
Figure 4-133: HC sample LT55 etched with Nital.
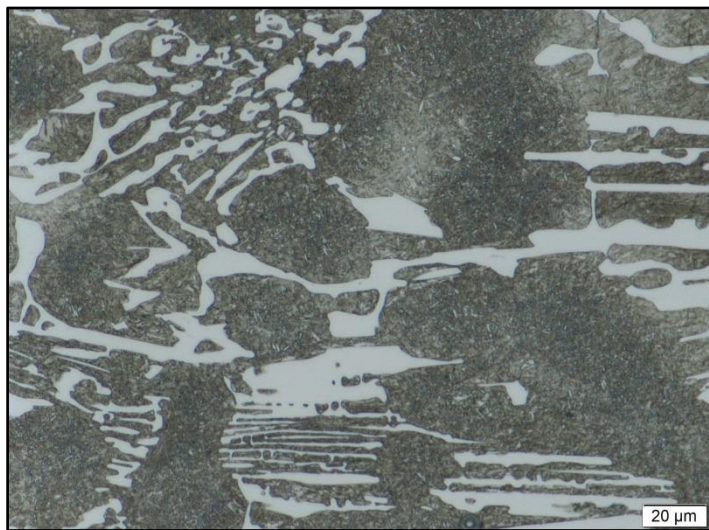
Figure 4-134: HC sample LT60 etched with Nital.

154

The general microstructure of all the HSS samples, as revealed with 5% Nital, consisted of networks of carbides located in a matrix consisting predominantly of plate martensite and retained austenite, see Figures 4-135 to 4-144. Unlike the benchmarked samples, the HSS reference material showed no pearlite. The retained austenite content varied depending on the degree of tempering. Isolated globular primary carbides were present within the interior of the matrix cells. Fine secondary carbides were observed within the matrix. The secondary carbides appeared to coarsen with increasing tempering temperature, but could not be clearly identified due to the lack of etching on some of the samples. The untempered samples LT0, ST0, LA85, LA85 and SA85T0 showed a general lack of etching compared to the tempered material, which was assumed to be related to higher levels of retained austenite, see Figure 4-142.
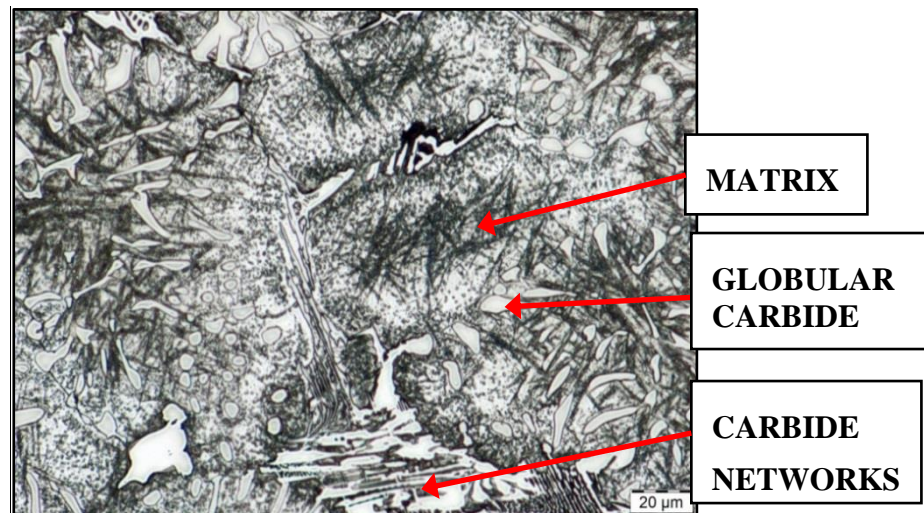
Figure 4-135: HSS sample Reference1 etched with Nital.
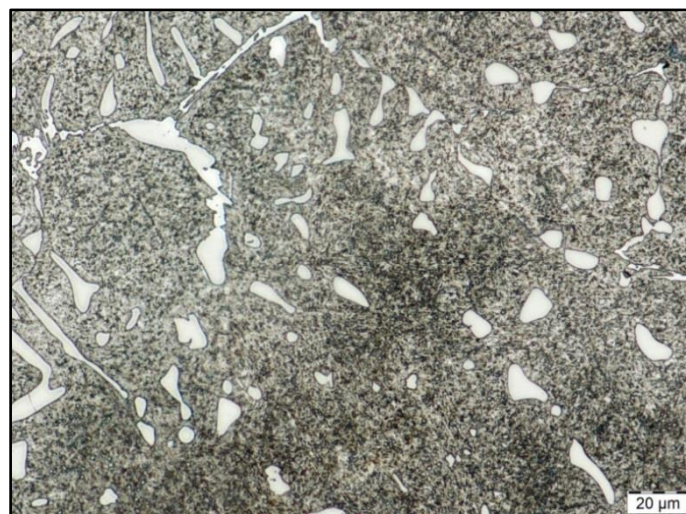
Figure 4-136: HSS sample LT45 etched with Nital.

155
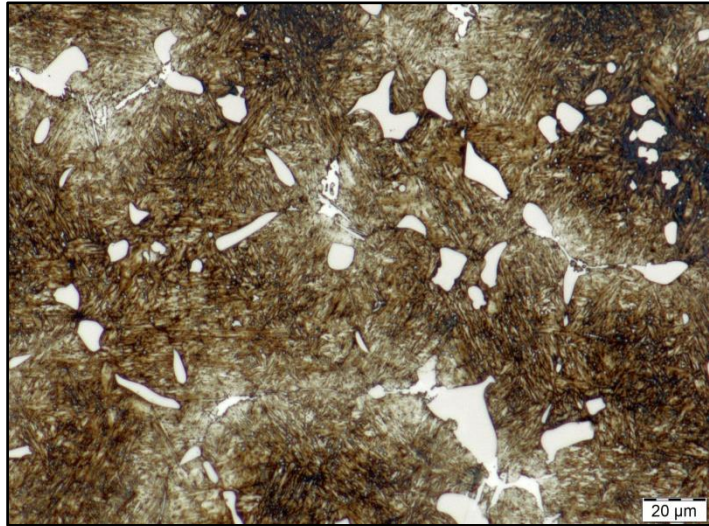
Figure 4-137: HSS sample LT58 etched with Nital.
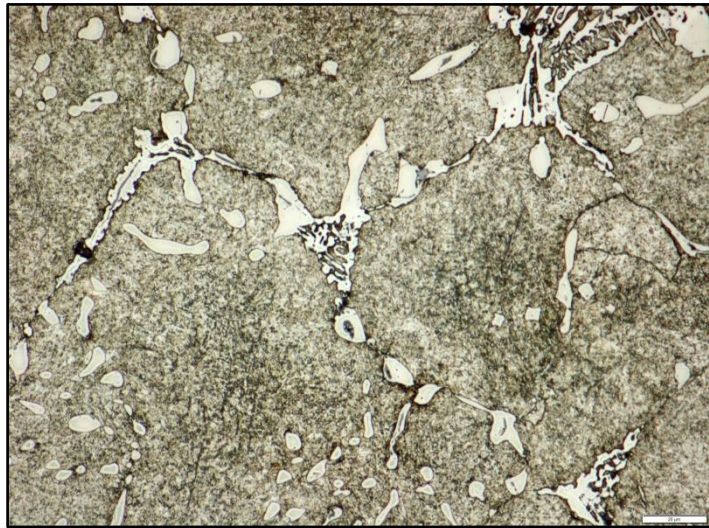
Figure 4-138: HSS sample ST43 etched with Nital.
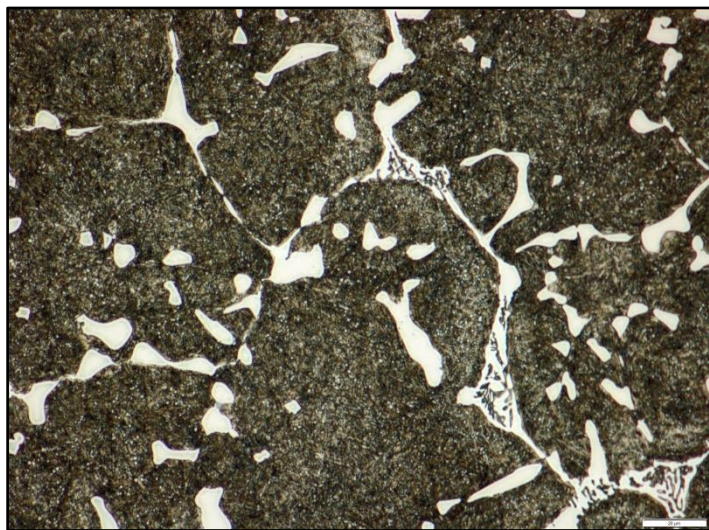
Figure 4-139: HSS sample ST55 etched with Nital.

156
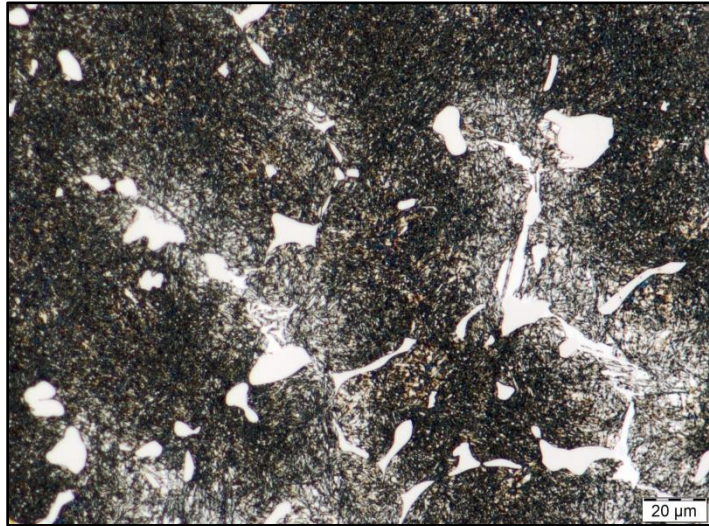
Figure 4-140: HSS sample LA48 etched with Nital.

Figure 4-141: HSS sample LA60 etched with Nital.
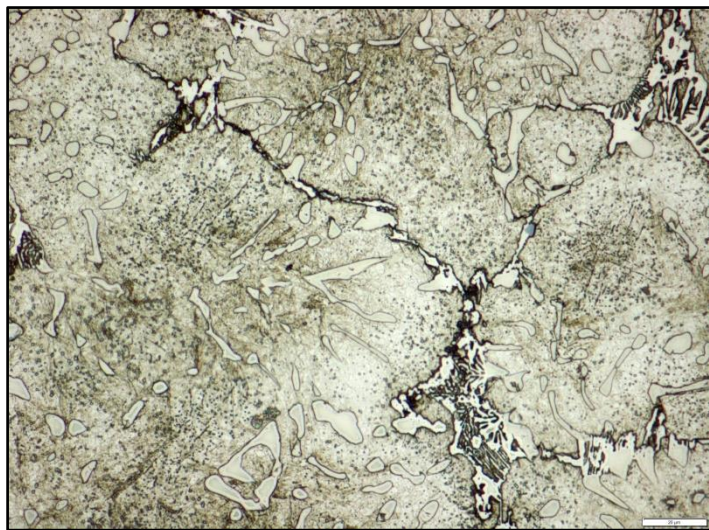
Figure 4-142: HSS sample SA85T0 etched with Nital.

157
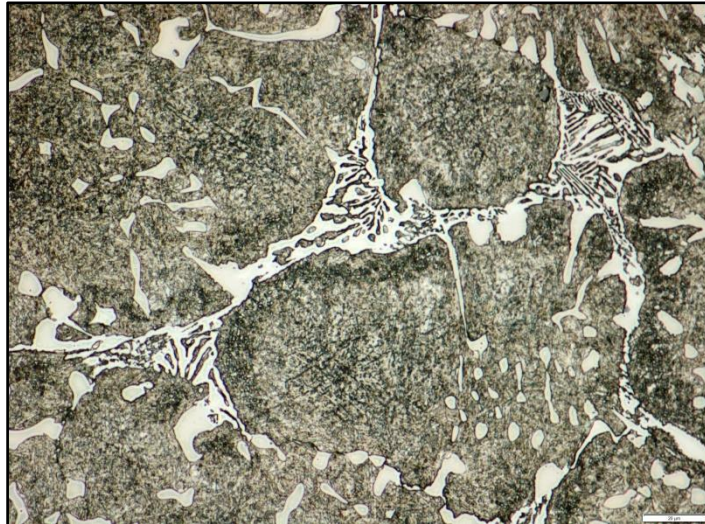
Figure 4-143: HSS sample SA85T40 etched with Nital.

Figure 4-144: HSS sample SA85T53 etched with Nital.

Image analysis to measure the volume fraction of the primary carbides could not be performed due to the lack of contrast associated with the RA.

4.2.3.2. Groesbeck's etchant

Groesbeck's etchant selectively etched the primary carbides of the HC samples, see Figures 4-145 to 4-151. The etchant confirmed that the primary carbides are of the M_7C_3 type. Groesbeck's etchant did identify minor amounts of M_6C primary carbides. Groesbeck's etchant outlined and etched the M_7C_3 carbides on the as-cast samples, with the colour ranging from brown/orange to green. Significant variation in the secondary carbide size and volume fraction was not apparent between the LT0 sample and the tempered samples up to peak hardness at 550°C (LT55). A notable increase

158

in carbide size and associated volume fraction was evident, however, once the peak hardness was exceeded at 575°C (LT58).

No secondary carbides were observed in the as-cast material (Reference 1) or any of the simulated samples (ST). This suggests that the secondary carbides associated with these samples may be of the $M_{23}C_6$ type and that the secondary carbides identified on the LT samples are of the M_7C_3 type [74].
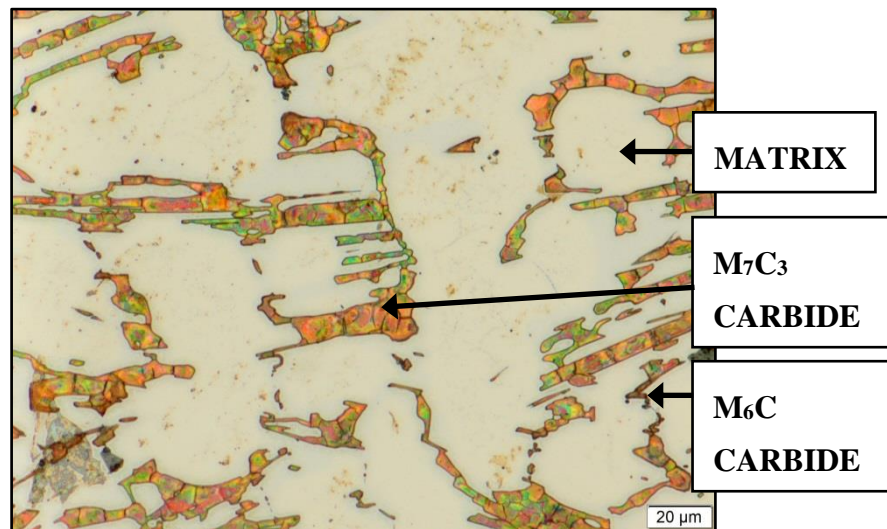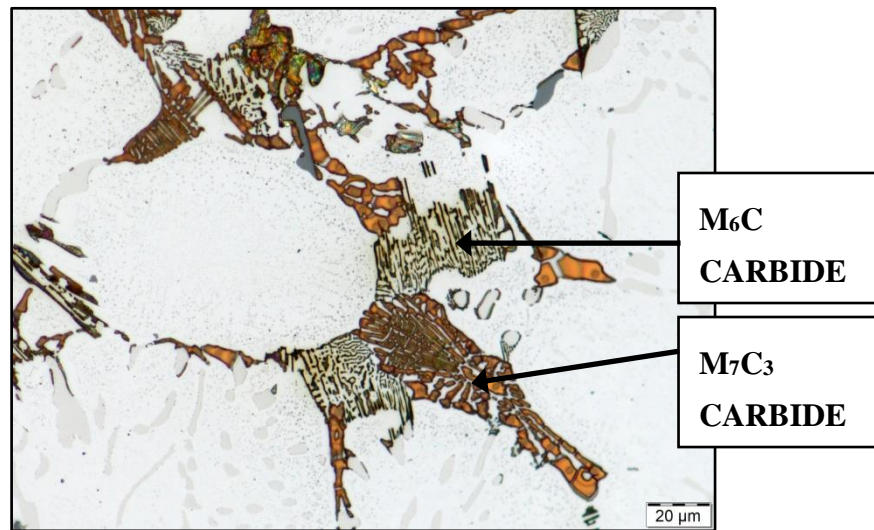

Figure 4-145: HC sample Reference1 etched with Groesbeck's etchant.
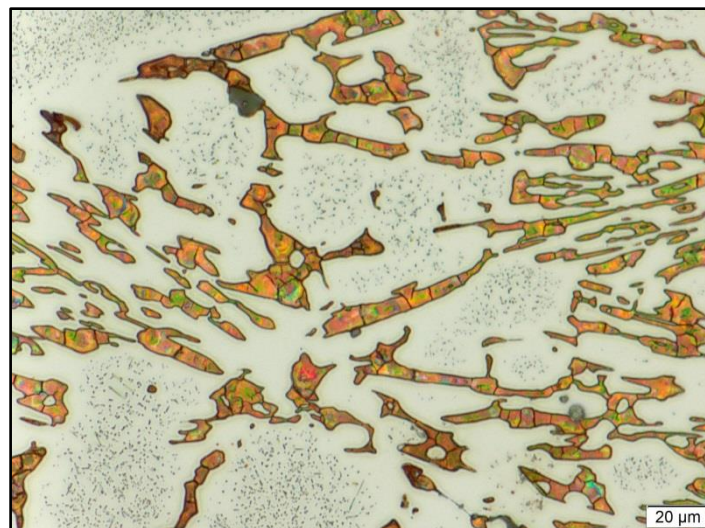
Figure 4-146: HC sample LT0 etched with Groesbeck's etchant.

159
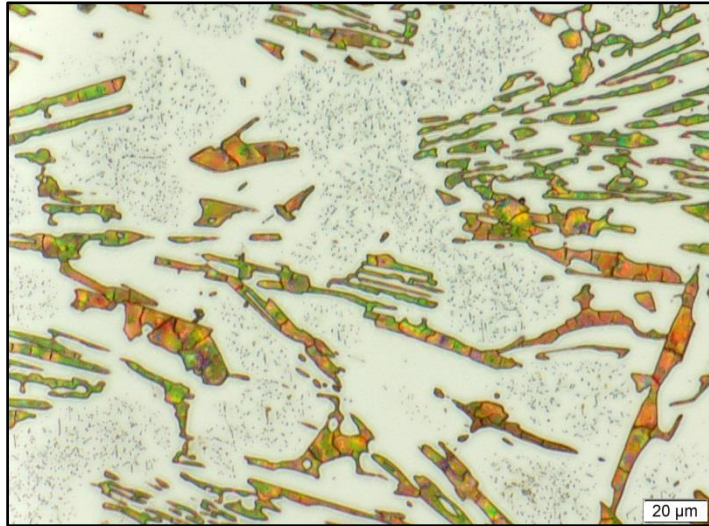
Figure 4-147: HC sample LT48 etched with Groesbeck's etchant.

SECONDARY
CARBIDE
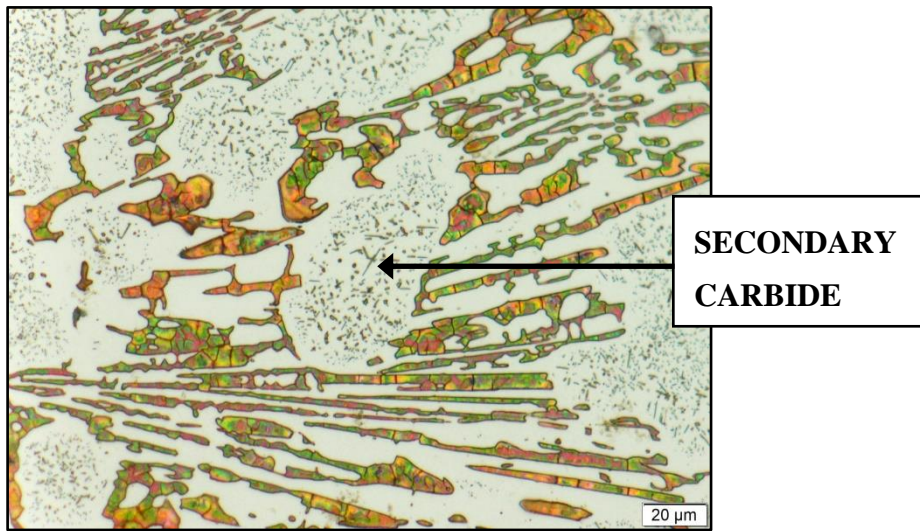
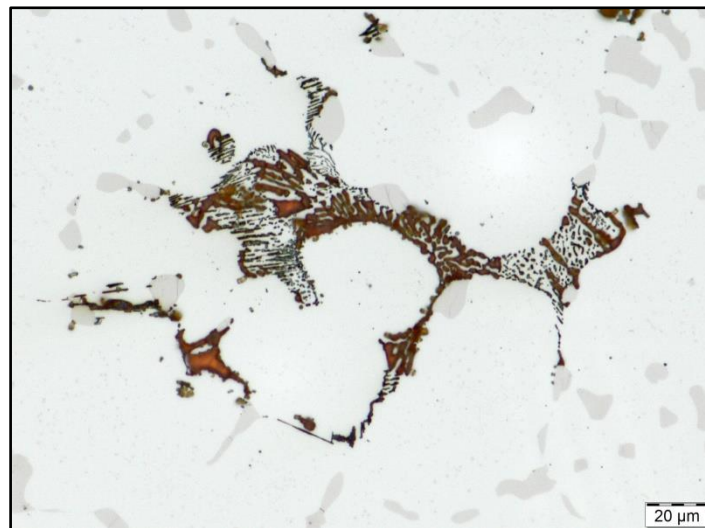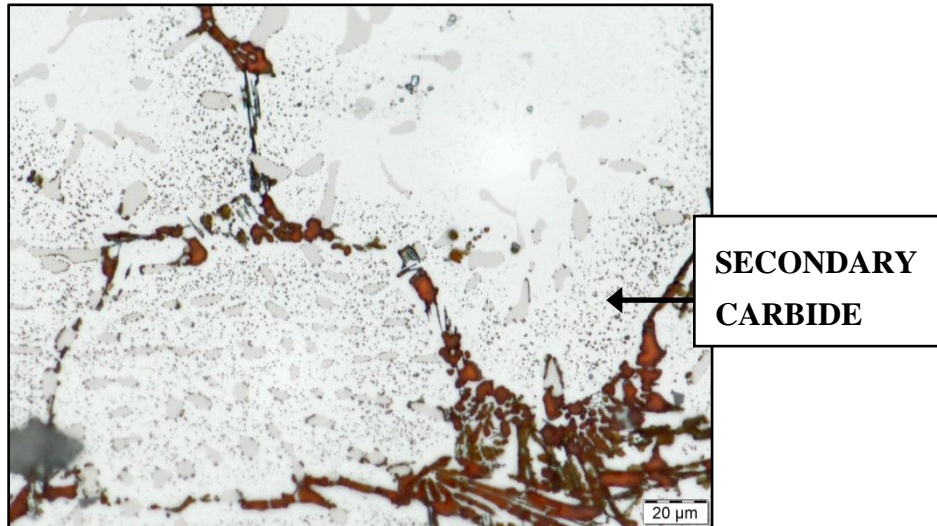Figure 4-148: HC sample LT60 etched with Groesbeck's etchant.
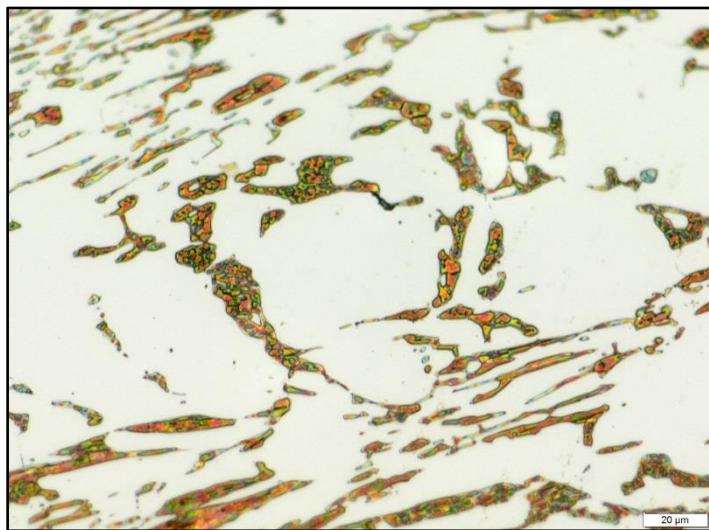
Figure 4-149: HC sample ST0 etched with Groesbeck's etchant.

160
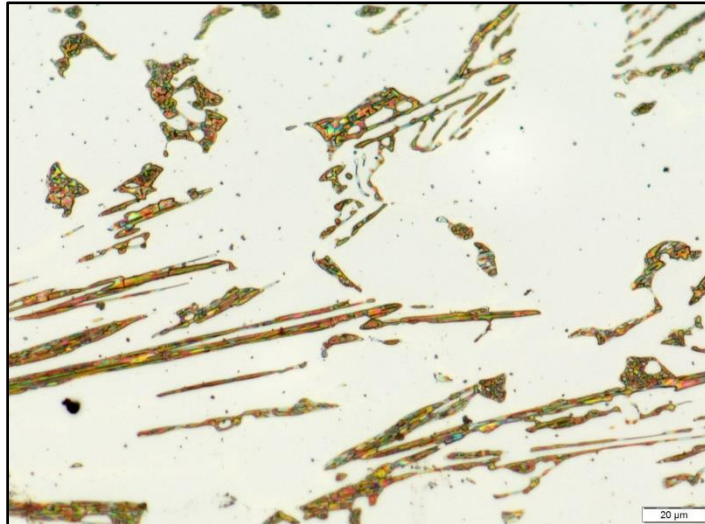
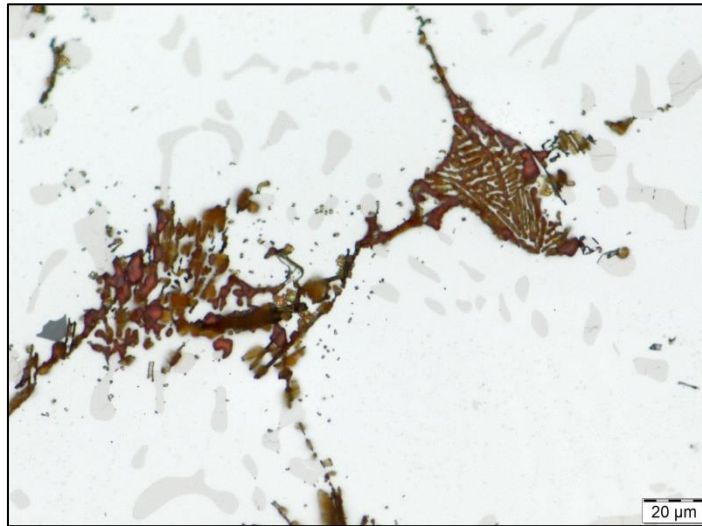Figure 4-150: HC sample ST45 etched with Groesbeck's etchant.
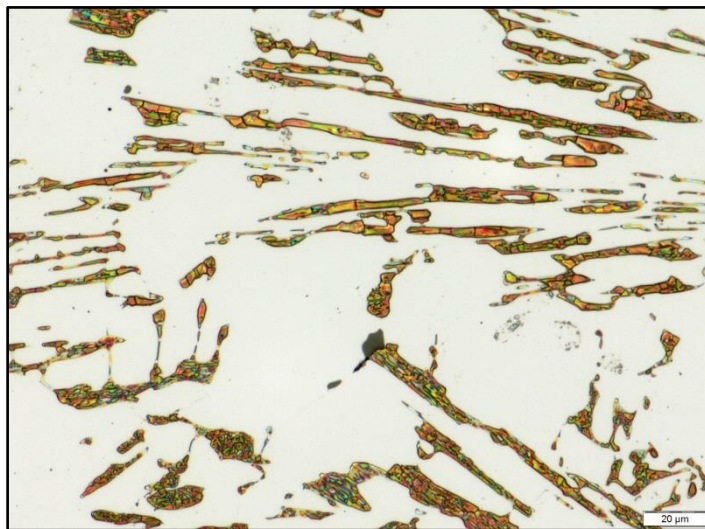
Figure 4-151: HC sample ST60 etched with Groesbeck's etchant.

Groesbeck's etchant selectively etched some of the primary carbides of the HSS material, see Figures 4-152 to 4-166. The etchant identified three distinct carbides. The most abundant showed a coarse fish bone structure and was located in the interdendritic areas, which was assumed to consist of M_7C_3 carbides. The M_7C_3 carbides ranged in colour from orange to light brown. The second carbide type etched dark brown and showed a thinner fish bone structure and was located at the interdendritic areas, which was assumed to be either M_2C or M_6C carbides. Groesbeck's etchant had no clear effect on globular, isolated carbides which were located both at the interdendritic regions and interiors of the dendrites, which was assumed to be MC carbides. The third carbide type occurred as fine secondary

161

carbides associated with the primary carbides at the interdendritic regions, similar to the benchmarked samples.

Figure 4-152: HSS sample Reference 1 etched with Groesbeck's etchant.

Figure 4-153: HSS sample LT0 etched with Groesbeck's etchant.

162

Figure 4-154: HSS sample LT45 etched with Groesbeck's etchant.

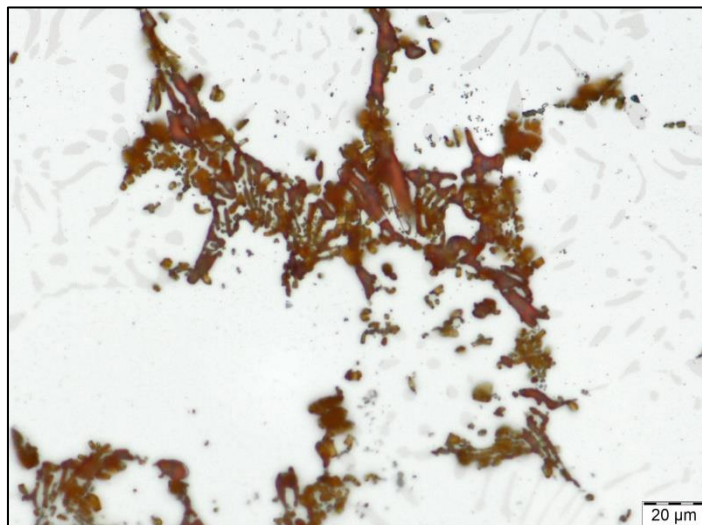Figure 4-155: HSS sample LT58 etched with Groesbeck's etchant.

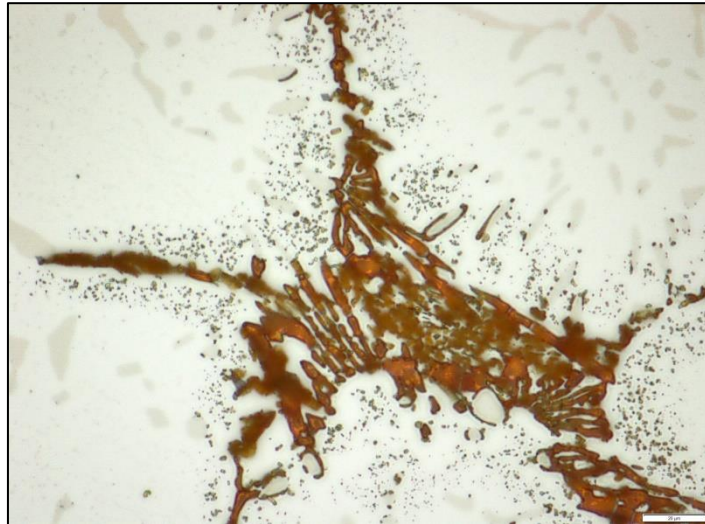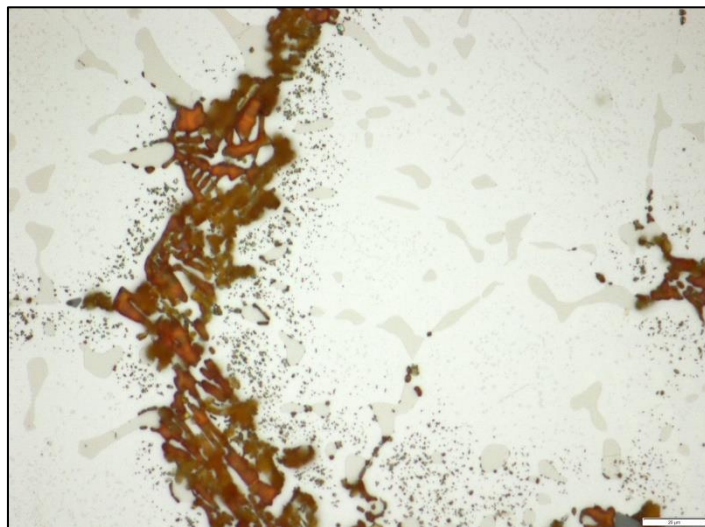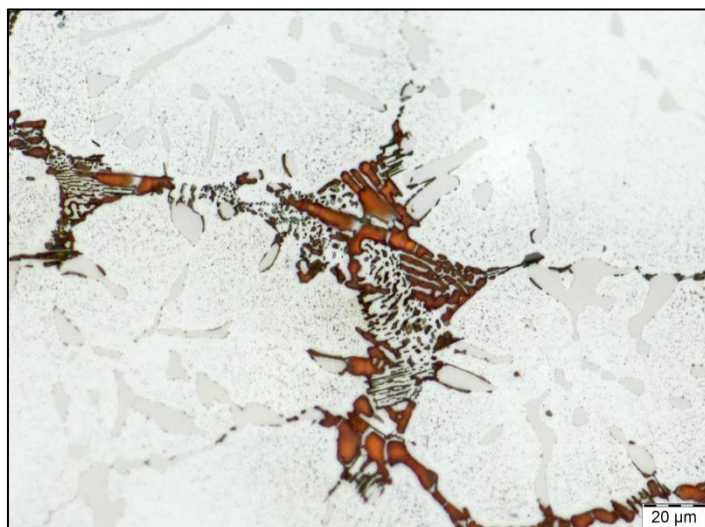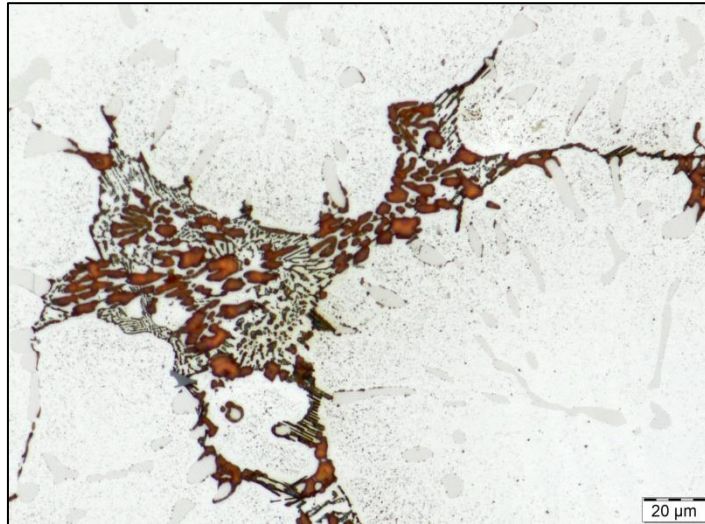Figure 4-156: HSS sample ST0 etched with Groesbeck's etchant.

163

Figure 4-157: HSS sample ST43 etched with Groesbeck's etchant.

Figure 4-158: HSS sample ST55 etched with Groesbeck's etchant.

Figure 4-159: HSS sample LA85 etched with Groesbeck's etchant.

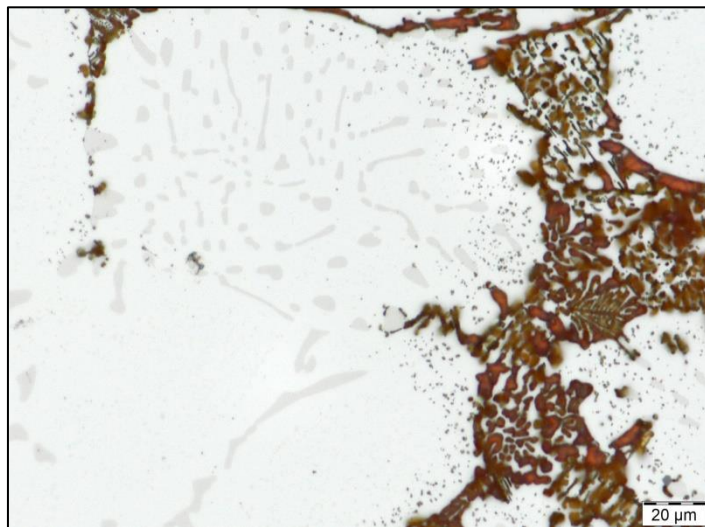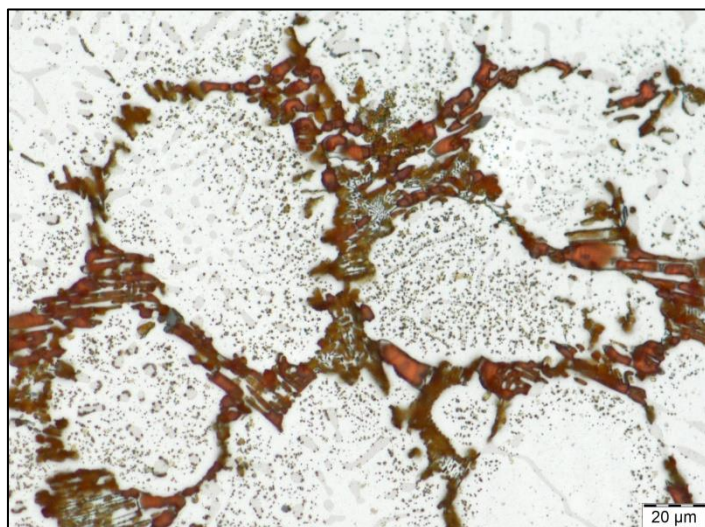Figure 4-160: HSS sample LA55 etched with Groesbeck's etchant.

Figure 4-161: HSS sample LA85T0 etched with Groesbeck's etchant.

Figure 4-162: HSS sample LA85T48 etched with Groesbeck's etchant.
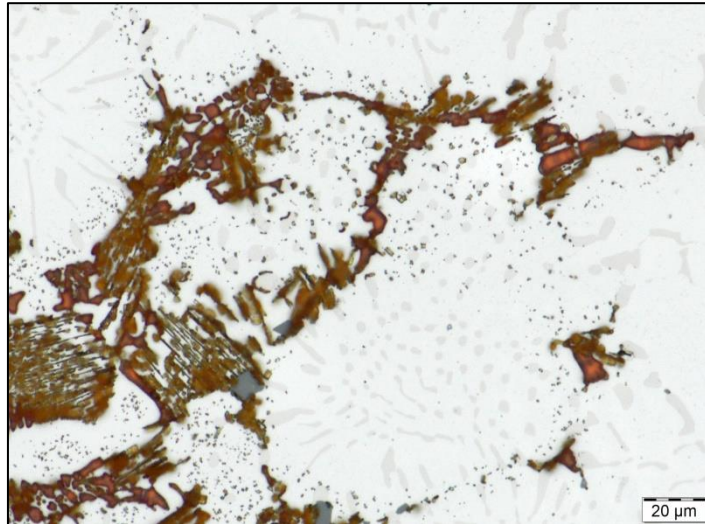
165

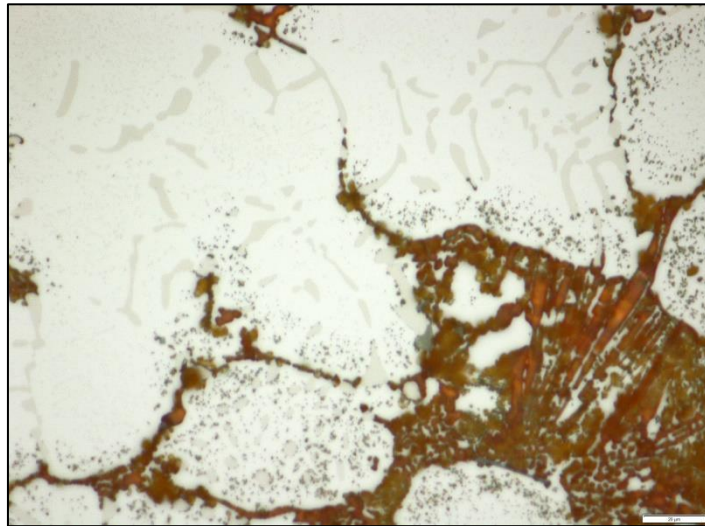Figure 4-163: HSS sample LA85T60 etched with Groesbeck's etchant.

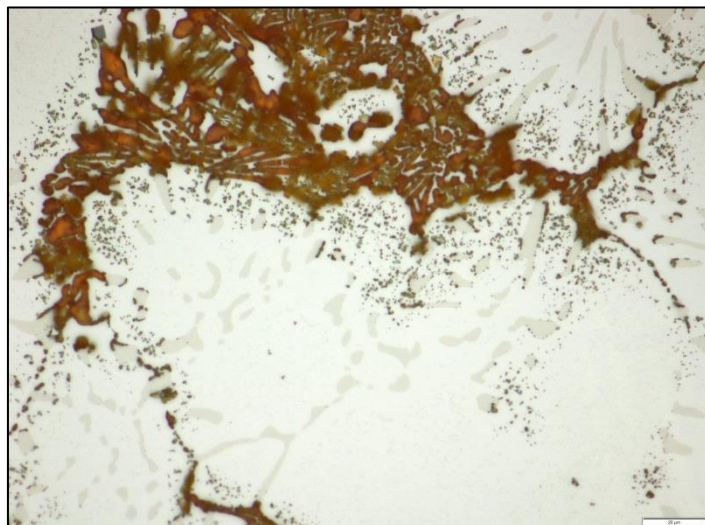Figure 4-164: HSS sample SA85T0 etched with Groesbeck's etchant.

Figure 4-165: HSS sample SA85T40 etched with Groesbeck's etchant.
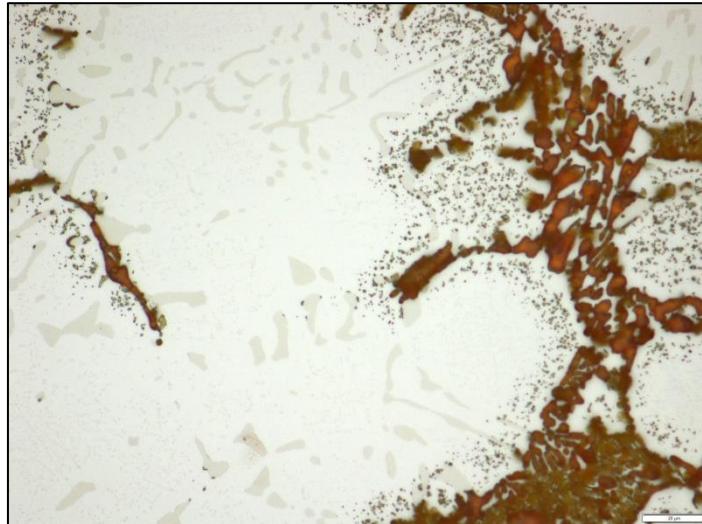
166

Figure 4-166: HSS sample SA85T53 etched with Groesbeck's etchant.

4.2.3.3.   Murakami's Etchant

Murakami's etchant showed similar results to that of Groesbeck's etchant for the HC material as expected, see Figures 4-167 to 4-170. Murakami's etchant outlined and etched the M_7C_3 carbides with the colour ranging from orange to brown.
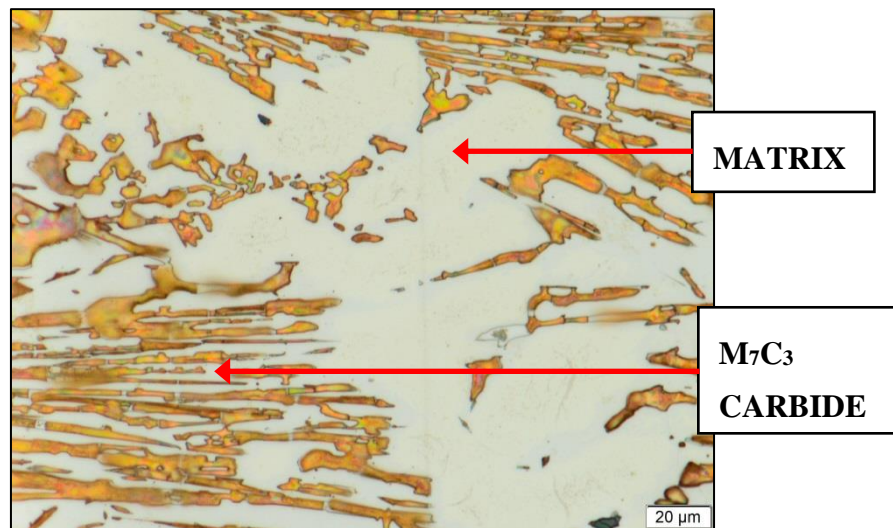

Figure 4-167: HC sample Reference 1 etched with Murakami's.
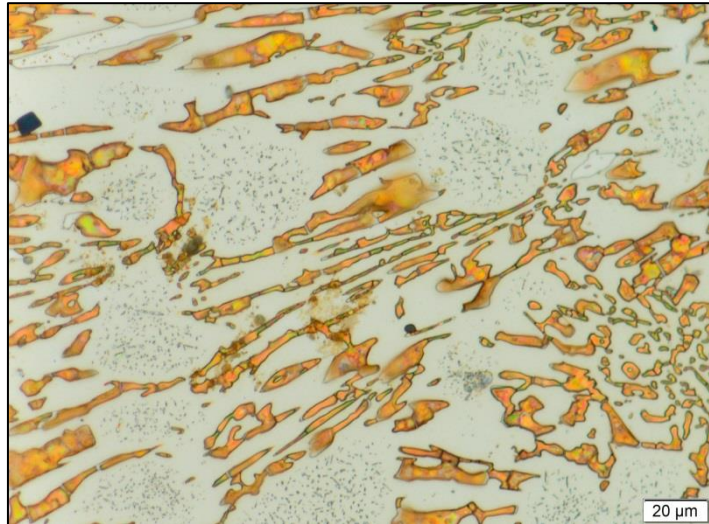
167

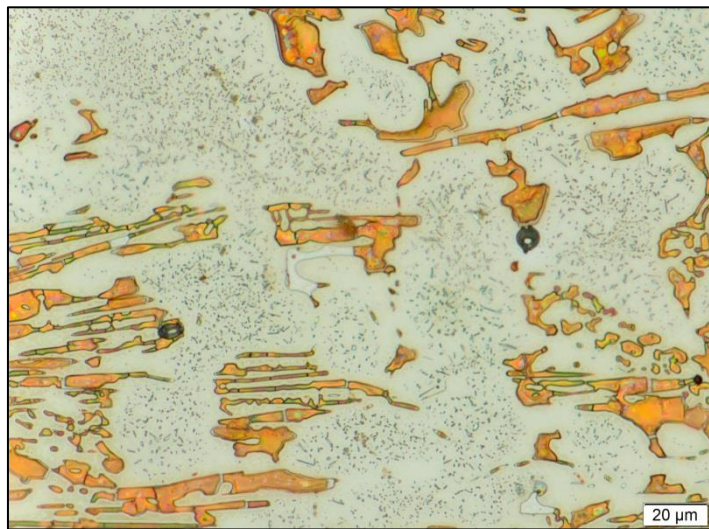Figure 4-168: HC sample LT0 etched with Murakami's etchant.

Figure 4-169: HC sample LT48 etched with Murakami's etchant.

Figure 4-170: HC sample LT58 etched with Murakami's etchant.

168

4.2.3.4. Combined Groesbeck and Murakami

The combination of Groesbeck with Murakami's etchant was utilised to merely confirm the secondary carbides are of the $M_{23}C_6$ type similar to the benchmarked samples, see Figures 4-171 to 4-185 [74]. Murakami's etchant also had no clear effect on the MC carbides, but did have a faint effect on the secondary carbides which are randomly distributed within the matrix.
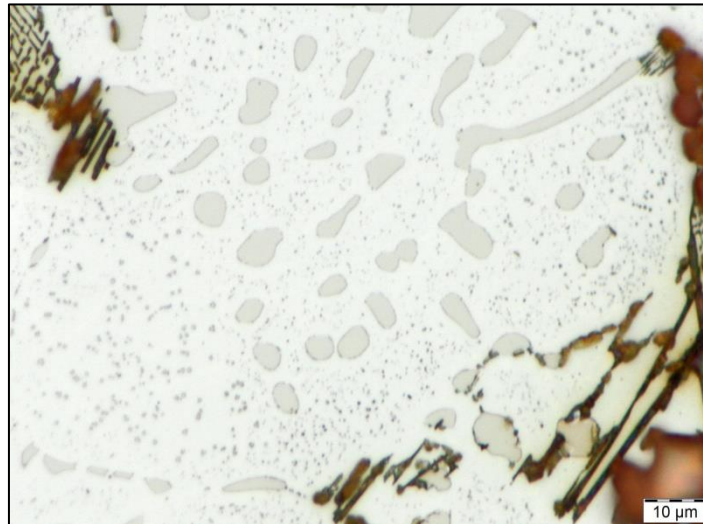

Figure 4-171: HSS sample Reference 1 etched with Groesbeck and Murakami's etchant.
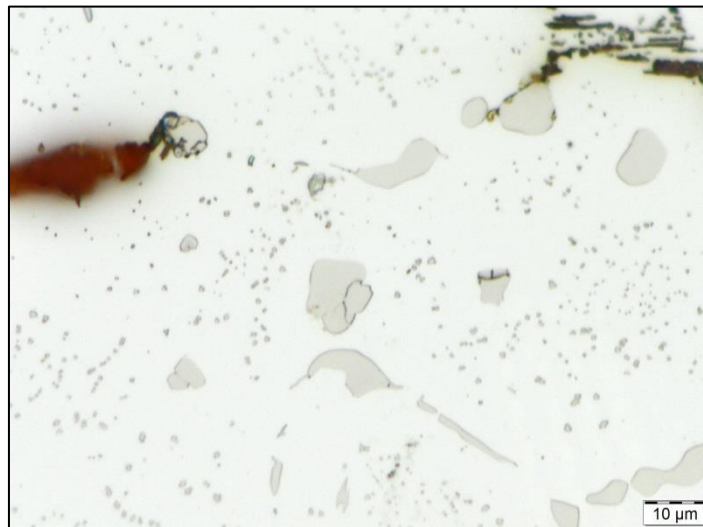

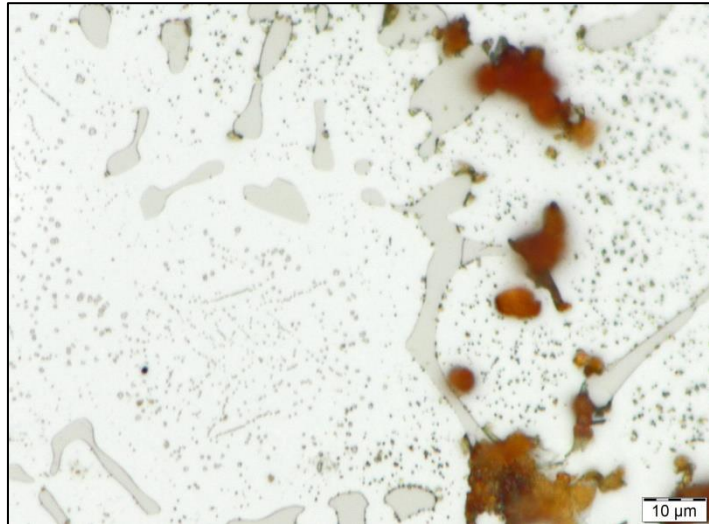Figure 4-172: HSS sample LT0 etched with Groesbeck and Murakami's etchant.

Figure 4-173: HSS sample LT45 etched with Groesbeck and Murakami's etchant.
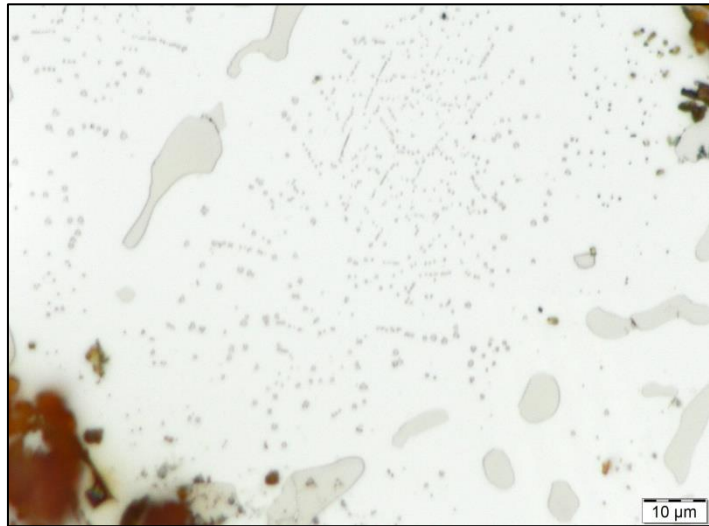

Figure 4-174: HSS sample LT58 etched with Groesbeck and Murakami's etchant.

Figure 4-175: HSS sample ST0 etched with Groesbeck and Murakami's etchant.

170

Figure 4-176: HSS sample ST43 etched with Groesbeck and Murakami's etchant.

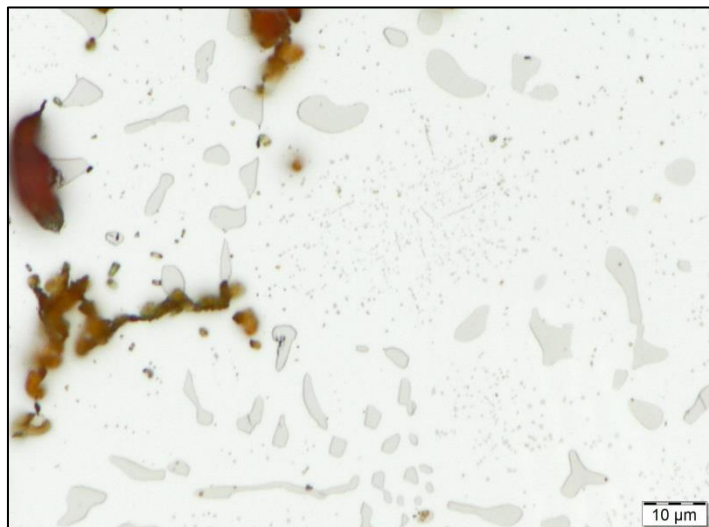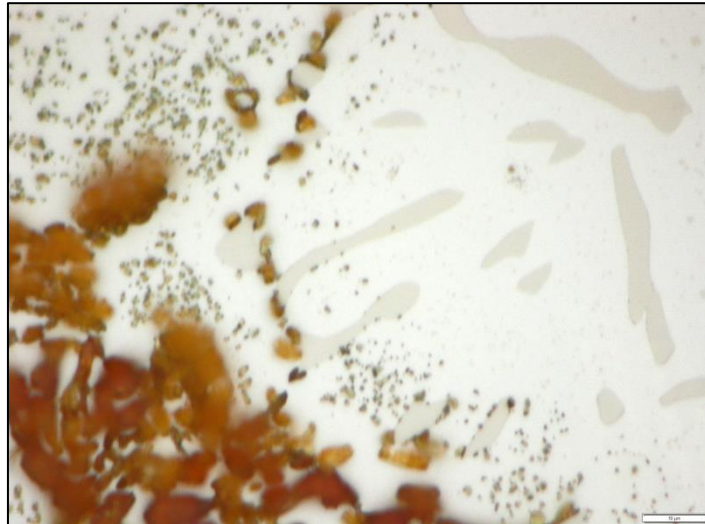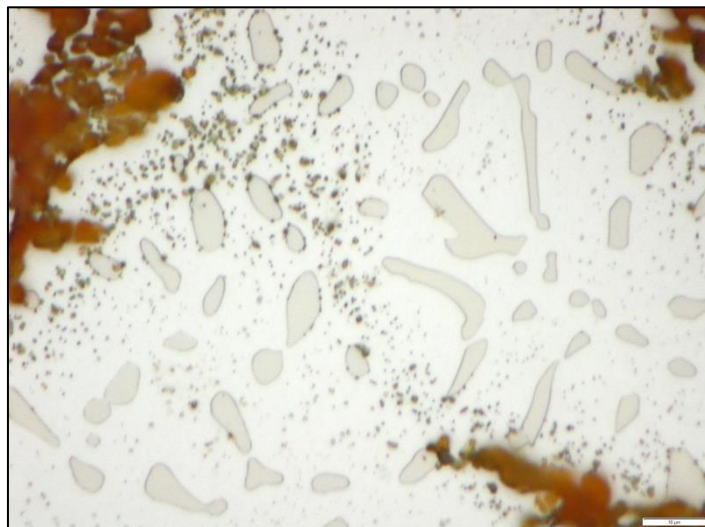Figure 4-177: HSS sample ST55 etched with Groesbeck and Murakami's etchant.

Figure 4-178: HSS sample LA85 etched with Groesbeck and Murakami's etchant.

171

Figure 4-179: HSS sample LA55 etched with Groesbeck and Murakami's etchant.

Figure 4-180: HSS sample LA85T0 etched with Groesbeck and Murakami's etchant.

Figure 4-181: HSS sample LA85T48 etched with Groesbeck and Murakami's etchant.
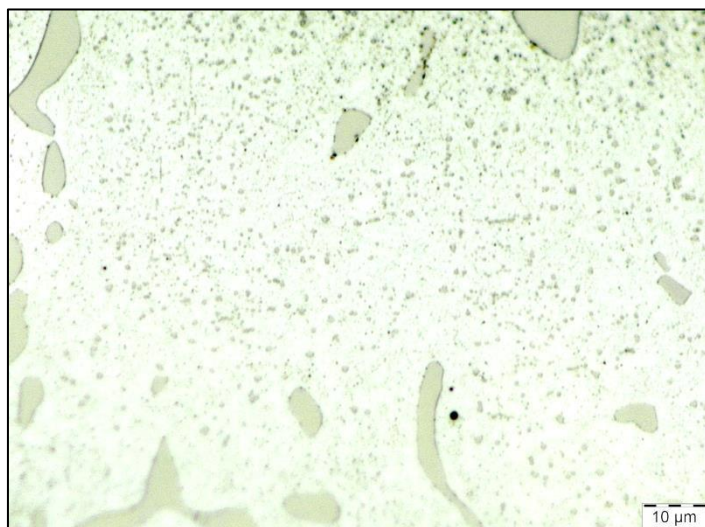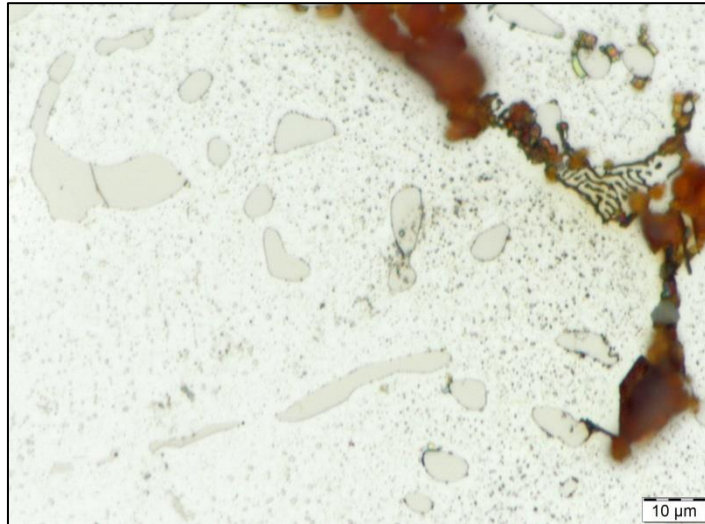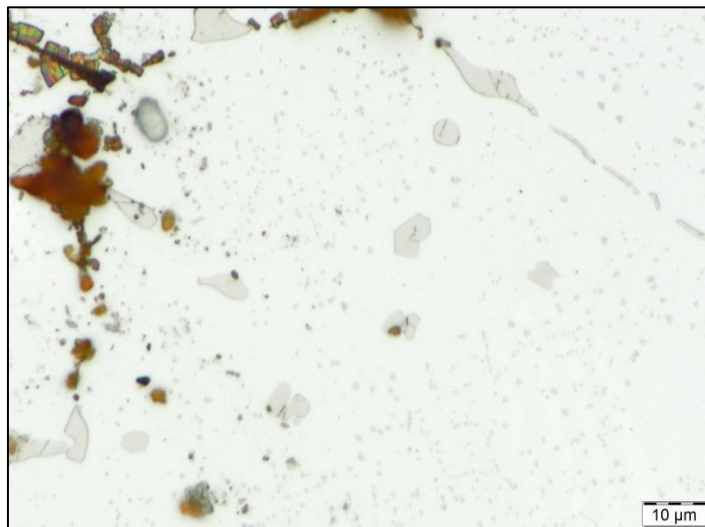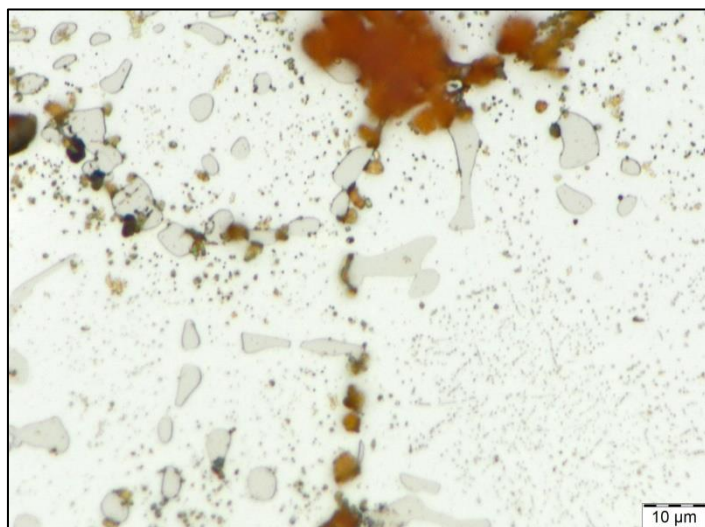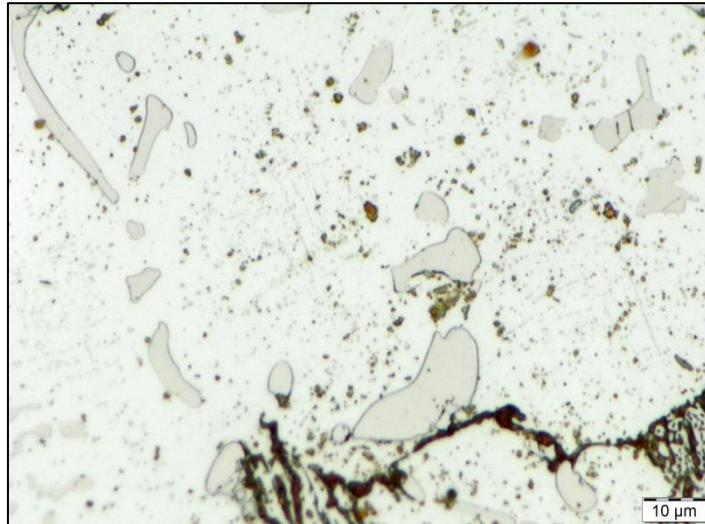
172

Figure 4-182: HSS sample LA85T60 etched with Groesbeck and Murakami's etchant.
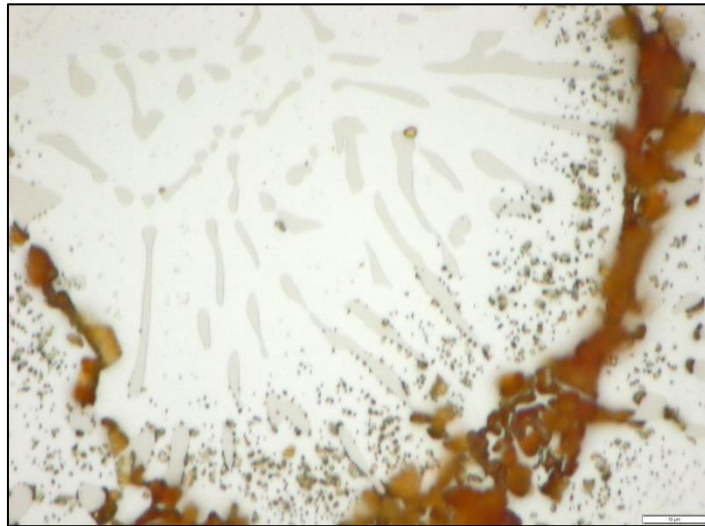
Figure 4-183: HSS sample SA85T0 etched with Groesbeck and Murakami's etchant.
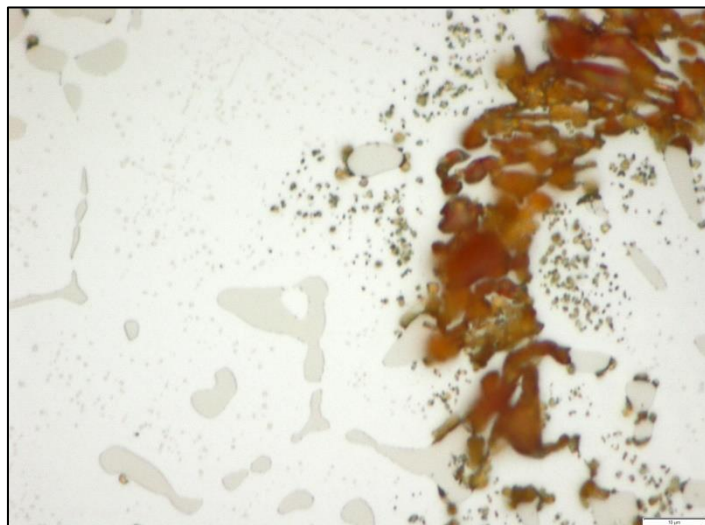
Figure 4-184: HSS sample SA85T40 etched with Groesbeck and Murakami's etchant.

173
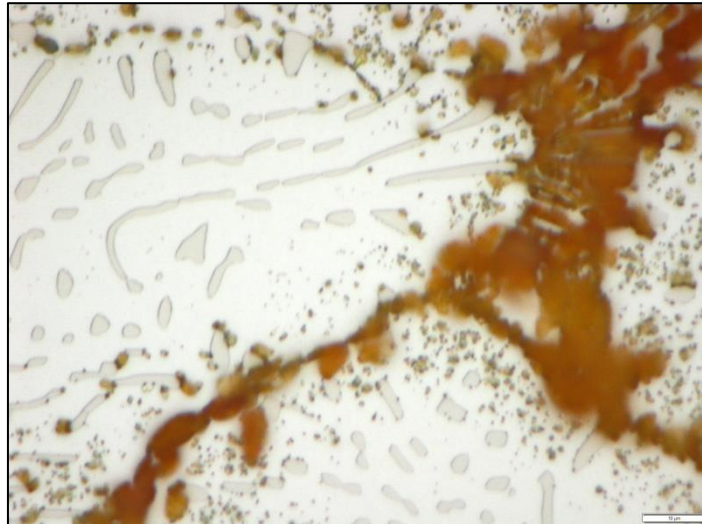
Figure 4-185: HSS sample SA85T53 etched with Groesbeck and Murakami's etchant.

4.2.3.5. Combined Groesbeck, Murakami and Chromic acid

The combination of Groesbeck, Murakami and Chromic acid etchants was utilised to confirm that the remaining un-etched primary carbides are of the MC type similar to the benchmark samples, see Figures 4-186 to 4-200. Chromic acid etched the globular primary carbides, which were confirmed to be of the MC type. The etchant also outlined the $M_{23}C_6$ secondary carbides [74]. The etchant further highlighted the $M_{23}C_6$ carbide-free regions associated with the MC carbides, especially where they occur at high concentrations, see Figures 4-201 to 4-206.

Figure 4-186: HSS sample Reference 1 etched with Groesbeck, Murakami and chromic acid.

174

Figure 4-187: HSS sample LT0 etched with Groesbeck, Murakami and chromic acid.

Figure 4-188: HSS sample LT45 etched with Groesbeck, Murakami and chromic acid.
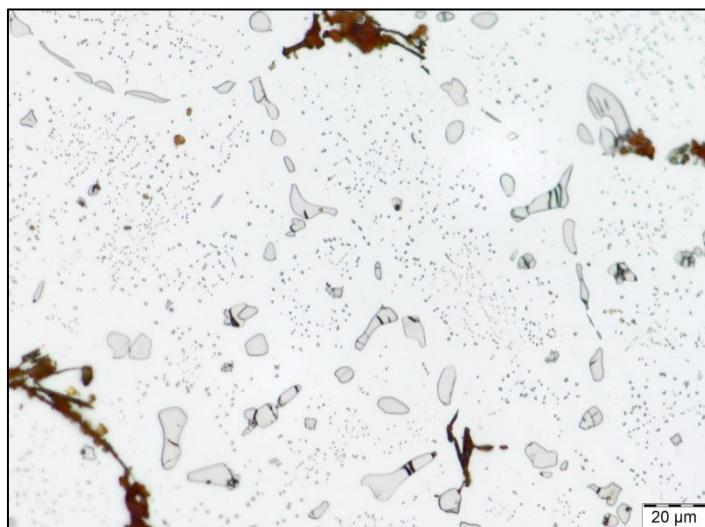
Figure 4-189: HSS sample LT58 etched with Groesbeck, Murakami and chromic acid.
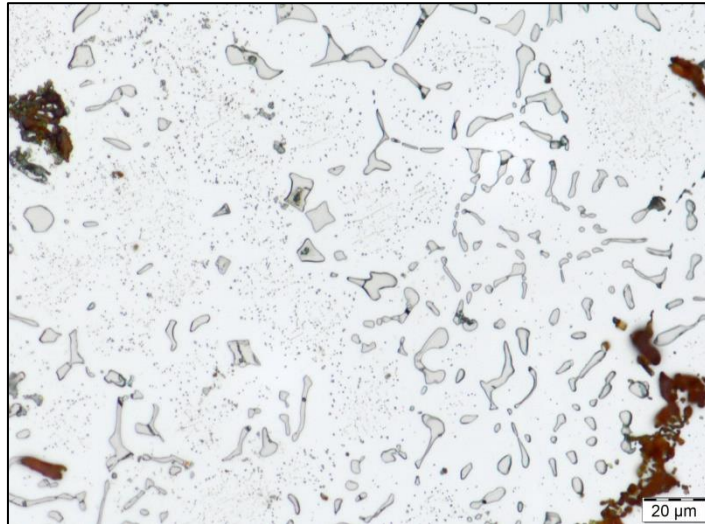
Figure 4-190: HSS sample ST0 etched with Groesbeck, Murakami and chromic acid.
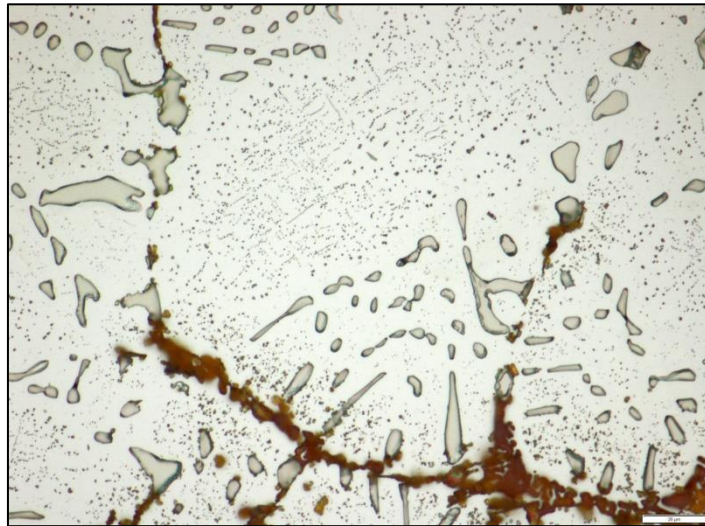
Figure 4-191: HSS sample ST43 etched with Groesbeck, Murakami and chromic acid.
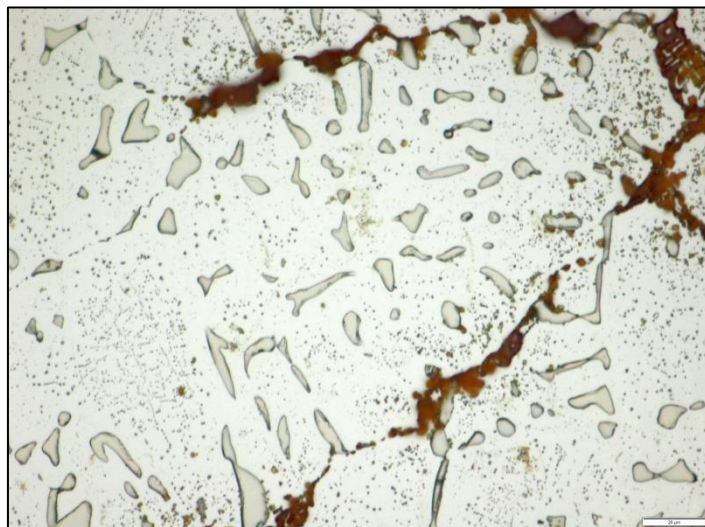
Figure 4-192: HSS sample ST55 etched with Groesbeck, Murakami and chromic acid.

176
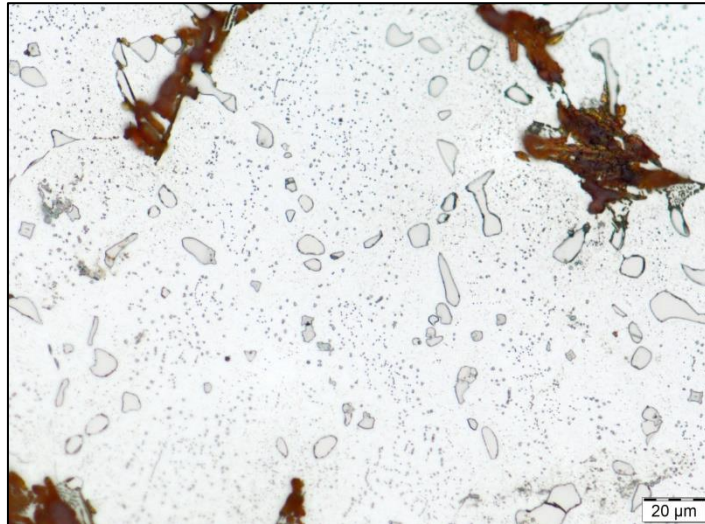
Figure 4-193: HSS sample LA85 etched with Groesbeck, Murakami and chromic acid.
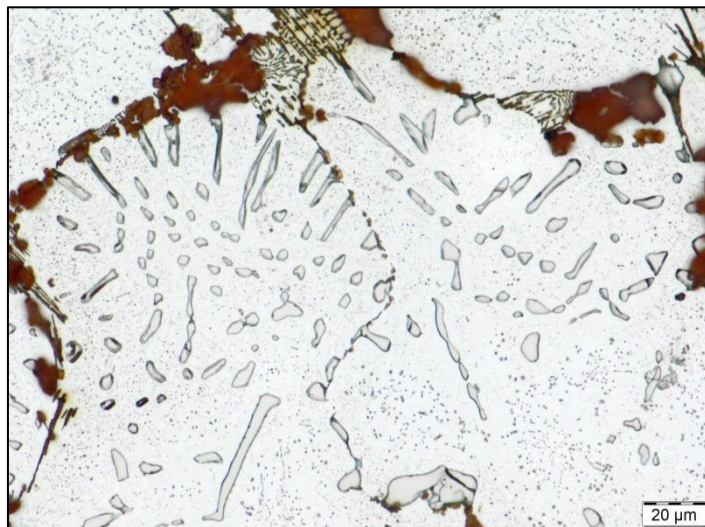
Figure 4-194: HSS sample LA55 etched with Groesbeck, Murakami and chromic acid.
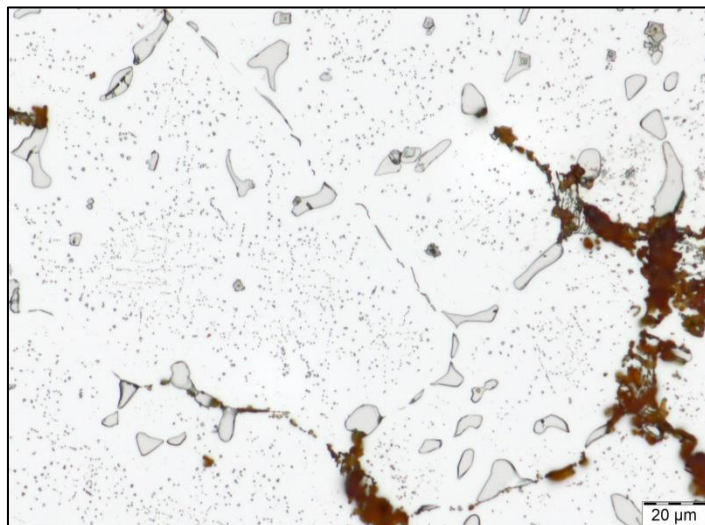
Figure 4-195: HSS sample LA85T0 etched with Groesbeck, Murakami and chromic acid.

177
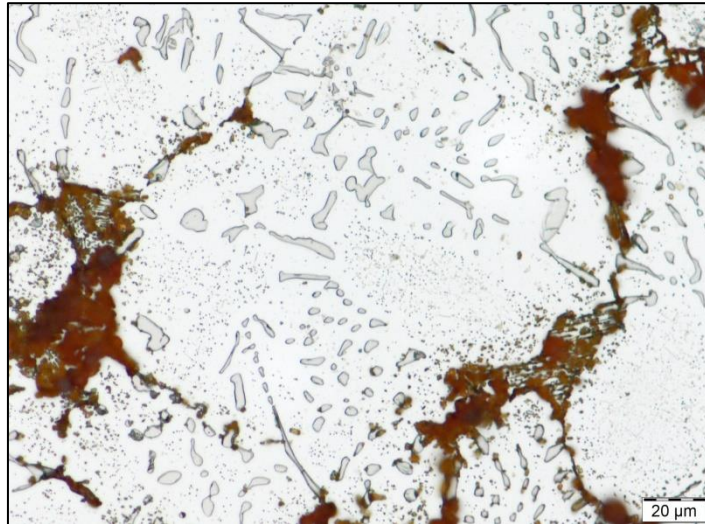
Figure 4-196: HSS sample LA85T48 etched with Groesbeck, Murakami and chromic acid.
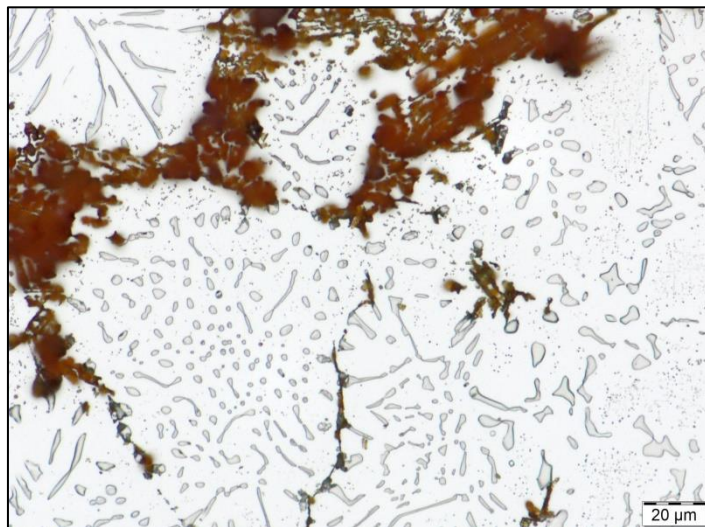
Figure 4-197: HSS sample LA85T60 etched with Groesbeck, Murakami and chromic acid.
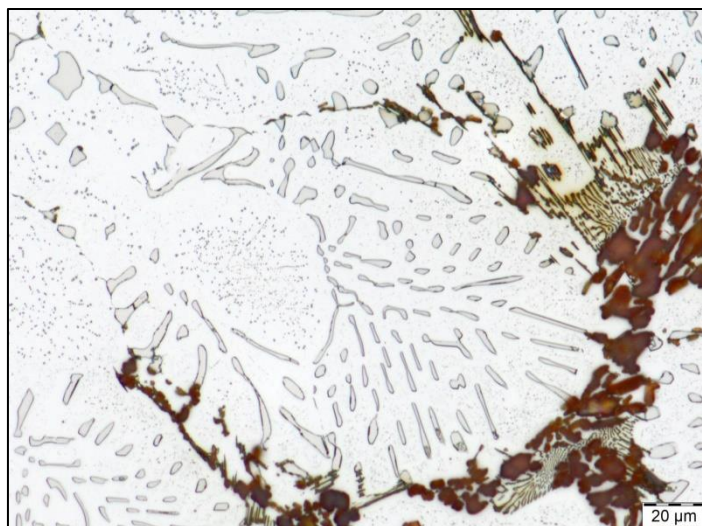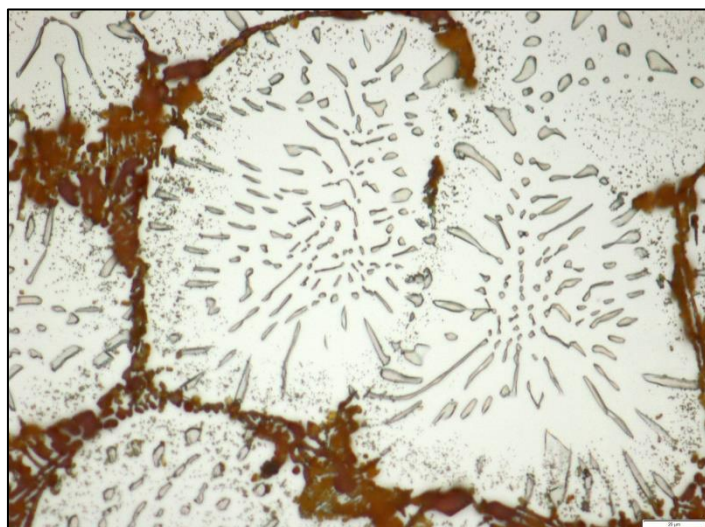

Figure 4-198: HSS sample SA85T0 etched with Groesbeck, Murakami and chromic acid.
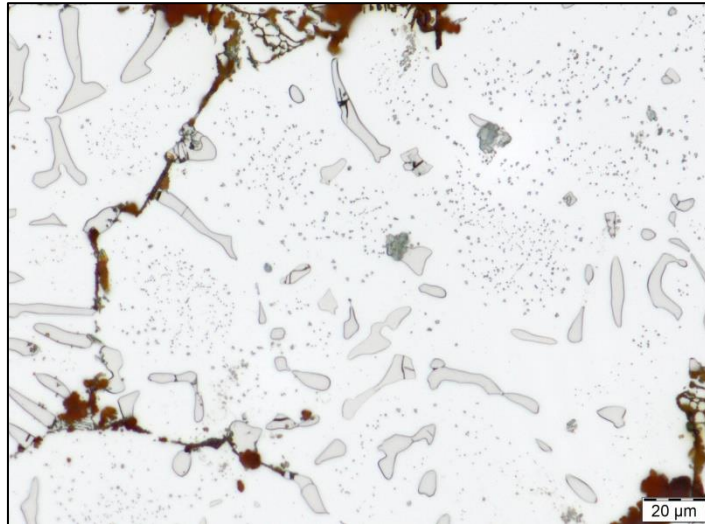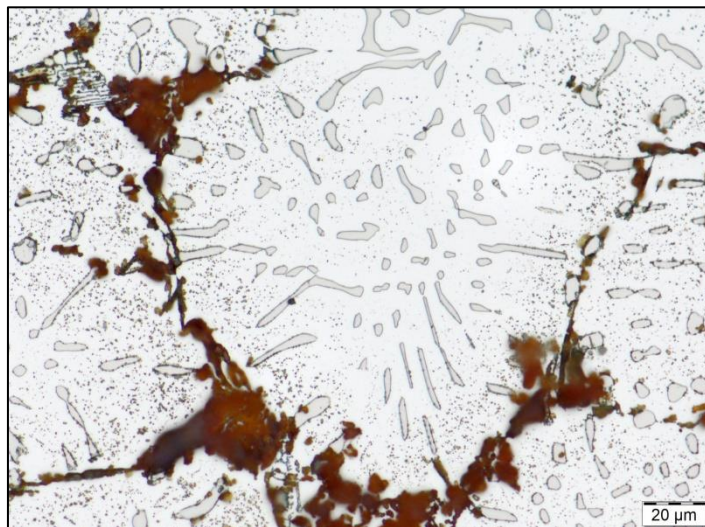
178
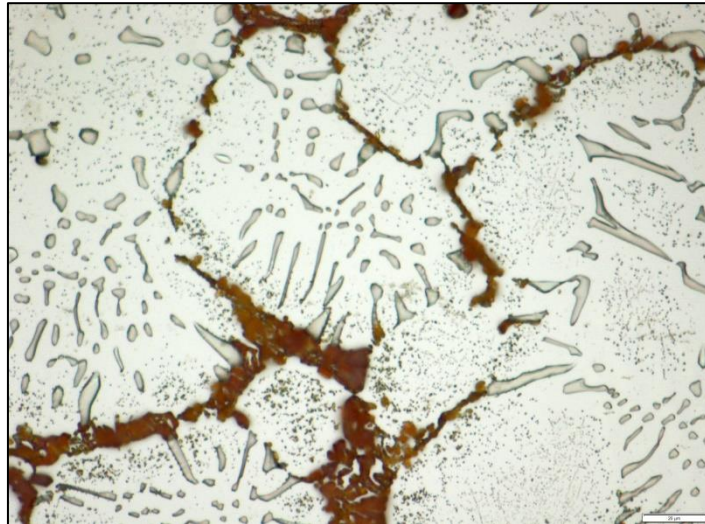
Figure 4-199: HSS sample SA85T40 etched with Groesbeck, Murakami and chromic acid.
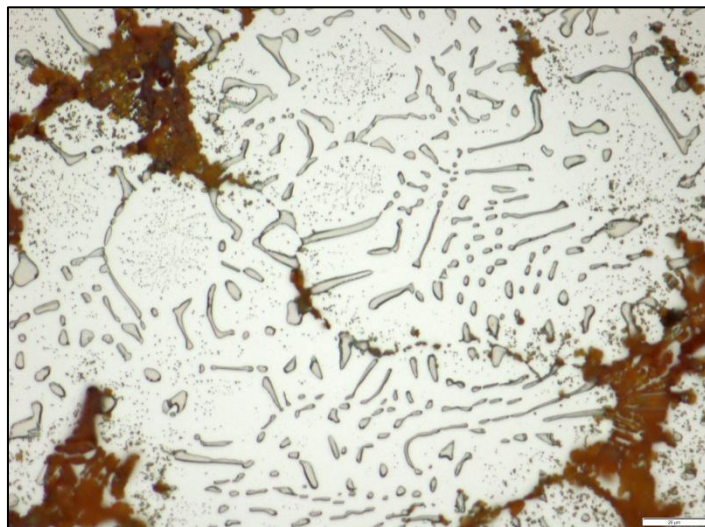
Figure 4-200: HSS sample SA85T53 etched with Groesbeck, Murakami and chromic acid.
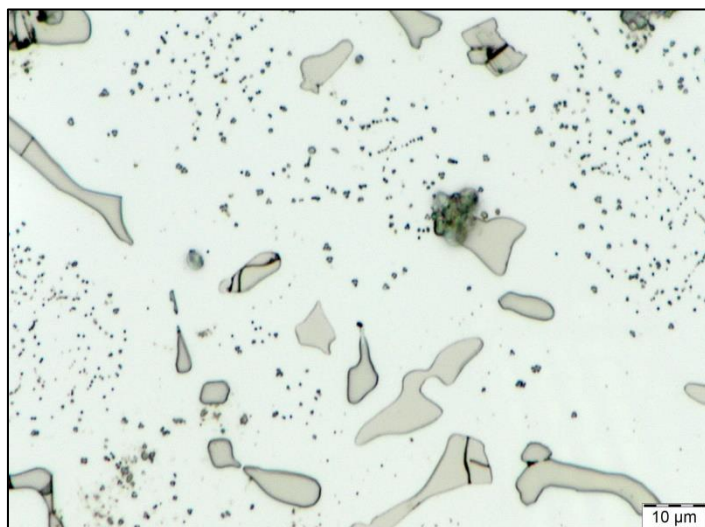
Figure 4-201: HSS sample LT0 at higher magnification, etched with Groesbeck, Murakami and chromic acid.

179

Figure 4-202: HSS sample LT58 at higher magnification, etched with Groesbeck, Murakami and chromic acid.
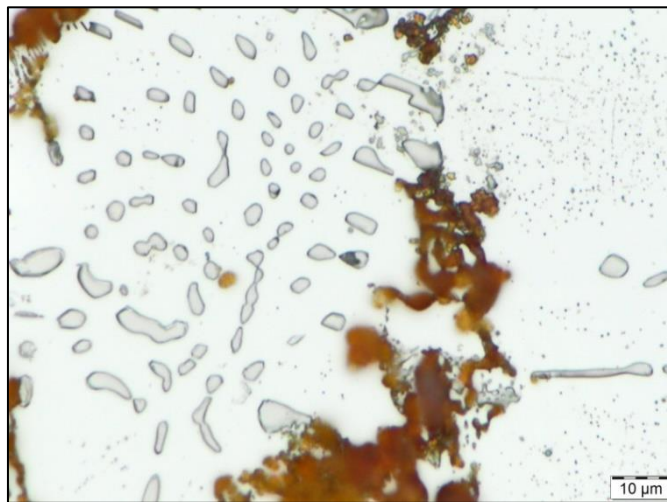
Figure 4-203: HSS sample ST0 at higher magnification, etched with Groesbeck, Murakami and chromic acid.

Figure 4-204: HSS sample LA85T48 at higher magnification, etched with Groesbeck, Murakami and chromic acid.
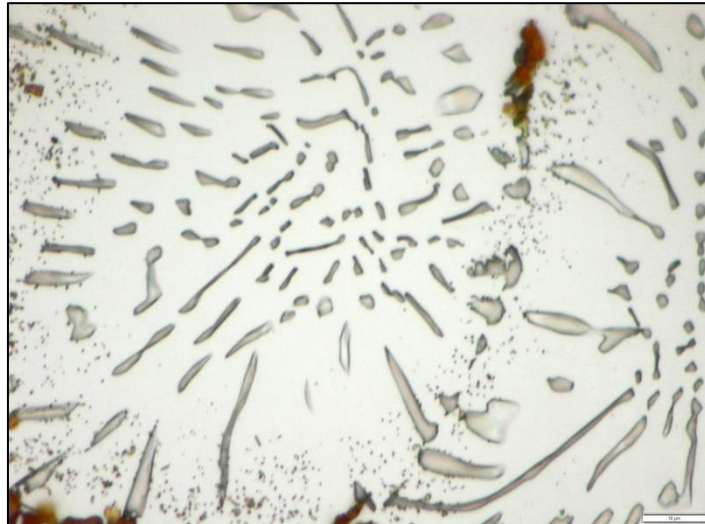
Figure 4-205: HSS sample SA85T0 at higher magnification, etched with Groesbeck, Murakami and chromic acid.
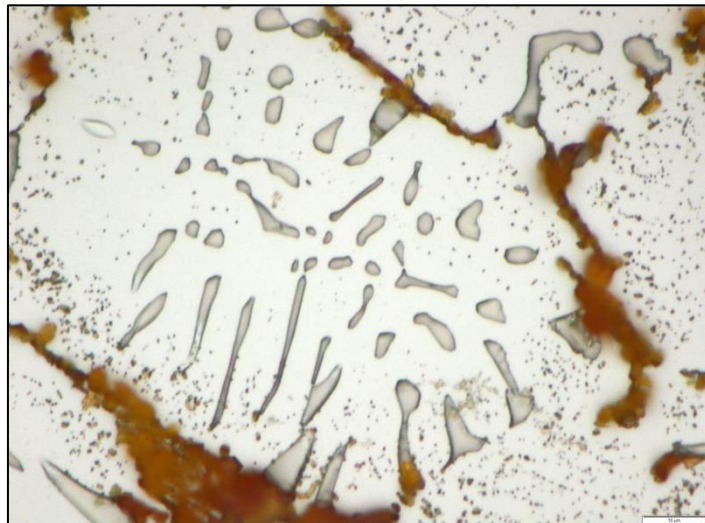
Figure 4-206: HSS sample SA85T40 at higher magnification, etched with Groesbeck, Murakami and chromic acid.

4.2.3.6. Alkaline Sodium Picrate (ASP)

The ASP etchant did not etch any of the carbides on the HSS as-cast sample (Reference 1). However, ASP did etch the M_6C carbides black in the temper samples, see Figures 4-207 to 4-219. ASP did not affect any of the other primary carbides in the shell other than M_6C in the tempered materials. ASP also etched fine secondary carbides associated with the primary carbides in the interdendritic regions. This suggests that their likely structure is also M_6C.

181

Figure 4-207: HSS sample Reference 1 etched with ASP.
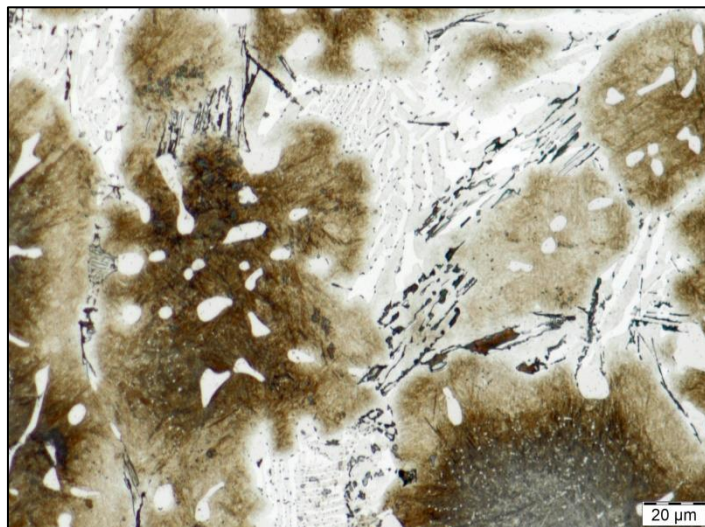
Figure 4-208: HSS sample LT0 etched with ASP.
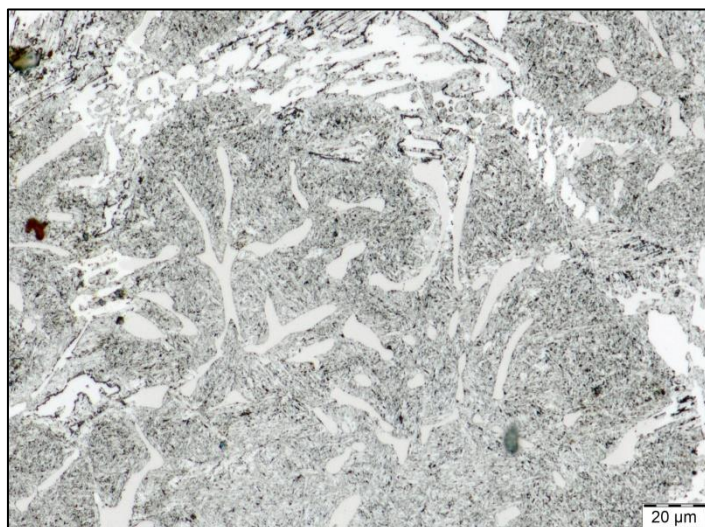
Figure 4-209: HSS sample LT45 etched with ASP.

182
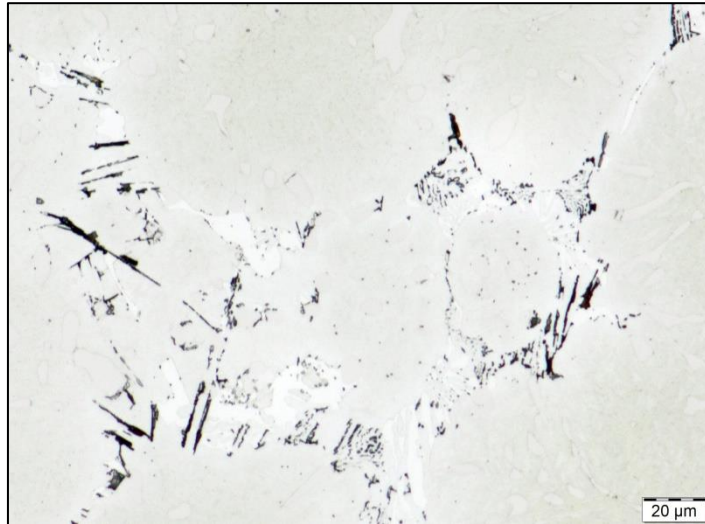
Figure 4-210: HSS sample LT58 etched with ASP.
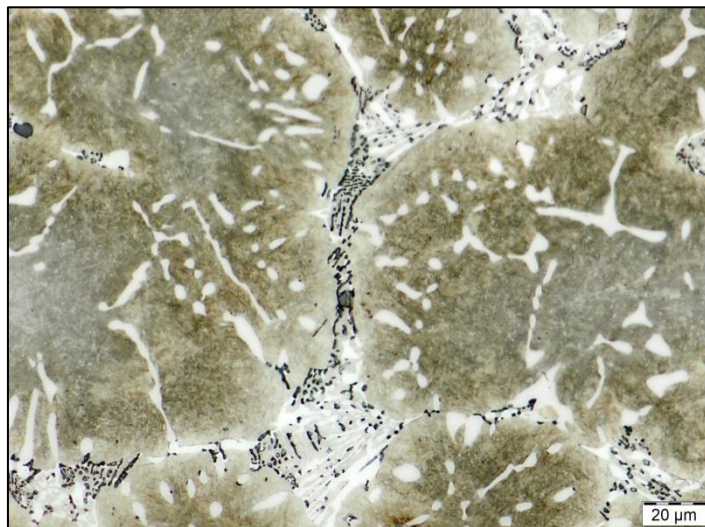
Figure 4-211: HSS sample ST0 etched with ASP.
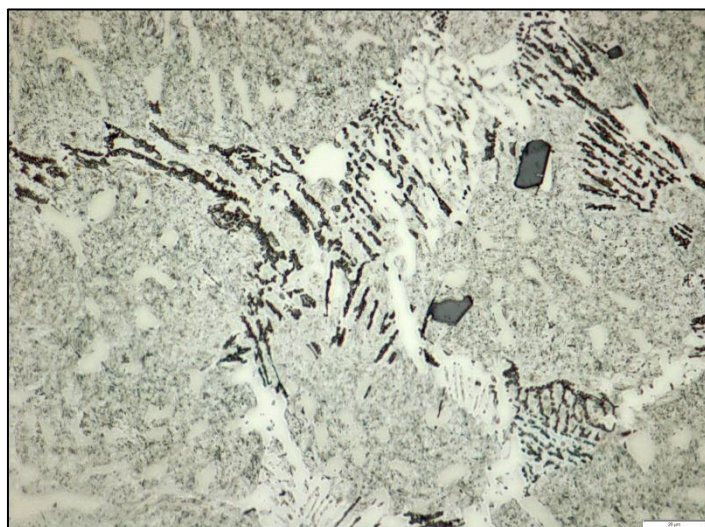
Figure 4-212: HSS sample ST43 etched with ASP.
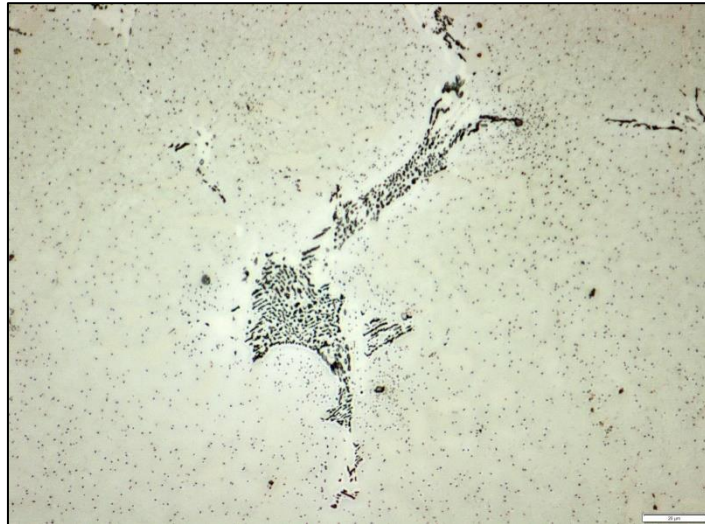
Figure 4-213: HSS sample ST55 etched with ASP.
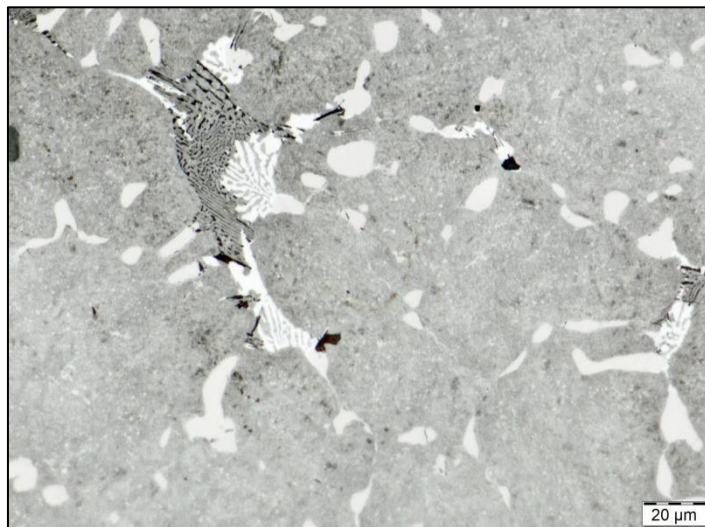
Figure 4-214: HSS sample LA85 etched with ASP.
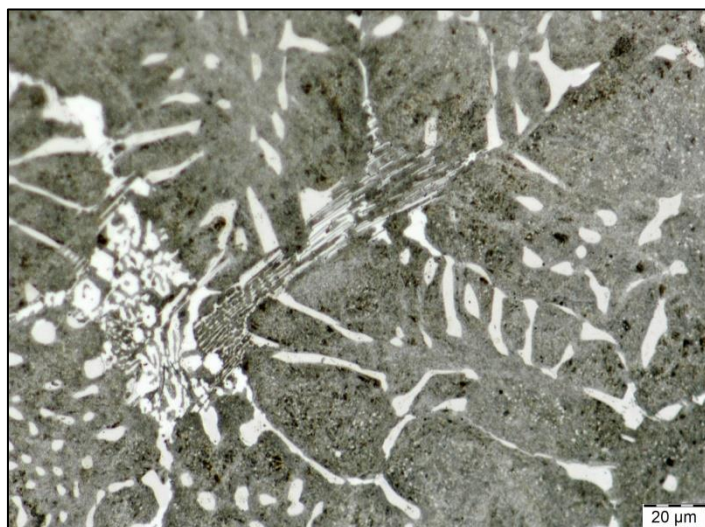
Figure 4-215: HSS sample LA55 etched with ASP.

184
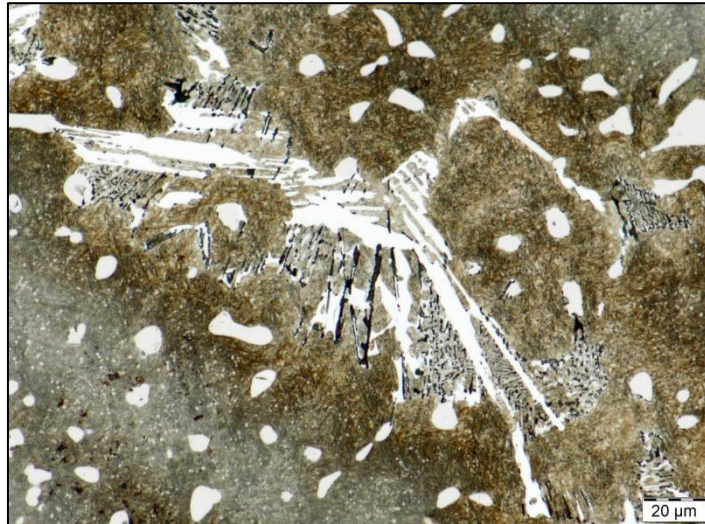
Figure 4-216: HSS sample LA85T0 etched with ASP.
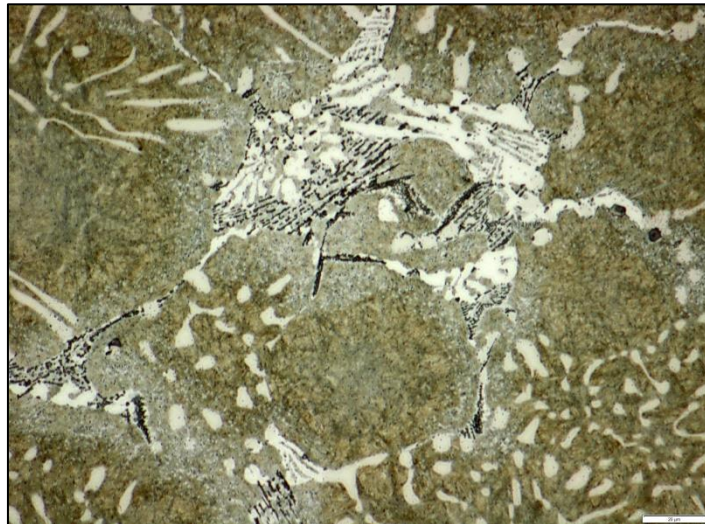
Figure 4-217: HSS sample SA85T0 etched with ASP.
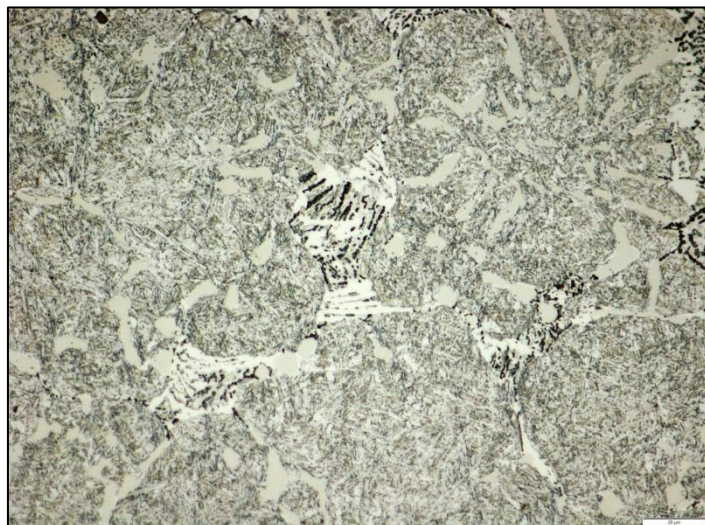
Figure 4-218: HSS sample SA85T40 etched with ASP.

185
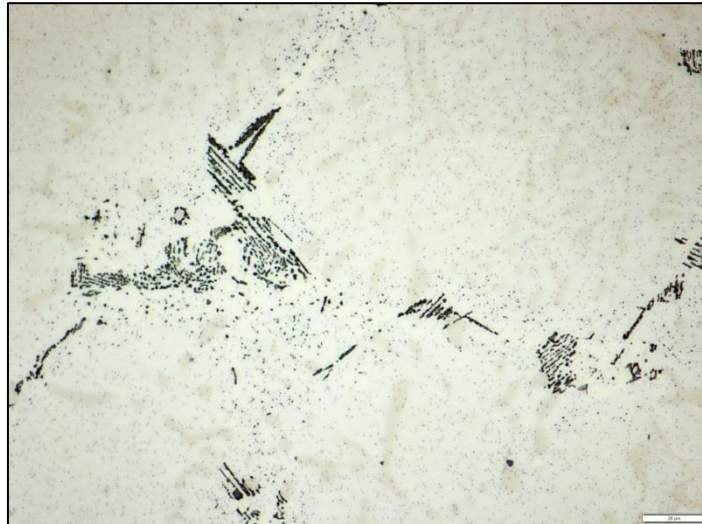
Figure 4-219: HSS sample SA85T53 etched with ASP.

4.2.3.7.   Beraha's Etchant

Beraha's etchant was used to identify chemical segregation and the presence of retained austenite. Significant retained austenite was identified on the HC samples, see Figures 4-220 to 4-228. The retained austenite of the LA samples was only largely eliminated once the material was over-tempered beyond peak hardness, as shown by sample LT58. The LT samples showed near complete matrix etching for all temper conditions, including the untempered LT0. However, Beraha's etchant still did not show sufficient contrast in order to quantify the primary carbide volume fraction. Alternative reagent concentrations and etching times were attempted to improve the etching, but proved ineffective. A number of alternative matrix etchants were reviewed, but showed similar results. It is not clear what the cause of the lack of etching is, since all of the etchants trialled are utilised for etching of austenitic material. The lack of etching could be related to chemical resistance associated with the high Cr levels.

The simulated material showed limited etching in the untempered condition (ST0) and showed an increasing degree of matrix etching as the tempering temperature increased. The development of the etched matrix initiated from the centre of the cell and increased towards the carbide containing grain boundaries.

Secondary carbide (matrix) coarsening on both LT and ST sample sets was also observed. However, the secondary carbides associated with the LT material appeared significantly coarser than the ST material at equivalent tempering temperatures, see Figures 4-224 and 4-228. This observation is in contradiction to the typical

186

observations, where carbide coarsening increases with increasing tempering time. The deviation appears to be related to the degree of dissolution during the austenitising treatment. The secondary carbides present in the as-cast material (Reference 1) are completely dissolved during the simulated treatment (ST0), but only partially dissolved under laboratory conditions (LT0). Hence, the coarser secondary carbides observed on the LT samples compared to the ST samples are related to the initial size difference of the secondary carbides and not the rate of coarsening.
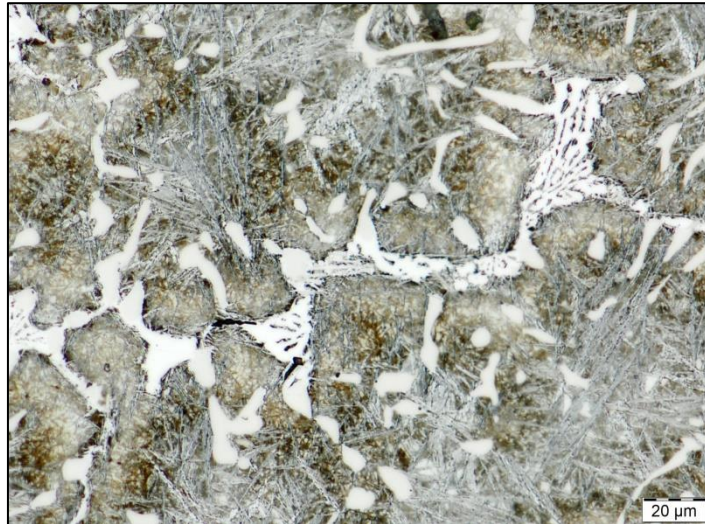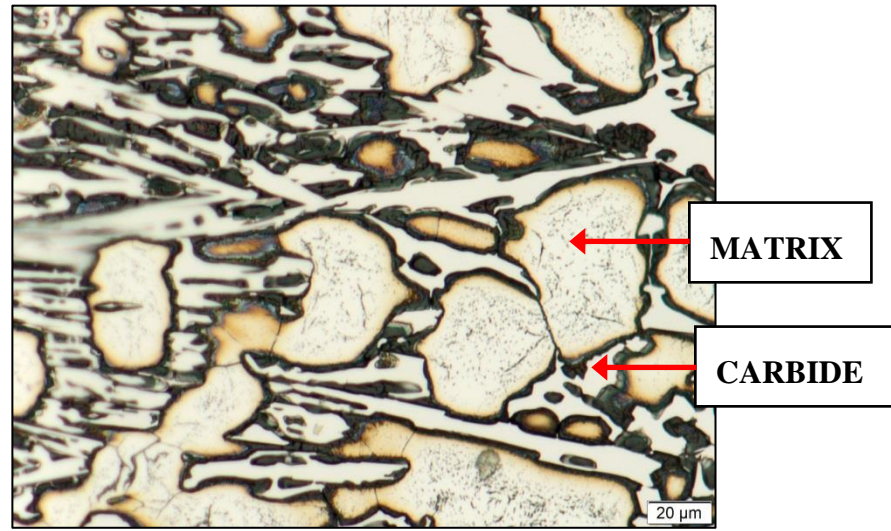

Figure 4-220: HC sample Reference 1 etched with Beraha.
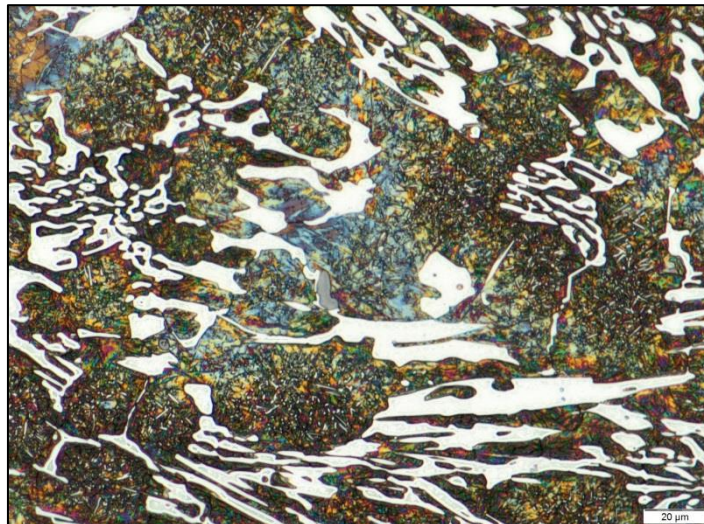
Figure 4-221: HC sample LT0 etched with Beraha.

Figure 4-222: HC ample LT48 etched with Beraha's etchant.

Figure 4-223: HC sample LT58 etched with Beraha's etchant.

Figure 4-224: HC sample LT60 etched with Beraha's etchant.

188
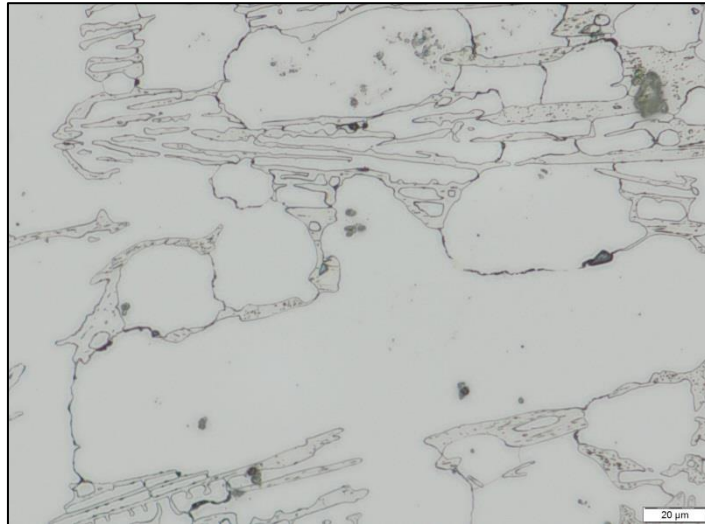
Figure 4-225: HC sample ST0 etched with Beraha's etchant.
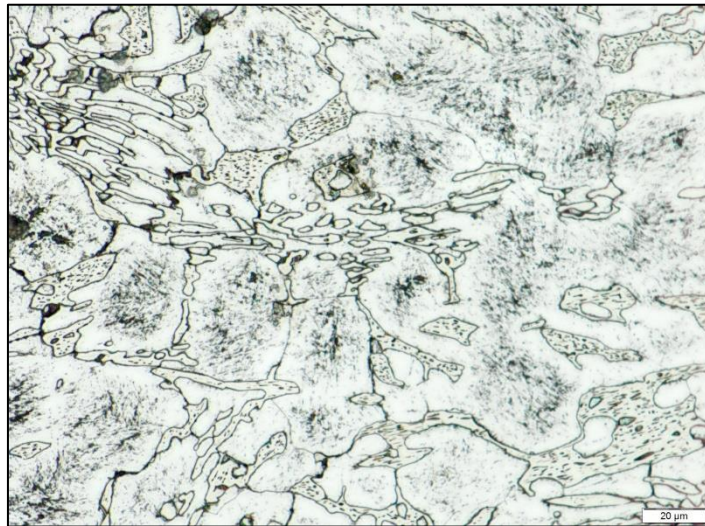
Figure 4-226: HC sample ST48 etched with Beraha's etchant.
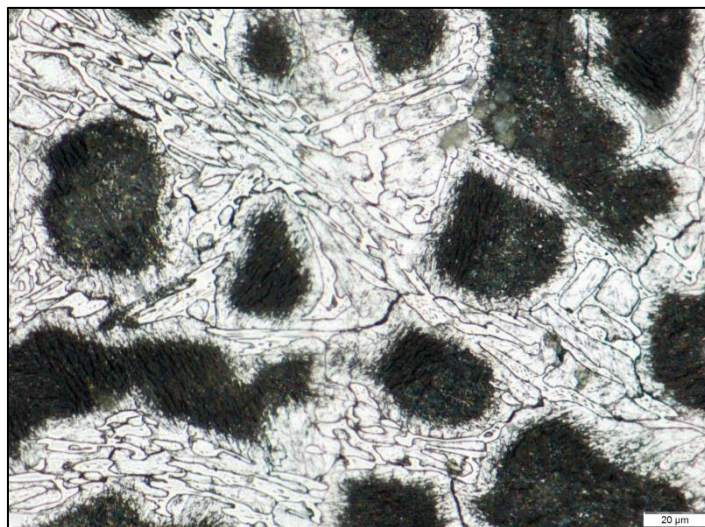
Figure 4-227: HC sample ST50 etched with Beraha's etchant.
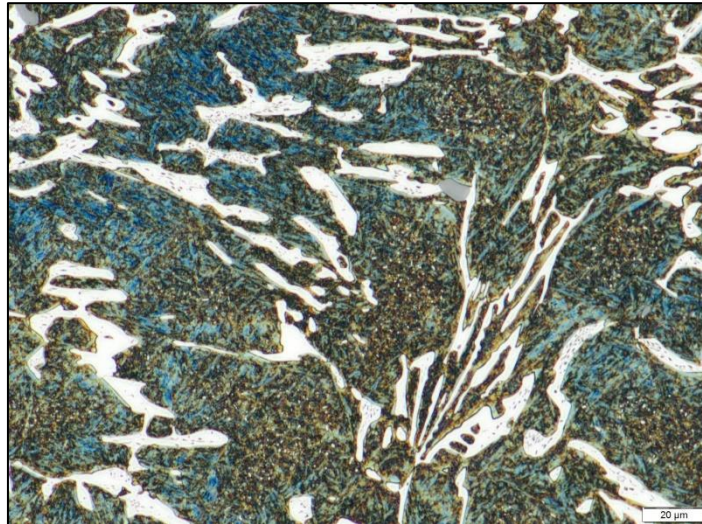
Figure 4-228: HC sample ST60 etched with Beraha's etchant.

The micrographs for the HSS samples etched with Beraha's etchant are shown in Figures 4-229 to 4-243. The untempered HSS samples (LT0, ST0, LA85T0 and SA85T0) showed indications of significant coring around the carbide cell boundaries, see Figures 4-230, 4-233, 4-238 and 4-241. This indicates the presence of chemical segregation. This also identified significant retained austenite, which was primarily associated with the carbide networks. The tempered samples showed limited chemical segregation and no retained austenite could be positively identified. It was also noted that no retained austenite could be positively identified on samples LA85 and LA55. There were slight indications of secondary carbide coarsening on all the samples sets. However, the secondary carbide size appeared to be comparable at equivalent tempering temperatures for the different sets.
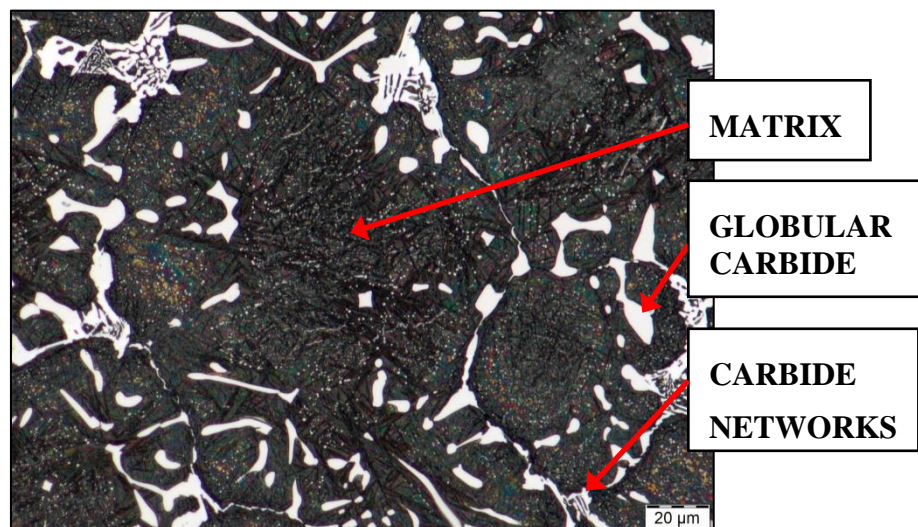
Figure 4-229: HSS sample Reference 1 etched with Beraha's etchant.

190
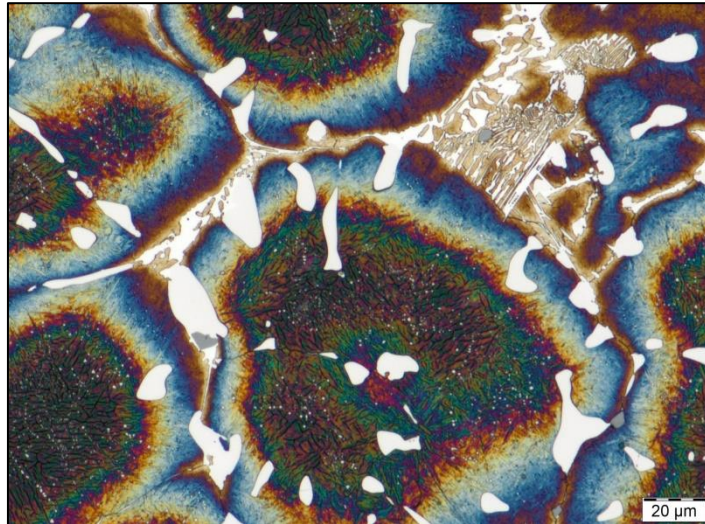
Figure 4-230: HSS sample LT0 etched with Beraha's etchant.
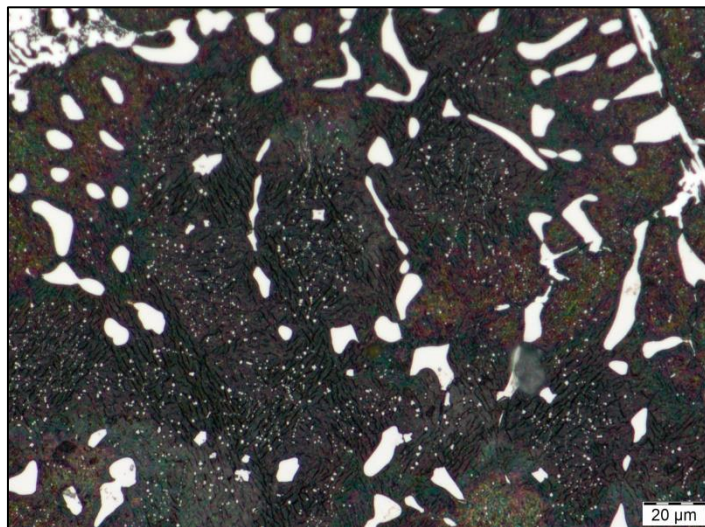
Figure 4-231: HSS sample LT45 etched with Beraha's etchant.
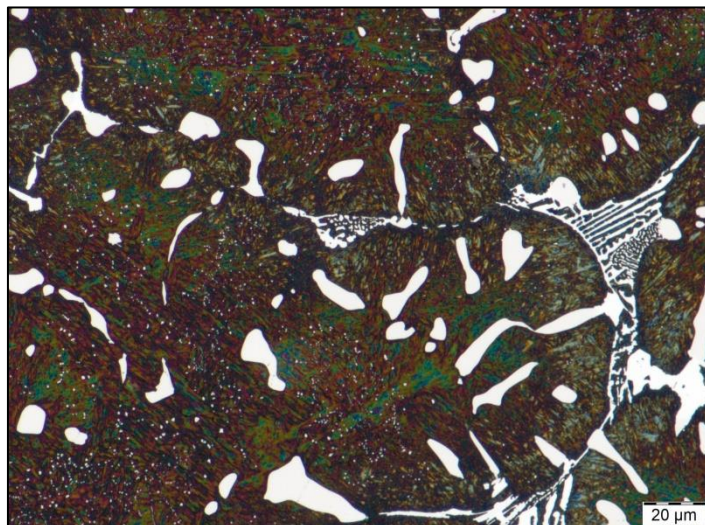
Figure 4-232: HSS sample LT58 etched with Beraha's etchant.

191
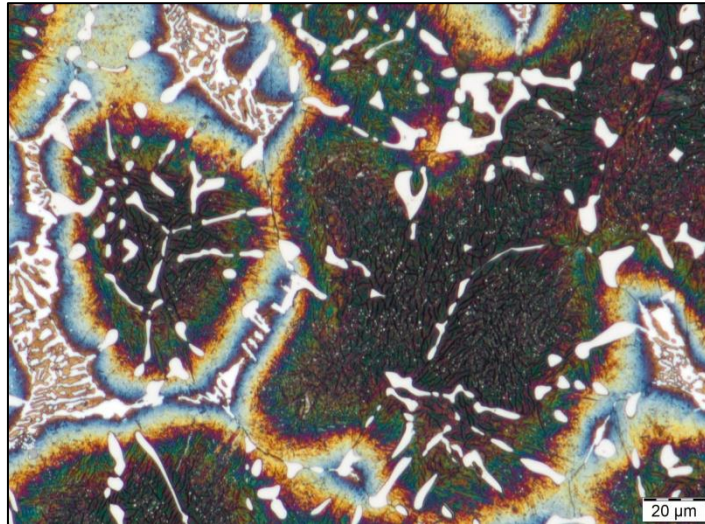
Figure 4-233: HSS sample ST0 etched with Beraha's etchant.
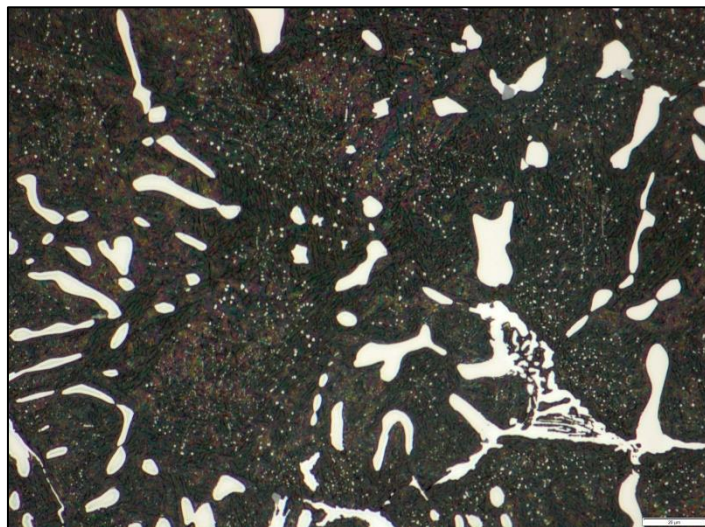
Figure 4-234: HSS sample ST43 etched with Beraha's etchant.

SECONDARY CARBIDES
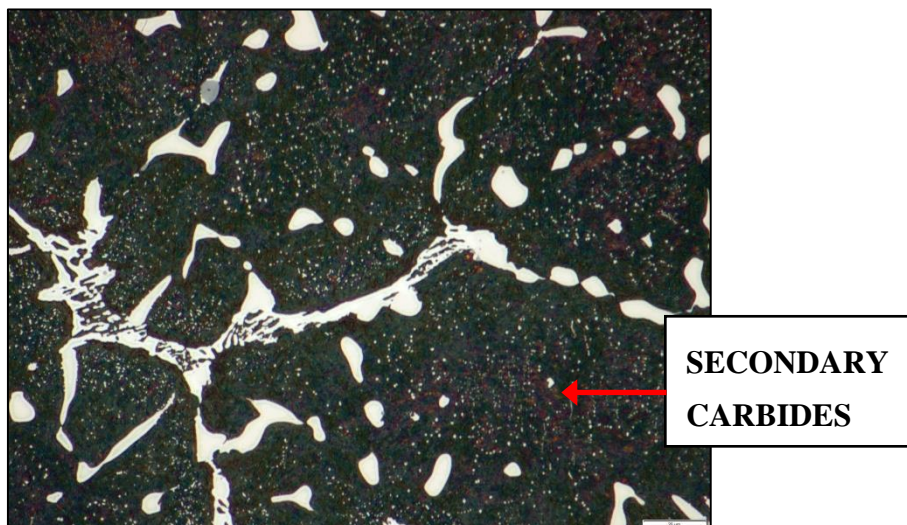
Figure 4-235: HSS sample ST55 etched with Beraha's etchant.

192

Figure 4-236: HSS sample LA85 etched with Beraha's etchant.
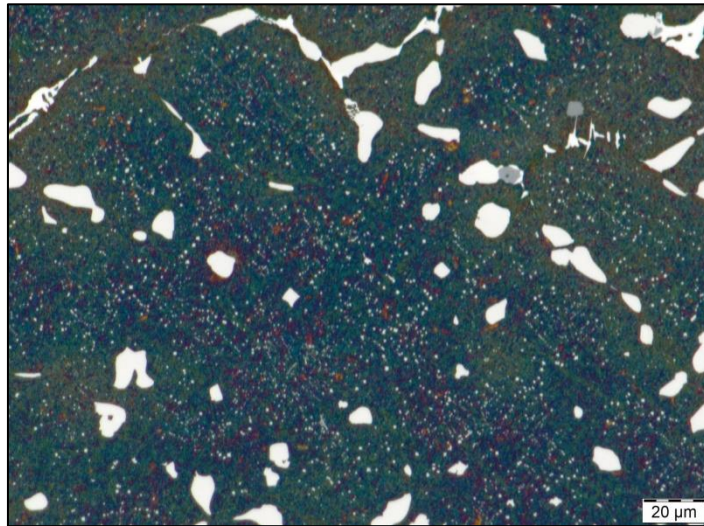
Figure 4-237: HSS sample LA55 etched with Beraha's etchant.
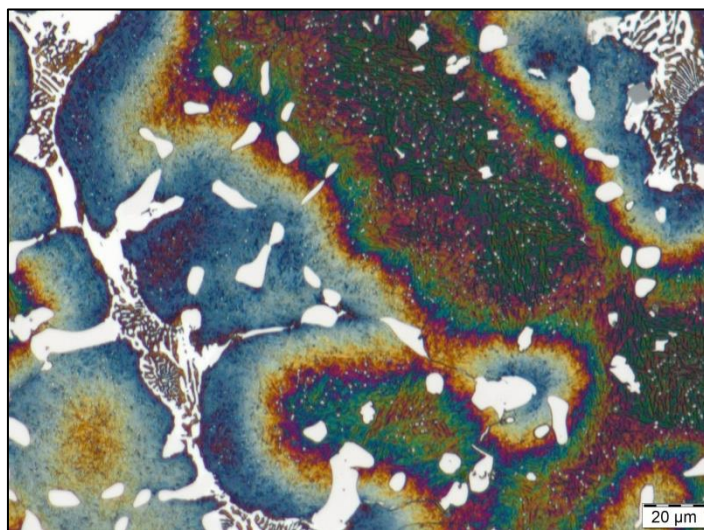
Figure 4-238: HSS sample LA85T0 etched with Beraha's etchant.

193
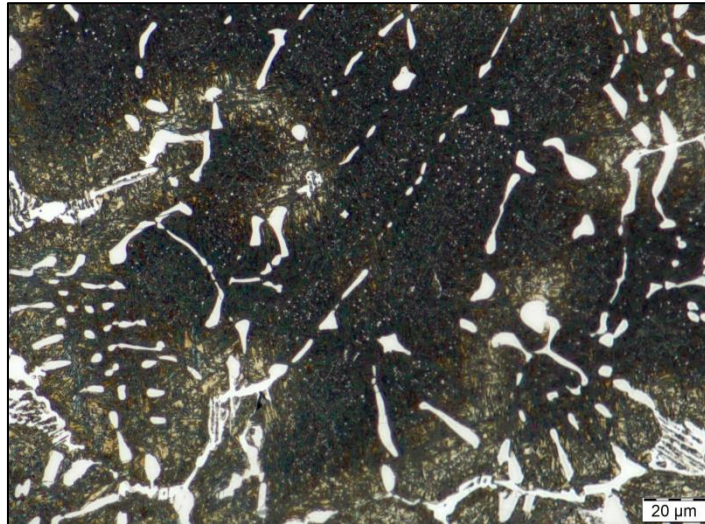
Figure 4-239: HSS sample LA85T48 etched with Beraha's etchant.
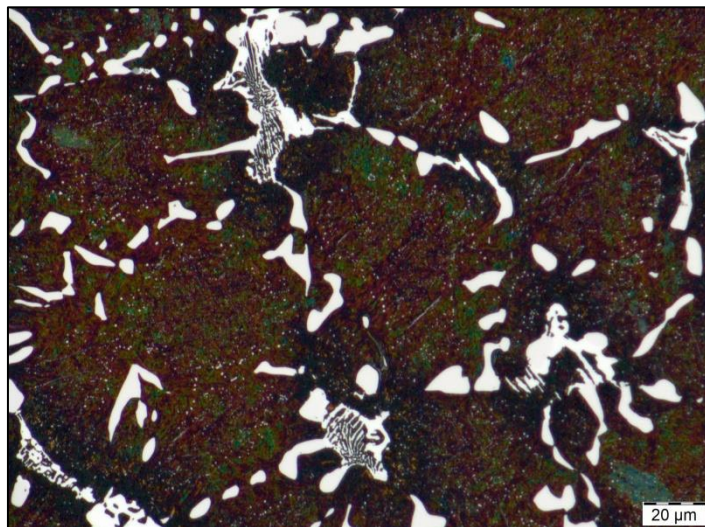
Figure 4-240: HSS sample LA85T60 etched with Beraha's etchant.
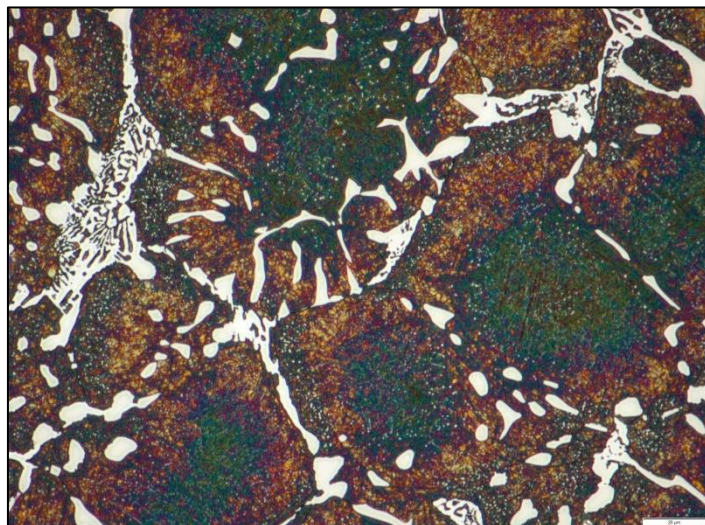
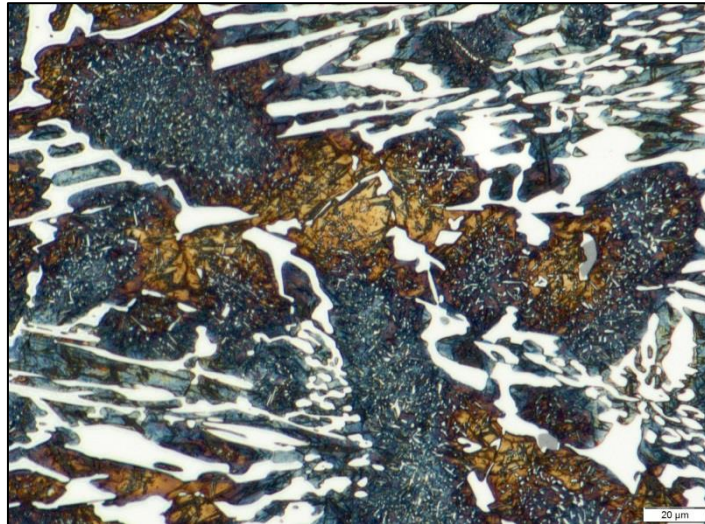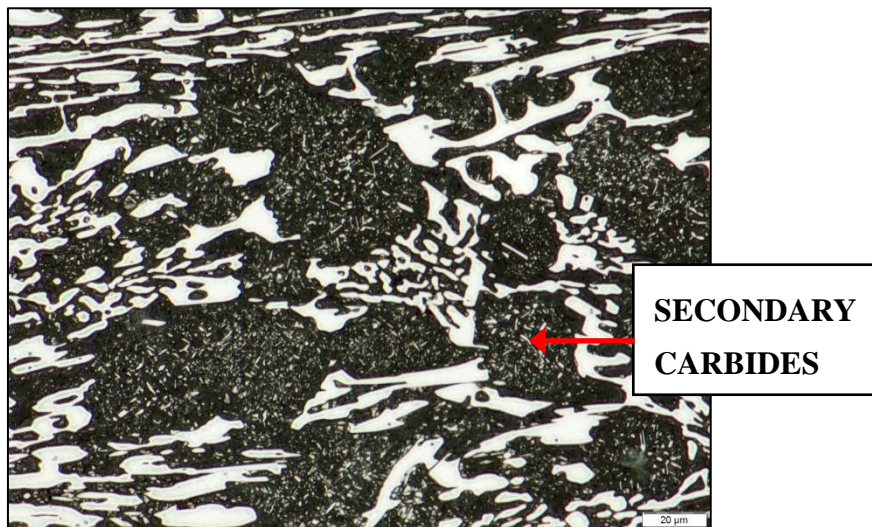Figure 4-241: HSS sample SA85T0 etched with Beraha's etchant.

194
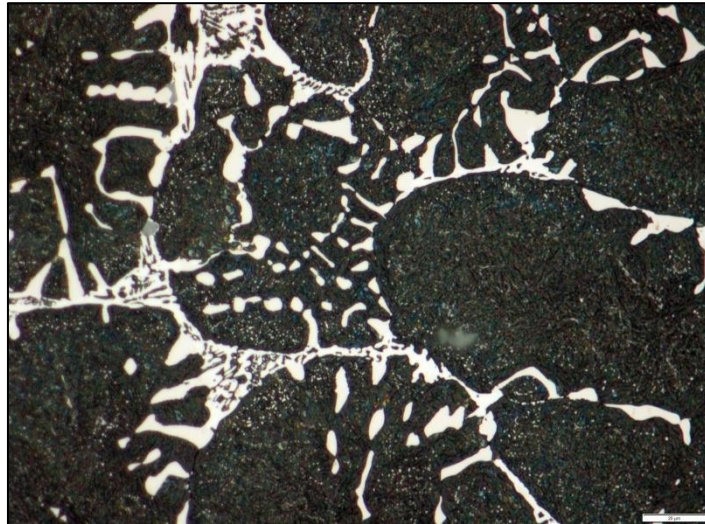
Figure 4-242: HSS sample SA85T40 etched with Beraha's etchant.
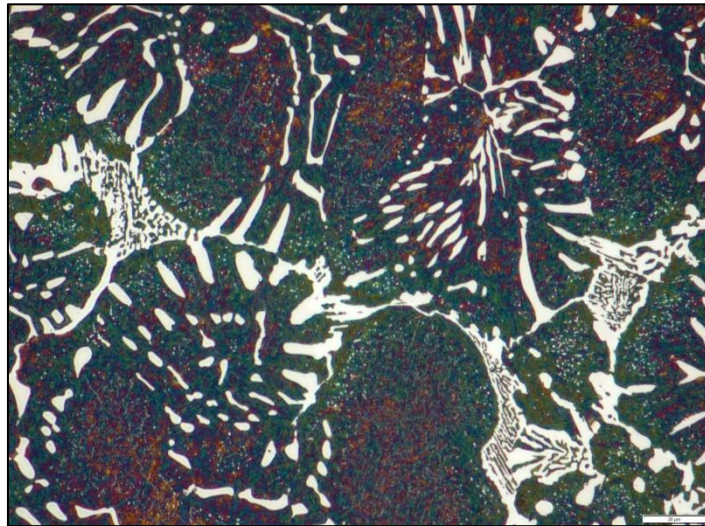
Figure 4-243: HSS sample SA85T53 etched with Beraha's etchant.
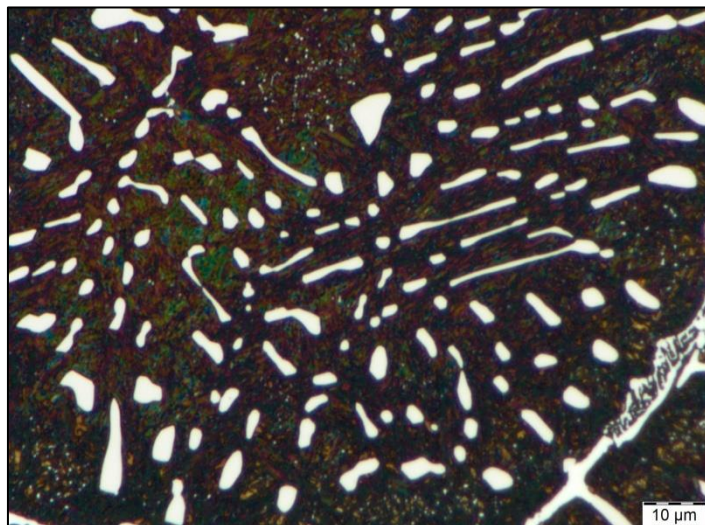
Figure 4-244: HSS sample LA85T60 at higher magnification, etched with Beraha's etchant.

195
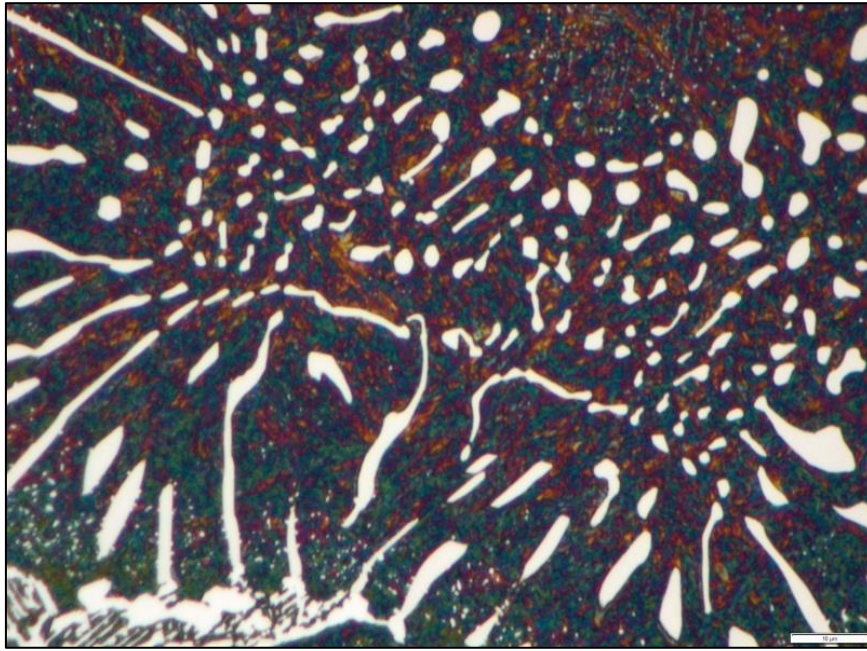
Figure 4-245: HSS sample SA85T53 at higher magnification, etched with Beraha's etchant.

It was also noted that the secondary carbides present in the matrix were absent in regions where the globular primary carbides were more abundant within the matrix, see Figures 4-244 and 4-245. The etched samples were used in order to determine the total carbide volume fraction using automated phase analysis, see Table 4-20. The total carbide content of the LT and ST sets showed a fairly small degree of variation between the samples, as expected, except for the untempered samples LT0 and ST0, see Figure 4-246. LT0 and ST0 also showed inferior accuracy as shown by the RA values of 12.1% and 6.7% respectively. This was attributed to the higher levels of retained austenite, which influence the degree of etching and reduce the level of contrast. The inferior contrast appears to introduce a bias while also increasing the variation between measurements as indicated by the CV and RA.

The total carbide content of the LA and SA sets also showed a fairly small degree of variation between the samples, as expected, except for the untempered sample LA85T0, see Figure 4-247. The deviation of sample LA85T0 was attributed to the higher levels of retained austenite and inferior contrast similar to the LT0 and ST0 samples. The standard deviation, coefficient of variance and relative accuracy values were acceptable indicating sufficient accuracy and repeatability, except for sample LT0, which showed an RA value in excess of 10%.

196

Table 4-20: Total carbide content analysis results.

Sample	Total Carbide Content (%)			Statistics			
	Minimum	Maximum	Average	S	CV	95%CL	RA
Reference 1	10.9	12.1	11.6	0.39	3.4%	0.29	2.5%
LT0	7.1	12.1	9.4	1.52	16.1%	1.14	12.1%
LT45	10.2	12.5	11.3	0.71	6.3%	0.54	4.7%
LT58	10.0	12.4	10.9	0.73	6.7%	0.55	5.0%
ST0	6.8	8.9	7.7	0.68	8.9%	0.51	6.7%
ST43	11.1	12.7	11.9	0.53	4.5%	0.40	3.4%
ST55	10.7	12.4	11.2	0.48	4.3%	0.36	3.2%
LA85	9.4	10.8	10.3	0.52	5.0%	0.39	3.8%
LA55	9.6	11.1	10.3	0.44	4.2%	0.33	3.2%
LA85T0	8.4	10.6	9.6	0.80	8.4%	0.60	6.3%
LA85T48	9.7	11.5	10.9	0.54	5.0%	0.41	3.7%
LA85T63	9.7	11.5	10.5	0.63	6.0%	0.48	4.5%
SA85T0	10.4	12.3	11.2	0.64	5.8%	0.49	4.3%
SA85T40	11.4	12.8	12.2	0.37	3.0%	0.28	2.3%
SA85T53	10.0	14.6	12.2	1.40	11.5%	1.05	8.7%
Minimum	6.8			0.37	3.0%	0.28	2.3%
Maximum	16.0			1.62	16.1%	1.22	12.1%
Average	10.8			0.70	6.5%	0.53	4.9%
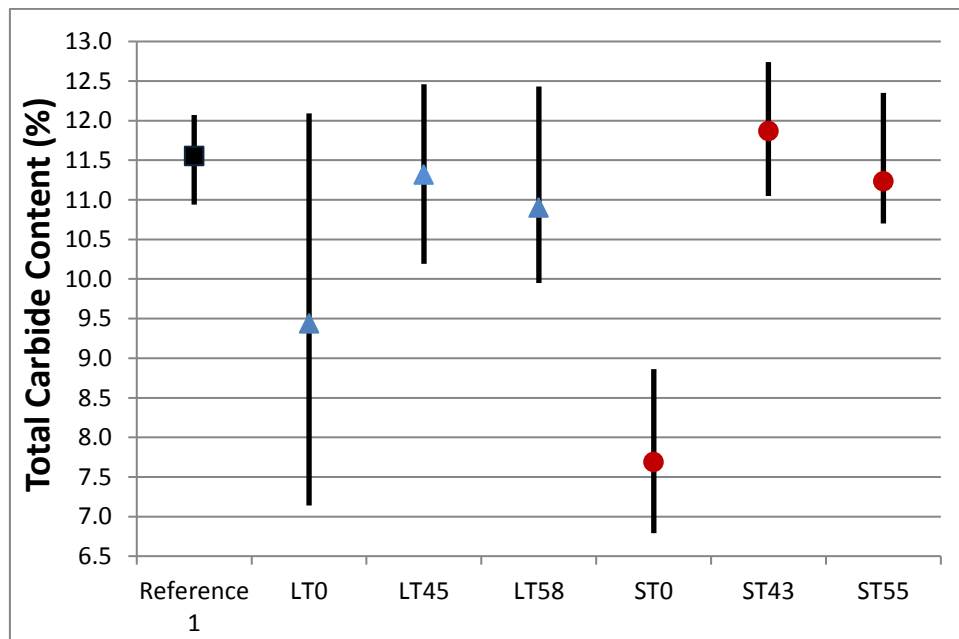
Figure 4-246: Average total carbide volume fraction measurement results and range of individual measurements for the LT and ST HSS sample sets.

197

Figure 4-247: Average total carbide volume fraction measurement results and range of individual measurements for the LA and SA HSS sample sets.

4.2.3.8. Combined Beraha's and Groesbeck's Etchant

In order to determine the total MC carbide volume fraction a combination of Groesbeck's and Beraha's etchants was used to achieve sufficient contrast for image analysis, see Figures 4-248 to 4-262.
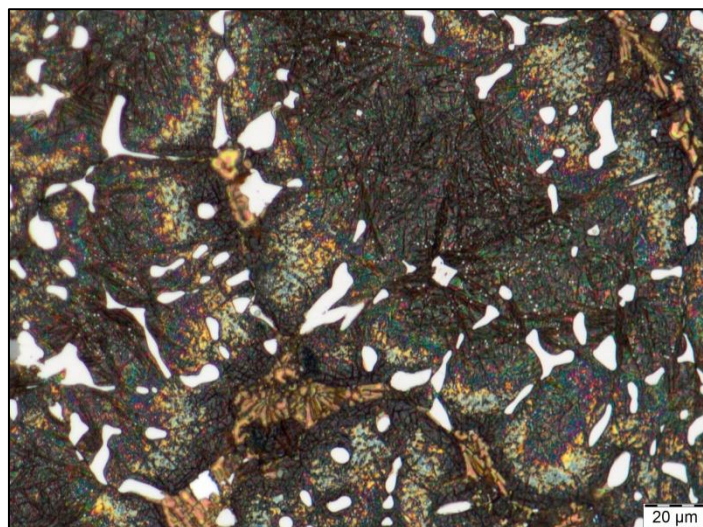
Figure 4-248: HSS sample Reference 1 etched with Beraha's and Groesbeck's etchant.
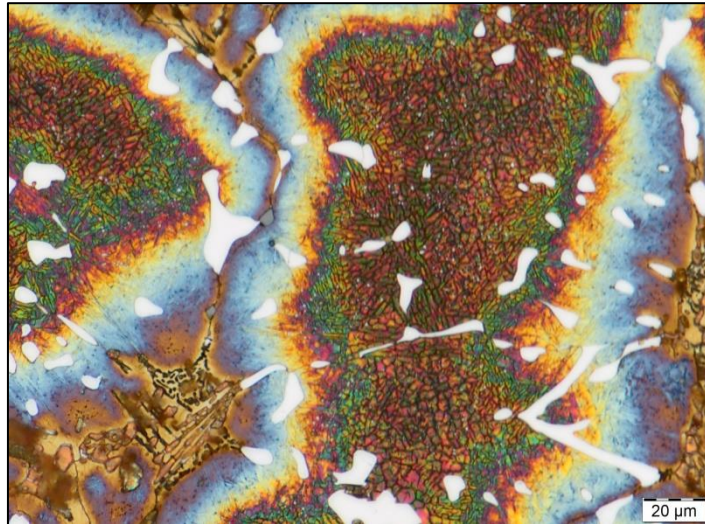
Figure 4-249: HSS sample LT0 etched with Beraha's and Groesbeck's etchant.
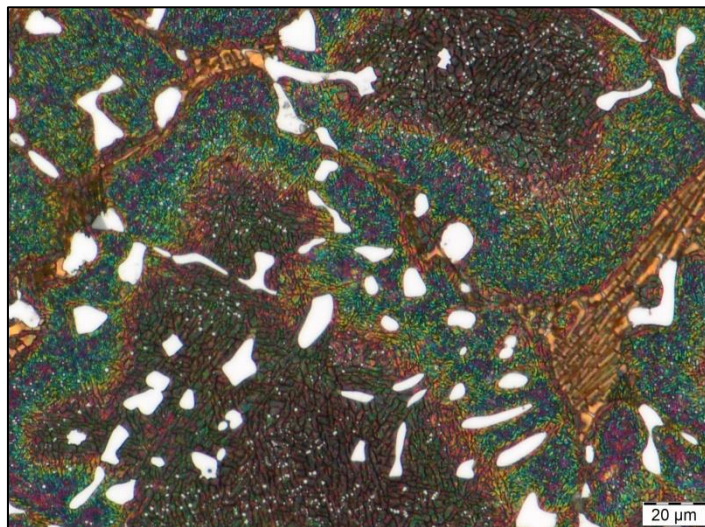
Figure 4-250: HSS sample LT45 etched with Beraha's and Groesbeck's etchant.
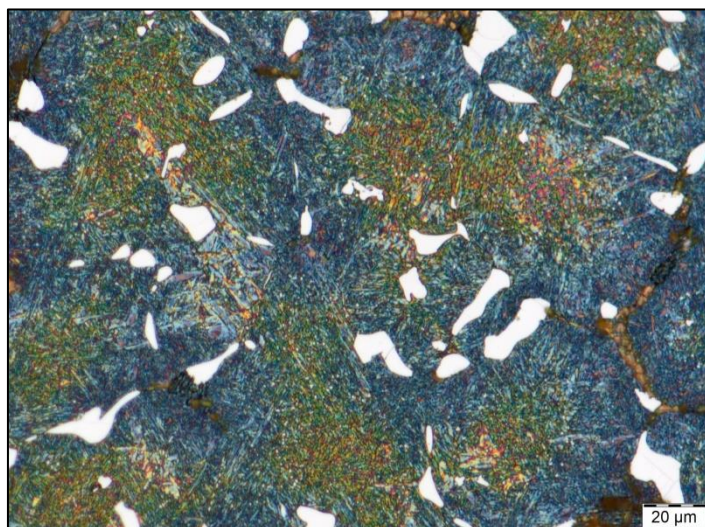
Figure 4-251: HSS sample LT58 etched with Beraha's and Groesbeck's etchant.

199
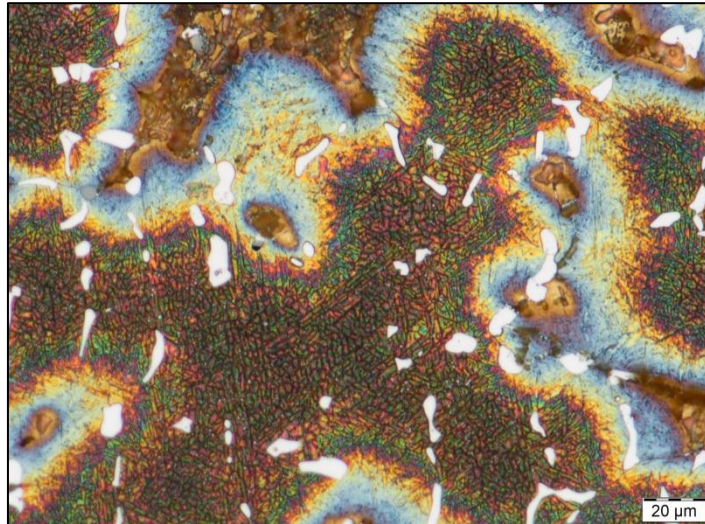
Figure 4-252: HSS sample ST0 etched with Beraha's and Groesbeck's etchant.
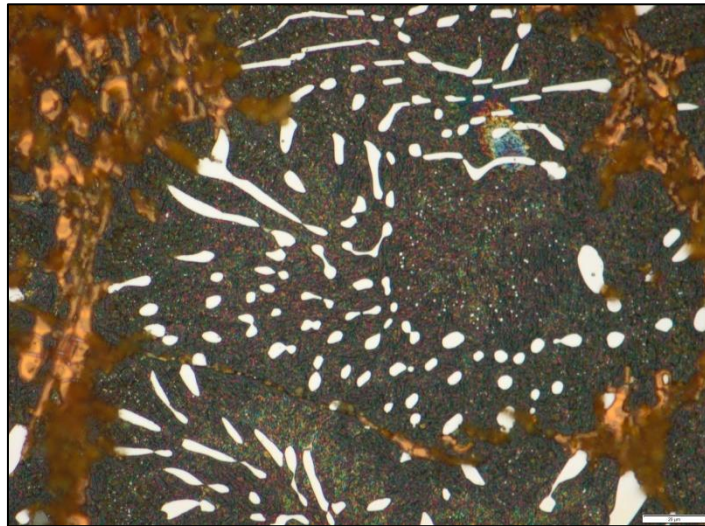
Figure 4-253: HSS sample ST43 etched with Beraha's and Groesbeck's etchant.
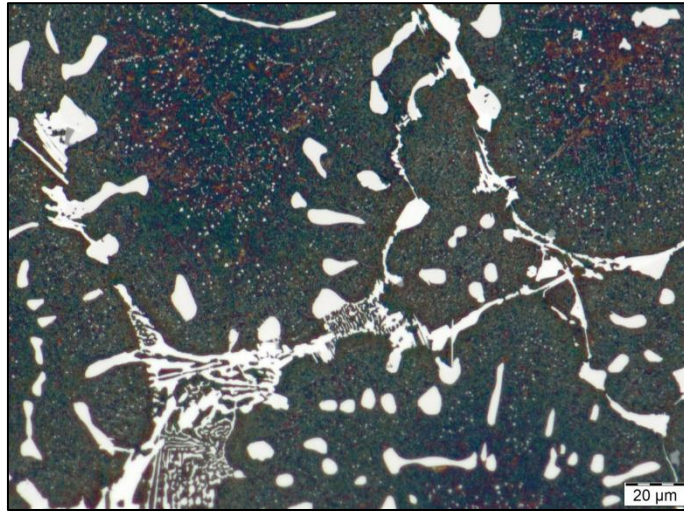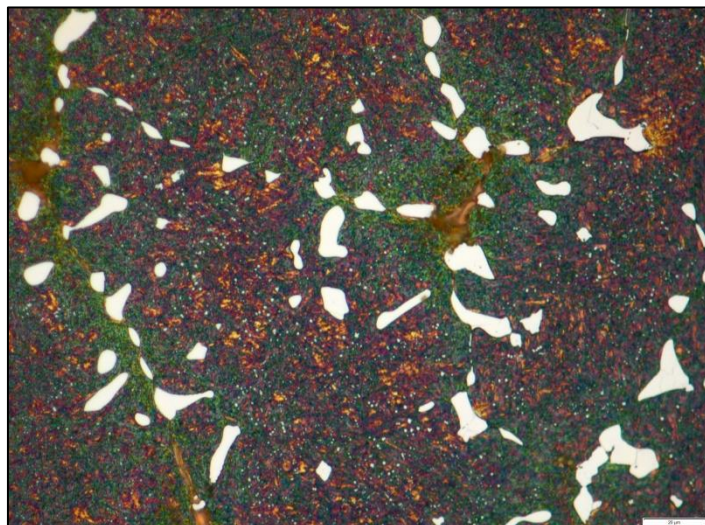

Figure 4-254: HSS sample ST55 etched with Beraha's and Groesbeck's etchant.

200
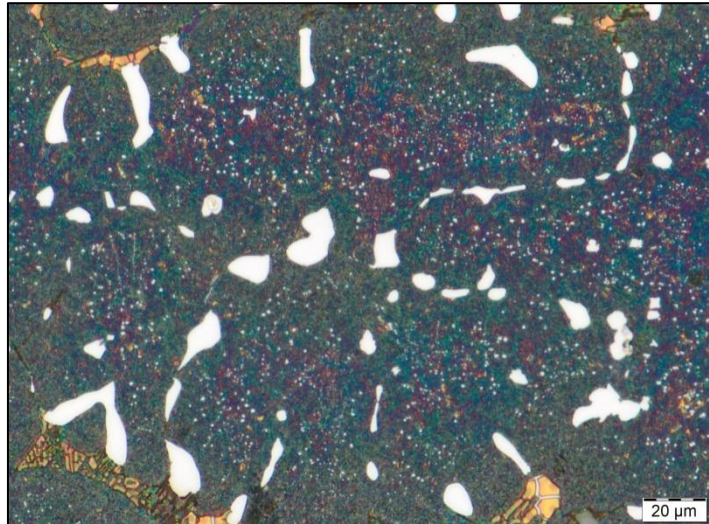
Figure 4-255: HSS sample LA85 etched with Beraha's and Groesbeck's etchant.
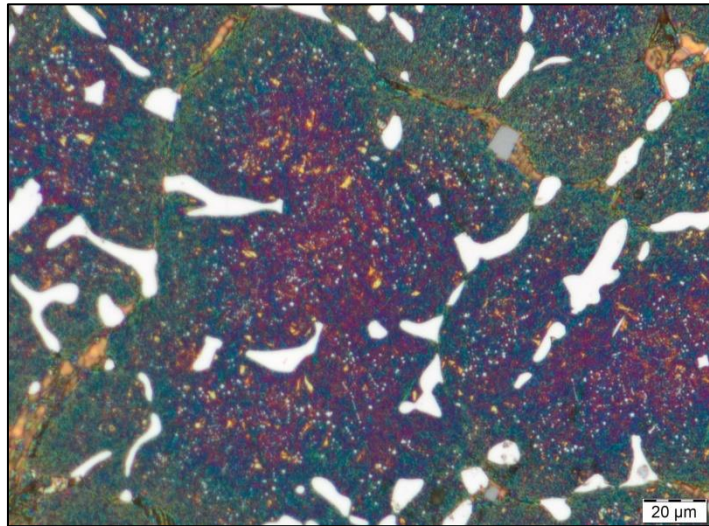
Figure 4-256: HSS sample LA55 etched with Beraha's and Groesbeck's etchant.
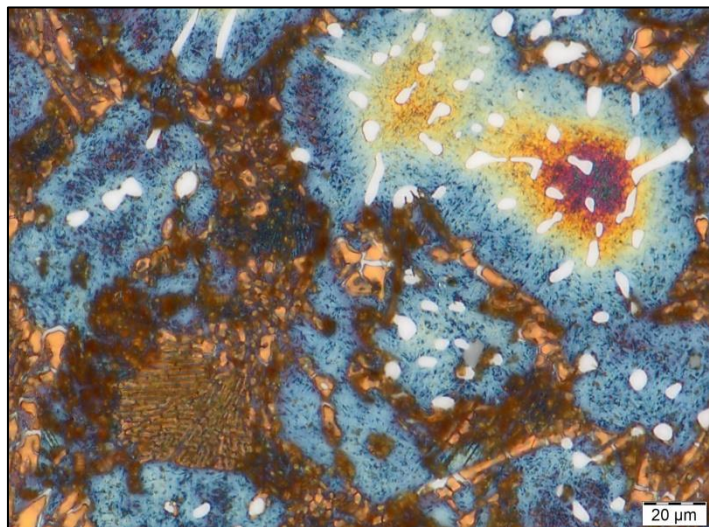
Figure 4-257: HSS sample LA85T0 etched with Beraha's and Groesbeck's etchant.

201
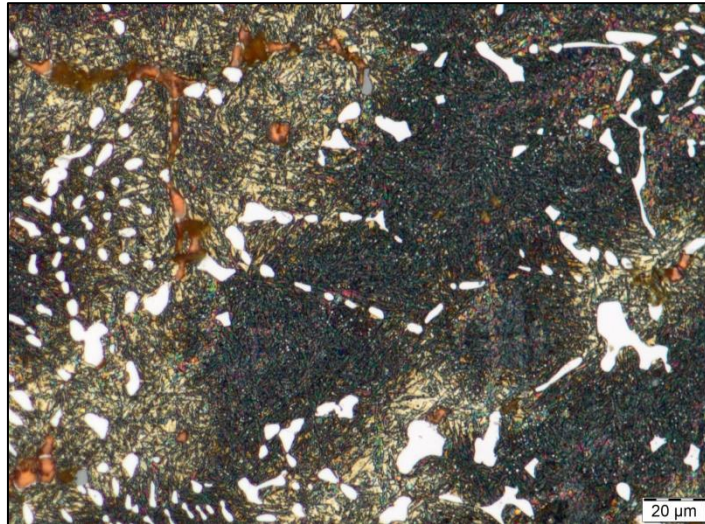
Figure 4-258: HSS sample LA85T48 etched with Beraha's and Groesbeck's etchant.
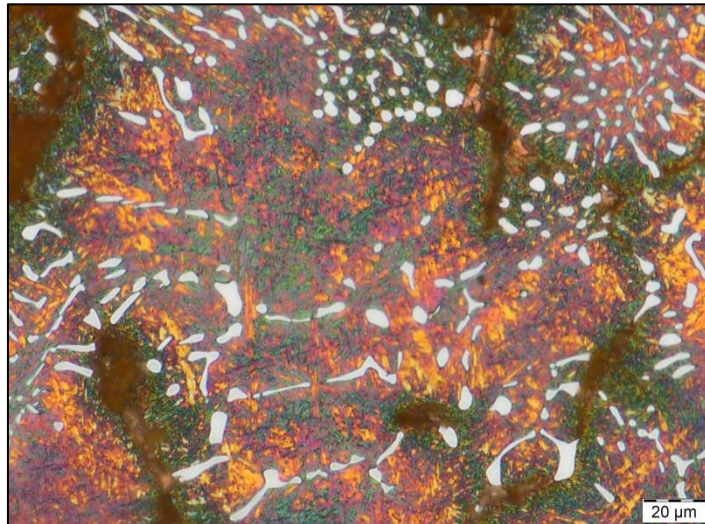
Figure 4-259: HSS sample LA85T60 etched with Beraha's and Groesbeck's etchant.
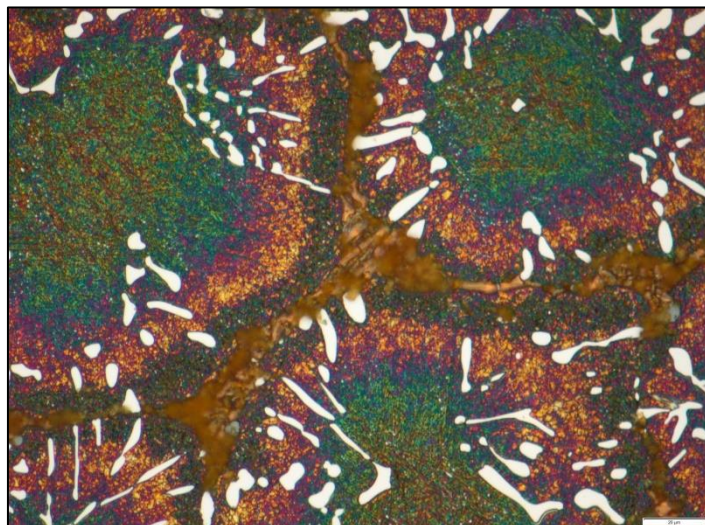
Figure 4-260: HSS sample SA85T0 etched with Beraha's and Groesbeck's etchant.

202
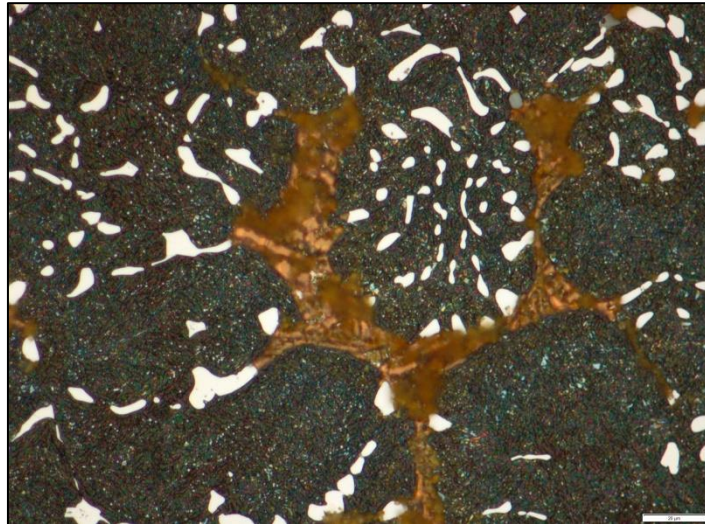
Figure 4-261: HSS sample SA85T40 etched with Beraha's and Groesbeck's etchant.
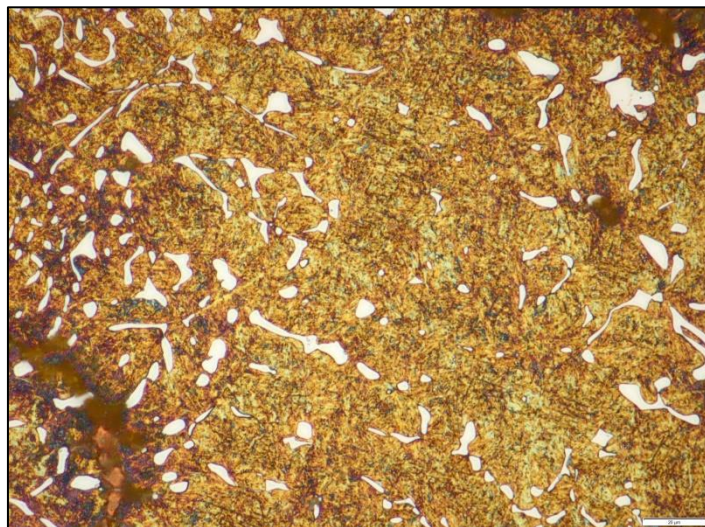
Figure 4-262: HSS sample SA85T53 etched with Beraha's and Groesbeck's etchant.

The results of the MC carbide volume fraction analysis is shown in Table 4-21, except for sample ST0, which showed insufficient contrast for the analysis. The total carbide content of the LT and ST sets showed a fairly small degree of variation between the samples, as expected, except for the untempered samples LT0, see Figure 4-263. The total carbide content of the LA and SA sets also showed a fairly small degree of variation between the samples, as expected, except for the untempered sample LA85T0 and sample SA85T53, see Figure 4-264. The low MC values of LT0 and LA85T0 were also attributed to the higher levels of RA, which influence the degree of etching and reduce the level of contrast, similar to the total carbide content analysis. The standard deviation, coefficient of variance and relative accuracy values were

203

acceptable indicating sufficient accuracy and repeatability. However, the RA value for sample LA85T63 was high at 9.6%.

Table 4-21: MC carbide content analysis results.

| Sample	MC Carbide Content (%)			Statistics			
	Minimum	Maximum	Average	S	CV	95%CL	RA
Reference 1	6.9	8.0	7.4	0.39	5.3%	0.30	4.0%
Reference 2	7.7	8.4	8.0	0.22	2.8%	0.17	2.1%
LT0	5.2	5.6	5.3	0.13	2.4%	0.10	1.8%
LT45	7.2	7.9	7.5	0.26	3.5%	0.20	2.7%
LT58	6.9	7.8	7.4	0.29	3.9%	0.22	2.9%
ST43	6.8	7.6	7.2	0.27	3.7%	0.20	2.8%
ST55	6.5	7.1	6.8	0.21	3.1%	0.16	2.3%
LA85	7.2	7.8	7.5	0.18	2.4%	0.13	1.8%
LA55	7.2	7.8	7.5	0.23	3.1%	0.18	2.4%
LA85T0	5.3	5.9	5.5	0.20	3.6%	0.15	2.7%
LA85T48	6.5	7.2	6.9	0.20	2.9%	0.15	2.2%
LA85T63	5.3	8.0	7.0	0.89	12.7%	0.67	9.6%
SA85T0	6.4	7.3	6.9	0.26	3.7%	0.19	2.8%
SA85T40	6.9	7.6	7.2	0.24	3.3%	0.18	2.5%
SA85T53	4.5	5.2	4.8	0.23	4.9%	0.18	3.7%
Minimum		4.5		0.13	2.4%	0.10	1.8%
Maximum		8.4		0.89	12.7%	0.67	9.6%
Average		6.8		0.28	4.1%	0.21	3.1%
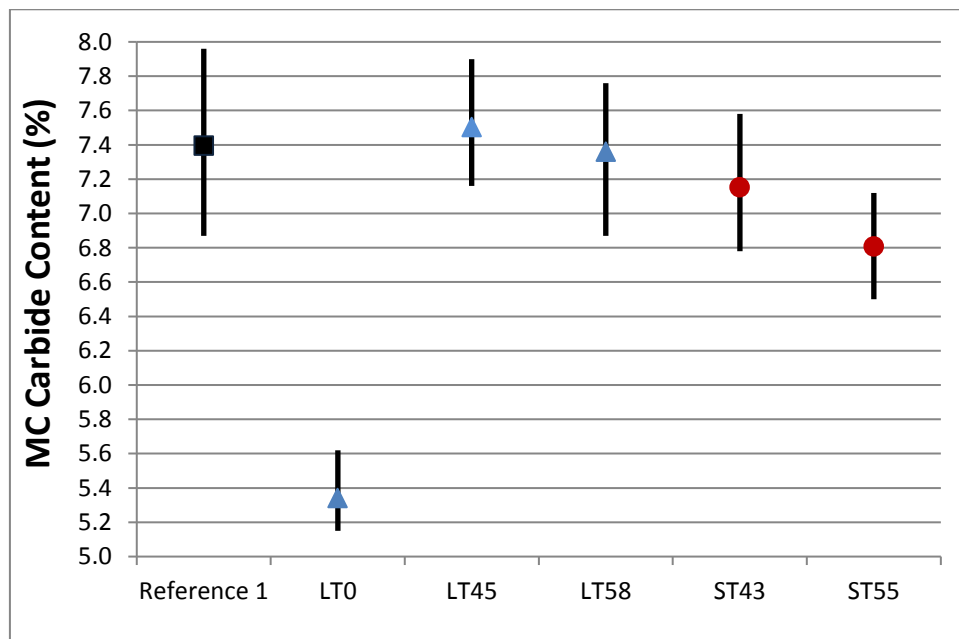
Figure 4-263: Average MC carbide volume fraction measurement results and range of individual measurements for the LT and ST HSS sample sets.
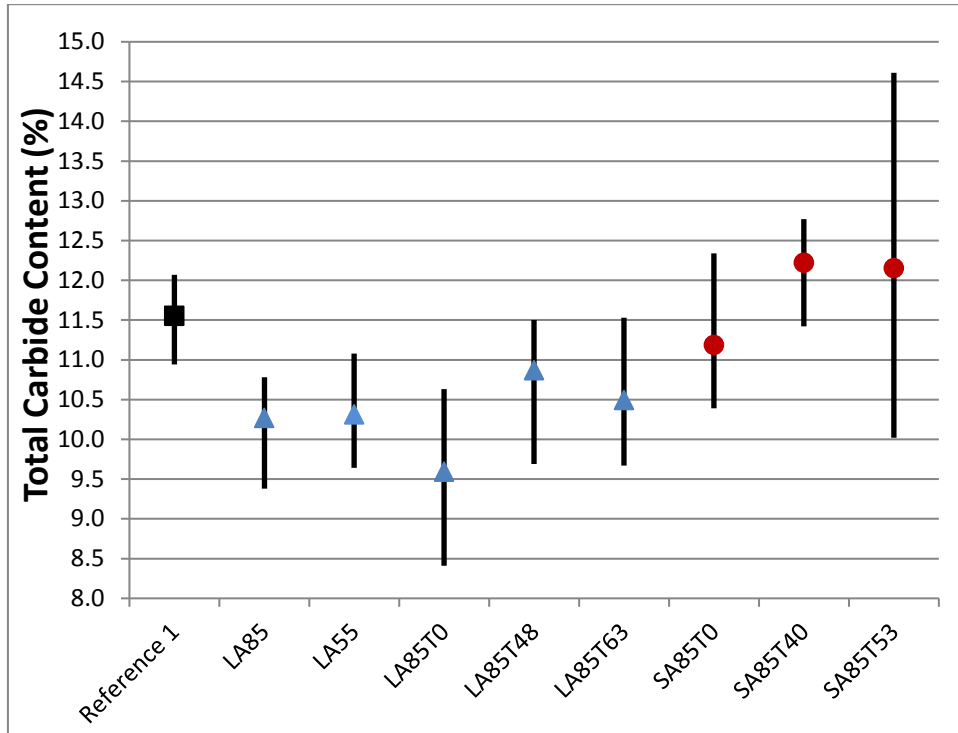
204
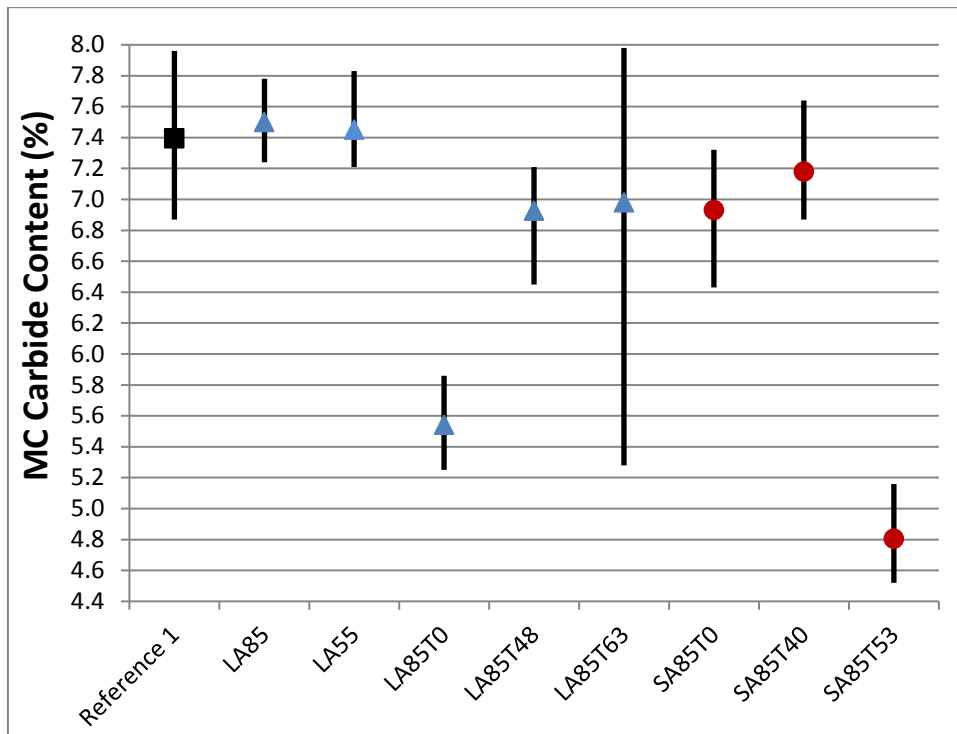
Figure 4-264: Average MC carbide volume fraction measurement results and range of individual measurements for the LA and SA HSS sample sets.

4.2.4. Scanning Electron Microscope (SEM) Analysis

The general structures of the HC samples examined by SEM were similar to the optical metallographic observations; see Figures 4-265 to 4-273. The most abundant carbide type was the M_7C_3, which was darker in contrast than the matrix and was found on the grain boundaries. Little to no M_6C/M_2C carbides were present as white carbides. The $M_{23}C_6/M_7C_3$ secondary carbides were also observed on all the samples except for Reference 1, ST0 and ST45. The results are in agreement with the metallography analysis.

205
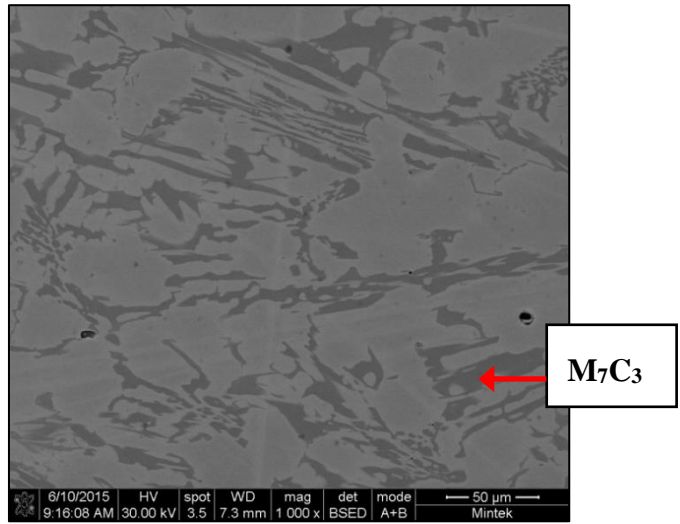
Figure 4-265: SEM image of HC sample Reference 1, showing no secondary carbides.
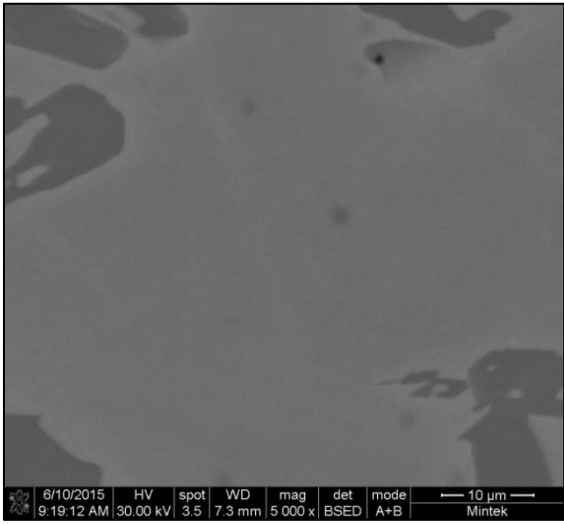
Figure 4-266: SEM image of HC sample Reference 1, showing no secondary carbides at higher magnification.
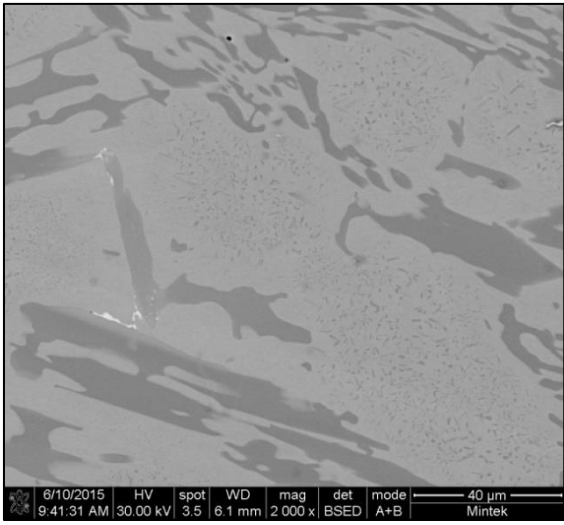
Figure 4-267: SEM image of HC sample LT0, showing secondary carbides.
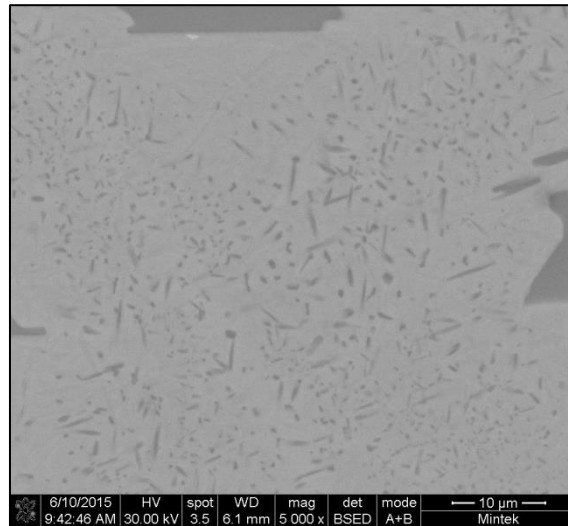
Figure 4-268: SEM image of HC sample LT0, showing secondary carbides at higher magnification.
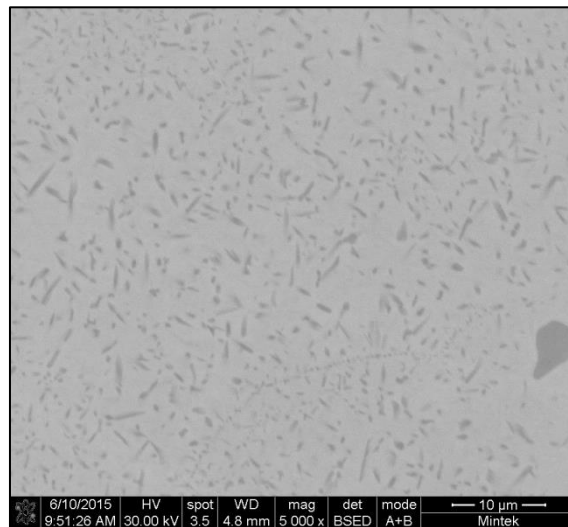
Figure 4-269: SEM image of HC sample LT48, showing secondary carbides.
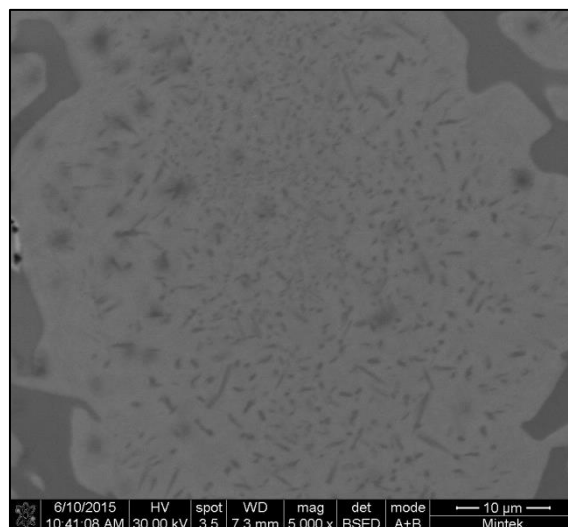
Figure 4-270: SEM image of HC sample LT58, showing secondary carbides.
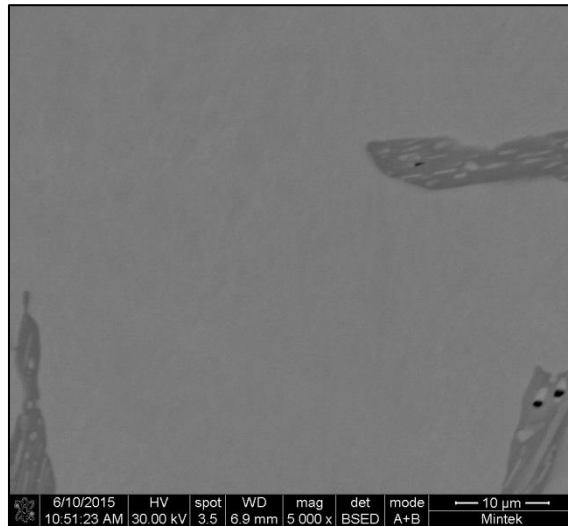
Figure 4-271: SEM image of HC sample ST0, showing no secondary carbides.
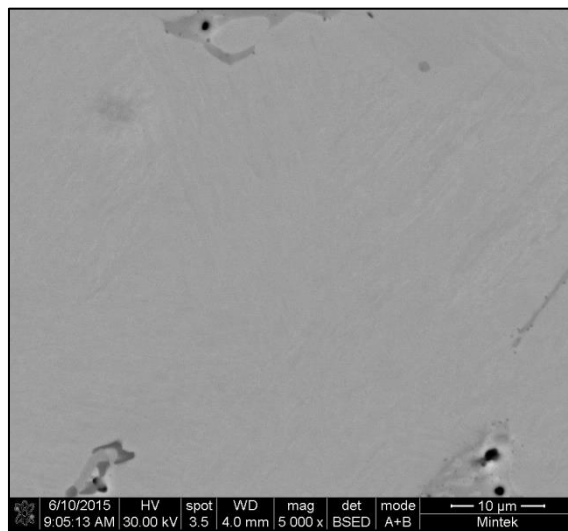
Figure 4-272: SEM image of HC sample ST45, showing secondary carbides.
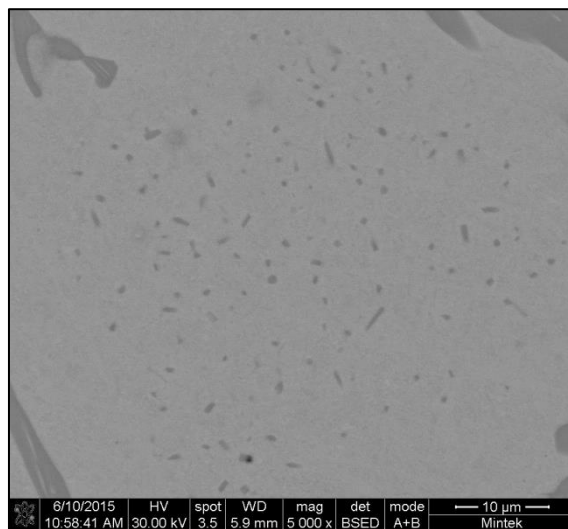
Figure 4-273: SEM image of HC sample ST60, showing secondary carbides.

208

The general structures of the HSS samples examined by SEM were similar to the optical metallographic observations and showed a matrix containing three distinct types of primary carbides, see Figures 4-274 to 4-309. The most abundant type was black in colour and was found predominantly within the matrix and not on the grain boundaries. These carbides are assumed to be MC carbides based on the size, shape and abundance shown during metallography. The second type was white in appearance and was limited to the grain boundaries. These carbides are assumed to be M_6C/M_2C carbides based on the shape and occurrence shown during metallography. The third type was grey in appearance similar to the matrix, which made them difficult to positively distinguish from the matrix on most of the samples, despite showing clear boundaries between the carbide and the matrix. The grey carbides were also limited to the grain boundaries, but were generally coarser than the white carbides with similar morphology. These carbides are assumed to be M_7C_3 carbides based on the shape and occurrence shown during metallography.
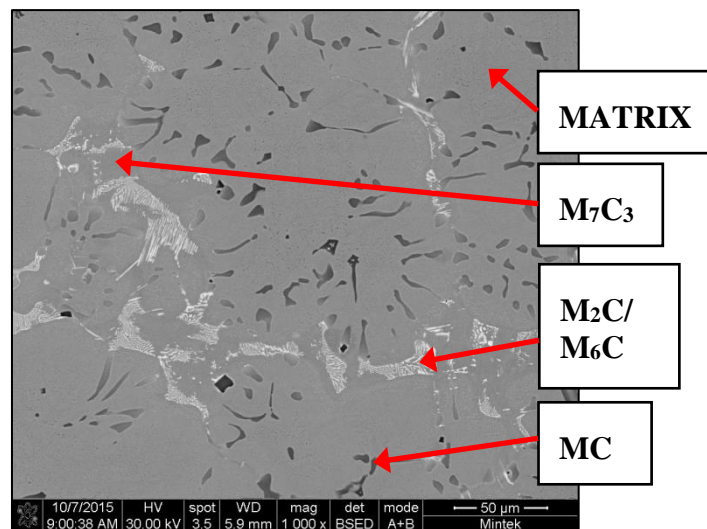
Figure 4-274: SEM image of HSS sample Reference 1.
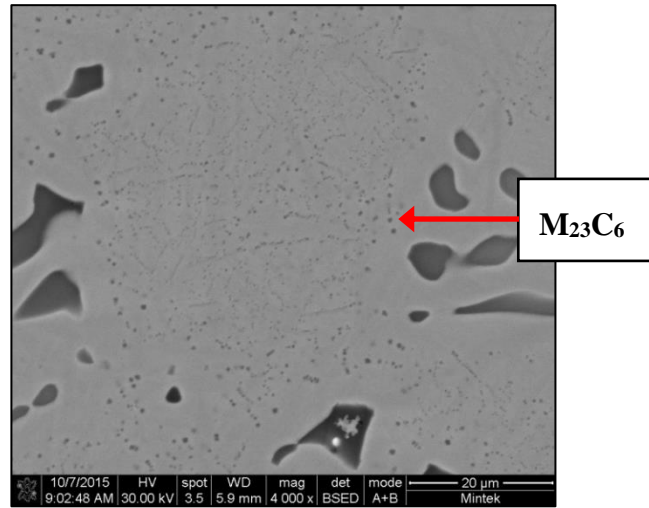
Figure 4-275: SEM image of HSS sample Reference 1 at higher magnification, showing $M_{23}C_6$ secondary carbides.
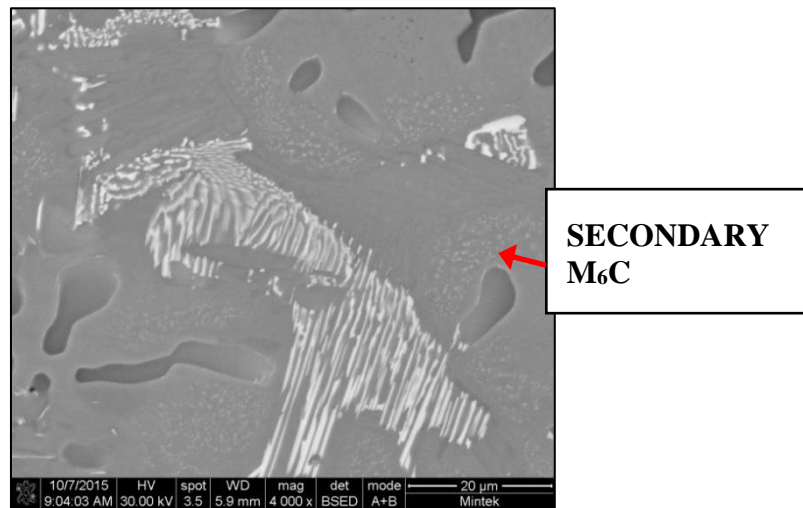
Figure 4-276: SEM image of HSS sample Reference 1 at higher magnification, showing no M_6C secondary carbides.
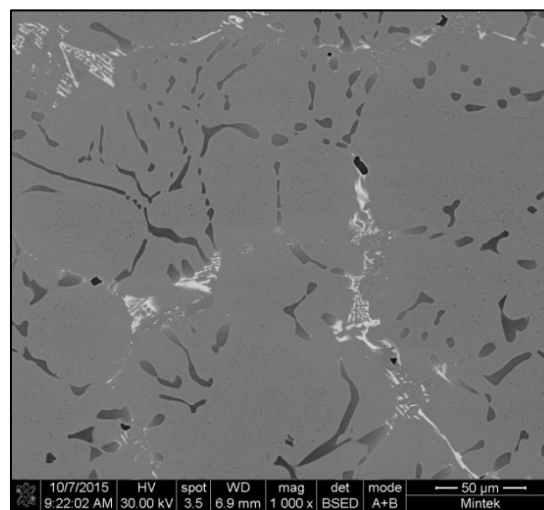
Figure 4-277: SEM image of HSS sample LT0.

210
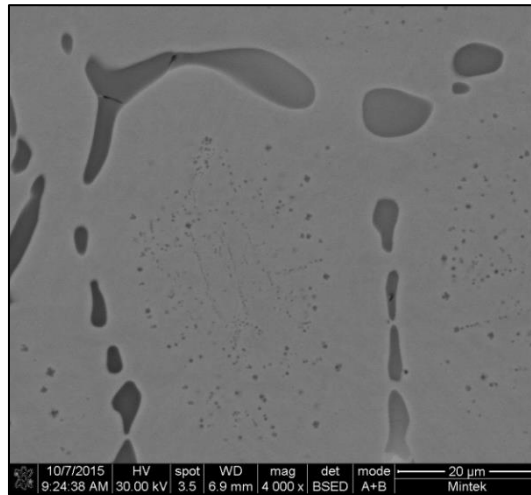
Figure 4-278: SEM image of HSS sample LT0 at higher magnification, showing $M_{23}C_6$ secondary carbides.
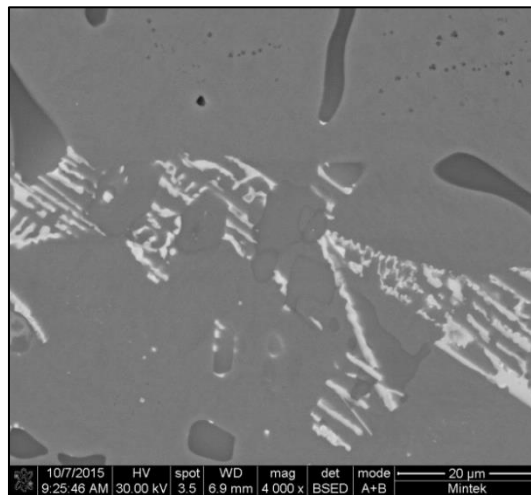
Figure 4-279: SEM image of HSS sample LT0 at higher magnification, showing no M_6C secondary carbides.
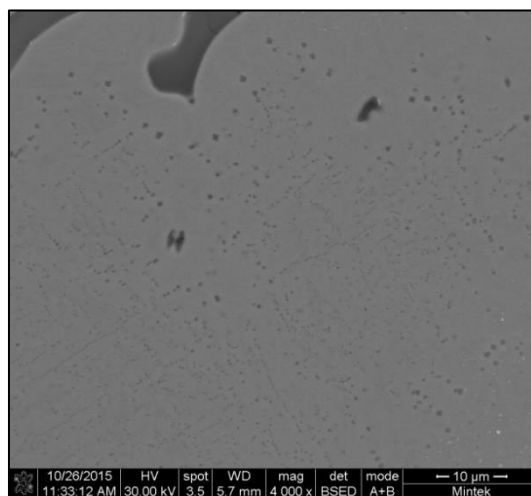
Figure 4-280: SEM image of HSS sample LT45 at higher magnification, showing $M_{23}C_6$ secondary carbides.

211
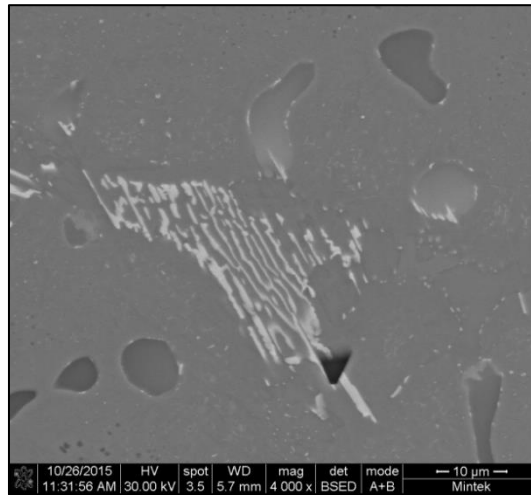
Figure 4-281: SEM image of HSS sample LT45 at higher magnification, showing some M_6C secondary carbides.
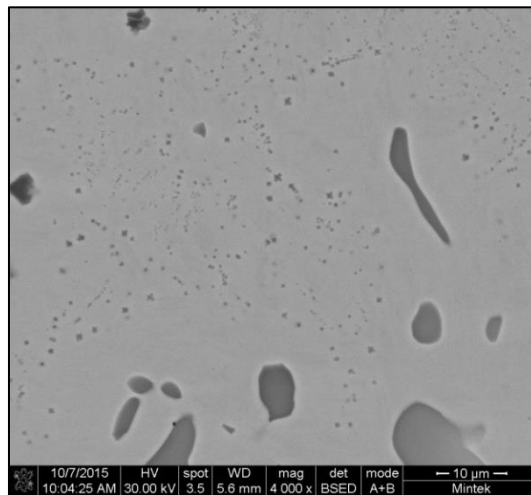
Figure 4-282: SEM image of HSS sample LT58 at higher magnification, showing $M_{23}C_6$ secondary carbides.
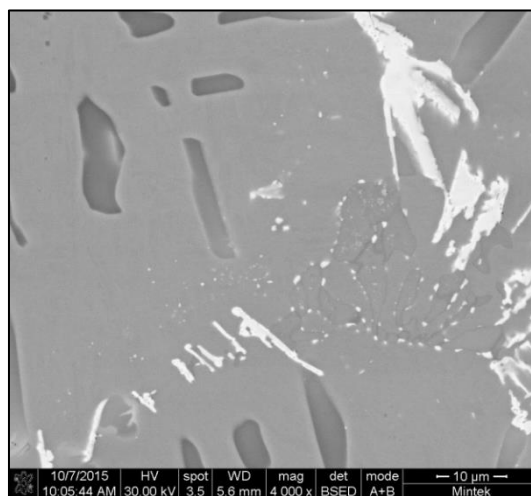
Figure 4-283: SEM image of HSS sample LT58 at higher magnification, showing M_6C secondary carbides.

212
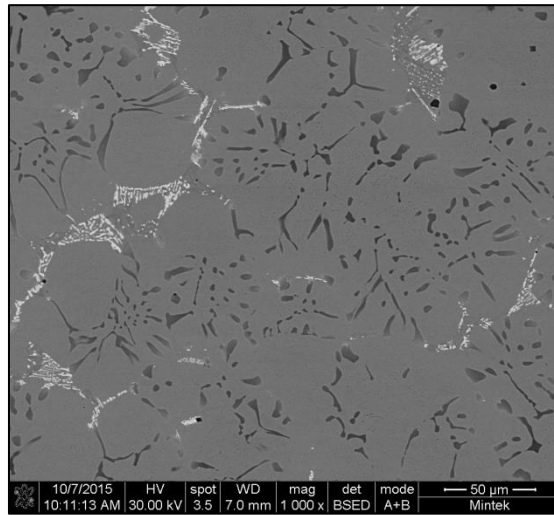
Figure 4-284: SEM image of HSS sample ST0.
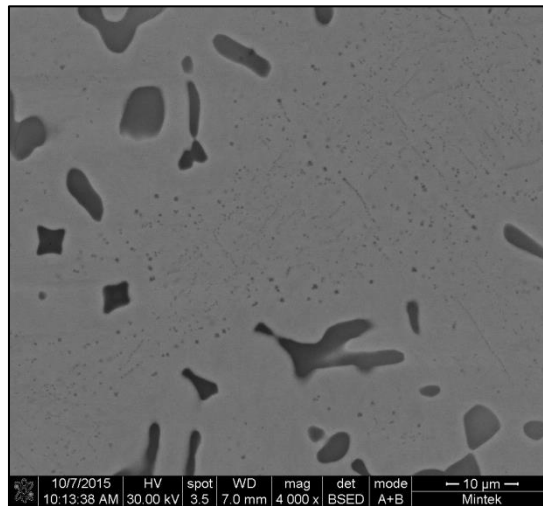
Figure 4-285: SEM image of HSS sample ST0 at higher magnification, showing $M_{23}C_6$ secondary carbides.
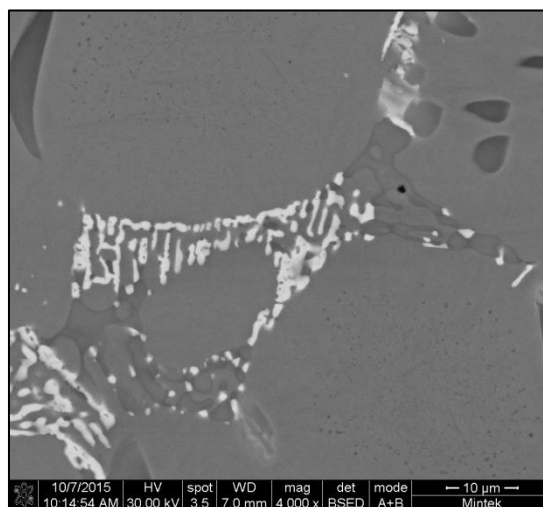
Figure 4-286: SEM image of HSS sample ST0 at higher magnification, showing no M_6C secondary carbides.

213
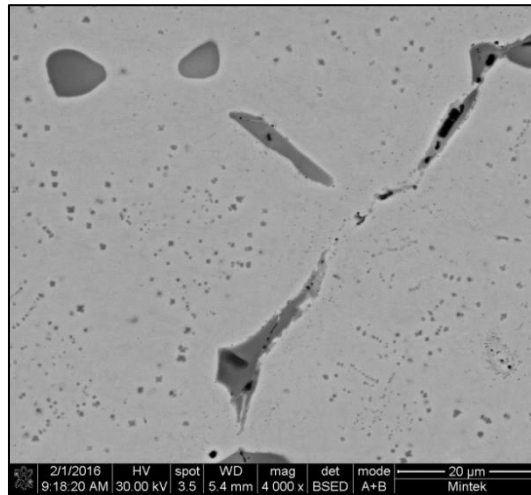
Figure 4-287: SEM image of HSS sample ST43 at higher magnification, showing $M_{23}C_6$ secondary carbides.
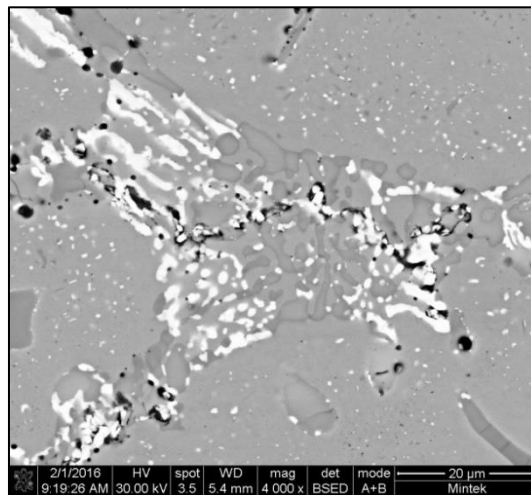
Figure 4-288: SEM image of HSS sample ST43 at higher magnification, showing M_6C secondary carbides.
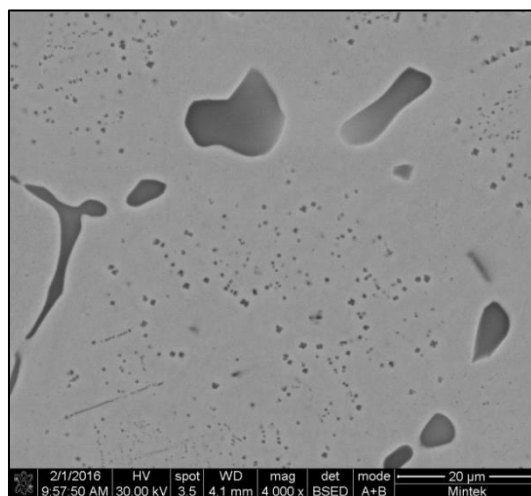
Figure 4-289: SEM image of HSS sample ST55 at higher magnification, showing $M_{23}C_6$ secondary carbides.

214
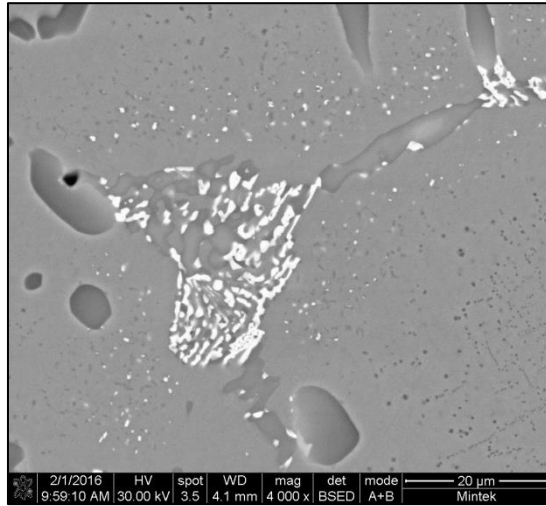
Figure 4-290: SEM image of HSS sample ST55 at higher magnification, showing no M_6C secondary carbides.
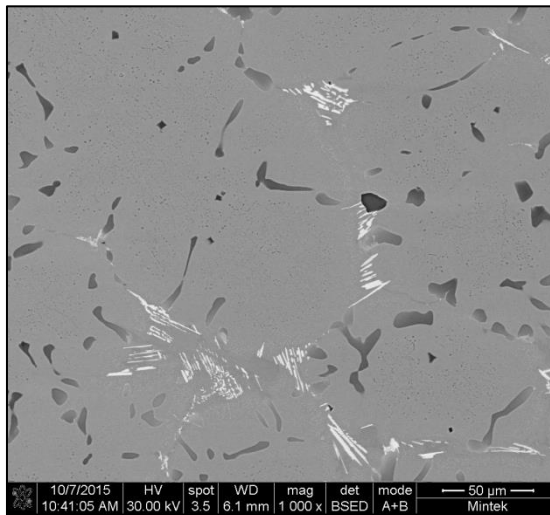
Figure 4-291: SEM image of HSS sample LA85.
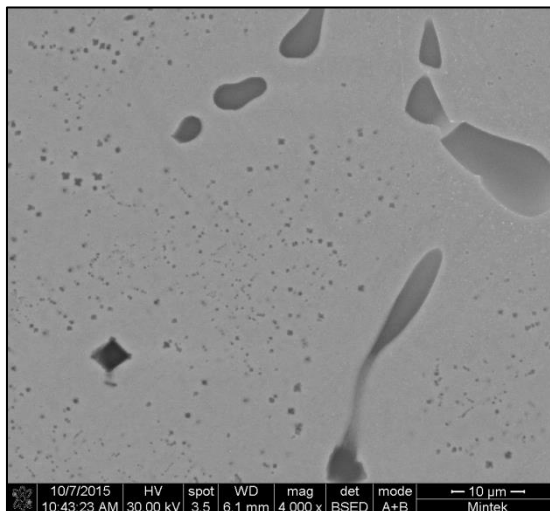
Figure 4-292: SEM image of HSS sample LA85 at higher magnification, showing $M_{23}C_6$ secondary carbides.

215
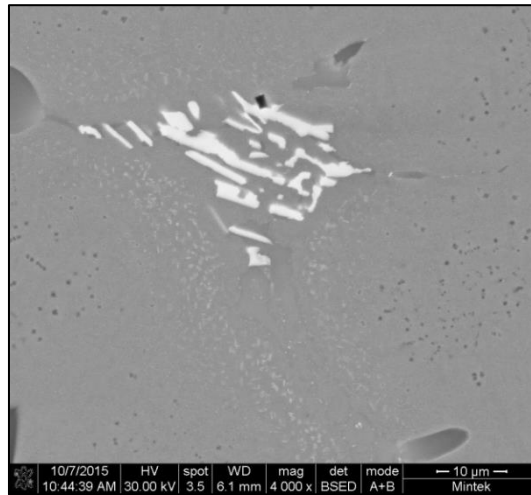
Figure 4-293: SEM image of HSS sample LA85 at higher magnification, showing fine M_6C secondary carbides.
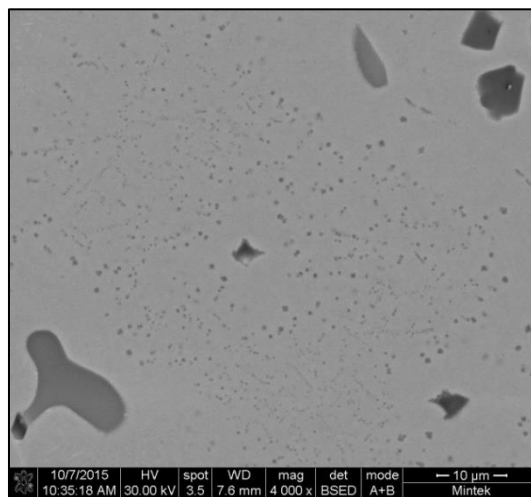
Figure 4-294: SEM image of HSS sample LA55 at higher magnification, showing $M_{23}C_6$ secondary carbides.
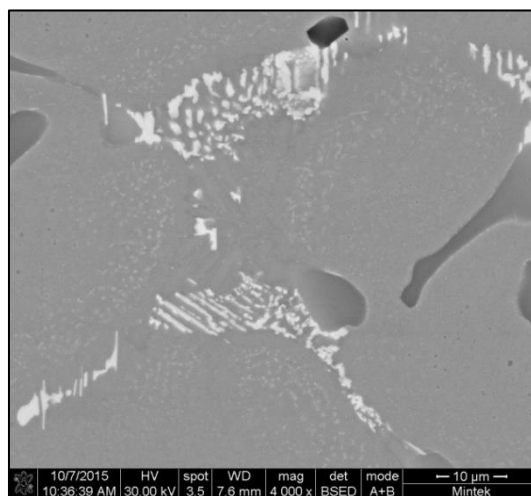
Figure 4-295: SEM image of HSS sample LA55 at higher magnification, showing fine M_6C secondary carbides.

216
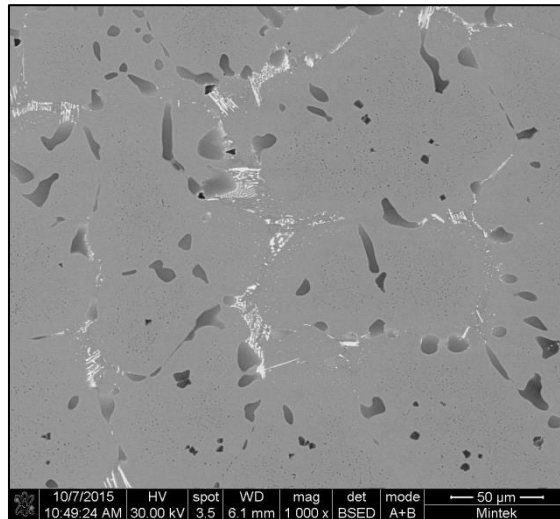
Figure 4-296: SEM image of HSS sample LA85T0.
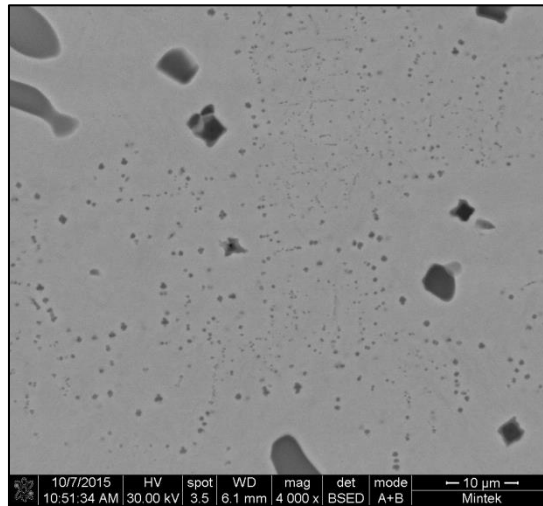
Figure 4-297: SEM image of HSS sample LA85T0 at higher magnification, showing $M_{23}C_6$ secondary carbides.
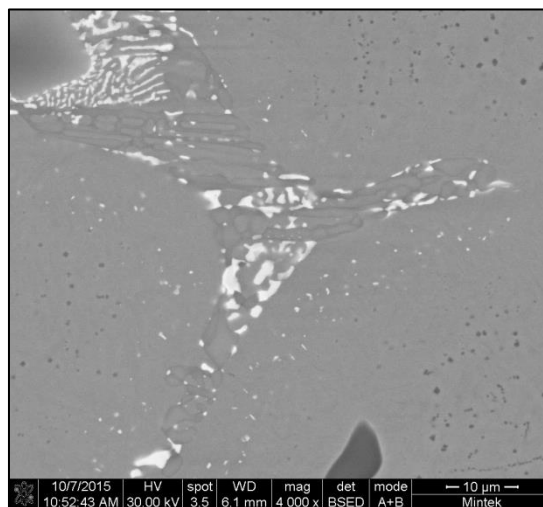
Figure 4-298: SEM image of HSS sample LA85T0 at higher magnification, showing M_6C secondary carbides.

217
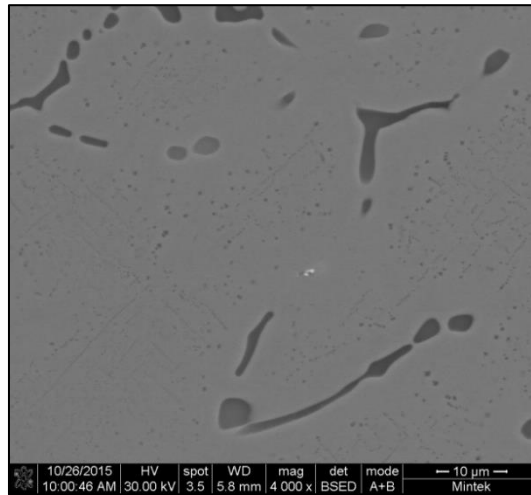
Figure 4-299: SEM image of HSS sample LA85T48 at higher magnification, showing $M_{23}C_6$ secondary carbides.
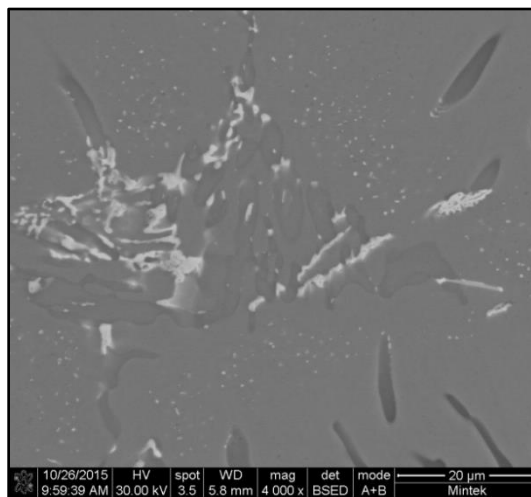
Figure 4-300: SEM image of HSS sample LA85T48 at higher magnification, showing no M_6C secondary carbides.
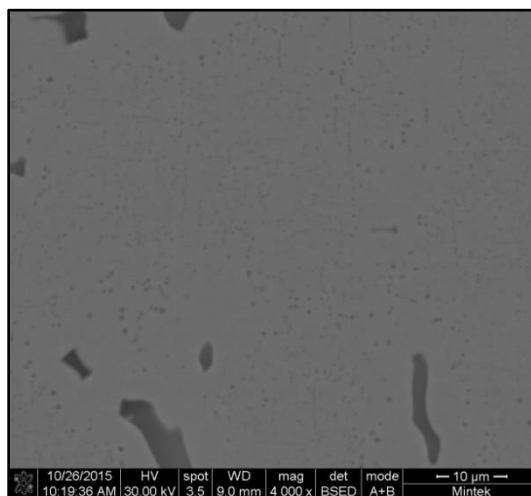
Figure 4-301: SEM image of HSS sample LA85T60 at higher magnification, showing $M_{23}C_6$ secondary carbides.

218
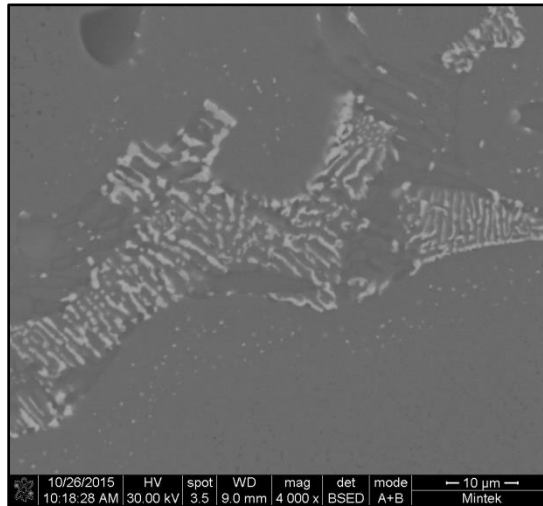
Figure 4-302: SEM image of HSS sample LA85T60 at higher magnification, showing M$_6$C secondary carbides.
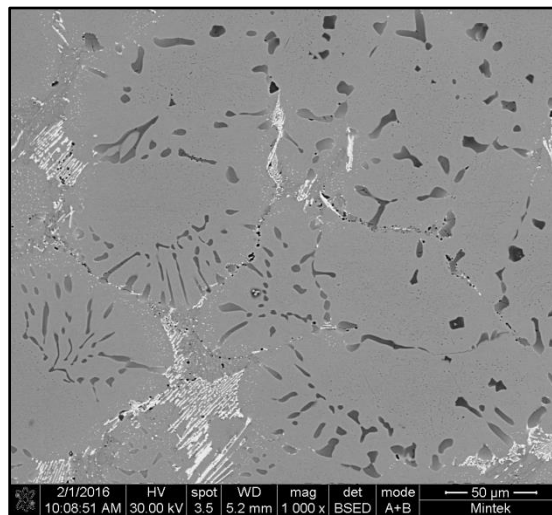
Figure 4-303: SEM image of HSS sample SA85T0.
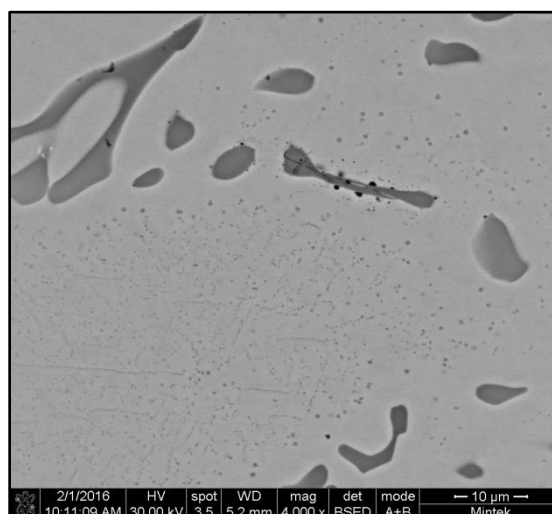
Figure 4-304: SEM image of HSS sample SA85T0 at higher magnification, showing M$_{23}$C$_6$ secondary carbides.

219
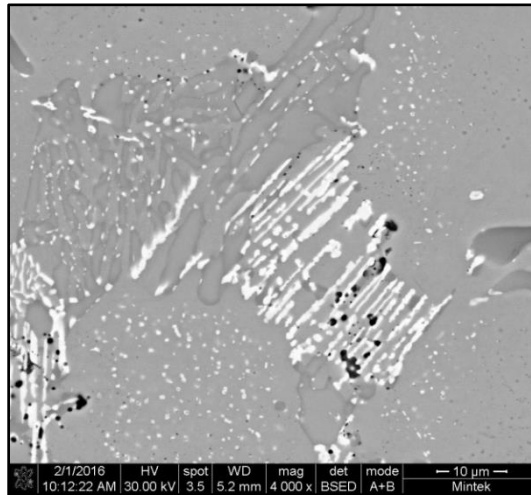
Figure 4-305: SEM image of HSS sample SA85T0 at higher magnification, showing no M_6C secondary carbides.
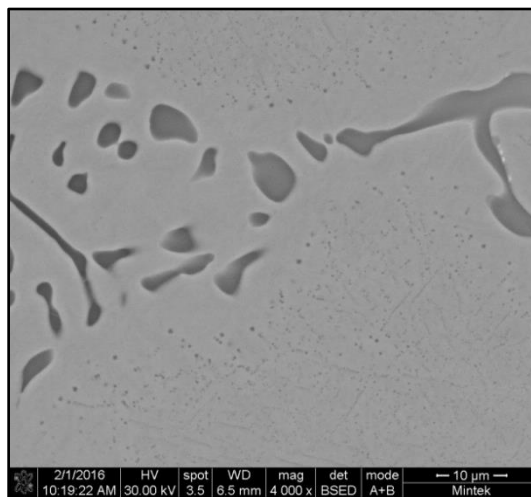
Figure 4-306: SEM image of HSS sample SA85T40 at higher magnification, showing $M_{23}C_6$ secondary carbides.
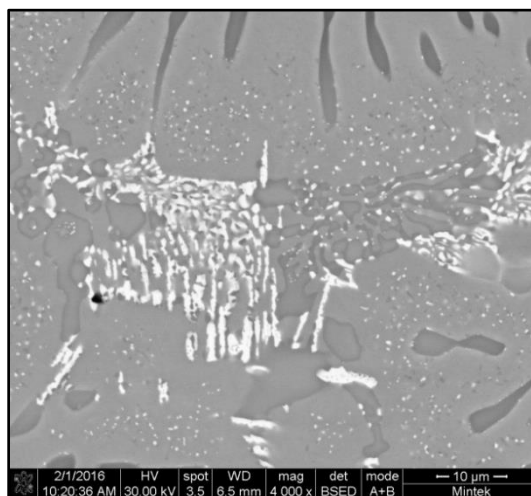
Figure 4-307: SEM image of HSS sample SA85T40 at higher magnification, showing no M_6C secondary carbides.

220
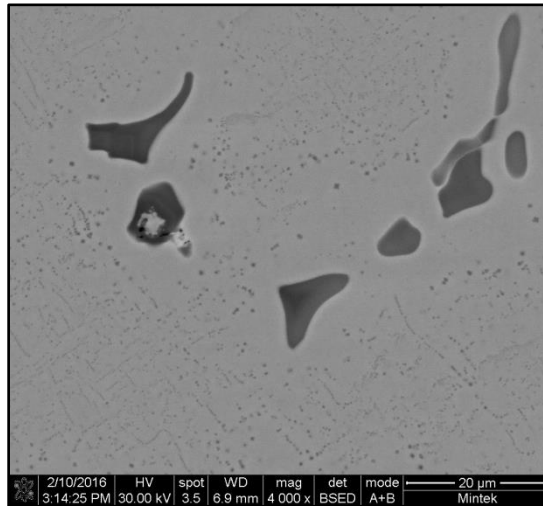
Figure 4-308: SEM image of HSS sample SA85T53 at higher magnification, showing $M_{23}C_6$ secondary carbides.
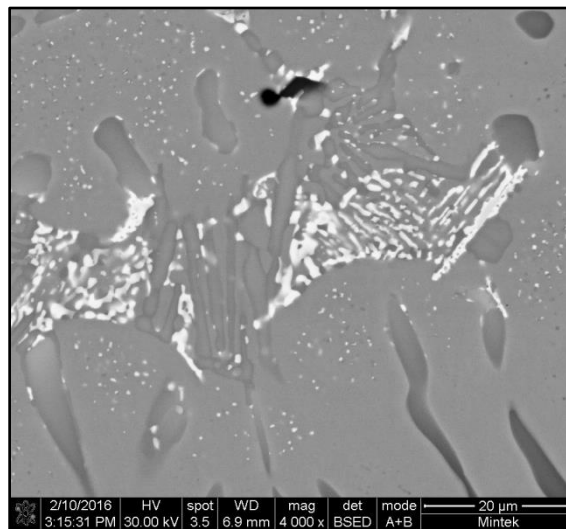
Figure 4-309: SEM image of HSS sample SA85T53 at higher magnification, showing no M_6C secondary carbides.

4.2.5. X-Ray Diffraction (XRD) Analysis

The XRD analysis identified three distinct phases within the HSS material, which included alpha iron, austenite and MC carbides, see Table 4-22. Indications of M_7C_3 M_2C/M_6C and $M_{23}C_6$ carbide were only identified on some of the samples by XRD, despite being confirmed to be present in all of the samples during metallography, see Figures 4-310 to 4-329. Hence, these carbides were excluded from the quantification as the analysis would be questionable.

221

Table 4-22: XRD analysis results.

Sample	Phase volume %		
	Austenite	Iron	MC
Reference 1	25.9	67.7	6.4
Reference 3	22.3	66.8	10.9
LT0	17.0	76.3	6.8
LT45	14.1	79.9	6.0
LT48	16.2	74.5	9.3
LT50	14.9	76.7	8.4
LT53	0.8	92.6	6.7
LT55	0.0	93.3	6.7
LT58	0.0	93.6	6.4
ST0	20.4	71.4	8.2
ST43	12.4	80.6	7.0
ST45	12.8	79.9	7.3
ST48	8.3	84.2	7.5
ST50	1.9	91.8	6.3
ST53	1.1	92.3	6.6
ST55	0.6	92.0	7.4
LA85	0.2	92.8	7.0
LA55	0.7	92.7	6.6
LA85T0	18.2	75.1	6.7
LA85T48	43.3	50.2	6.4
LA85T50	27.9	61.6	10.5
LA85T53	16.7	77.4	5.9
LA85T55	9.1	82.6	8.3
LA85T58	1.1	90.2	8.7
LA85T60	1.3	90.2	8.5
LA85T63	0.0	93.1	6.9
SA85T0	9.6	84.3	6.1
SA85T40	12.7	79.8	7.5
SA85T43	11.2	81.0	7.9
SA85T45	8.1	85.1	6.9
SA85T48	1.6	91.6	6.9
SA85T50	0.2	94.0	5.9
SA85T53	0.1	92.0	7.9
SA85T55	0.0	92.3	7.7

The austenite content generally decreased with increasing tempering temperature, as expected. The difference in austenite content between the heat treatment conditions was offset by the change in Fe content. This is expected since the austenite is transformed to martensite during heat treatment.

222

The MC carbide content showed a fair degree of variation between the heat treatment conditions and should be regarded as semi quantitative. The peak retained austenite content was similar for the different conditions and ranged from 13-16%, except for the LA sample set that showed a peak retained austenite content in excess of 40%.

The retained austenite was predominantly eliminated on both the LT and ST sample sets at 525°C. The retained austenite was predominantly eliminated on the LA and SA samples sets at 575°C and 500°C respectively.
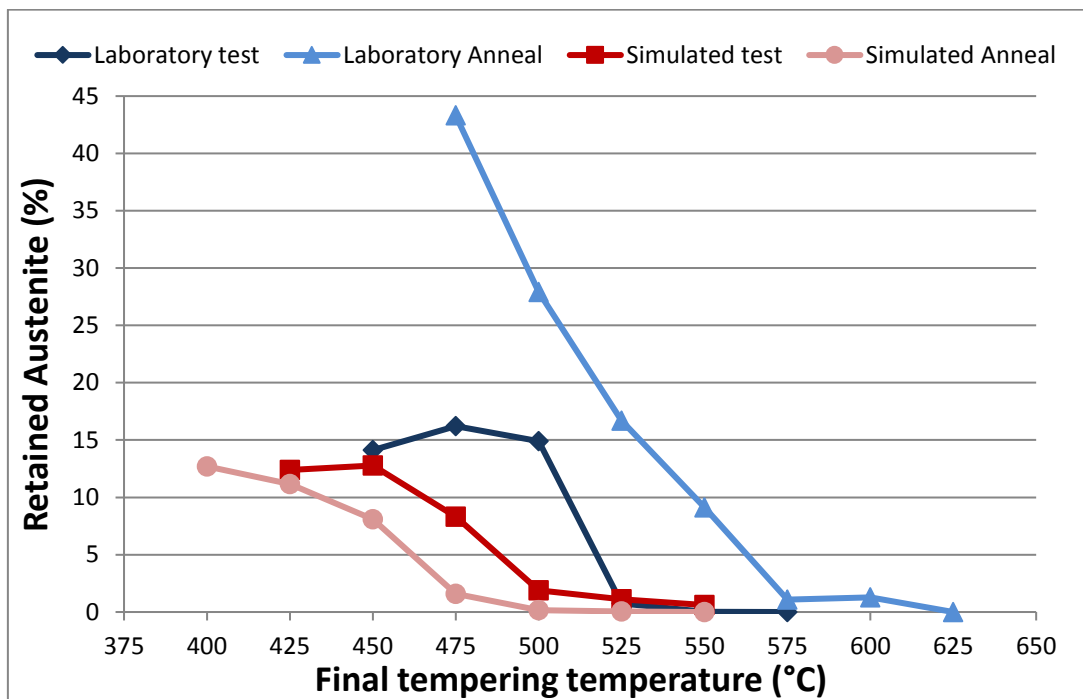
Figure 4-310: Change in retained austenite content with tempering temperature.
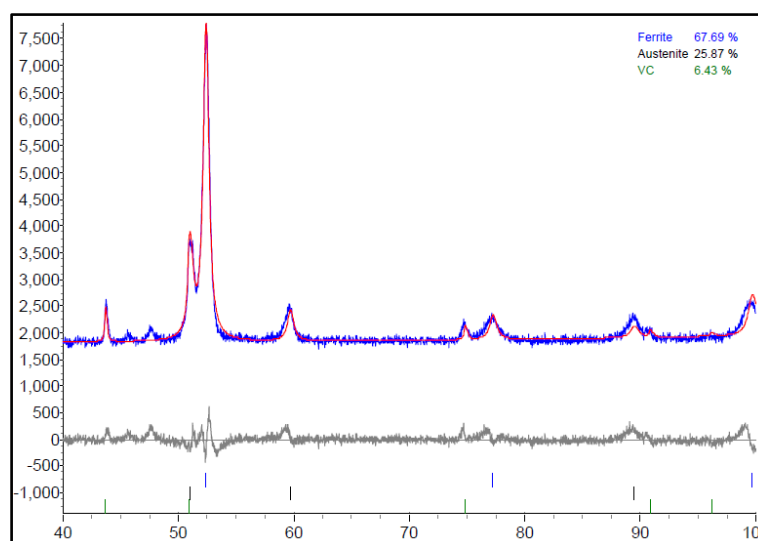
Figure 4-311: XRD spectrum for Reference 1.
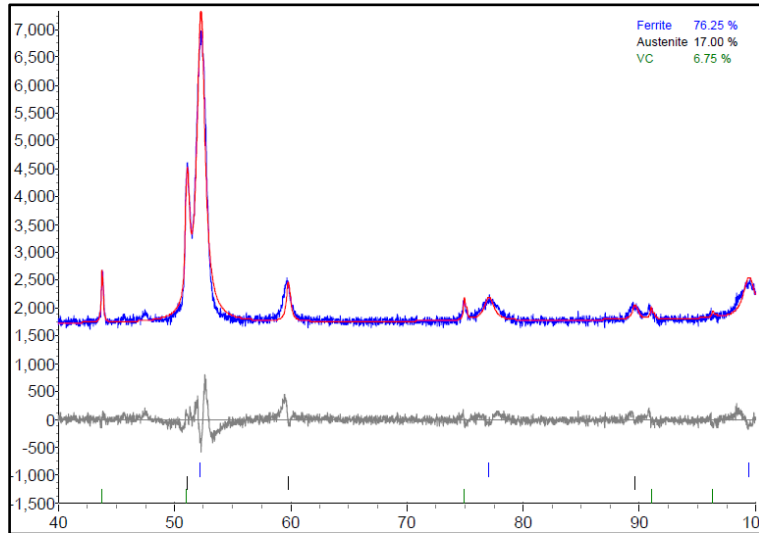
Figure 4-312: XRD spectrum for LT0.
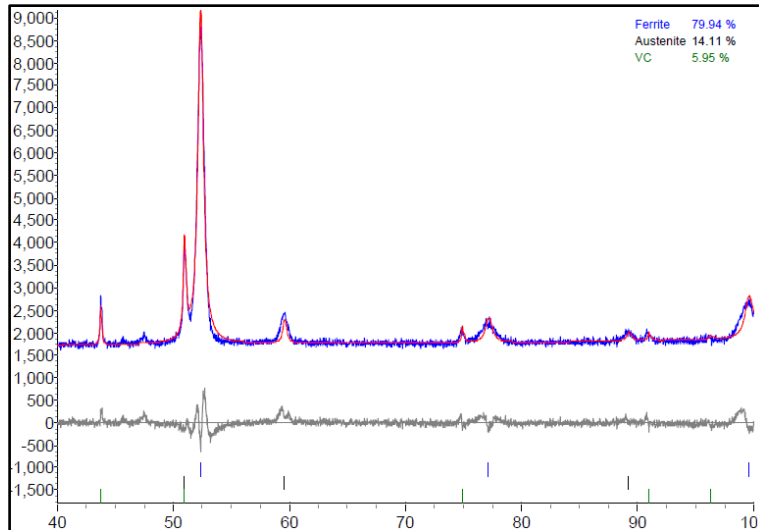
Figure 4-313: XRD spectrum for LT45.
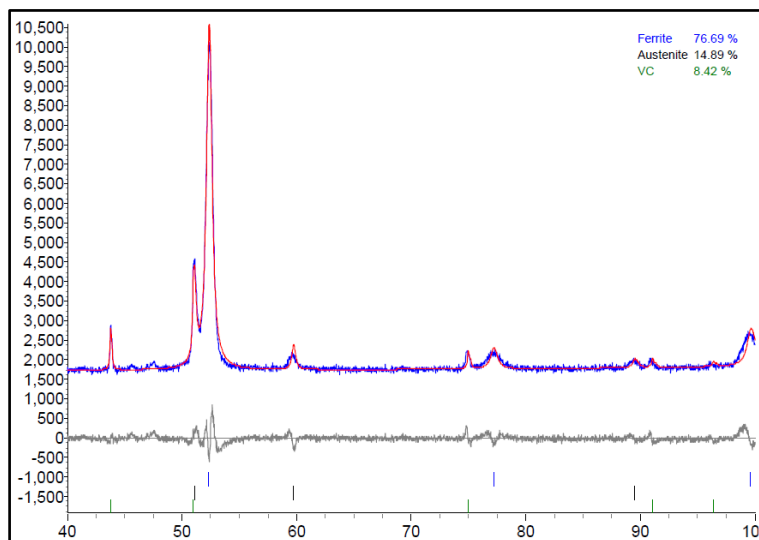
Figure 4-314: XRD spectrum for LT50.

224
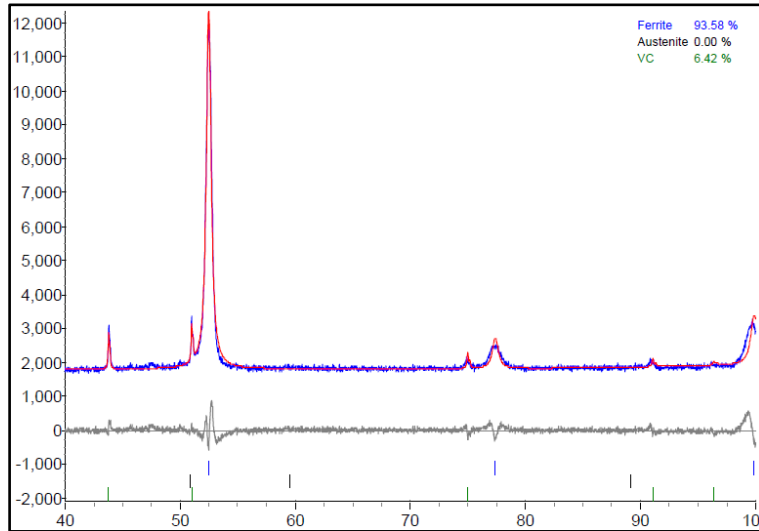
Figure 4-315: XRD spectrum for LT58.
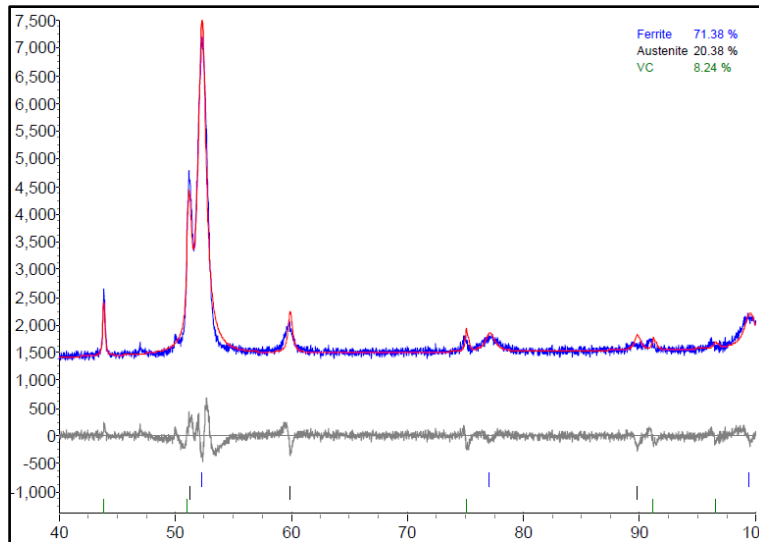
Figure 4-316: XRD spectrum for ST0.
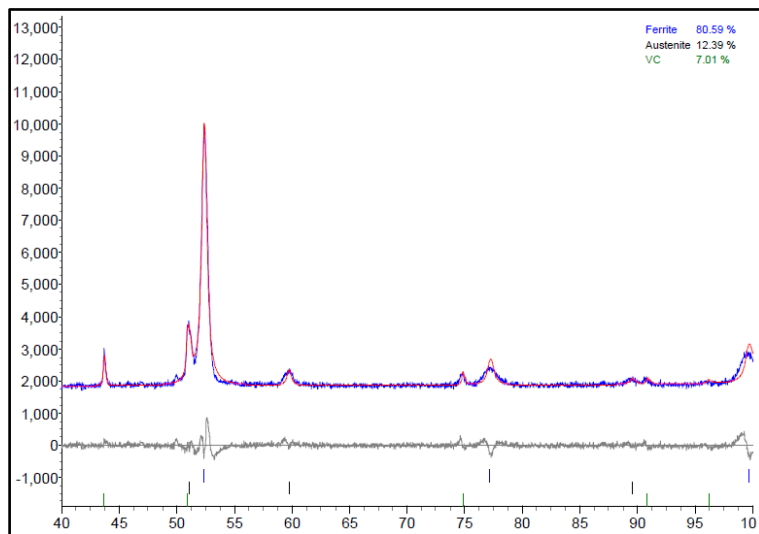
Figure 4-317: XRD spectrum for ST43.

225
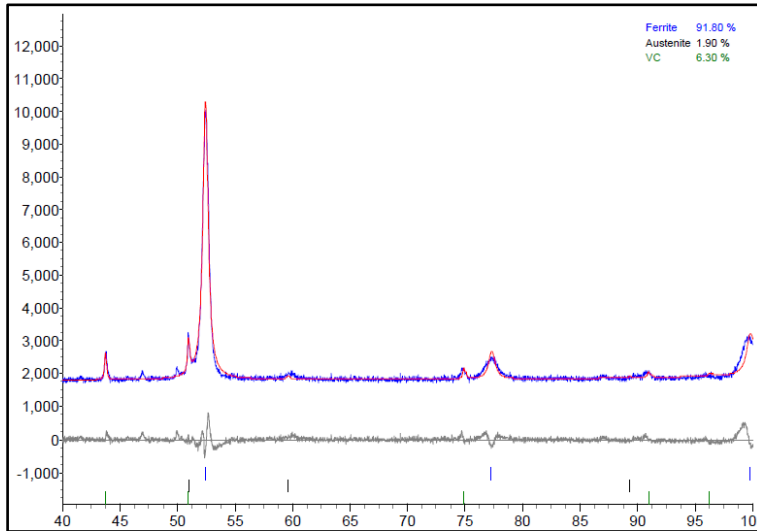
Figure 4-318: XRD spectrum for ST50.
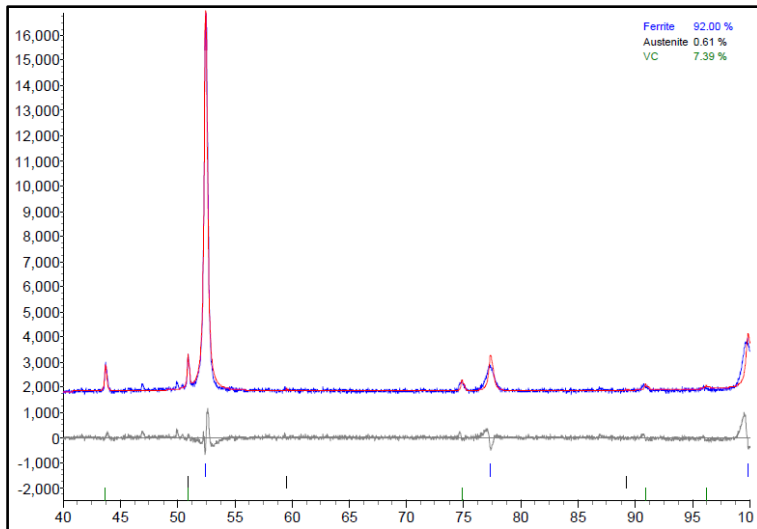
Figure 4-319: XRD spectrum for ST55.
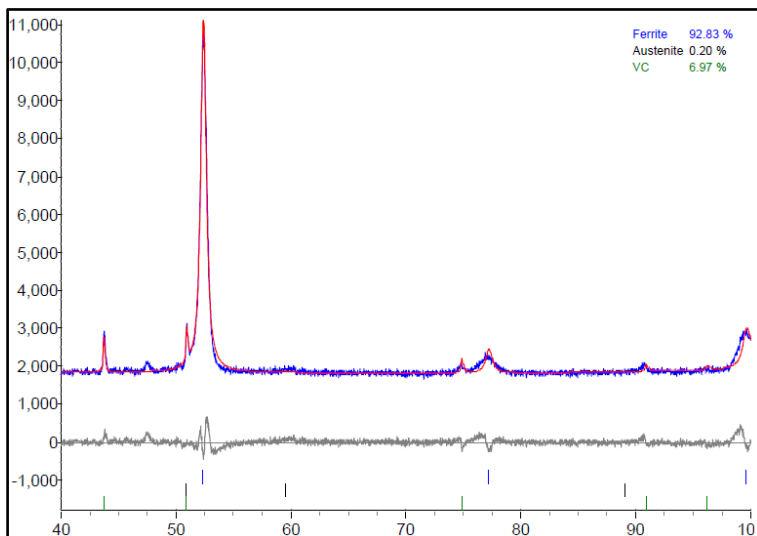
Figure 4-320: XRD spectrum for LA85.

226
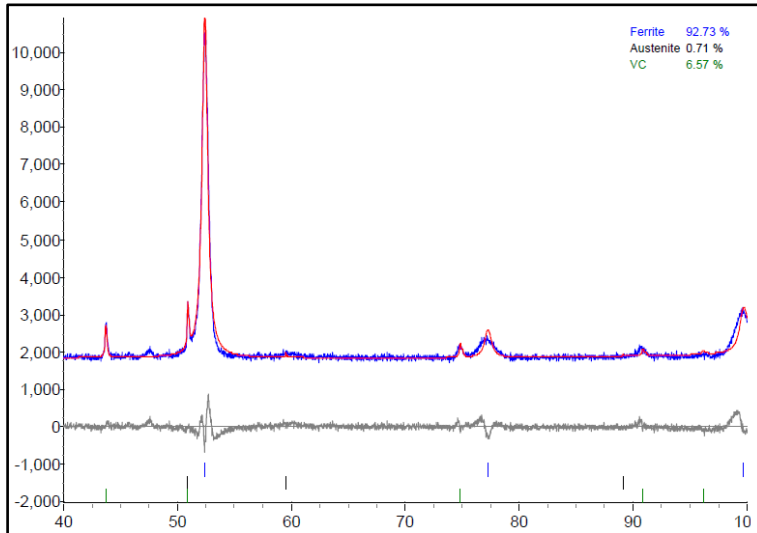
Figure 4-321: XRD spectrum for LA55.
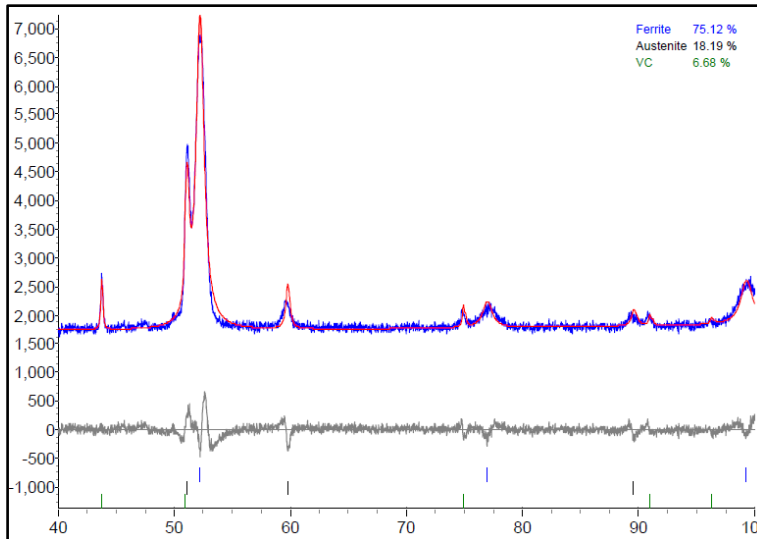
Figure 4-322: XRD spectrum for LA85T0.
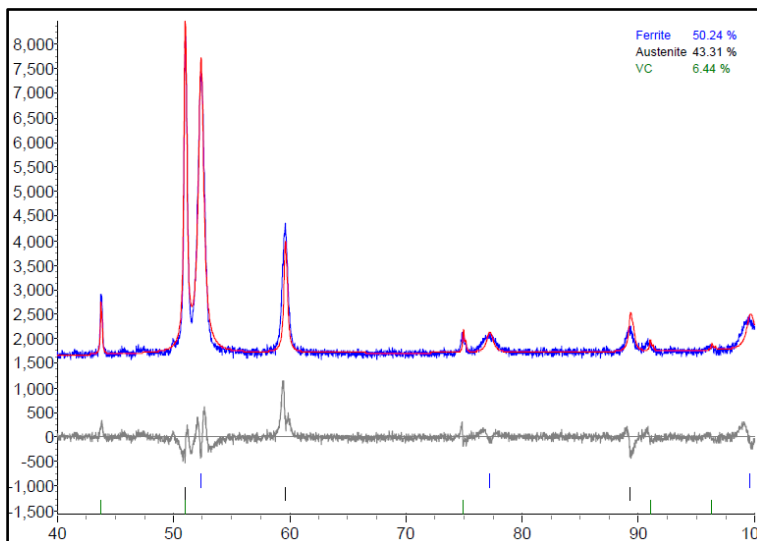
Figure 4-323: XRD spectrum for LA85T48.

227
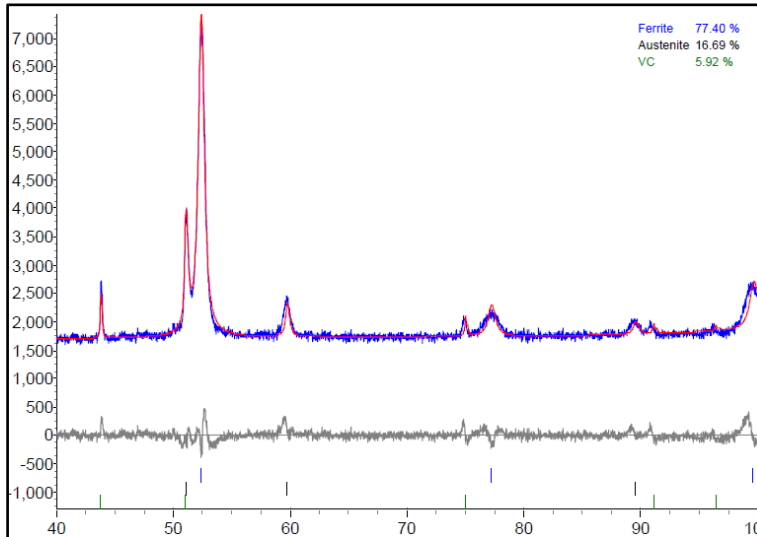
Figure 4-324: XRD spectrum for Reference LA85T53.
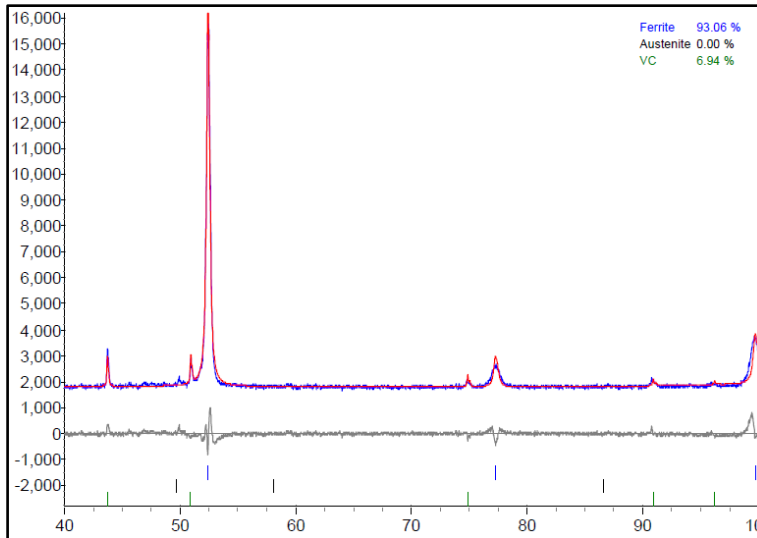
Figure 4-325: XRD spectrum for LA85T63.
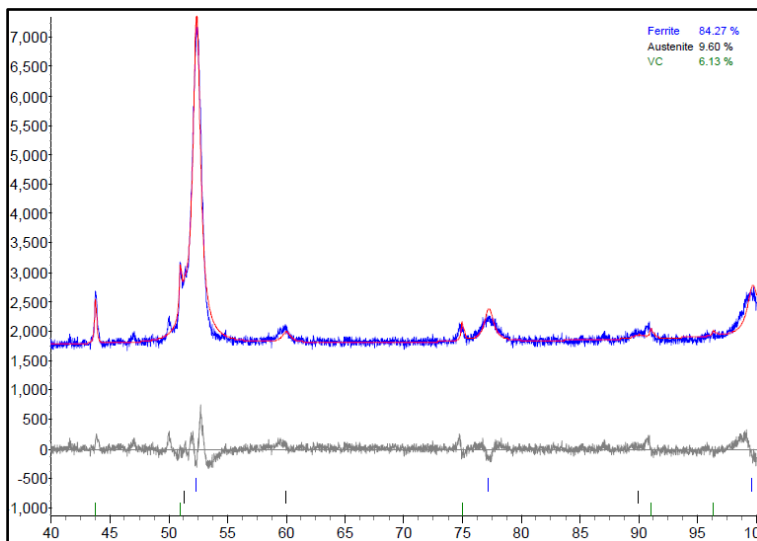
Figure 4-326: XRD spectrum for SA85T0.

228
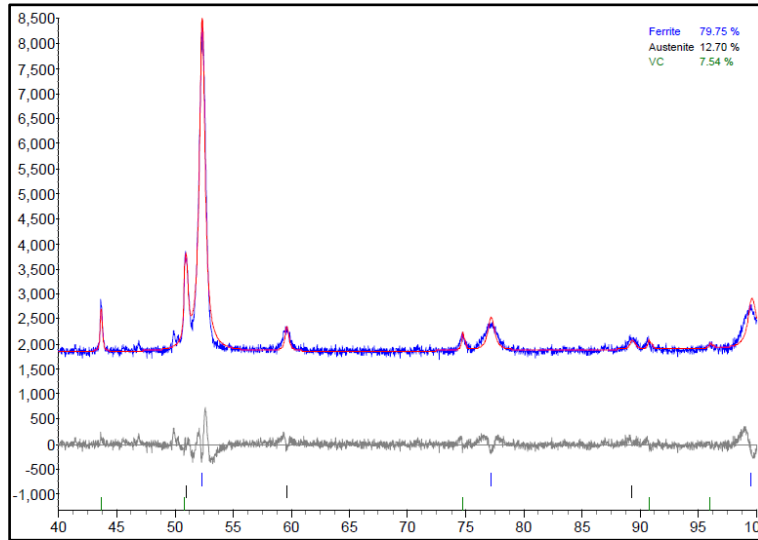
Figure 4-327: XRD spectrum for SA85T40.
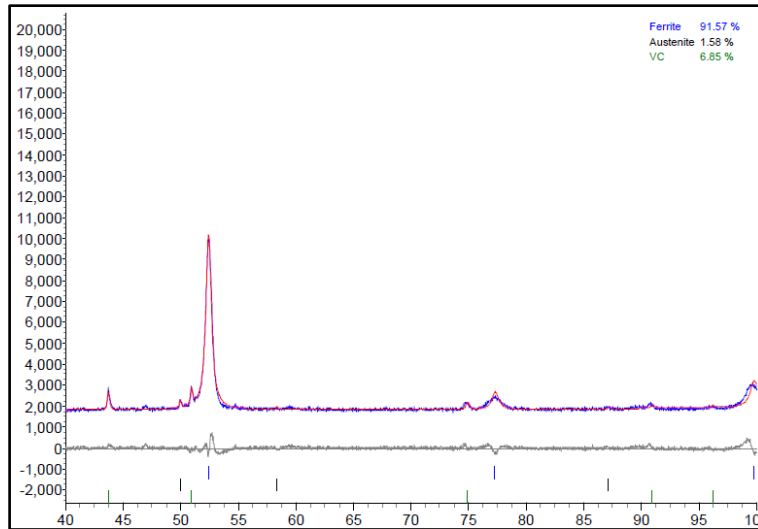
Figure 4-328: XRD spectrum for SA85T48.
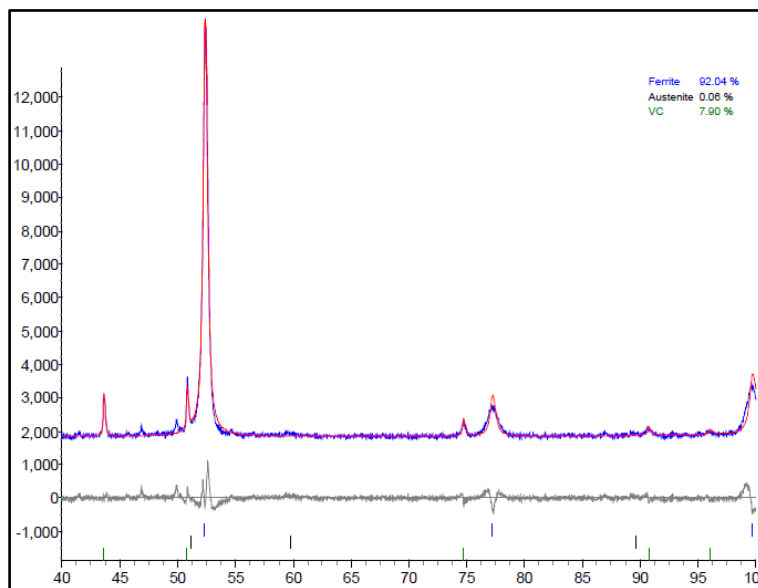
Figure 4-329: XRD spectrum for SA85T53.

229

4.2.6. Simultaneous Thermal Analysis (STA)

The STA analysis was separated into a heating and cooling section in order to analyse the phase transformations. Figures 4-330 and 4-331 show the heating curves for the STA analysis. Figure 4-330 shows the total temperature range for heating while Figure 4-331 shows only the temperature range of interest where the phase transformations take place. The curves for the three repeat samples were similar, showing two distinct peaks at approximately 1185°C and 1320°C, see Table 4-23. On closer inspection it was identified that the peak at 1320°C appears to be an overlap of three individual peaks. This was evident from the bowed edge of the peak at approximately 1335°C, which would likely correspond with the liquidus temperature. In addition the peak also showed a wide tip, where two distinct peaks could be identified on both samples 2 and 3. It was also evident that there may be a number of minor transformations occurring in the temperature range of 650-900°C, as indicated by the changes in profile. These are believed to be reverse austenitic transformations [9]. Hence, five potential phase transformations were identified during heating. The relative peak intensity in combination with the metallography results were utilised in order to identify the most probable transformation. The STA testing also confirmed that the 850°C utilised during the pre-annealing heat treatments were sufficient to achieve austenitisation of the matrix.
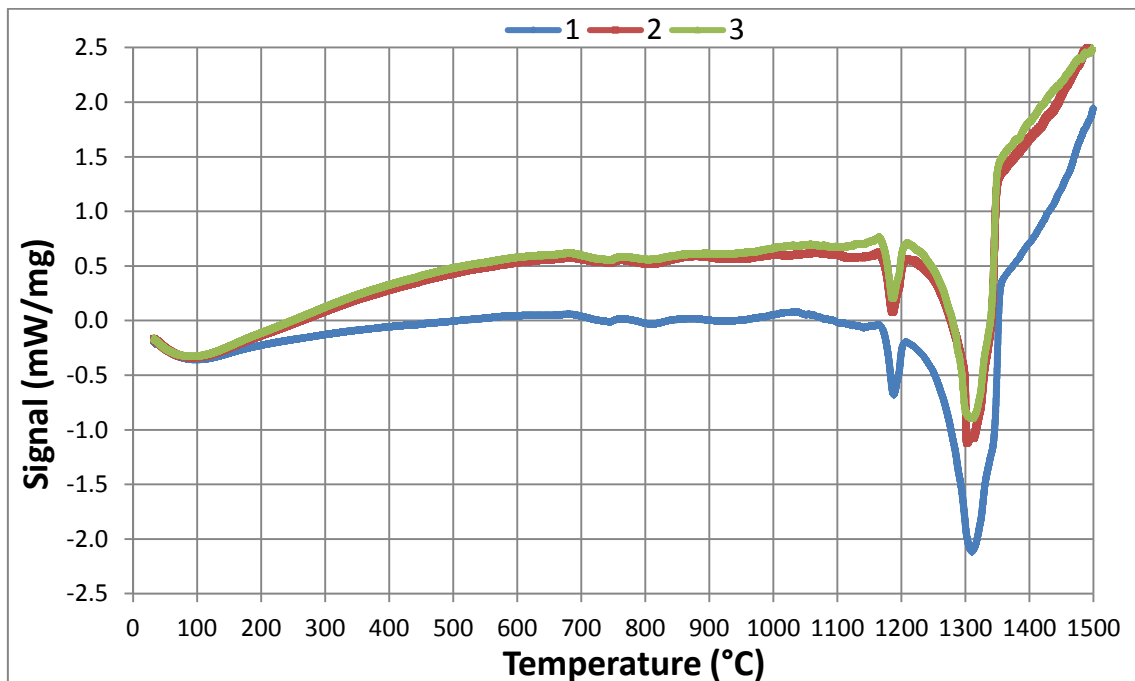
Figure 4-330: STA curve for the complete heating cycle of the as-cast material.

230

Table 4-23: STA heating results of Figure 4-331 [9].

Peak no.	Transformation	Temperature (°C)			
		1	2	3	Average
1	Reverse austenitic	650-900			
2	$M_6C/M_2C \rightarrow \gamma$	1186	1187	1184	1186
3	$M_7C_3 \rightarrow \gamma$	1307	1304	1302	1304
4	$MC \rightarrow \gamma$		1314	1312	1311
5	$\gamma \rightarrow L$	1340	1330	1334	1335
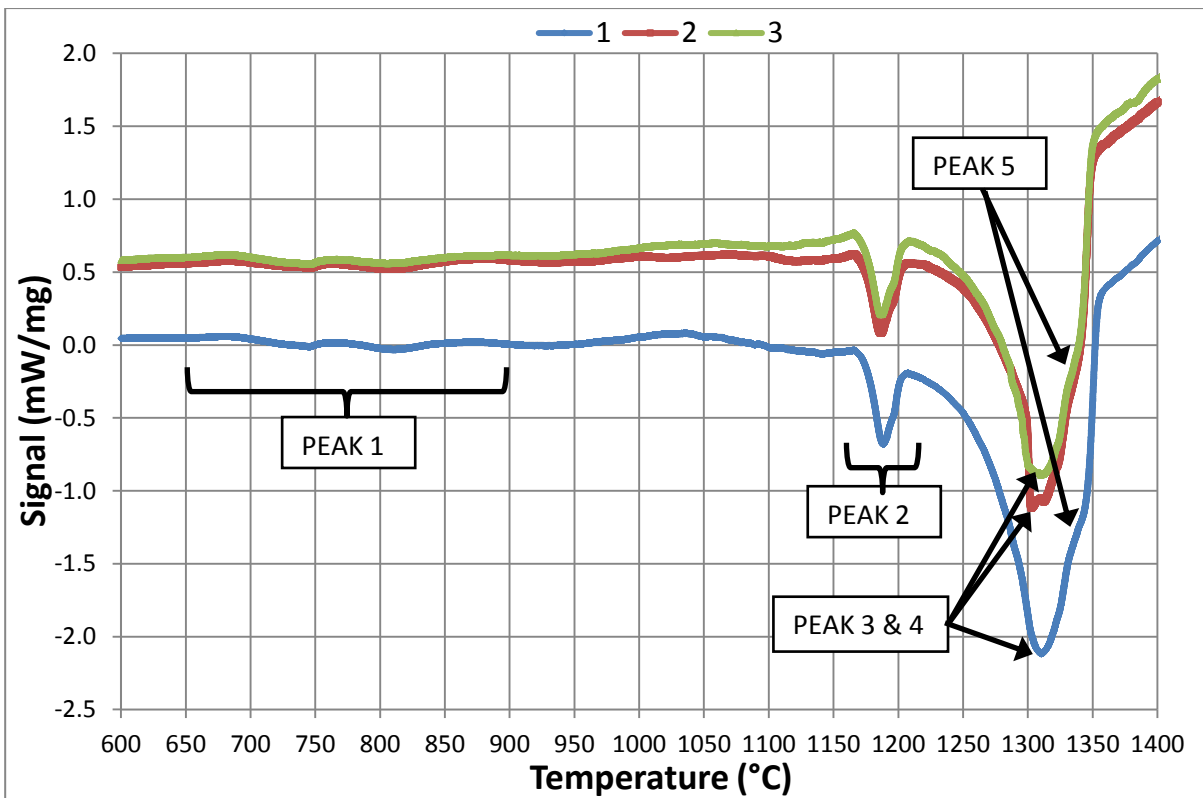
Figure 4-331: STA curve of the 600-1400°C heating section of the as-cast material.

The heating curves showed more deviation in profile and peak occurrence when comparing the repeat samples, see Figures 4-332 and 4-333. Figure 4-332 showed no definite phase transformations over the temperature range of 150-1100°C, confirming that the M_s temperature is below 150°C. Figure 4-333 shows the 1125-1350°C temperature range in greater detail. Five potential peaks were identified and the peak intensity and metallography results were utilised for the most probable phase identification, see Table 4-24. The average temperature for peak one was 1327°C and was identified as the primary austenite formation peak from the liquid metal. This was followed by peaks two and three, which were identified as the MC (average temperature of 1292°C) and M_7C_3 (average temperature of 1281°C) formation peaks,

231

respectively. The fourth and fifth peaks appear to correspond to M_6C (average temperature of 1193°C) and M_2C (average temperature of 1158°C) formation, respectively. The M_6C peak was ill defined, which is suspected to be due to the low amounts attained as M_2C is typically favoured under non-equilibrium cooling conditions.
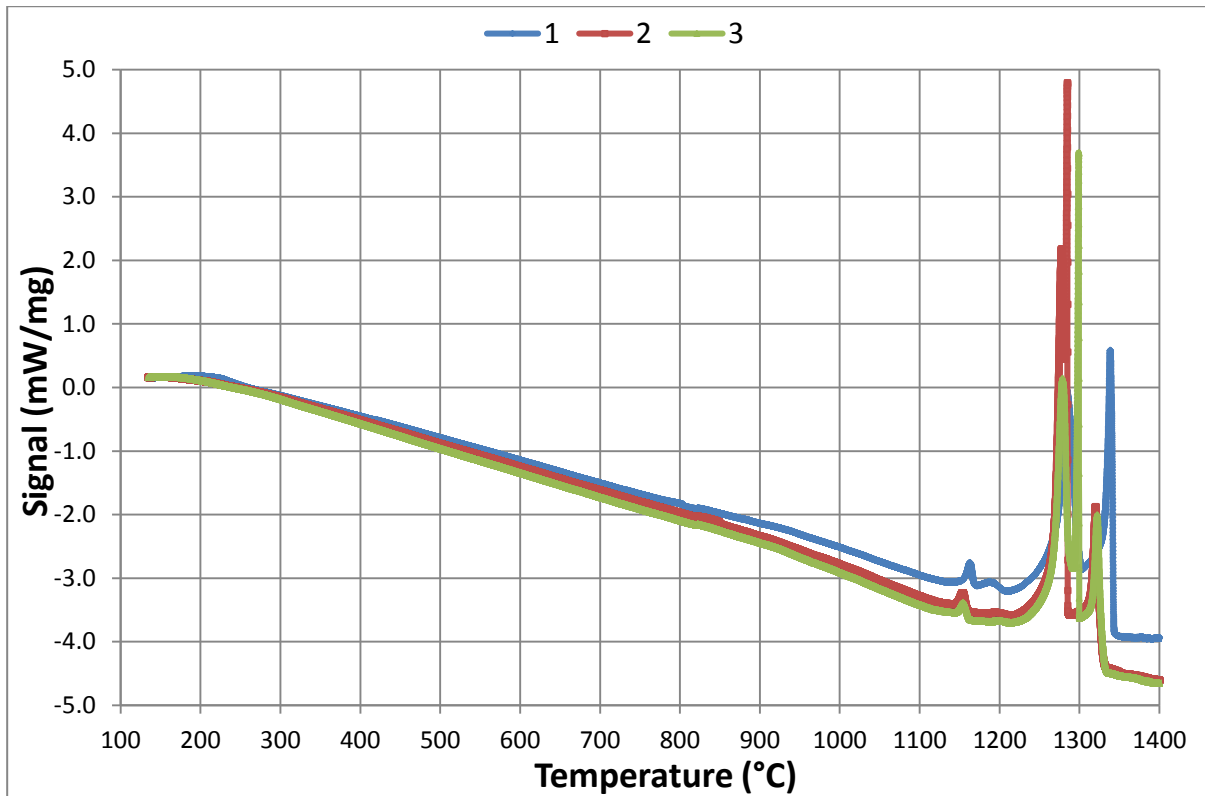
Figure 4-332: STA curve for the complete cooling cycle of the as-cast material.

Table 4-24: STA cooling results [3, 5, 9, 22].

Peak no.	Transformation	Temperature (°C)			
		1	2	3	Average
1	$L_0 \rightarrow \gamma_0 + L_1$	1339	1319	1323	1327
2	$L_1 \rightarrow (\gamma_1 + MC) + L_2$	1292	1285	1299	1292
3	$L_2 \rightarrow (\gamma_2 + M_7C_3)$	1285	1277	1280	1281
4	$L_2 \rightarrow (\gamma_3 + M_6C)$	1189	1193	1198	1193
5	$L_2 \rightarrow (\gamma_3 + M_2C)$	1164	1153	1156	1158
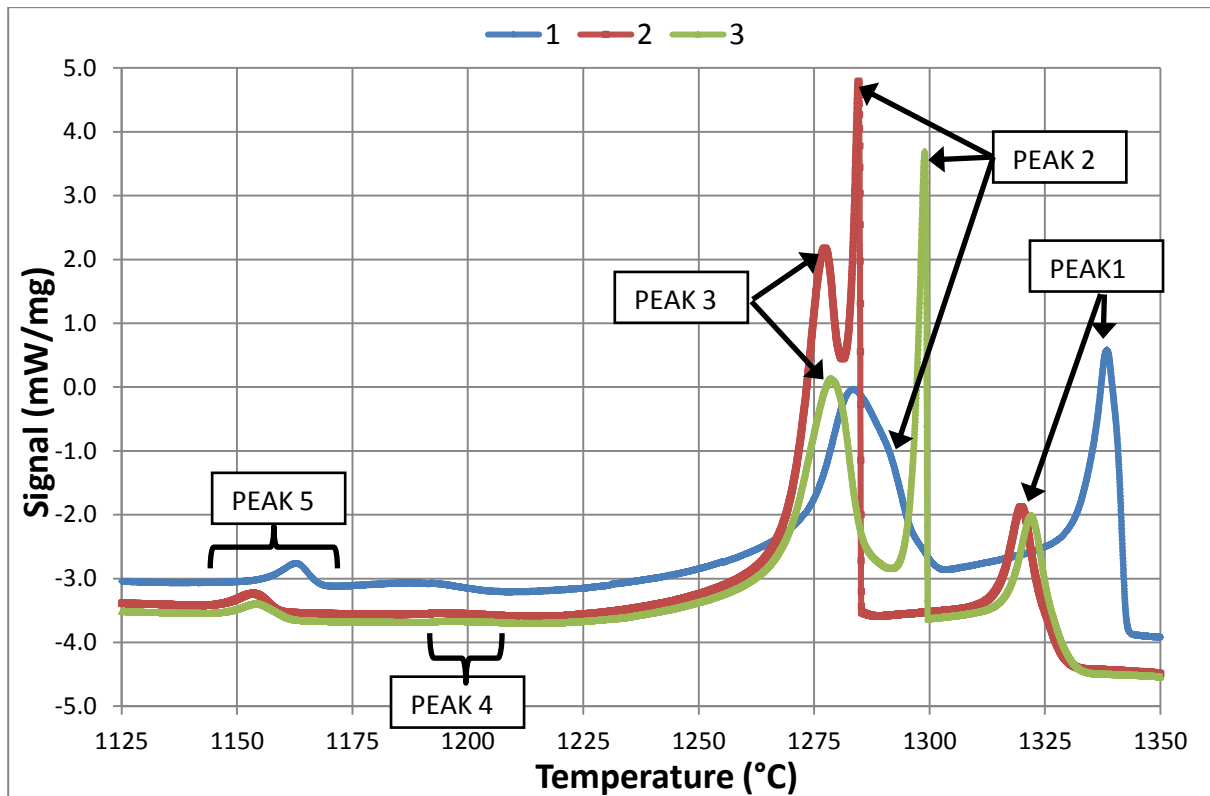
Figure 4-333: STA curve of the 1100-1400°C cooling section of the as-cast material.

4.2.7. Tensile Testing

The tensile testing of the heat treated material proved unsuccessful. The high hardness of the specimens resulted in the inability of the wedge grips to sufficiently secure the shoulders. This causes slippage of the samples relative to the grips and the inability to determine the tensile properties.

Dumbbell type specimens could be utilised for the testing as an alternative. However, due to the nature of the rolls, the total length of the specimen is approximately 50mm. Special grips would have to be manufactured to test these samples. In addition when the applicable sample dimensions are applied, which are below the traditional sub size specimen, the gauge region is no longer representative of the shell material utilised for rolling.

4.2.8. Impact Testing

Impact testing was performed on the peak hardness samples, and also on the 50°C over peak hardness and 75°C over peak hardness on all the sample sets. The average results from at least 2 specimens are shown in Table 4-25. It was noted that the as-cast specimens showed some of the highest impact values, which were higher than

233

most of the tempered samples. This observation is believed to be related to the higher retained austenite content increasing the impact energy. The remainder of the sample sets showed an increase in impact toughness with increasing tempering temperature, see Figure 4-364. The impact energy values of the samples treated beyond the peak hardness were generally similar for the LT, ST and LA sample sets, with the LA sample set showing slightly higher impact values. The SA samples showed similar values at peak hardness compared to the other sample sets, whilst also showing significantly higher impact energy values in the samples treated beyond the peak hardness compared to the other conditions.

It should be noted that all the impact values were concentrated at the lower portion of the measurement scale. This questions the accuracy of the results and the related comparison between the different samples and conditions.

Table 4-25: Impact testing results.

Sample	Energy*
Unit	kJ/m^2
Reference 1	21.3
LT50	15.3
LT55	15.9
LT58	16.6
LA53	16.6
LA58	17.8
LA60	18.3
ST50	14.0
ST55	16.9
ST58	17.4
SA48	14.9
SA53	21.4
SA55	21.7

*Note: The Charpy impact test values in kJ/m^2, should only be used on equivalent-sized samples for comparison.
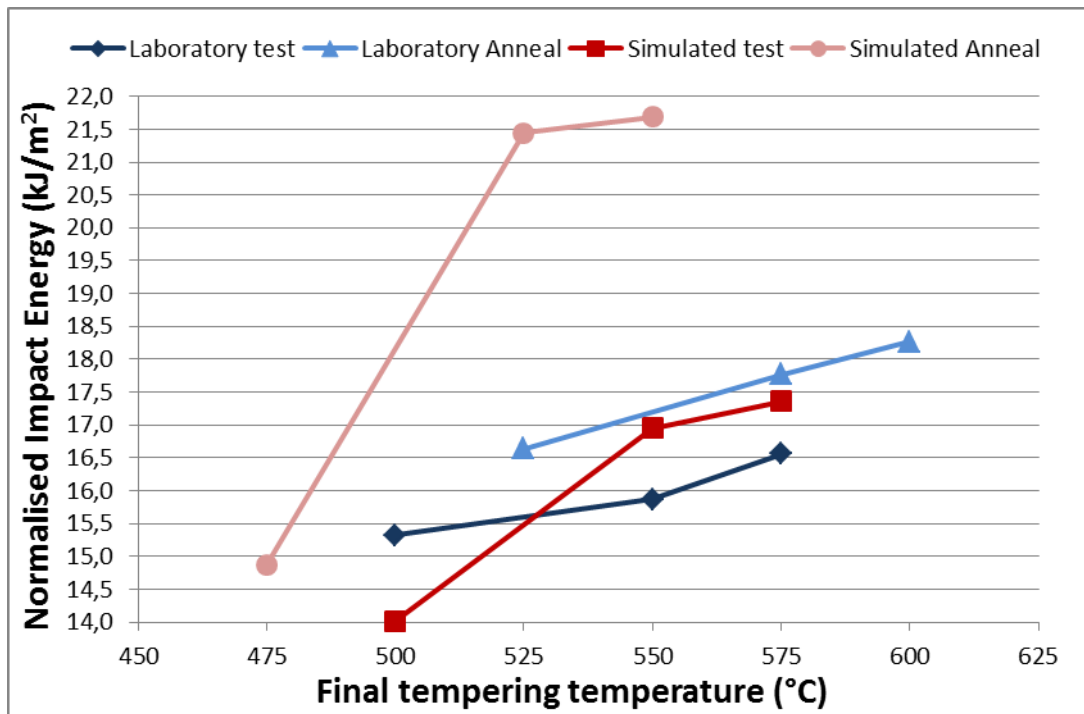
Figure 4-334: Influence of tempering temperature on the impact energy of the HSS material.

The load versus time curves of the samples sets are shown in Figures 4-335 to 4-338. Generally the curves were very similar for all the conditions and showed an initial load peak which is related to the initial crack initiation at the notch tip. None of the curves showed a yield load, which is related to the very brittle nature of the material where the yield load is effectively equal to the peak load. The peak load is reduced and followed by a second, wider, flatter peak which represents the crack propagation load across the specimen. The relationship between the peaks confirms the brittle behaviour of the material, which indicates greater energy required for initial crack initiation compared to the ease of crack propagation throughout the brittle material.

The exception to the general trend was found with the SA55 sample, which showed a higher, larger second peak compared to the first. The sample also showed the highest average impact energy of all the samples. This indicates a higher degree of energy consumed during crack propagation relative to the crack initiation. This observation was also consistent with the fracture surfaces, which were generally flat, except for the SA55 samples which showed a more profiled surface across the specimen. This suggests that potential toughness benefits can be achieved by a pre-annealing heat treatment, which could resist crack initiation and propagation in service.

235
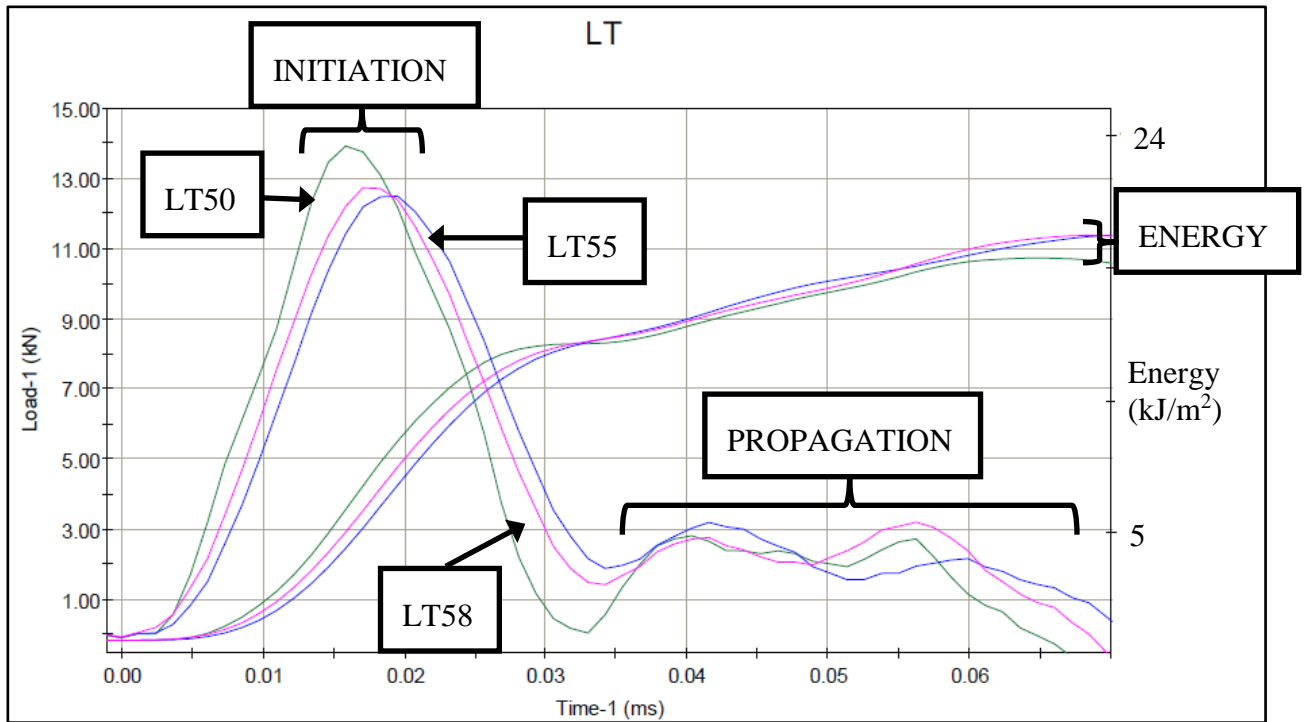
Figure 4-335: Graph showing the measured load and absorbed energy against time for the LT HSS material.
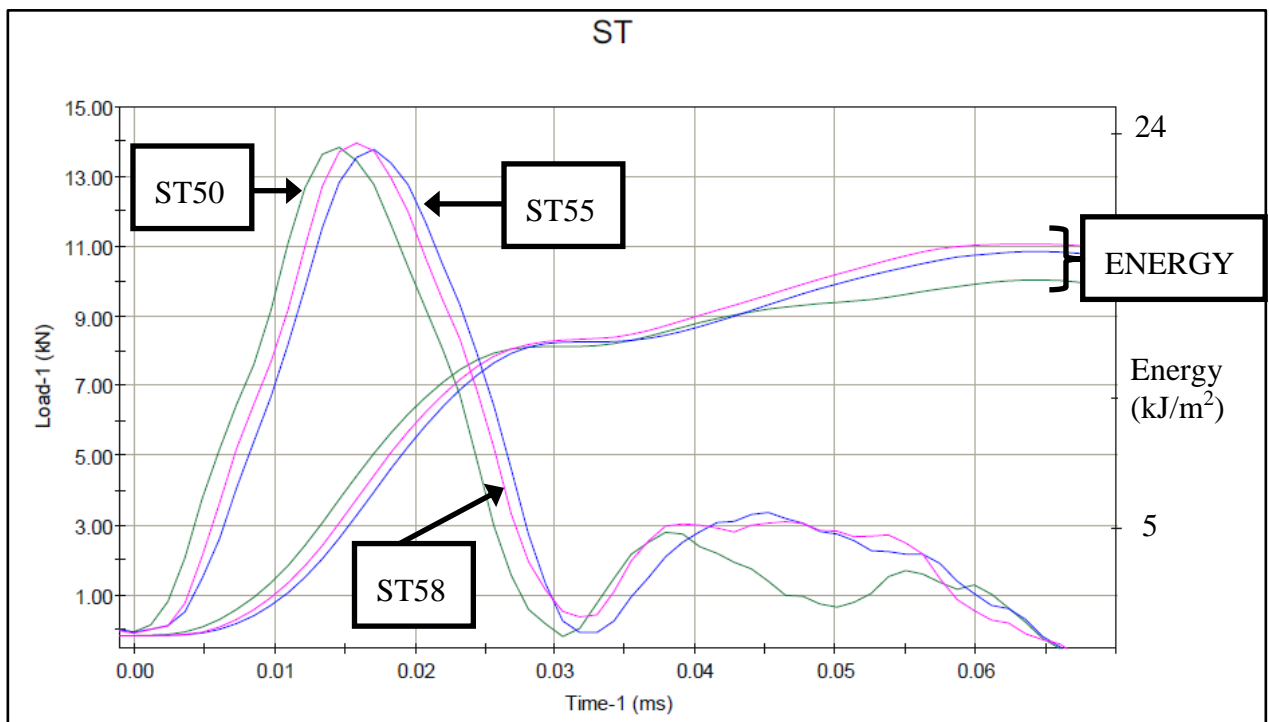
Figure 4-336: Graph showing the measured load and absorbed energy against time for the ST HSS material.
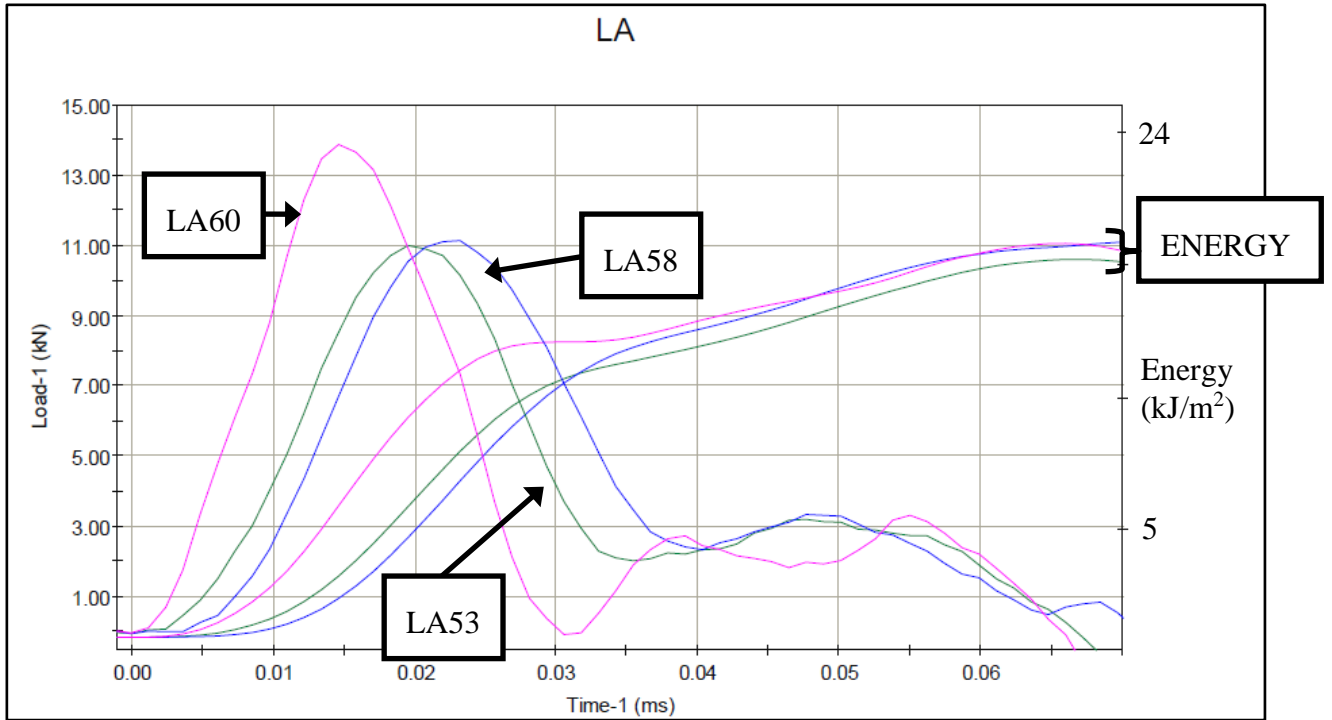
Figure 4-337: Graph showing the measured load and absorbed energy against time for the LA HSS material.
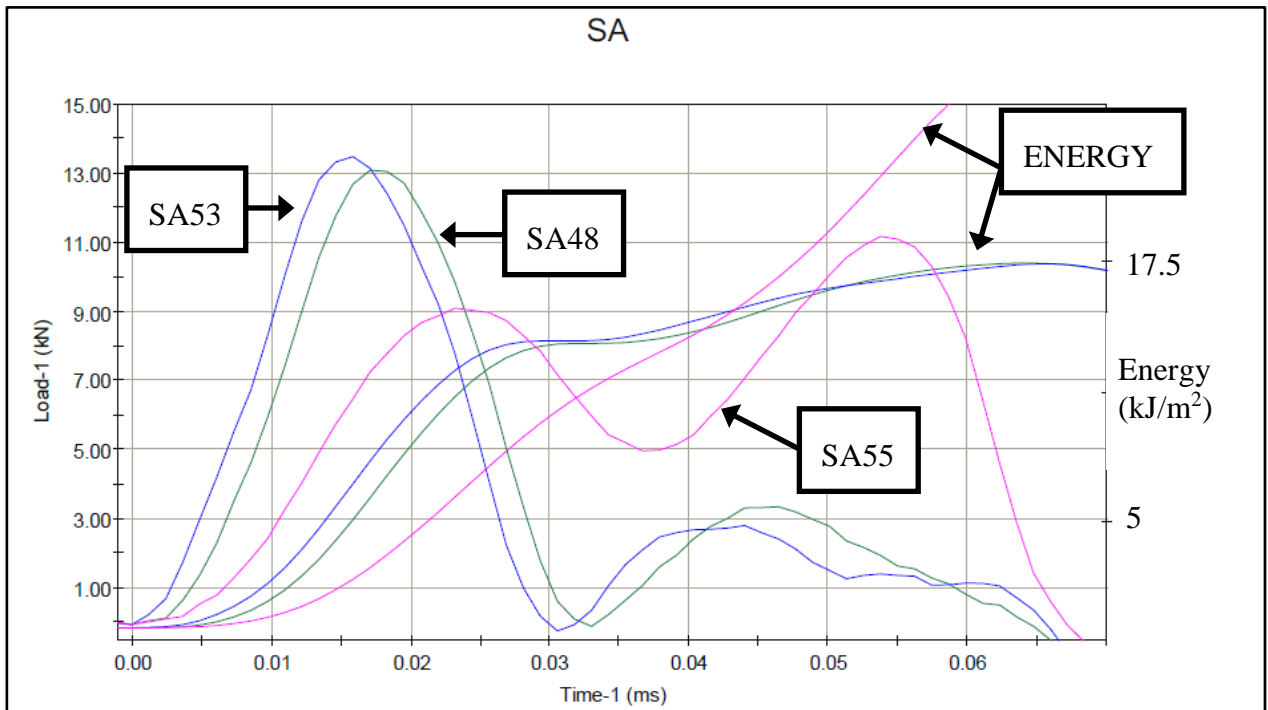
Figure 4-338: Graph showing the measured load and absorbed energy against time for the SA HSS material.

237

5. CHAPTER 5: DISCUSSION

5.1. Benchmarking

5.1.1. Shell Material

The general microstructure of the as-cast samples and tempered material were similar and consisted of networks of carbides located in a matrix consisting predominantly of martensite. The as-cast samples contained some pearlite, which was absent in the tempered samples. Both the as-cast and first temper samples contained significant retained austenite, which had been largely eliminated on the final temper samples. No consistent trend in total carbide volume fraction was observed over shell depth, while a clear increase in MC carbide content with shell depth was evident.

The carbide etchants showed that the M_2C primary carbide present in the as-cast condition, transformed to M_6C after austenitising. The behaviour appears to be related to both the relatively high cooling rates experienced during the initial CC and the effect of V. The higher cooling rate promotes the formation of the lower surface energy, coherent M_2C carbides over the higher surface energy, incoherent M_6C carbides. In addition V stabilises the M_2C carbide relative to M_6C. Both as-cast and tempered conditions showed homogenously distributed $M_{23}C_6$ carbides within the matrix, while only the tempered samples showed additional fine M_6C, secondary carbides located adjacent to the larger primary M_6C carbides. This was confirmed by the increase in the Mo, Cr and C content compared to the bulk of the matrix. It is assumed that the formation of the M_6C secondary carbides is associated with the Mo and W enrichment of the surrounding matrix during austenitising.

Clustered carbides in the shell may lead to variations in roll properties (hardness, wear resistance) over the surface and may lead to surface defects such as hard spots, during rolling. The carbide clusters will not be eliminated completely even after heat treatment, similar to the other M_7C_3 carbides within the matrix. However, the clusters were only found on the as-cast material and not on the related material.

No chemical segregation over the shell depth was observed for V, W or Mo. The low W content decreases the W and Mo carbides (M_2C and M_6C) formed within the structure. The high Ni content should increase the hardenability of the HSS material, while significantly increasing the toughness. The bulk hardness remained constant over the working portion of the shell.

238

Despite no indications of chemical segregation, indications of MC carbide segregation with an increasing MC carbide content with shell depth were evident. This is expected given the lower density of the MC carbides and lower associated centrifugal force during CC. No indications of M_2C/M_6C carbide segregation were evident, which is in contrast with literature observations. The lack of M_2C/M_6C carbide segregation is expected to be related to the lower W and associated lower M_2C/M_6C carbide content.

Sample T3 showed a lower average V and a higher Ni contents compared to samples T1-2 and T2-2. Hence, sample T3 showed lower average vanadium carbide content and an associated lower hardness. Although this should cause inferior wear resistance and a reduced service life, sample T3 is expected to show superior toughness and durability in service with greater resistance to fracture during mill incidents.

5.1.2. Core Material

The core microstructure consisted of graphite nodules intermittently surrounded by some ferrite, in a matrix consisting of pearlite (bull's eye structure), which also contained M_3C carbides. The transition from the shell to the core (bond zone) was characterised by a transition in the matrix from martensitic to pearlitic, and also a transition in the carbide type to M_3C. Clustered M_3C carbides appear to induce defects at the bond zone, which is probably related to the difference in thermal expansion coefficients between the carbides and matrix.

5.2. Heat Treatment

5.2.1. HC

The HC material appears to be more sensitive to both temperature and time variations in heat treatment than HSS, as indicated by the significant difference in both peak hardness and the temperature at which peak hardness is achieved for the LT and ST sample sets. The higher hardness of the HC material under laboratory conditions (LT) was surprising, since HSS traditionally matches or exceeds the hardness achieved by HC. The secondary carbide size appeared to be fairly stable up to peak hardness, followed by more rapid coarsening, as expected. The secondary carbides associated with the as-cast and simulated samples could only be identified at higher tempering temperatures beyond the peak hardness. This also gave rise to the observation that the LT samples showed coarser secondary carbides compared to the ST samples at equivalent tempering temperatures.

5.2.2. HSS

The HSS material showed similar hardness profiles under both laboratory (LT) and simulated (ST) conditions and compared well with most HSS material, despite the peak hardness temperature being slightly lower than most HSS [61]. The LT set also showed a more gradual decrease in hardness once peak hardness was achieved.

The higher peak hardness achieved and more gradual hardness reduction beyond the peak hardness caused by pre-annealing under laboratory scale conditions, was not attributed to grain refinement, as no substructure or refinement was observed. The lack of grain refinement is attributed to the absence of any phase refining transformations during pre-annealing that could induce grain refinement, as explained below.

The as-cast matrix structure consists predominantly of retained austenite and martensite, with small amounts of discontinuous transformation phases (pearlite). With conventional heat treatment the martensite and pearlite are re-austenitised with the austenite becoming more supersaturated than during initial cooling after casting. This prevents the pearlite formation during cooling after austenitising that was previously formed after casting. The austenite matrix is systematically transformed to martensite and tempered during double tempering.

The pre-annealing is expected to transform the martensite and pearlite to austenite prior to the austenitising treatment. However, since the roll is cooled to 550°C and not to room temperature, the martensite formation does not occur prior to austenitising. The remainder of the heat treatment is similar to the conventional treatment and yields the same basic phase constituents after final tempering (tempered martensite and alloy carbides).

If it were postulated that the matrix microstructure of the as-cast HSS contained predominantly discontinuous/displacive phases (pearlite/bainite) instead of martensite and retained austenite, grain refinement within the cells could be feasible. The initial austenite cells formed during solidification are refined during the proposed discontinuous/displacive transformation by the formation of individual pearlite/bainite nodules/packets, see Figure 5-1. If this postulated as-cast structure were subjected to a similar pre-annealing treatment, the pearlite/bainite would be re-austenitised with the nodule/packet boundaries now forming the new austenite grain boundaries. If the

structure is then cooled to 550°C and held for a sufficient time a refined structure could form from the refined austenite. If the remainder of the typical heat treatment is performed the refined structure will be retained, resulting in a refined cell structure within the matrix. The illustration of the expected refinement is shown in Figure 5-1. Hence, it is expected that grain refinement can be achieved by implementing pre-annealing if the pearlite content of the as-cast material can be increased, or other displacive phases such a bainite can be introduced. However, alteration of the chemical composition and/or casting procedure will also influence the final microstructure and properties attained after the remainder of the traditional heat treatment is performed.
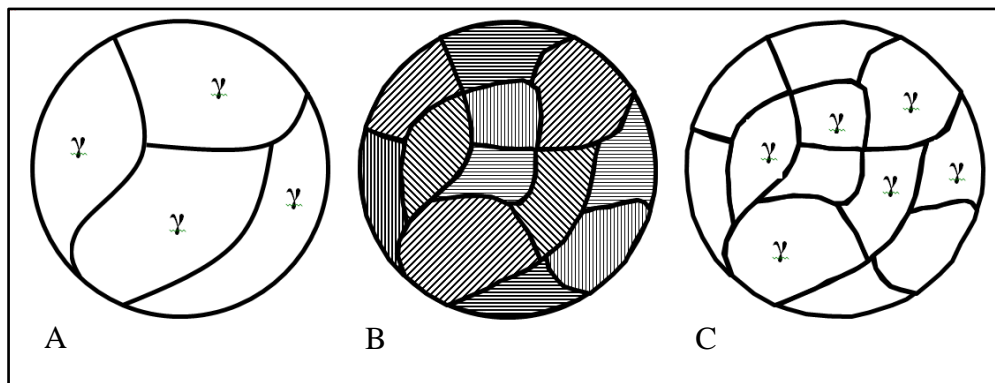
Figure 5-1: Illustration of the grain refinement induced by the transformation of the initial austenitic matrix (A) to pearlite/bainite (B), which is inherited by the re-austenitisation during pre-annealing (C).

Since the increase in hardness was not attributed to grain refinement, it appeared to be related to the increased level of retained austenite, which modifies the softening behavious during tempering, see Figures 5-2 and 5-3.
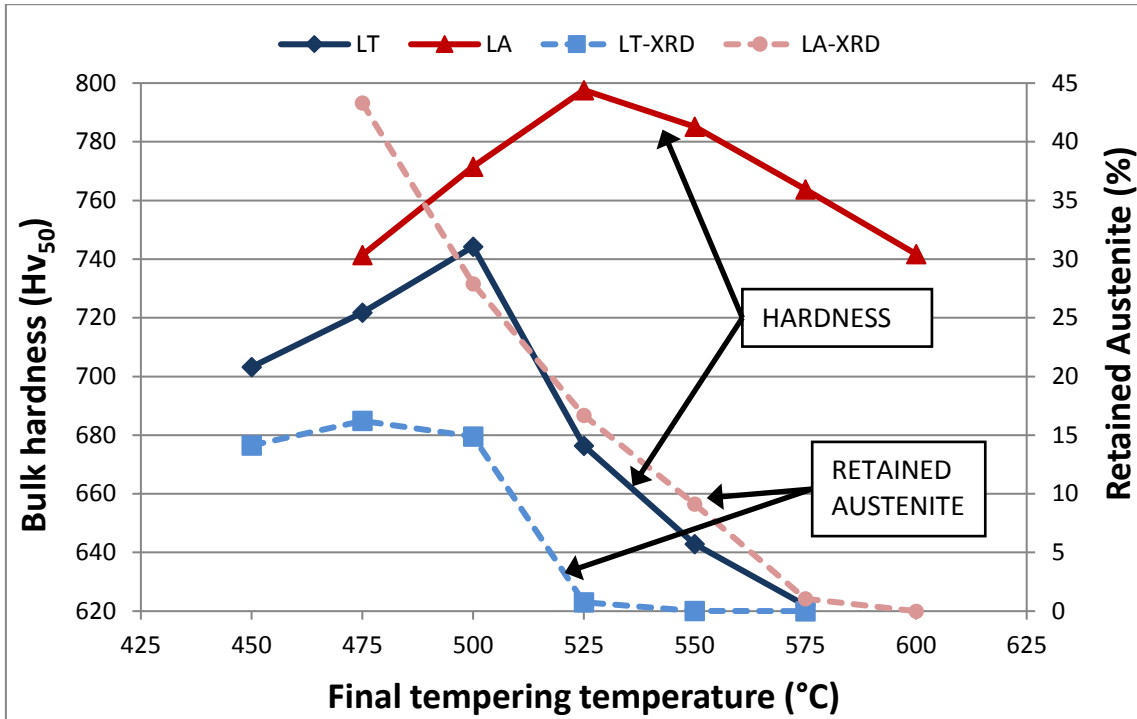
Figure 5-2: Hardness and retained austenite combination graph for LT and LA.
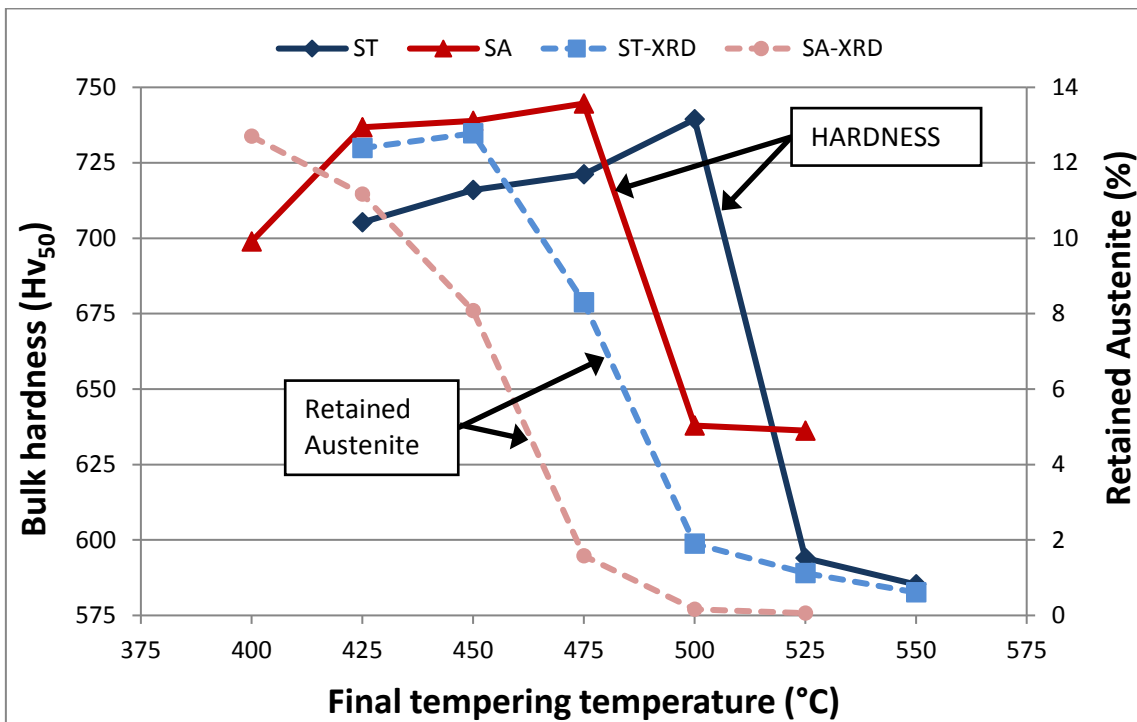
Figure 5-3: Hardness and retained austenite combination graph for ST and SA.

The higher hardness and more gradual reduction in hardness beyond the peak suggest potential performance benefits in service, since the wear resistance improves with bulk hardness. However, the increased hardness was not found under simulated conditions, indicating that the desired effect will not necessarily be achieved in

242

practice. The reason for the difference between the LA and SA observation was probably related to a temperature and time effect, which dissipated at longer holding times.

This is also a potential cause of the more abrupt decrease in hardness beyond the peak hardness for the simulated samples compared to the laboratory sample sets. Since the holding times at temperature were significantly longer, an equivalent change in tempering temperature will have a greater effect on the reduction in hardness under simulated conditions compared to laboratory conditions.

The HSS material showed an increase in impact toughness with increasing tempering temperature. The SA samples showed similar values at peak hardness compared to the other sample sets, while showing significantly higher impact energy values over peak hardness compared to the other conditions. This was attributed to more energy consumed during crack propagation relative to the crack initiation if compared to all the other samples.

Potential benefits can be gained from pre-annealing under industrial conditions as suggested by the slightly higher hardness level over peak hardness and increased toughness for the SA material compared to the ST samples. The relevance arises from the need to temper beyond peak hardness in order to improve the toughness. However, the minor improvement in hardness and toughness will have to be weighed against the increased cost and time of heat treatment. The toughness benefits could resist crack initiation and propagation in service.

The $M_{23}C_6$ secondary carbides present in the HSS matrix were absent in regions where the MC carbides were more abundant within the matrix, creating a precipitate-free boundary surrounding the MC carbides.

Generally it is clear from the study that the heat treatment behaviour of both HSS and HC material cannot be accurately simulated under shorter time laboratory scale conditions (LT and LA). The simulated test conditions (ST and SA) more accurately simulated the industrial roll microstructures and associated industrial conditions. The effect is primarily related to the carbide dissolution, carbide decomposition, alleviation of chemical segregation and carbide precipitation, which is not sufficiently simulated when shorter treatment times are imposed. This is evident from the more uniform secondary carbide distribution, greater depth of M_6C secondary carbide formation from

243

the primary networks and increased M_2C carbide decomposition of the ST and SA samples relative to the LT and LA samples.

6.   CHAPTER 6: CONCLUSIONS

The combination of performance and durability of the HSS rolls produced at SARCO appears to be the product of the following factors:

- Addition of grain refiners to form a refined structure.

- High Ni additions for improved toughness.

- Low W:Mo ratios which decrease the grain boundary carbides and limit segregation.

- High carbon content which ensures a complete plate martensite matrix.

- Elevated temperatures during heat treatment to form additional M_6C secondary carbides.

- Balanced carbide former additions to eliminate hardness variations within the shell depth.

The following conclusions can be drawn from this heat treatment study:

- HC material appears to be more sensitive to both temperature and time variations in heat treatment than HSS.

- Higher hardness and more gradual reduction in hardness beyond the peak suggest potential performance benefits in service for HSS material, but the increased hardness was not found under simulated conditions, indicating that the desired effect will not necessarily be achieved in practise.

- Potential benefits in terms of higher hardness levels beyond the peak hardness of HSS can be achieved in practice with pre-annealing, but the minor improvement in hardness will probably prove less cost effective considering the increased cost and time of heat treatment.

- HSS and HC heat treatments are not accurately simulated under laboratory testing (LT and LA) when shorter treatment times are utilised. Implications of this observation include the inability to apply treatment parameters identified during shorter time treatments directly to industrial production.

7. CHAPTER 7: RECOMMENDATIONS

The following recommendations can be made with regard to further investigations:

- The effects of pre-annealing should be researched on lower alloy bainitic HSS material, as this could have the beneficial grain refining effect intended for this study. It is not clear how feasible achieving this structure may be in practise, given the large diameter of the work rolls and the associated slow cooling rates.

- The improved wear resistance benefits of pre-annealing could be quantified by performing industrial trials. This will also enable the assessment of whether pre-annealing can be cost effectively applied in industry.

- The expected improvements in impact toughness due to pre-annealing could be verified by performing fracture toughness testing if possible.

8. REFERENCES

1. Nannan, S., Yikun, L., Yunlong, B., Xiuhong, K., Lijun, X. and Dianzhong, L., 2009, 'Computer simulation of core filling process of cast high speed steel roll', *China Foundry* 6(4), 314-318.

2. Collins D.B., 2002, 'The metallurgy of high speed steel rolls', *Rolls for the metalworking industries*, pp. 83-91, Iron and Steel Society.

3. Lecomte-Beckers, J., Sinnaeve, M. and Tchuindjang, J., 2011, 'Comparison between high chromium steel and semi HSS used in hot strip mill roughing stands', *Southern African Roll Users Conference 2011 proceedings*, Vanderbijlpark, South Africa, October 6-11, 2011, pp. 35-40.

4. Breyer, J.P., Herman, M. and Lecomte-Beckers, J., 2006, 'Influence of carbide precipitation on hot hardness of high speed steel rolls', *Southern African Roll Users Conference 2006 proceedings*, Vanderbijlpark, South Africa, May 11, 2006, pp.28-33.

5. Boccalini, M., Serantoni, C., Sinatora, A. and Matsubara, Y., 2001, 'Effect of vanadium content and cooling rate on the solidification of multi-component white cast iron'.

6. Fu, H., Xiao, Q. and Jian-Dong, X., 2008, 'A study on the crack control of a high-speed steel roll fabricated by a centrifugal casting technique', *Materials Science and Engineering A* 474, 82-87.

7. Fu, H., Zhao, A. and Xing, J., 2003, 'Development of centrifugal casting high speed steel rolls', *Journal of the University of Science and Technology Beijing* 10(6), 61-66.

8. Hwang, K.C., Lee, S. and Lee, H.C., 1998, 'Effects of alloying elements on microstructure and fracture properties of cast high speed steel rolls Part 1: Microstructural analysis', *Materials Science and Engineering* A254, 282-295.

9. Lecomte-Beckers, J., Tchuindjang, J., Ernst, R. and Breyer, J.P., 2004, 'Structural investigations of HSS rolls for hot strip mill', *41ste Rolling Seminar Processes: Rolled and Coated Product*, Joinville, Brasil, October 26-28, 2004.

10. Nakamura, H., Kurahashi, R., Nishiyama, Y., Kouga, T. and Hashimoto, M., 1990, 'Development of hot work roll made of matrix hardened high speed tool steel', *CAMP-ISIJ (Japanese)* 3, 418.

11. Park, J.W., Lee, H.C. and Lee, S., 1999, 'Composition, microstructure, hardness and wear properties of high-speed steel rolls', *Metallurgical and Materials Transactions* 30A, 399-409.

12. Wang, M., Mu, S., Sun, F. and Wang, Y., 2007, 'Influence of rare earth elements on microstructure and mechanical properties of cast high-speed steel rolls', *Journal of Rare Earths* 25, 490-494.

13. Roberts, G.A., Hamaker, J.C. and Johnson, A.R., 1962, *Tool Steels*, 3rd Edition, ASM.

14. Kang, Y.J., OH, J.C., Lee, H.C. and Lee, S., 2001, 'Effect of carbon and chromium additions on the wear resistance and surface roughness of cast high-speed steel rolls', *Metallurgical and Materials Transactions* 32A, 2515-2525.

15. Pellizzari, M., Cescato, D. and De Flora, M.G., 2009, 'Hot friction and wear behaviour of high speed steel and high chromium iron for rolls', *Wear* 267, 467-475.

16. Zhang, H., Gandin, C.A., He, J. and Nakajima, K., 2012, 'Prediction of solidification path and carbide precipitation in Fe-C-V-Cr-Mo-W high speed steels', *Materials Science and Engineering* 33.

17. Transactions of the American Society for Metals, 1949, Vol. 41, pp. 12-47.

18. Boccalini, M. and Goldenstein, H., 2001, 'Solidification of High speed steels', *International Materials Review* 46(2), 109-115.

19. Pan, Y., Yang, H., Liu, X. and Bian, X., 2004, 'Effect of K/Na on microstructure of high-speed steel used for rolls', *Materials Letters* 58, 1912-1916.

20. Qu, H., Liao, B., Liu, L., Li, D., Guo, J., Ren, X. and Yang, Q., 2012, 'Precipitation rule of carbides in new high speed steel for rollers', *CALPHAD: Computer Coupling of Phase Diagrams and Thermochemistry* 36, 144-150.

21. Pacyna, J., 1984, 'The effect of molybdenum upon the transformations in the matrix of high-speed steels during austenitizing and quenching', *Arch. Eisenhuttenwes*.

22. Gontarev, J., Dobersek, M., Medved, J. and Mrvar, P., 2011, 'Solidification of Hipereutectoid high speed steel for rolls', *METALURGIJA* 50(1), 29-32.

23. 2nd European Rolling Conference: Section Hot strip rolling 2, Sweden, 2000.

24. Molinari, A., Styraffelini, G., Tomasi, A., Biggi, A. and Corbo, G., 2000, 'Oxidation behaviour of ledeburitic steels for hot rolls', *Materials Science and Engineering* A280, 255-262.

25. Jiangtao, D., Zhiqiang, J. and Hanguang, F., 2007, 'Effect of RE-Mg complex modifier on structure and performance of high speed steel roll', *Journal of Rare Earths* 25, 259-263.

26. Wang, M., Chen, L., Wang, Z. and Bao, E., 2012, 'Effect of rare earth addition on continuous heating transformation of a high speed steel for rolls', *Journal of Rare Earths* 30(1), 84-89.

27. Li, Y.J., Jiang, Q.C., Zhao, Y.G. and He, Z.M., 1996, 'Modification of M2 cast high speed steel', *Acta Metall.* 32, 313-317.

28. Yu, X.Q., Guan, S.K., Wang, L.G., Gan, Z.P. and Chuan, X.Z., 2003, 'Effect of modification on microstructure and mechanical property of high speed steel used for composite roll', *Journal of Iron and Steel Research* 15, 46-51.

29. Dobrzanski, L.A., Zarychta, A. and Ligarski, M., 1997, 'High-speed steels with addition of niobium or titanium', *Journal of Materials Processing Technology* 63, 531-541.

30. Hashimoto, M. and Takigawa, T., 1996, *37th MWSP Conference 1996* proceedings, Vol. 33, pp. 275-282.

31. Li, Y.J., Jiang, Q.C., Zhao, Y.G. and He, Z.M., 1997, 'Behaviour of aluminium in M2 steel', *Scripta Mater* 37(2), 173-177.

32. Pan, F., Ding, P., Zhou, S., Kang, M. and Edmonds, D.V., 1997, 'Effects of silicon additions on the mechanical properties and microstructure of high speed steels', *Acta Mater.* 45(11), 4703-4712.

33. Oda, N., Fleiner, P. and Hattori, T., 2013, 'Latest developments of a new technology HSS work roll for later stands (F4-F7) in hot strip mill finishing strains', *Association of Iron and Steel Technology Conference 2013 proceedings*, Pittsburgh, USA, November, 2011, pp. 56-62.

34. Oda, N., Segawa, T. and Nozaki, Y. (Hitachi Metals) 2015, *Centrifugally cast composite roll and it's production method*, US Patent 9 221 232.

35. Astini, V., Prasetyo, Y. and Beak, E.R., 2012, 'Effect of boron addition on the microstructure and mechanical properties of 6.5%V-5%W High speed steel', *Met. Mater. Int.* 18(6), 923-931.

36. Cen, Q. and Fu, H., 2013, 'A study of heat treatment of high-boron high-speed steel roll', *Mat. Wiss. Werkstofftech* 44(7), 612-617.

37. Fu, H., Zhongze, D., Ping, L., Yehua, J., Rong, Z., Qihong, C., Jianqiang, H., Yongping, L. and Hongxing, G., 2012, 'On microstructure and performance of tempered high-boron high-speed steel roll', *China Foundry* 9(3), 252-257.

38. Karagoz, S. and Fischmeister, H., 1987, *Steel Res.* 58.

39. Zhang, X., Liu, W., Sun, D. and Li, Y., 2007, 'The transformation of carbides during austenization and its effect on the wear resistance of high speed steel rolls', *Metallurgical and Materials Transactions* 38A, 499-505.

40. Brandis, H., Haberling, E. and Weigand H.H., 1983, 'Metallurgical aspects of carbides in high speed steels', *Thyssen Edelstahl: Technische Berichte Special Issue*.

41. Vitry, V., Nardone, S., Breyer, J.P., Sinnaeve, M. and Delaunois, F., 2012, 'Microstructure of two centrifugal cast high speed steels for hot strip mills applications', *Materials and Design* 34, 372-378.

42. Lecomte-Beckers, J. and Tchuindjang, J.T., 2005, 'Use of microscope for identification of complex MC, M_2C, M_7C_3, M_6C and $M_{23}C_6$ carbides in high speed steels', *G.I.T Imaging and Microscopy* 2, 2-3.

43. Luan, Y., Song, N., Bai, Y., Kang, X. and Li, D., 2010, 'Effect of solidification rate on the morphology and distribution of eutectic carbides in centrifugal casting high-speed steel rolls', *Journal of Materials Processing Technology* 210, 536-541.

44. Honeycombe, R. and Bhadeshia, H.K.D.H., 1995, *Steels: Microstructure and Properties*, London, chapter 5.

45. Benazza, A., Ziadi, A., Serier, B., Bouiadjra, B.B. and Moutabout, B., 2007, 'Hot compression and fracture toughness of HSS composed hot strip work rolls', *Journal of Materials Science* 42, 834-840.

46. Kim, C.K., Lee, D.G. and Lee, S., 2007, 'Correlation of microstructure and fracture properties of five centrifugal cast high speed steel rolls', *Materials Science and Technology* 23(9), 1065-1074.

47. De Colnet, L., Pirard, E., Lecomte-Beckers, J., Boeraeve, P., Ghfiri, R. and Tchuindjang, J.T., 2001, 'Quantitative description of MC, M2C and M7C3/M6C carbides in high speed steel rolls', *MSMF-3rd International Conference 2001 proceedings*, Czech republic.

48. Akersrolls n.d., *Akers SPECTRA R Product Data Sheet*, viewed 20 February 2016, from http://www.akersrolls.com/globalassets/the-akers-group/products/product-data-sheets/steel-grades---forged-rolls/cluster-mill-rolls---narrow-strip-mill-rolls/supra-1_edition0905.pdf.

49. Marichal Ketin n.d., *Marichal Ketin AURORA High Speed Steel*, viewed 20 February 2016, from http://www.mkb.be/Qualities/MK-Aurora.pdf.

50. Marichal Ketin n.d., *Marichal Ketin KOSMOS High Speed Steel*, viewed 20 February 2016, from http://www.mkb.be/Qualities/MK-Kosmos.pdf.

51. Marichal Ketin n.d., *Marichal Ketin SIRIUS High Speed Steel*, viewed 20 February 2016, from http://www.mkb.be/Qualities/MK-Sirius.pdf.

52. Zhou, L., Sun, D., Liu, C., Li, C. and Yao, L., 2008, 'Scratch behaviour of high speed steels for hot rolls', *Journal of University of Science and Technology Beijing* 15, 402-406.

53. Thonus, P., Herman, J.C., Breyer, J.P., Sinnaeve, M., Charlier, A., Liquet, D. and Marquet, R., 1997, *38th MWSP Conf. 1997 proceedings*, Warrendale, pp. 43-49.

54. Adams, T.P. and Collins, D.B., 1998, *40th MWSP Conference 1998 proceedings* 36, pp. 427-431.

55. Adams, T.P. and Collins, D.B., 1999, 'Properties of hot strip mill rolls and rolling', *Rolls for the metalworking industries*, Iron and Steel Society.

56. Lecomte-Beckers, J., Tchuindjang, J.T., Ernst, R. and Breyer, J.P., 2004, 'Structural Investigations of HSS rolls for hot strip mill', *41st Rolling Seminar Processes: Rolled and Coated Product 2004 proceedings*.

57. Martiny, F. and Sinnaeve, M., 2001, 'Improved roughing work rolls for the hot rolling of low carbon and stainless steel', *43rd Mechanical Working and Steel Processing Conference 2001 proceedings*.

58. Hwang, K.C., Lee, S. and Lee, H.C., 1998, 'Effects of alloying elements on microstructure and fracture properties of cast high speed steel rolls Part 2: Fracture Behaviour', *Materials Science and Engineering* A254, 296-304.

59. Boccalini, M., Sinatora, A. and Matsubara, Y., 2000, *Rolling Seminar: Processes and Rolled and Coated Products*, Curitiba, Brazil.

60. Fu, H., Qu, Y., Xing, J., Zhi, X., Jiang, Z., Li, M. and Zhang, Y., 2008, 'Investigations on heat treatment of a high-speed steel roll', *Journal of Materials Engineering and Performance* 17(4), 535-542.

61. Fu, H. and Jiangdong, X., 2002, '7th Study of centrifugal casting technology of high speed steel compound roll collar', *65th World Foundry Congress 2002 proceedings*, Gyeongju, Korea, pp. 297-303.

62. Fu, H., Cheng, X., Du, Z., Lei, Y. and Feng, Z., 2009, 'Effect of quenching temperature on structure and properties of centrifugal casting high speed steel roll', *China Foundry Research and Development*, 15-19.

63. Rodenburg, C. and Rainforth, W.M., 2007, 'A quanitative analysis of the influence of carbides size distributions on wear behaviour of high speed steel in dry rolling/sliding contact', *Acta. Mater.* 55, 2443-2454.

64. Fu, H., Xiao, Q. and Xing, J., 2008, 'A study of segregation mechanism in centrifugal cast high speed steel rolls', *Materials Science and Engineering* 479A, 253-260.

65. Ichino, K., 1997, 'Development of centrifugal cast roll with high wear resistance for finishing stands of hot strip mill', *Kawasaki Steel Technical Report Number 37*.

66. Takigawa, H., Tanaka, T., Ohtomo, S. and Hashimoto, M., 1997, 'Development of high-speed tool steel rolls and their application to rolling mills', *Nippon Steel Technical Report Number 74*.

67. Tahir, M. and Widell, B., 2003, 'Roll wear evaluation of HSS, HiCr, and IC work rolls in hot strip mill', *Steel Research* 10, 624-630.

68. Hanlon, D.N. and Rainforth, W.M., 2003, 'The rolling sliding wear response of conventionally processed and spray formed high-speed steel at ambient and elevated temperature', *Wear* 255, 956-966.

69. Li, C.S., Liu, X.H. and Wang, G.D., 2008, 'New method for evaluating thermal wear of rolls in rolling process', *Journal of Iron and Steel Research* 15(6), 52-55.

70. Garza-Montez-de-Oca, N.F. and Rainforth, W.M., 2009, 'Wear mechanisms experienced by a work roll grade high speed steel under different environmental conditions', *Wear* 267, 441-448.

71. Zamri, W.F.H., Kosasih, P.B., Tieu, A.K., Zhu, Q. and Zhu, H., 2012, 'Variations in the microstructure and mechanical properties of the oxide layer on high speed steel hot rolling work rolls', *Journal of Materials Processing Technology* 212, 2597-2608.

72. Webber, R., 2011, '20th Anniversary of the HSS finishing mill work roll', *Southern African Roll Users Conference 2011 proceedings*, Vanderbijlpark, South Africa, October 6-11, 2011, pp. 80-83.

73. Davis, J.R. (ed.), 1995, *ASM Speciality Handbook: Tool Materials*, ASM International, USA.

74. Vander Voort, G.F., Manilova, E.P., Michael, J.R., Lucas, G.M., 2004, 'Study of Selective Etching of Carbides in Steel', *Microstructure and Microanalysis, 10*.

75. Vander Voort, G.F., 1999, 'Metallography Principles and Practice', *ASM International*.

76. Vander Voort, G.F. and Manilova, E.P., 2005, *Imaging Phases in Steels*, Advanced Materials and Processes.

77. Klimek, E.J., 1975, *A Metallographic Method for Measuring of Retained Austenite*, Metals Engineering.

78. Tayo Rolls n.d., *Tayo Rolls Limited High Speed Steel Rolls*, viewed 20 February 2016, from http://www.tayo.co.in/product-pdf/cr.pdf.

79. Hitachi Metals n.d., *Hitachi Metals America Limited High Speed Steel Rolls*, viewed 20 February 2016, from http://www.hitachimetals.com/materials-products/rolls/documents/HighSpeedSteelRolls.pdf.

80. Gontermann-Peipers n.d., *GPI – Product Catalogue Cast Roll*, viewed 20 February 2016, from http://www.gontermann-peipers.com/pdf/PRODUCT%20CATALOGUE%20CAST%20ROLLS.pdf.

81. Villares Rolls n.d., *Work Rolls for Hpt Strip Mills*, viewed 20 February 2016, from https://www.villaresrolls.com/web/en/produtos/Pages/produto7.aspx.

82. ESW n.d., *ESW Technical Information*, viewed 20 February 2016, from http://www.esw.co.at/docs/schmal_breitband_englisch_hot.pdf.